O'Brien, P.E., Cooper, A.K., Richter, C., et al., 2001
Proceedings of the Ocean Drilling Program, Initial Reports Volume 188

3. SITE 1165[1]

Shipboard Scientific Party[2]

PRINCIPAL RESULTS

Hole 1165A

Position: 64°22.22′S, 67°13.14′E
Start hole: 1500 hr, 28 January 2000
End hole: 0515 hr, 29 January 2000
Time on hole (hr): 14.25
Seafloor (drill-pipe measurement from rig floor, mbrf): 3548.1
Distance between rig floor and sea level (m): 11.1
Water depth (drill-pipe measurement from sea level, m): 3537
Total depth (drill-pipe measurement from rig floor, mbrf): 3553.5
Penetration (mbsf): 5.4
Coring totals: type: APC; number: 1; cored: 5.4 m; recovered: 100.6%.
Lithology: Unit I–diatom ooze and diatom clay

Hole 1165B

Position: 64°22.78′S, 67°13.14′E
Start hole: 0515 hr, 29 January 2000
End hole: 0530 hr, 4 February 2000
Time on hole (hr): 144.25
Seafloor (drill-pipe measurement from rig floor, mbrf): 3548.7
Distance between rig floor and sea level (m): 11.05
Water depth (drill-pipe measurement from sea level, m): 3537.65
Total depth (drill-pipe measurement from rig floor, mbrf): 4230.9
Penetration (mbsf): 682.2
Coring totals: type: APC; number: 18; cored: 148.3 m; recovered: 86.4%; type: XCB; number: 58; cored: 533.9 m; recovered: 57.3%.

[1]Examples of how to reference the whole or part of this volume.
[2]Shipboard Scientific Party addresses.

Ms 188IR-103

Lithology:
Unit I–diatom ooze and diatom clay
Unit II–diatom clay and diatom-bearing clay with color bands
Unit III–clay(stone) and diatom-bearing clay(stone)

Hole 1165C

Position: 64°22.77′S, 67°13.08′E
Start hole: 530 hr, 4 February 2000
End hole: 2030 hr, 14 February 2000
Time on hole (hr): 255.00
Seafloor (drill-pipe measurement from rig floor, mbrf): 3548.7
Distance between rig floor and sea level (m): 11.15
Water depth (drill-pipe measurement from sea level, m): 3537.55
Total depth (drill-pipe measurement from rig floor, mbrf): 4547.8
Penetration (mbsf): 999.1
Coring totals: type: RCB; number: 35; cored: 335.7 m; recovered: 80.2%
Lithology: Unit III–claystone and diatom-bearing claystone

Site 1165 is situated on the continental rise offshore from Prydz Bay over mixed pelagic and hemipelagic sediments of the central Wild Drift. The drift is an elongate sediment body formed by the interaction of sediment supplied from the shelf and westward-flowing currents on the continental rise. The site is in 3537 m of water and was selected to provide a record of sedimentation that extends back to the onset of contour current–influenced deposition on the rise. The main objective was to obtain a proximal continental rise record of Antarctic glacial and interglacial periods for comparison with other sites around Antarctica and with those of Northern Hemisphere ice sheets.

Prior to drilling, a single seismic-reflection profile was recorded across the location of Site 1165, using the ship's water gun, to verify the location of the site. Three holes were drilled at the site. Hole 1165A consisted of a mudline core that was dedicated to high-resolution interstitial water sampling. Hole 1165B was cored with the advanced piston corer (APC) to 147.9 meters below seafloor (mbsf) (86.4% recovery) and deepened with the extended core barrel corer (XCB) to 682.2 mbsf (57.3% recovery). Hole 1165C was washed down to a depth of 54 mbsf, where a single core was taken at an interval that had been missed in Hole 1165B. Continuous rotary core barrel (RCB) coring began at 673 mbsf and continued to a total depth of 999.1 mbsf, with 80% recovery. Coring operations were interrupted by five icebergs that came to within 200 m of the drill site and caused a total loss of 98 hr. Hole 1165C was successfully logged with the triple combination (triple combo) tool string from 176 to 991 mbsf and with the sonic tool from 176 to 580 mbsf.

Drilling at Site 1165 yielded a relatively continuous 999-m-thick sedimentary section of early Miocene- to Pleistocene-age terrigenous and hemipelagic deposits with only few minor (<2 m.y.) disconformities. Dispersed clasts (ice-rafted debris [IRD]) are present down to the bottom of the hole, but lonestones are infrequent below 500 mbsf (lower Miocene). Both dispersed clasts and lonestones are relatively abundant above 300 mbsf (middle Miocene and younger).

The sedimentary section is divided into three lithostratigraphic units that are characterized by cyclic variations between biogenic-bearing (lighter) and terrigenous-dominated (darker) intervals. The cyclic varia-

tions in lithology are also recorded as visual color alternations and cycles in spectrophotometer lightness factor (L*), bulk density, magnetic susceptibility, and other laboratory and downhole log parameters to varying degrees. In general, cores get darker downhole as biogenic intervals become thinner relative to the thickness of terrigenous-bearing intervals. For the same reason, light-dark cyclicity is more prominent above ~400 mbsf. Darker units generally have higher bulk density, magnetic susceptibility, and organic carbon (OC) values. The sediment consists mostly of quartz, calcite, plagioclase, K-feldspar, and a mixture of clay minerals, as well as minor hornblende and pyrite. Silt-sized components are mainly quartz, but plagioclase, biotite, amphibole, and other heavy minerals are common.

Unit I (0–63.8 mbsf) consists of structureless brown clay and diatom-bearing clay. There are beds with minor diatom-bearing greenish gray clay that have dispersed sand grains, granules, and lonestones. There is minor laminated silt and minor brown foraminifer-bearing clay. Foraminifers comprise 5%–15% of the sediment above 13 mbsf. One interval within Unit I (20–30 mbsf) is characterized by alternations between two facies like those of Unit II (i.e., Facies II-1 and II-2).

Unit II (63.8–307.8 mbsf) is characterized by alternations of two main facies that differ in color and composition. Facies II-1 consists of structureless, homogeneous, greenish gray diatom clay, and Facies II-2 is mostly dark gray diatom-bearing clay with some intervals of scattered silt laminae. Many lower boundaries of Facies II-2 are sharp, and upper boundaries are transitional with bioturbation that increases upward into Facies II-1. Higher amounts of siliceous microfossils and IRD (floating sand grains and pebbles) are found in Facies II-1 than II-2. Facies II-1 is characterized by lower grain density because of the higher diatom content. A third facies (II-3) occurs rarely and consists of several 15- to 40-cm-thick nannofossil chalk beds that have a sharp base and pass gradually up into Facies II-1. Within Unit II, three subunits are identified based on the different proportions of Facies II-1 and II-2. Subunit boundaries are at 160 and 252 mbsf and partially denote amounts of IRD, with greater amounts of IRD in Subunits IIA and IIC than in Subunit IIB.

Unit III (307.8–999.1 mbsf) comprises a section of thinly bedded planar-laminated claystone that is divided, like Unit II, into two main facies that differ in color, composition, and bedding characteristics. Facies III-1 consists of greenish gray bioturbated structureless clay and claystone and diatom-bearing clay and claystone with dispersed coarse sand grains and rare granule to pebble-sized lonestones. Facies III-2 is composed of dark gray thinly bedded planar-laminated clay and claystone with abundant silt laminae. Lonestone (dolerite, diorite gneiss, and mudstone) abundance in Unit III is low and decreases downhole.

In Facies III-1, the thickness of the greenish gray intervals is generally <1 m and some intervals have higher concentrations of silt- and sand-sized material. The upper contacts are commonly sharp, laminae are rare, and bioturbation increases upcore. Angular mud clasts and benthic foraminifers are present in this facies below 800 mbsf. Siliceous microfossil content is low.

Facies III-2 becomes increasingly fissile with depth and changes to very dark gray or black below 894 mbsf. Bioturbation is rare in Facies III-2, and light-color silt laminae are a conspicuous feature (average = 150–200 laminae/m). Many cross-laminated silt ripples are present, and ripples are more common below 673 mbsf than above. Microfossils are rare and seem to disappear completely below ~600 mbsf. Below 842

mbsf, laminae with calcite cement are present and sections of the core become increasingly cemented with what are most likely authigenic carbonates. A change to darker-color claystones occurs at 894 mbsf, where fracture patterns also become curved.

In both Facies III-1 and III-2, individual 0.5-cm-sized horizontal *Zoophycos* burrows are evident along with clusters of unidentified millimeter-sized burrows.

An excellent record of siliceous microfossils is found at Site 1165 down to 600 mbsf, where biogenic opal disappears because of an opal-A/opal-CT diagenetic transition. Neogene high-latitude zonal schemes for both diatoms and radiolarians yielded identification of 21 diatom and 12 radiolarian biostratigraphic datums between 0 and 600 mbsf. Below 600 mbsf, age assignments are inferred from calcareous nannofossils, which are present in only a few discrete intervals with moderate to good preservation of low-diversity assemblages. Nannofossils yield Pleistocene to earliest Miocene ages. Benthic foraminifers are more common than planktonics, which are rare. The foraminifers indicate several intervals of redeposited material.

A magnetostratigraphy was determined for Site 1165 for the interval 0–94 mbsf and below 362 mbsf. The magnetostratigraphic record and biostratigraphic ages, when combined, yield an age vs. depth model that shows relatively rapid deposition in early Miocene time (~120 m/m.y.), somewhat slower deposition in middle to late Miocene time (~50 m/m.y.), and even slower deposition since late Miocene time (~15 m/m.y.). From magnetostratigraphy, the bottom of Hole 1165C (999.1 mbsf) has an age of ~21.8 Ma. The uncertainty in ages is larger below 600 mbsf, where only few biostratigraphic ages exist to constrain the paleomagnetic reversal stratigraphy.

Measurements of rock magnetic properties in the interval 114–370 mbsf indicate that magnetic mineral concentrations (i.e., concentrations of magnetite) drop significantly, with nearly a complete loss of magnetic intensity. Shipboard analysis suggests that this unusual loss of magnetic signal is caused by diagenetic dissolution of magnetite in the presence of silica-rich pore-waters. A zone of low grain density is observed in cores from part of this zone ~140 mbsf and may also coincide with the disappearance of magnetite.

The interstitial water profiles document increasing downhole sediment diagenesis at Site 1165. Sulfate values decrease linearly from 30 to 2 mM in the interval from 0 to 150 mbsf, but increases occur in ammonium (20 to 384 µM), phosphate (3 to 10 µM), and alkalinity (3 to 8 mM) throughout the same interval because of destruction of organic matter. Ammonium increases (to 800 µM), phosphate decreases (to 0), and alkalinity decreases linearly (to 1 mM at 999 mbsf) throughout the interval from 150 to 400 mbsf. Concentrations of dissolved silica increase from 522 µM at the seafloor to a maximum of 1000 µM at 200 mbsf and reflect the dissolution of abundant siliceous microfossils. Silica values decrease from 400 to 999 mbsf. The theoretical opal-A/opal-CT transition is at ~600 mbsf based on measured downhole temperatures. A strong seismic reflection is observed at this depth. Below 150 mbsf, calcium and magnesium values correlate inversely, which suggests diagenetic control and an unidentified Ca-rich lithology below the drilled section. A decrease in potassium values below 50 mbsf and an increase in fine-grained K-feldspar, identified by X-ray diffraction (XRD) measurements, suggests an authigenic origin for the K-feldspars.

Hydrocarbon gas contents of cores are low (<400 ppmv) within the sulfate reduction zone down to ~150 mbsf. Below 150 mbsf, methane

increases rapidly and reaches values of 20,000–40,000 ppmv between 270 and 700 mbsf, and 40,000–100,000 ppmv from 700 to 970 mbsf. These headspace gas measurements indicate only the residual gas in the pore water of cores after outgassing upon retrieval to the surface. The gas concentrations are equivalent to ~8 to 35 mM dissolved methane when adjusted for sample size variation, density, and porosity. Cores deeper than 700 mbsf may contain more gas because of increased lithification and retarded outgassing. Ethane is present in headspace gas samples deeper than 157 mbsf, and the C_1/C_2 value shows the expected decrease with depth for the observed geothermal gradient at this site (secant temperature gradient of 43.6°C/km). OC contents of Site 1165 sediments are low (0.1 to 0.8 wt%), except for high OC (1.8–2 and 1.3 wt%) beds at 122 and 828 mbsf. Cores from within the gas hydrate stability zone (seafloor to 460 mbsf) were examined immediately upon recovery, but no hydrates were observed.

Acoustic velocities and shear-strength measurements increase as a result of normal compaction (in the upper 500 mbsf) and diagenesis (with a greater effect below 600 mbsf). Horizontal downhole *P*-wave velocities increase abruptly at 114 mbsf from ~1535 to 1575 m/s and then linearly from 114 to 603 mbsf. Other significant downhole *P*-wave velocity increases occur at 692 mbsf, 800 mbsf (to 2660 m/s), and 960 mbsf (to 2840 m/s). These abrupt increases are observed as reflections on seismic data.

Hole 1165C was logged with a single pass of the triple-combo tool from 176 to 994 mbsf and a single pass of the sonic tool from 176 to 580 mbsf. Total gamma-ray and bulk-density log traces covary, suggesting that lower-density diatom-bearing strata are present throughout the hole. The boundary between lithostratigraphic Units II and III at 305 mbsf is marked by a large fluctuation in total gamma-ray values, which suggests a shift in clay content at the boundary. The distinct silica- and calcite-cemented intervals observed in the cores are marked by inflections in most log traces.

Site 1165 provides paleontologic and sedimentologic evidence that numerous alternations or cycles between biogenic material and clay-sized terrigenous debris from Antarctica have occurred since earliest Miocene time. The cyclicity observed in the lightness values for two intervals (83–100 mbsf and 107–123 mbsf; in lithostratigraphic Unit II) in the cores was analyzed for spectral content to evaluate the potential effect of Milankovitch periodicities on biogenic/terrigenous sedimentation cycles at this site. For the shallower interval, significant spectral peaks are found at periods of 3.28, 1.45, 1.08, and 0.64 m thickness. A sedimentation rate of 3.5 cm/k.y. is reasonably well constrained for the interval and gives periods of 93.7, 41.5, 20.8, and 18.2 k.y., respectively. These periods are similar to the Milankovitch cycles of 100 k.y. (eccentricity), 41 k.y. (obliquity), 23 k.y., and 19 k.y. (precession), suggesting an orbitally forced origin for the light–dark cyclicity. For the deeper interval, significant spectral peaks are at 4.27, 1.55, 0.95, and 0.72 m, which have similar peak periodicity ratios to the upper interval, again suggesting an orbital origin for the deeper cycles. In the deeper interval, the sedimentation rate is less well constrained. But, by using the peak-to-peak ratios as a guide, an inferred sedimentation rate of 3.8 to 4.1 cm/k.y. would give the same periods as the shallow interval (i.e., 93.7, 41.5, 20.8, 18.2 k.y.). The observed lightness changes correlate also to variations in bulk density and magnetic susceptibility, indicating that the lightness (color) data likely document orbitally driven changes in the Site 1165 depositional environment since at least early Miocene

time. A similar approach has been used recently to detect orbital signals in upper Oligocene to lower Miocene sedimentary sequences drilled in the Ross Sea, Antarctica, by the Cape Roberts Project (Claps et al., in press). Milankovitch cyclicities have been reported for late Miocene-age and younger diatom-bearing hemipelagic and terrigenous sediments at ODP Site 1095 from a drift deposit, like the Wild Drift, adjacent to the Antarctic Peninsula (Shipboard Scientific Party, 1999).

In addition to the cyclic variations, significant uphole changes occurred at Site 1165 from early to late Miocene times (Units III and II), and include an eightfold decrease in average sedimentation rates from 12 to 1.5 cm/k.y., an increase in the total clay content, an increase in amount of sand-sized and lonestone IRD, and other changes (e.g., first appearance of glauconite). The changes likely reflect shifts in the onshore Prydz Bay region (sediment source area) to paleoenvironments that produced less terrigenous sedimentation, a lower-energy current regime, and more floating ice at Site 1165 starting in middle Miocene time. The uphole shift to increased clay (~305 mbsf) and first appearance of glauconite (~220 mbsf) heralds (1) a mid-Miocene change to erosion of sedimentary basins on the shelf and (2) subsequent inferred overdeepening of the shelf to the large water depths of today. Such deep-cut erosion would be by grounded glaciers crossing the continental shelf and dispersing icebergs with entrained sediment. The times of lowest sediment supply, in the latest Neogene (i.e., above 60 mbsf), have upward-decreasing silica contents (i.e., fewer diatoms and sponge spicules) and varied (cyclic?) IRD concentrations, which may reflect increasing extent of sea ice cover and ice sheet fluctuations. During latest Neogene time, a widely recognized period of intense Antarctic (and Arctic) glacier fluctuations, thick debris flows blanketed the adjacent continental slope (Site 1167), but little sediment was deposited on Wild Drift (Site 1165).

BACKGROUND AND OBJECTIVES

Site 1165 is situated on the continental rise offshore from Prydz Bay (Fig. F1). It targets mixed sediment-drift channel-levee sediments of the central Wild Drift, an elongate sediment body formed by the interaction of sediment supplied from the shelf and westward-flowing currents on the continental rise. The site is in 3525 m of water and was selected to provide a record of sediment that extends back to the onset of contour current–influenced deposition on the rise.

The Prydz Bay continental slope and rise are underlain by >6000-m-thick post-Lower Cretaceous sediments. Kuvaas and Leitchenkov (1992) recognized two prominent seismic unconformities (P1 and P2). Reinterpretation of prior and recent seismic reflection data by the Prydz Bay Antarctic Offshore Stratigraphy Project (ANTOSTRAT) regional working group has resulted in the mapping of several unconformities (e.g., P3 and PP15) younger than P1 and P2 (Fig. F2). Surface P1 marks the transition from a lower, homogeneous acoustic unit with intermittent and irregular reflectors to an upper, heterogeneous unit denoted by well-stratified seismic facies. Kuvaas and Leitchenkov (1992) interpreted P1 to be a result of changes brought about by the start of glaciation in late Eocene to early Oligocene times; however, more-distal, recent seismic reflection data and drilling results near Kerguelen Plateau suggest that P1 may be as old as Cretaceous age (G. Leitchenkov, pers. comm., 1998). Surface P2, which denotes a distinct upward transition to seismic

F1. Bathymetry of the Prydz Bay region, p. 77.

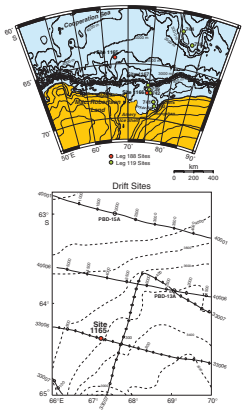

F2. Seismic section showing Reflectors PP12, P3, P2, and P1, p. 78.

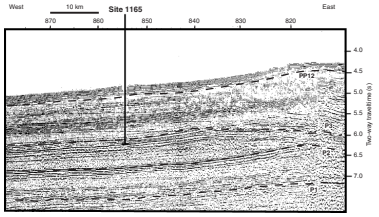

facies characteristic of submarine canyons with channel and levee deposits, reflects an increase in the bottom-current activity along the continental margin. The change in depositional environments may be due to initiation of the Antarctic Circumpolar Current in late Oligocene time (Kuvaas and Leitchenkov, 1992) or an episode of glaciation in early Oligocene time, when grounded ice sheets arrived at the continental shelf edge (ANTOSTRAT working group). P2 marks a time when large amounts of glacially derived sediment were initially deposited in thick prograding foreset beds (above P2) on the continental slope across the front of Prydz Bay and were carried oceanward by downslope turbidity flows and contour currents.

Unconformity P3 lies above P2 and forms the base of deposits that contain abundant well-stratified sediment-drift facies, including sediment waves. Such features imply that strong, presumably westerly flowing, bottom currents played a significant role in drift formation (Fig. F2). The changes at this level could be related to enhanced current activity resulting from the opening of deep-ocean gateways (e.g., South Tasman Rise from Antarctica and/or Drake Passage). A shallower unconformity, PP12 (i.e., Reflector "A" of Mizukoshi et al., 1986), marks the start of deposition of the Prydz Channel Trough Mouth Fan and the distal well-stratified hemipelagic and turbidite deposits on the continental rise. Sediments above PP12 are believed to be of late Miocene or younger age from correlations with Ocean Drilling Program (ODP) Site 739 (ANTOSTRAT working group).

Site 1165 was placed in the central part of the Wild Drift where sediment is relatively thin to acquire a nearly complete record of the section down to unconformity P3 (Fig. F2). This site location would provide a record of ocean and ice sheet interactions (i.e., glacial–interglacial fluctuations of grounded ice within Prydz Bay) throughout the Neogene. Drilling at this site would also provide information on the timing of the major change in continental rise sedimentation denoted by regional unconformity P3 in addition to evidence of reasons for the change. The depth to P3 at Site 1165 is ~1020 mbsf, and if the position of the unconformity is—as anticipated—approximately lower Miocene, then average sedimentation rates would be ~40 m/m.y. If older, then rates will be lower. Glacial events recorded in sediments recovered at Site 1165 will be compared with those observed in slope and shelf drill sites from Leg 188 and prior ODP Leg 119 sites in Prydz Bay. The ultimate objective is to obtain a proximal continental-rise record of Antarctic glacial and interglacial periods for comparison with sites around Antarctica and with those near Northern Hemisphere ice sheets.

OPERATIONS

Port Call

Leg 188 began on 10 January 2000 at 1027 hr with passage of the first line ashore to Berth "E" of Victoria Quay, Fremantle, Australia. After a 6-day port call, the last line was released at 0606 hr on 16 January from the pier, and the *JOIDES Resolution* transited to a location off Rottnest Island for shallow-water positioning testing. Approximately 8 hr was spent testing two custom-built Nautronix positioning beacons in ~30 m of water. By 1800 hr on 16 January 2000, the *JOIDES Resolution* was under way at full speed to the first site of Leg 188.

Fremantle to Site 1165

The 2676-nmi sea voyage to proposed site PBD-12B was accomplished in 12 days at an average speed of 9.6 kt. Several severe (force 10/12) gales were encountered en route. The storms led to several course changes and speed reductions that were due to sea state. At times the vessel was rolling 10°–15° and pitching 6°–8°. Swells of 12 m and seas as high as 3 m were not uncommon. Conditions began to improve considerably near 60°S latitude.

At 0930 hr on 28 January 2000, the vessel slowed down to 6 kt while the seismic equipment was deployed. The objective was to conduct a single-channel seismic survey to confirm the precruise survey data. The seismic survey was concluded by 1400 hr on 28 January, and the seismic equipment was retrieved.

Site 1165

Hole 1165A

A beacon was dropped on the Global Positioning System (GPS) coordinates of Site 1165 at 1500 hr on 28 January 2000. Once the hydrophones and thrusters were deployed and the vessel settled on location, the corrected precision depth recorder (PDR) depth referenced to the dual elevator stool indicated a seafloor depth of 3552.4 meters below rig floor (mbrf), equivalent to 3541.3 meters below sea level (mbsl).

Hole 1165A was spudded using the APC at 0450 hr on 29 January 2000. The hole was scheduled for a single mudline core, which recovered 5.43 m of sediment and placed the drill pipe–measured seafloor depth at 3537.0 mbsl. The bit was pulled clear of the mudline, and the hole was abandoned at 0515 hr.

Hole 1165B

An offset was not deemed necessary, and Hole 1165B was spudded at 0610 hr on 29 January 2000. The APC bit was positioned at 3534.95 mbsl and the water depth was established at 3537.65 mbsl, based on recovery of the mudline core. APC coring continued through Core 18H to a depth of 148.3 mbsf (Tables T1, T2). Piston coring was abandoned at that depth because of a continuing problem with jammed liners and poor recovery. Adara temperature tool measurements were taken at the mudline and at the depth of Cores 4H, 7H, 10H, and 14H. Data from the position of Core 7H could not be retrieved. Coring proceeded using the XCB. Operations were suspended when iceberg Nora approached to within 2.0 nmi of the drill site. Core 29X was recovered from a depth of 252.4 mbsf, and the drill string was pulled up to 50 mbsf. At 1630 hr on 30 January 2000, the iceberg had moved to a distance of 2.6 nmi on a course that was taking it directly away from the drill ship. XCB coring resumed at 1800 hr on 30 January. Coring proceeded with excellent results through Core 67X to a depth of 607.3 mbsf. The XCB system was pushed in hard material beyond its normal use to a depth of 682.2 mbsf (Core 76X) because it was assumed that the hard formation might be penetrated in a few tens of meters. Unfortunately, the steadily declining rate of penetration and poor core recovery indicated that this was not the case. The last XCB core was recovered on 3 February at 1500 hr, and the decision was made to terminate coring in Hole 1165B in favor of RCB coring. The hole was displaced with 18.8 bbl of cement, and the

T1. Coring summary, p. 173.

T2. Expanded coring summary, p. 174.

pipe was tripped back to the surface. The rotary table was cleared at 0530 hr on 4 February, ending operations at Hole 1165B.

Hole 1165C

The vessel was offset 50 m to the west, and Hole 1165C was spudded at 1805 hr on 4 February. The seafloor depth was established as 3537.55 mbsl. The hole was washed down to a depth of 54.0 mbsf, where Core 1R was taken from 54.0 to 63.6 mbsf, recovering an interval missed in Hole 1165B. A center bit was deployed, and the hole was drilled down to a depth of 673.0 mbsf. Continuous RCB coring (Tables **T1, T2**) began at that depth and continued until 1445 hr on 6 February, when iceberg Mona came to within 4 nmi of the drill site. Core 5R was recovered, the drill pipe was pulled back to a depth of 75.1 mbsf, and a free-fall funnel was deployed.

Mona approached within 2.1 nmi before moving on a path away from the ship. The pipe was tripped back in the hole at 0500 hr on 7 February, and RCB coring resumed at 1015 hr. A total of 19.25 hr was lost as a result of the approach of iceberg Mona. Continuous RCB coring continued until iceberg Lea headed toward the drill site on a southeasterly course. At 2015 hr on 8 February, coring had to be suspended after recovering Core 13R from a depth of 893.6 mbsf. Lea was moving rapidly toward the drill site at a speed of 0.7 kt and with a closest point of approach of 1.0 to 3.0 nmi, depending on the assumed course. The drill string was pulled to a depth of 75.1 mbsf. At 0600 hr on 8 February, the iceberg reversed course to north-northwest and sped up to 0.3 kt. Lea appeared to be moving away by 1115 hr on 8 February and was no longer considered a threat to drilling operations. The drilling assembly was run to bottom, and at 1515 hr on 9 February continuous RCB coring resumed. A total of 19.0 hr was lost due to the first encounter with iceberg Lea.

Coring proceeded with excellent results until Lea turned around and headed back toward the location, closing to within 5.0 nmi. Coring was suspended with the recovery of Core 32R from a depth of 970.2 mbsf, and the drill string was pulled to a depth of 75.1 mbsf. Lea moved to within 0.5 nmi of the ship's position at 2015 hr, on a course and bearing likely to bring it even closer to the drillship. The decision was made to pull the drill pipe clear of the seafloor and to move the ship 0.7 nmi away from the location. Lea passed within 200 m of Site 1165. Ultimately Lea moved away, and the ship moved back over the location. Hole 1165C was reentered at 0250 hr on 11 February, the pipe was run to bottom, and coring was resumed by 0915 hr. A total of 25.0 hr was lost as a result of the second encounter with iceberg Lea.

Only one core (33R) was recovered before another iceberg, Bertha, approached to within 5.0 nmi of Site 1165. The drill string was pulled to the surface for the third time. Before Bertha moved out of range, another smaller, apparently wind-driven iceberg, Bertie, moved into the safety zone. At 1145 hr on 12 February, Bertie was 3.7 nmi away from the location and moving away. The drill string was run back into the hole. A total of 28.0 hr was lost because of icebergs Bertha and Bertie.

Cores 34R and 35R were recovered before coring ended at a total depth of 999.1 mbsf. The pipe was raised to 89.7 mbsf, and preparations for logging were made.

Logging Operations in Hole 1165C

The first suite of logging tools was ready to be deployed at 0915 hr on 13 February. A 2-hr interruption was caused by an iceberg that was

headed to the location from a distance of 3.9 nmi but changed course abruptly away from the drill site. The first logging string, the triple combo, was deployed at 1200 hr. The triple-combo string was composed of the dual-induction tool model E (DITE), high-temperature lithodensity sonde (HLDS), neutron array porosity sonde (APS), and high-temperature natural gamma sonde (HNGS). Unfortunately, the winch operator was unable to lower the tools past 118.3 mbsf. All attempts to pass beyond the tight spot or ledge were futile, and the decision was made to recover the logging tools and lower the drill string three additional stands to 175.9 mbsf. This time the tools reached 991.3 mbsf, or 7.8 m above the total depth of the hole. Good logs were recovered from this run, and the tools were recovered at 2400 hr.

The tools for the second logging run consisted of the Formation MicroScanner (FMS), dipole sonic imager (DSI), and natural gamma tool. This string was run in the hole at 0215 hr on 14 February; however, a restriction in the hole prevented passage beyond 580.3 mbsf. A complete hardware failure prevented any FMS data from being collected. Sonic and natural gamma radiation (NGR) data were successfully obtained from the upper part of the hole. Hole 1165C was abandoned by setting a 30-m balanced plug cement.

The pipe trip from the seafloor commenced at 1315 hr, and by 2030 hr on 14 February the rig floor was secured, the thrusters were raised, the beacons were recovered, and the ship was under way for Site 1166.

SITE GEOPHYSICS

A short geophysical survey was performed upon approach to Site 1165 to verify prior multichannel seismic reflection (MCS) data used for site selection. The MCS survey had been conducted with transit satellite navigation, resulting in possible navigational errors. The Site 1165 presite survey consisted of one track line across the site (Fig. **F3**) using 3.5-kHz bathymetry and water gun seismic systems. A description of these systems is provided below.

The seismic line was run from southeast to northwest across the site at an average speed of ~6.5 kt. Good quality data were obtained (Fig. **F4**) following initial problems with the performance of the water gun in the cold water conditions. The presite survey confirmed that the proposed site was in the proper stratigraphic position, and drilling was completed as planned.

F3. Presite survey track line, p. 79.

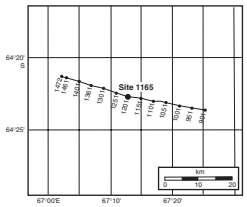

F4. Predrilling seismic survey, p. 80.

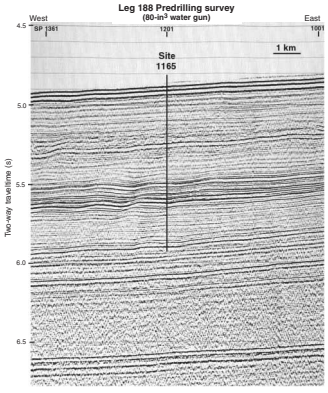

Navigation

Navigation data were collected in the underway geophysics laboratory using Ashtech GG24 conventional GPS navigation and were recorded by the WINFROG software system on a dedicated PC. Ship position was recorded every 60 s during transit and every 10 s during presite seismic surveys.

Bathymetry

Bathymetric data were obtained using a 3.5-kHz echo sounder (PDR) with a Raytheon CESP III Correlator driven by a Raytheon PTR105B transceiver. The 2-kW transmitter included a single EDO-type 323C transducer mounted in a sonar dome attached to the hull 40 m forward of the center of the moonpool. The signal was recorded on an EPC 8082

analog line-scanning recorder at a sweep speed of 1 s (750-m scale). The recorder was automatically annotated at fixed intervals with navigation system information. Depth readings were taken manually and entered into an Excel spreadsheet.

Seismic Reflection Profile

The seismic reflection profile was obtained using one 80-in^3 water gun as the seismic source. The gun was operated at ~1900 psi, towed ~20 m behind the ship, and fired every 10 s. The shot interval was equivalent to ~33 m at 6.5 kt. Reflections were recorded by a Teledyne model 178 hydrophone streamer with a 100-m-long active section containing 60 hydrophones, a 25-m-long stretch section, and a 150-m-long lead section. The seismic source and streamer were towed at estimated depths of 12–18 m. Depth-stabilizing "birds" were not available for use on the streamer.

Analog seismic data were displayed in real time on two graphic recorders, Raytheon model 1807M and EPC 8082, at sweep rates of 2 and 4 s with band-pass filter settings of 30–150 Hz. Data from each 10-s shot were sampled every 4 ms over a 4-s window. They were digitally recorded on a Sun Sparcstation 10 in SEG-Y format, using the "a2d" acquisition package, after application of a 20- to 250-Hz filter. Seismic data were copied to both 4- and 8-mm digital audiotapes during the site survey, then transferred to the Geoquest IESX system in the downhole measurements laboratory for evaluation and calculation of synthetic seismic traces. A large-scale seismic section was plotted in the underway geophysics laboratory for use during Site 1165 drilling.

LITHOSTRATIGRAPHY

Site 1165 is divided into three lithostratigraphic units (Fig. **F5**). Lithostratigraphic subdivision is based on a combination of the following data (Fig. **F6**): (1) visual core description, (2) biogenic and mineralogic composition from smear slides, (3) XRD mineralogy, (4) X-ray photographs, and (5) spectrophotometer reflectance.

Unit I, the uppermost lithostratigraphic unit, consists of structureless brown diatom clay with minor diatom-bearing greenish gray clay with lonestones (Fig. **F7A**). The upper part of this unit contains foraminifers. The underlying Unit II is composed of interbedded, structureless greenish gray diatom clay and dark gray diatom-bearing clay (Fig. **F7B**). The uppermost and lower parts of Unit II contain dispersed sand grains, granules, and lonestones. The lowermost unit, Unit III, consists of interbedded, dark gray, thinly bedded, planar-laminated claystones with abundant silt laminae and thin beds of greenish gray bioturbated claystone containing rare dispersed sand grains and granules (Fig. **F7C, F7D**). Bioturbation is pronounced in Unit I and the upper part of Unit II but decreases in the lower part of Unit II; bioturbation in Unit III is rare.

Unit I

Intervals: Cores 188-1165B-1H through 6H and Core 188-1165C-1R
Depth: 0–63.8 mbsf
Age: Pleistocene to early Pliocene.

F5. Lithostratigraphic subdivision, p. 81.

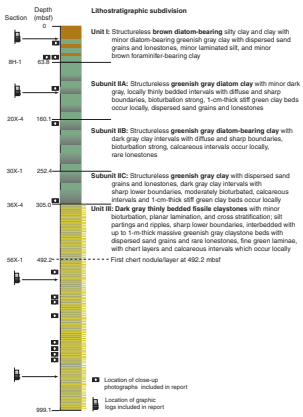

F6. Composite stratigraphic section, p. 82.

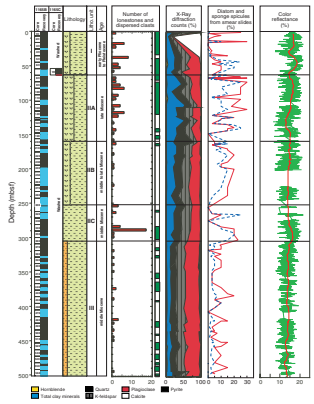

F7. Graphic logs illustrating facies associations, p. 85.

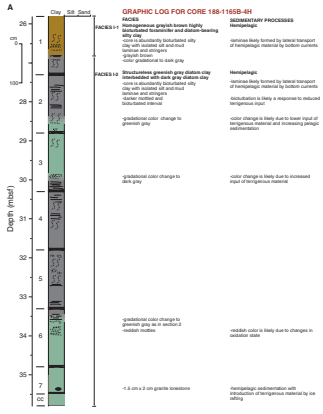

Unit I is characterized by a transition from grayish brown diatom ooze to structureless yellowish gray to brown diatom clay that becomes increasingly interbedded with structureless greenish gray diatom clay downhole. Four facies are recognized in Unit I (Table T3). Facies I-1 consists of structureless yellowish gray (2.5Y 5/2) to brown (10YR 4/2) diatom clay. Siliceous microfossils are abundant and foraminifers are common. Facies I-2 consists of structureless greenish gray (5GY 5/1) diatom clay interbedded with dark grayish brown (2.5Y 4/2) to dark gray (2.5Y 4/0) diatom clay (Fig. F8). Silt laminae and stringers are present in Facies I-2 between 26.6 and 33.5 mbsf (Fig. F9). Facies I-3 consists of dark grayish brown (2.5Y 4/2) diatom ooze. Facies I-4 consists of yellowish gray to brown diatom clay similar to Facies I-1 with scattered mud clasts and sharp flamelike contacts (e.g., Fig. F10; Sample 188-1165C-1R-6, 20–90 cm), and in one bed (Sample 188-1165B-6H-5, 70–75 cm), reworked pseudomorphs of Paleogene foraminifers are present (see "Biostratigraphy and Sedimentation Rates," p. 21).

In both Facies I-1 and I-2, a reddish brown color (5YR 5/3) with diffuse boundaries is observed in some decimeter-scale intervals. Reddish brown and dark brown mottling is also common. Bioturbation is pervasive, but individual burrows can be identified locally. Diatom ooze (Facies I-3) is present downhole only from 0 to 2.5 mbsf. Based on smear slides, siliceous microfossils (primarily diatoms), sponge spicules, and radiolarians are abundant throughout Unit I. Locally, foraminifers constitute between 5% and 15% of total sediment components in the upper 13.3 m of Unit I. Below 20 mbsf, the diatom-bearing clays contain more silt and the biogenic components gradually decrease downhole. The silt grains are predominantly composed of quartz with minor feldspar and opaques. Dispersed sand grains, granules, and pebble-sized lonestones are present throughout Unit I. Clast lithologies are mainly granite, gneiss, and dolerite.

Interpretation

Facies I-1 has a high biogenic component, is bioturbated, and lacks sedimentary structures that would indicate current activity; therefore, it is a hemipelagic sediment that drapes the seafloor. Facies I-2 is probably of similar hemipelagic origin, but minor current activity during deposition caused the observed laminations and interbedding of different colored beds. Facies I-3 has a high concentration of biogenic material (e.g., diatoms), indicating that it is a pelagic deposit. Facies I-4 displays soft-sediment deformation features, mud clasts, and irregular bedding contacts indicative of mass movement. The presence of reworked pseudomorphs of Paleogene foraminifers, probably derived from erosion of the adjacent continental shelf, suggests mass movement originally on the upper slope or continental shelf break.

Lonestones and dispersed sand grains indicate ice rafting during deposition of Unit I. The increase in biogenic components uphole throughout Unit I suggests a gradual reduction in the relative input of fine siliciclastic material over time. The patchy presence of foraminifers may indicate episodic increases in foraminifer population in the overlying waters or occasional changes in the carbonate compensation depth (CCD).

T3. Facies description and characteristics, p. 175.

F8. Diatom clay (Facies I-2) in Unit I, p. 89.

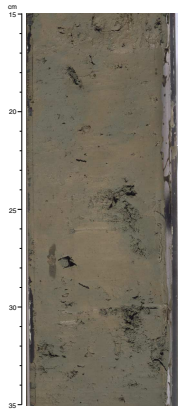

F9. Silt laminae and stringers in Unit I, p. 90.

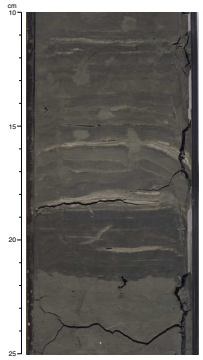

F10. Injection structure and abrupt color changes in Unit I, p. 91.

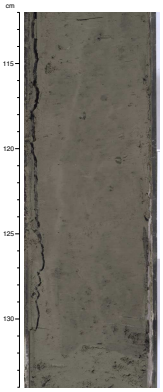

Unit II

Interval: Cores 188-1165B-8H through 36X
Depth: 63.8–307.8 mbsf
Age: middle to late Miocene

Subunit IIA

Interval: Cores 188-1165B-8H through 20X
Depth: 63.8–160.1 mbsf
Age: middle to late Miocene

Subunit IIB

Interval: Cores 188-1165B-20X through 28X
Depth: 160.1–252.4 mbsf
Age: middle to late Miocene

Subunit IIC

Interval: Cores 188-1165B-30X through 36X
Depth: 252.4–307.8 mbsf
Age: middle to late Miocene

Unit II, which begins at 63.8 mbsf, is defined by the absence of brown clay at the top of Core 188-1165B-8H. Unit II is characterized by alternations of two main facies. A third facies is recognized in a few beds. Facies II-1 consists of structureless, homogeneous greenish gray (5GY 5/1) diatom clay, whereas Facies II-2 consists of mostly dark gray (5GY 4/1) diatom-bearing clay that shows local thin color banding that may be parallel lamination (Fig. F11). Some intervals of Facies II-2 contain scattered silt laminae, and many lower boundaries of Facies II-2 are sharp. Facies II-1 contains higher amounts of siliceous microfossils and floating sand grains and pebbles than Facies II-2 (Fig. F12). Facies II-1 has rare darker green laminae and up to 1-cm-thick clay beds that contain glauconite, scattered fish teeth, and a higher proportion of diatoms than surrounding sediment. XRD measurements demonstrate that the dominant clay minerals in Facies II-1 are illite, kaolinite, minor chlorite, and illite-smectite mixed-layer clays (see "X-Ray Diffraction Mineralogy," p. 17). Facies II-2 has clay composition similar to Facies II-1 but lacks illite-smectite mixed layer clays. Silt grains identified in smear slides include quartz, feldspar, and opaques. Sand and silt-sized glauconite grains are present in trace amounts down to 213.9 mbsf.

Facies II-3 is represented by several 15- to 40-cm-thick beds of nannofossil chalk (e.g., Samples 188-1165B-20X-5, 114–131 cm; 24X-3, 68–105 cm; and 24X-CC). The chalk beds have sharp bases and pass gradually up into Facies II-1 with increasing diatom abundance and decreasing proportions of nannoplankton. Paleontological examination of the best-developed bed of Facies II-3 in Sample 188-1165B-24X-CC reveals an almost monospecific deposit of *Reticulofenestra perplexa* (see "Biostratigraphy and Sedimentation Rates," p. 21). The sediment color changes from white at the base to green gray at the top (5BG 7/1 to 5G 7/1).

The difference in proportions of the two main facies can be used to subdivide Unit II into three subunits. Subunit IIA starts at 63.8 mbsf and is dominated by Facies II-1. The thickness of Facies II-1 beds varies

F11. Color banding and planar lamination in Unit II, p. 92.

F12. Photomicrographs of dark gray diatom-bearing clay and greenish gray diatom clay, p. 93.

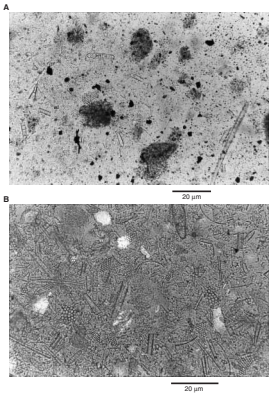

from 1.5 to 5 m, whereas the Facies II-2 beds are <1 m thick. Subunit IIA contains up to 1-cm-thick stiff clay beds in Facies II-1 (e.g., Samples 188-1165B-13H-3, 88–89 cm, and 96–97 cm) and rare planar silt laminae within Facies II-2 (e.g., Sample 188-1165B-13H-2, 80 cm; Fig. F11).

The top of Subunit IIB is placed at 160.1 mbsf, where a general decrease in siliceous microfossils, compared to Subunit IIA, occurs. In Subunit IIB, Facies II-1 and II-2 are of similar thickness, generally 1–2 m. In the upper part of Subunit IIB, two beds of Facies II-3 are present (Fig. F13), and bioturbation is moderate throughout the subunit. The silt fraction of Subunit IIB contains quartz, feldspar, and opaques, and up to 2% garnet. Subunit IIB has fewer pebble-sized lonestones, floating granules, and sand grains than Subunits IIA and IIC.

The Subunit IIB/IIC boundary occurs at 252.4 mbsf, based on a downhole increase in coarse material (>2 mm) and an increase in the proportion of Facies II-1. Some Facies II-2 beds in Subunit IIC exhibit dispersed sand grains, granules, and lonestones and rare planar silt laminae (Fig. F14). Facies II-2 interbeds in this subunit have sharp lower boundaries, and some beds show thin color banding. Overall bioturbation is moderate. The proportion of pebble-sized lonestones, granules, and sand grains in Subunit IIC is similar to that in Subunit IIA and is higher than in Subunit IIB. The main clast lithologies are granite, biotite gneiss, dolerite, and black, high-grade metamorphic rock types.

F13. Thick calcareous bed within Subunit IIB, p. 94.

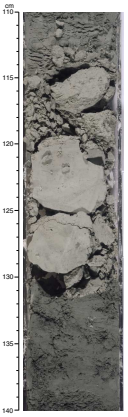

F14. Planar silt laminae within Subunit IIIC, p. 95.

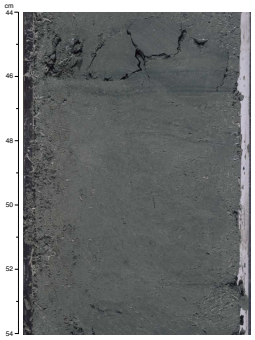

Interpretation

Facies II-1 has a high biogenic component and contains minimal evidence of current sorting. The laminae containing glauconite and fish teeth indicate periods of very slow terrigenous sedimentation. Therefore, Facies II-1 is interpreted as a hemipelagic sediment. Facies II-2 is a similar hemipelagic sediment, but its higher terrigenous content and silt laminae suggest higher siliclastic input and current activity than Facies II-1. The greater proportion of lonestones and floating sand grains in Facies II-1 than in Facies II-2 reflects a higher relative concentration of IRD. The higher IRD content in Facies I-1 may be a result of lower input of fine terrigenous sediment, so the IRD is less diluted (cf. Barker, Camerlenghi, Acton, et al., 1999). Facies II-3 is a pelagic sediment formed by an influx of nannoplankton caused by a brief period of high productivity and depression of the CCD (see "Biostratigraphy and Sedimentation Rates," p. 21). The uphole increase in the proportion of Facies II-1 relative to Facies II-2 from Subunits IIC to IIA indicates a progressive decrease in fine siliciclastic input and bottom-current activity.

Unit III

Interval: Cores 188-1165B-37X through 76X; 188-1165C-2R through 35R
Depth: 307.8–999.1 mbsf
Age: early Miocene

The Unit II/Unit III boundary is placed at 307.8 mbsf, based on the first downhole occurrence of thinly bedded planar-laminated claystone beds at 307.8 mbsf, a change in XRD mineralogy between 303.3 and 312.7 mbsf, and a change in composition based on smear-slide observations between 301.15 and 307.8 mbsf (Fig. F6). Unit III is characterized by an interbedding of two facies types, which differ in color, composition, and bedding characteristics. Facies III-1 is composed of dark gray

(5GY 4/1) thinly bedded planar-laminated clay and claystone that change color to very dark gray or black (N4) below 893.6 mbsf. Facies III-1 contains abundant silt laminae. Facies III-2 consists of greenish gray (5G 4/1) bioturbated, structureless clay and claystone and diatom-bearing clay and claystone with dispersed coarse sand grains and rare granule to small pebble-sized lonestones (Fig. F15). Planar to wavy lamination is present at the bottom of some units in Facies III-2.

The dark gray claystone of Facies III-1 becomes increasingly fissile with depth. Beds are generally <1 cm thick, and silt partings are present along bedding planes, where horizontal planar fractures occur (Fig. F16). Well-preserved sections of core show millimeter-scale silt laminations within the clay beds. Centimeter-scale, structureless, coarse sand beds are present locally between clay laminae (e.g., Samples 188-1165C-30R-5, 35 and 40 cm). Bioturbation is rare and is found in discrete decimeter-sized intervals.

Light-colored silt laminae are a conspicuous feature of Facies III-1. They are mostly flat or wavy 1- to 2-mm-thick single laminae but are also found as packets of several laminae of variable thickness, small lenses up to 3 mm thick, and isolated ripples with loaded bases (Fig. F17). The abundance of silt laminae varies through the section with some 1- to 3-m-thick intervals having several laminae per centimeter. On average, between 150 and 200 laminae are counted per meter, but laminae may be as frequent as 50 per decimeter. Many cross-laminated silt ripples are present. Ripples are more common below 673 mbsf than above. Silt laminae and silt ripples that are larger than elsewhere in the core are most common between 788 and 807 mbsf. Loading of silt ripples into underlying clay laminae is common. Between 788 and 807 mbsf, the thickness of the silt ripples increases up to 1 cm (Fig. F17). In this interval, some cores also display convergence between packages of silt laminae.

Smear slides of Facies III-1 show that siliceous microfossils are rare, and seem to disappear completely below ~600 mbsf. Below 841.5 mbsf, white-colored, calcite-containing laminae are present and sections of core become increasingly carbonate cemented. This carbonate appears to be diagenetic. Two deformed intervals are present, one in Core 188-1165C-10R between 755.2 and 755.6 mbsf and another in Cores 188-1165C-18R and 19R between 828.4 and 839.4 mbsf. The deformation consists of conjugate microfaults, folded silt laminae, and inclined bedding (Fig. F18). Below 893.6 mbsf, a change in color toward darker (N4) planar-laminated claystones occurs and the fracture patterns are curved as well as planar. Between ~675 and 850 mbsf, reflectance values intensify. Over the same interval, OC values increase (see "Organic Geochemistry," p. 47), suggesting that sediment geochemistry may affect the reflectivity.

In Facies III-2, laminae are rare and are generally present at the bottom of the beds in which they are found. Bioturbation increases upward. The thickness of the greenish gray intervals is usually <1 m. Upper contacts are generally sharp and in some intervals erosive, with sand grains concentrated as a lag along the contact with overlying Facies III-1 claystone. Arenaceous deep-water benthic foraminifers (see "Biostratigraphy and Sedimentation Rates," p. 21) and angular mud clasts are present in this facies below 799.5 mbsf (Fig. F19). The siliceous microfossil content is very low and decreases downhole. Some of the greenish gray intervals reveal higher concentrations of up to coarse sand-sized material (Sample 188-1165C-15R-2, 36–37 cm). Several beds

F15. Greenish gray claystone (Facies III-2) of Unit III, p. 96.

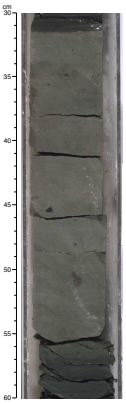

F16. Dark gray claystone (Facies III-1) of Unit III, p. 97.

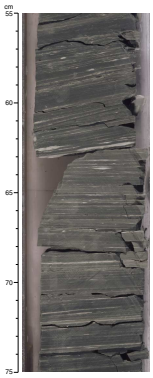

F17. Silt within dark gray claystone (Facies III-1) of Unit III, p. 98.

F18. Deformed interval within Unit III, p. 99.

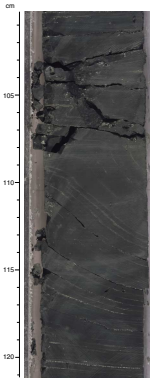

near the bottom of the sequence have sharp basal contacts with angular mud clasts along the base.

In both Facies III-1 and III-2, individual horizontal burrows ~0.5 cm in diameter (*Zoophycos*) can be distinguished as well as clusters of millimeter-sized burrows (Figs. F20, F21). The silt laminae and ripples of Unit III are quartz rich. Small amounts of quartz and feldspar are present within the clay. At 646.1 mbsf (Core 188-1165B-73X), a smear slide displays the presence of highly angular quartz grains (Fig. F22). Amphibole is present in trace amounts with a peak abundance of 2%–7% between 675 and 802 mbsf. Lonestone abundance in Unit III is low and decreases downhole. Pebble-sized lonestones are absent in Facies III-1 and are rare in Facies III-2 beds (Fig. F23). Lonestone composition is mainly dolerite, diorite gneiss, and mudstone. Below 492.2 mbsf, chert beds and nodules are present.

Interpretation

Facies III-1 has many characteristics of contourites (e.g., Gonthier et al., 1984; Rebesco et al., 1997; Heezen et al., 1966; Stow and Piper, 1984). The presence of packages of silt laminae within the claystone reflects the increase in strength of relatively slow-moving, near-continuous bottom currents. Other features characteristic of contourites are lag surfaces that record increased bottom-current velocities and extensively burrowed intervals that reflect comparatively low deposition rates (Wetzel, 1984). The intervals with microfaults and folded laminae were probably remobilized as local slumps. The convergence between packets of silt laminae may indicate deposition on low-angle bedforms or filling of scours.

Facies III-2 shows a high level of bioturbation with only rare laminae, indicating slow hemipelagic deposition accompanied by low current activity. The presence of reworked arenaceous deep-water benthic foraminifers confirms the low current activity. The sand grains and rare pebbles in this facies were either introduced by ice rafting or by sediment gravity flows originating on the upper slope. The few beds with sharp bases and mud clasts are probably local debris flows produced by slumping.

Smear-Slide Analysis

Smear slides were prepared from all major and minor lithologies comprising the sedimentary column of Site 1165. In the lower half of the column, smear slides were replaced by strewn slides, prepared from material scratched from the surface of the lithified sediment. The vast majority of the sedimentary column consists of fine-grained terrigenous material, largely in the clay size range, with various admixtures of silt-sized materials, with the addition of biogenic opal in the upper half of the sediment column (Fig. F12). Foraminifers are found in smear slides only in the first 13.3 m of Hole 1165B. The clay-sized components cannot be sufficiently resolved for analysis under the petrographic microscope but consist of both clay and primary minerals, according to XRD analyses (see "X-Ray Diffraction Mineralogy," p. 17). Silt-sized components are mainly quartz, but plagioclase, biotite, amphibole, and other heavy minerals are also present. The silt-sized quartz grains are angular to subangular, as are the few plagioclase grains. Plagioclase grains appear to be remarkably fresh and without any associated alteration products. Opaque minerals are present

F19. Benthic foraminifers and rip-up clasts (Facies III-2) of Unit III, p. 100.

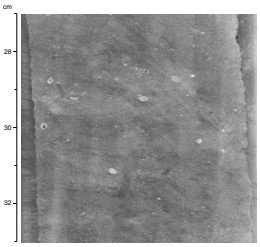

F20. Well-preserved trace fossil in claystone of Unit III, p. 101.

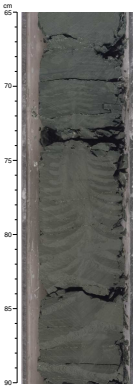

F21. Burrows and *Zoophycos* trace fossils from Unit III, p. 102.

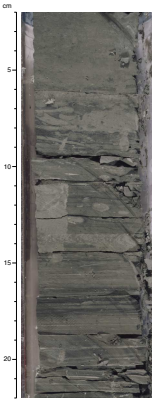

F22. Photomicrograph of metamorphic rock fragments in Unit III claystone, p. 103.

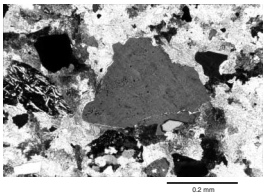

throughout but seem to be concentrated in the darker lithologies. Glauconite could be identified in a few smear slides, prepared from greenish gray clay (e.g., Sample 188-1165C-23R-6, 36 cm; 882.16 mbsf). These slides also contain a few fish teeth.

Silt persists throughout the entire sediment column; however, in Units I and II, where the contrast between "lighter" and "darker" lithologies is well developed, silt seems to form a higher percentage in the "green" sediment varieties compared to the "dark" ones. Individual silt laminae are particularly conspicuous in Unit III. Smear slides from these laminae reveal the predominance of well-sorted silt-sized quartz, in addition to clay-sized materials that could not be further identified. Near the bottom of Hole 1165C, white, thin (millimeter thick) laminae consist of micrite.

A graph representing the major biogenic opal components of the smear slides prepared from Holes 1165B and 1165C clearly illustrates the trend of diminishing biogenic opal with depth (Fig. F6). Units I and II (0–307.8 mbsf) show relatively high but variable percentages (between 1% and ~30%) of diatom frustules and sponge spicules. At the top of Unit III, the biogenic opal content decreases sharply to an estimated average of ~8%, although major fluctuations in biogenic opal content are clearly identifiable on smear slides. At ~490 mbsf, a further very sharp reduction in opal is evident. This reduction is associated with the first appearance of chert as a nodule or layer at 492.2 mbsf. The association between the disappearance of biogenic opal and the first appearance of identifiable chert probably reflects a diagenetic process (see "Inorganic Geochemistry," p. 43) and sets depth limitations on the interpretation of siliceous microfossils as paleoproductivity proxies at this site.

Calcium carbonate in the form of micrite appears on smear slides as an admixture to other sediment types, as matrix in thin laminae of silt and clay-sized components, or as pure micrite either in laminae or near-vertical veinlets (in the lower portion of Unit III). It is likely that the micrite is a replacement after nannofossil ooze, but further studies are needed to test this hypothesis.

Although smear slides are invariably biased against coarser (sand sized) components, the overall impression gleaned from the smear slides remains one of relative uniformity of the depositional environment, with grain-size variations largely confined to the silt and clay size ranges (sand-sized components are described in the barrel sheets).

X-Ray Diffraction Mineralogy

At Site 1165, 127 samples were analyzed for bulk mineralogy, and four samples were taken from the greenish gray and dark gray diatom-bearing clay beds of Facies II-1, II-2, III-1, and III-2 for clay mineralogy analysis. The bulk samples are primarily composed of quartz, calcite, plagioclase, K-feldspar, and a mixture of clay minerals, as well as minor amounts of hornblende and pyrite (Fig. F6). Within the first 140 mbsf, total clay content is relatively high compared to the lower depths. In Subunit IIA, the greenish gray diatom-bearing 1-cm-thick clay beds (Facies II-1) within the 107–110 mbsf interval have a lower relative abundance of feldspars, whereas the clay mineral content is slightly higher. Below 307.8 mbsf (Unit III), the relative abundance of plagioclase increases and the abundance of clay minerals decreases. Facies III-2 contains constant proportions of plagioclase, K-feldspar, and quartz throughout the interval from 307 to 999.1 mbsf.

F23. Lonestones within greenish gray beds of Unit III, p. 104.

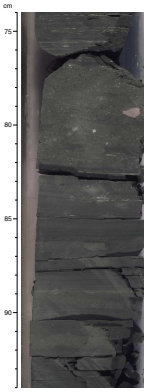

In Cores 188-1165B-14H (122.01 and 122.20 mbsf) and 37X (315.51 and 317.01 mbsf), four samples were taken from depths where alternations in color suggested a possible change in clay mineralogy. In each sample, the clay consists of illite, kaolinite, and minor chlorite. However, the greenish gray sediments (Facies II-1 and Facies III-2) exhibit a poorly defined phase with a broad and variable diffraction peak between 6° and 9°2θ that shifted after glycolation (Figs. F24, F25). This phase is tentatively identified as a minor variable amount of mixed-layer clay, most likely smectite-illite. After heating to 550°C, kaolinite was removed from all samples. Resultant relative abundances of clay minerals vary slightly. The greenish bed (Facies II-1) at 122.2 mbsf contains minor chlorite and has relatively smaller amounts of illite than the dark gray interval immediately above it at 122.01 mbsf (Fig. F24). A greenish clay bed of Facies III-2 at 315.51 mbsf contains illite, minor kaolinite, and mixed-layer illite-smectite, which are not identified in the darker Facies III-1 layer immediately below them at 317.01 mbsf (Fig. F25).

F24. X-ray diffractograms of clay-sized fractions of sediment from Hole 1165B, p. 105.

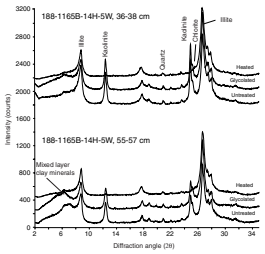

F25. X-ray diffractograms of clay-sized fractions of sediment from Hole 1165C, p. 106.

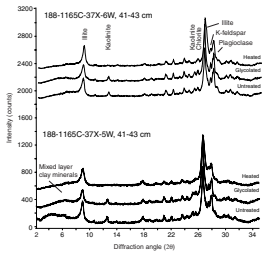

Ice-Rafted Debris

The fine-grained nature of the sediments at Site 1165 facilitates identification of lonestones (isolated clasts >2 mm). Lonestone lithologies are variable and include igneous intrusive (granite), extrusive (dolerite), metamorphic (gneiss and quartzite), and rare sandstone clasts. Most lonestones are subrounded to subangular. A rough estimate of IRD abundance and general characteristics was determined by visual examination of split cores and the use of X-radiographs. Thirty ~20-cm intervals of core were examined for IRD content using a portable veterinarian X-radiograph unit (see "Lithostratigraphy," p. 5 in the "Explanatory Notes" chapter).

In general, the number of ice-rafted clasts decreases downhole and isolated lonestones become rare below 500 mbsf (Fig. F6). Unit I contains common pebble-sized lonestones including large (>2 cm diameter) granite, dolerite, gneiss, and sandstone clasts. Dispersed pebbles, sand, and granules are particularly common in Cores 188-1165B-1H, 2H, 3H, 5H, and 6H (0–63.8 mbsf) and are rare in Core 4H (25.8–35.7 mbsf).

Scattered grains and granules are common throughout Subunits IIA and IIC but are less common in Subunit IIB. Gravel-sized lonestones are also less abundant within Subunit IIB. Subunit IIC contains an anomalously high number of lonestones within Core 188-1165B-34X (281.20–290.99 mbsf). This core was fractured and biscuited, and the observed lonestones are present within drilling slurry, suggesting that the high lonestone content within this core could be the result of drilling disturbance and downhole contamination.

In Unit III, isolated lonestones are present from 307.8 to ~500 mbsf. Below this depth lonestones are rare. The interval below 500 mbsf contains thin (<50 cm thick) structureless greenish gray claystone units with dispersed granules and sand grains.

Terrigenous IRD in the form of quartz grains (many with breakage features), lithic grains, and heavy minerals are also conspicuous in the coarse-grained fraction (>125 µm) of core-catcher samples used for foraminifer analysis (see "Appendix," p. 74). These results demonstrate that ice-rafted mineral and lithic grains are largely restricted to the sediment column above 500 mbsf (Fig. F26) and imply that the sediment delivery system changed at the 500-mbsf level.

F26. Downhole abundance of terrigenous debris in the >125-µm grain-size fraction, p. 107.

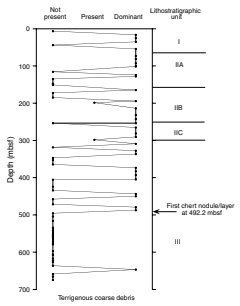

X-radiographs were chosen primarily so we could determine the difference in IRD content within greener and darker intervals from selected cores (188-1165B-10H through 188-1165C-5R). Examination of X-radiographs indicates that greener clays have a higher content of IRD than darker clay intervals; however, more green intervals than dark intervals were examined in the upper part of the hole (Units I and II), and some dark intervals studied do contain common IRD (Table T4).

T4. Lonestone content of different-colored facies from X-radiographs, p. 176.

Although downhole contamination of pebble-sized lonestones is a potential problem in unlithified segments of the succession, we suggest that the combined record of pebble-sized lonestones, granules, and sand grains within the sediments represents background IRD sedimentation caused by glacier ice reaching sea level in East Antarctica. Long-term variations are evident in the flux of IRD at Site 1165 and may result from glacial–interglacial climate variations; however, additional studies are needed to determine the details of these fluctuations. IRD content decreases downhole, has a low abundance within Subunit IIB, and has a much lower concentration in the lower part of Unit III below 500 mbsf. The low abundance of IRD in Subunit IIB suggests that few icebergs were nearby during the time of deposition. Within Units I and II, IRD was identified in X-radiographs within both green and dark intervals. In Unit III, dispersed grains are concentrated within Facies III-2 intervals. Some of these grains may have been introduced by mass-wasting processes, but others seem to be IRD. The small-scale changes in IRD concentration may reflect pulses of sedimentation, perhaps associated with rapid and multiple advance/retreat cycles of glaciers from surrounding regions or changes in fine-grained terrigenous input, resulting in dilution of IRD concentrations.

The majority of lonestones are high-grade metamorphic and granitic igneous rocks typical of large areas of East Antarctica and therefore of limited use in tracking provenance; however, two distinctive rock types are present in trace amounts that indicate a probable source in the Lambert Glacier drainage basin. The first is a red quartzose coarse sandstone that resembles the undated nonmarine red beds penetrated at Site 740 located in inner Prydz Bay. These sediments are part of the fill of the Lambert Graben and Prydz Bay Basin and are unlikely to be present anywhere else in the region. The other is a green phyllite or slate. Such low-grade rocks are known only in the region from the southern Prince Charles Mountains (Tingey, 1991); the northern Prince Charles Mountains and coastal areas are dominated by very high grade metamorphic rocks.

Discussion and Preliminary Interpretation

The sediments cored at Site 1165 may be generally interpreted as a succession of muddy contourites and hemipelagic deposits. They are fine grained and lack obvious graded bedding. Silt laminae and ripple crossbedding are present in the lower part of the hole, supporting the contourite interpretation.

Unit III is characterized by interbedded, dark gray, laminated claystones and thin (<50 cm thick) greenish gray claystones, which represent cyclical changes in depositional environments during the early to middle Miocene. Average sedimentation rates based on the age model range up to ~15 cm/k.y. for the lower Miocene part of the succession, and the abundance of silt laminae in the dark gray facies is substantial. Bioturbation is rare and lamination is well preserved, but graded beds were not observed. A possible explanation for the relatively high aver-

age sediment accumulation rates found in Unit III is high terrigenous input from East Antarctica. The increasing amount of silt and the presence of silt ripples and cross-bedding indicate stronger bottom-current activity for the lower part of the succession. The silt ripples may represent traction surfaces where the finer fraction has been winnowed during short periods of increased current activity. The greenish gray facies in Unit III contains lonestones and dispersed sand grains. Some intervals have angular mud clasts near the base of the structureless interval, which may be interpreted as rip-up clasts. The lonestones and sand grains may represent IRD, or they may have been introduced by local debris flows, as suggested by the rip-up clasts.

Unit II consists of alternating bioturbated dark and greenish gray clay facies, which probably represent cyclical changes from more hemipelagic facies (Facies II-1) to muddy contourites (Facies II-2). Average sedimentation rates based on the age model are up to ~5 cm/k.y. Similar structureless, strongly bioturbated, fine-grained facies are described from Pliocene–Pleistocene drift sediments in the North Atlantic (Stow and Holbrook, 1984). The subunits of Unit II result from variations in the proportion of more terrigenous-rich (II-2) and more hemipelagic (II-1) facies. Subunit IIC signals a change to lower current regimes and terrigenous input than during the deposition of Unit III. This change is partially reversed in Subunit IIB with an increase in the proportion of Facies II-2, but Facies II-2 does not display the same evidence for current activity as Facies III-2. Subunit IIA contains a greater proportion of hemipelagic sediment than Subunit IIB. The Unit III–Unit II transition also marks the beginning of significant IRD input (Fig. **F6**).

Unit I consists of hemipelagic and pelagic sediments and has several time breaks in the section (see **"Biostratigraphy and Sedimentation Rates,"** p. 21). The composition of Unit I is characterized by an upward decreasing terrigenous component. Below 2.5 mbsf, the terrigenous component is up to 50%, silt laminae are locally present, and the sediments are strongly bioturbated. The uppermost strata (0–2.5 mbsf) have a biogenic content of >50%, consistent with hemipelagic deposition with seasonal ice-free conditions. The age model for the hole (Fig. **F27**) demonstrates average sedimentation rates of 1.5 cm/k.y. for Unit I. The presence of glauconite and pseudomorphs of Paleogene foraminifers suggests that detritus from erosion of sedimentary sequences on the shelf was supplied to the site. The alternation of colored units suggests the possibility of glacial–interglacial cycles (cf. Barker, Camerlenghi, Acton, et al., 1999); however, further study is needed to establish this cyclicity.

The vertical facies distribution and mineralogical composition of the sediments suggests that a shift in depositional environment occurs at ~300 mbsf, the transition from Unit III to Unit II. The IRD content of the sediments rises, whereas average sedimentation rates progressively decrease throughout Units II and I. The shift to a high relative abundance of clay minerals and the presence of glauconite and shelf-derived foraminifers above ~300 mbsf, in contrast to below, reflect a change in provenance during the middle Miocene. Possible explanations for the uphole decrease in terrigenous sedimentation rates and increase in IRD concentrations in Unit I and II are (1) a decrease in bottom-current activity, inhibiting deposition from bottom currents on the continental rise; (2) a reduction in sedimentation rates related to drift development and its changing relief and morphology; or (3) a decrease in input of fine material by East Antarctic ice because of a reduction in basal melting and a transition to polar ice sheet conditions. Further studies, in

F27. Age-depth plot for the composite section represented by Holes 1165B and 1165C, p. 108.

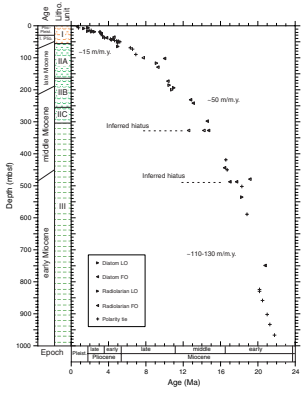

combination with evidence from other holes closer to the continent (e.g., Site 1167), will evaluate the relationship between Antarctic glaciation, drift development, and bottom-current activity.

BIOSTRATIGRAPHY AND SEDIMENTATION RATES

Introduction

Holes 1165B and 1165C represent a composite section of ~1000 m, which is divided into three primary lithostratigraphic units. Unit I (0 to ~64 mbsf) consists of a brown diatom-bearing silty clay spanning the uppermost Pleistocene to lowermost Pliocene. A disconformity (~1 m.y.) between uppermost Pleistocene and lower Pleistocene sediments is identified within Unit I at ~6 mbsf, based on integrated diatom and magnetostratigraphic data. Unit II (~64 to ~305 mbsf) is a greenish gray diatom-bearing clay spanning the uppermost Miocene to middle Miocene. Unit III (~305 to ~999 mbsf) is composed of dark gray, thinly bedded fissile claystones assigned to the lower middle Miocene to lower Miocene. Two possible hiatuses are identified in Unit III from biostratigraphic data. A middle Miocene hiatus (~2 m.y. in duration) at ~328 mbsf is identified from radiolarian data, and a possible hiatus of ~1 m.y. is also identified in the lower Miocene, at ~485–495 mbsf, from diatom data.

The approximate positions of the upper Pliocene to lower Miocene subepoch boundaries in Hole 1165B are recognized from diatom and radiolarian biostratigraphy. The lower Pliocene/upper Pliocene boundary is placed at ~30 mbsf (within Core 188-1165B-4H). The Miocene/Pliocene boundary is identified at ~50 to ~70 mbsf (between Cores 188-1165B-6H and 8H). The middle Miocene/upper Miocene boundary is placed at ~190–215 mbsf (within Cores 188-1165B-24X to 26X). The lower Miocene/middle Miocene boundary is recognized at ~450–485 mbsf (within Cores 188-1165B-51X to 55X).

Biostratigraphic zonal assignments and paleoenvironmental interpretations for Site 1165 are based on shipboard analysis of diatoms, radiolarians, benthic foraminifers, planktonic foraminifers, and calcareous nannofossils. The results of these initial investigations are summarized in Figures F28A, F28B, and F29 and are described below.

Planktonic Foraminifers

Introduction

Planktonic foraminifers are present in few samples at Site 1165. All records presented here are based on examination of 10-cm³ samples, predominantly from the core catchers. Preparation was designed to produce the residue on a 125-µm sieve, but the 63- to 125-µm fraction was also retained and examined.

Planktonic foraminifers were very rare in samples from Site 1165, which is not surprising in light of the water depth at the site and estimates of the depth of the CCD at ~1500 m (Quilty, 1985). Planktonic foraminifers contribute little to the chronostratigraphy at the site except, potentially, in the Pliocene–Pleistocene section.

F28. Core recovery, lithologic units, magnetostratigraphy, and biostratigraphic zones for Hole 1165B, p. 109.

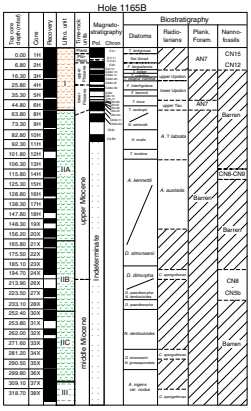

F29. Core recovery, lithologic units, magnetostratigraphy, and biostratigraphic zones for Hole 1165C, p. 111.

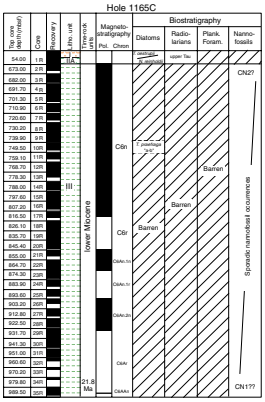

Hole 1165A

The record from Hole 1165A consists of one mudline core, Core 1H. A sample from the core catcher contains a few *Neogloboquadrina pachyderma* (Ehrenberg), which show signs of dissolution.

Hole 1165B

N. pachyderma is very abundant in the >125-µm fraction in Sample 188-1165B-1H-CC and constitutes ~80% of the residue. Specimens in this sample show signs of dissolution and commonly are partly infilled with black manganese oxides. They are accompanied by a minor benthic fauna. *N. pachyderma* is present through Cores 1H and 2H but is rare below that depth because of dissolution effects. Sample 188-1165B-6H-CC also contains very rare specimens of *N. pachyderma*.

Sample 188-1165B-2H-1, 70–75 cm, contains the most diverse late Neogene foraminifer fauna recovered in Hole 1165B. It is affected by CCD influence, but planktonic foraminifers are the dominant contributors to the residue. The sample contains *N. pachyderma* accompanied by *Globorotalia puncticulata* Deshayes and *Globorotalia scitula* Brady, an association that is not present elsewhere in the hole. This fauna seems anomalous, as it was at Site 747 (Berggren, 1992; ODP Leg 120). *G. puncticulata* is now routinely taken as a Pliocene species (some even regard it as more restricted to the early and mid-Pliocene) and *G. scitula* ranges through to the Holocene, although not at Site 747 nor here. Berggren (1992) referred to the Site 747 range as anomalous for *G. puncticulata*. At Site 747, the three species are present together at the bottom of Core 120-747A-2H, and Sample 188-1165B-2H-1, 70–75 cm, seems to be the equivalent. In Hole 747A, this level appears to be at ~2 Ma, applying the time/depth curve in Harwood et al. (1992)—an age that puts the expected foraminifer-based age in Hole 1165B in conflict with the paleomagnetic/diatom data. It is clear that the Pliocene–Pleistocene section at Site 747 needs to be reexamined. Another consequence of this sample is that it implies a warm-water influence to explain the presence of two species of *Globorotalia*.

An interesting "fauna" is present in Sample 188-1165B-6H-5, 70–75 cm. This sample contains thousands of particles in the 100- to 300-µm fraction that appear to be composed of dolomite. Compositional documentation will require postcruise investigation. Many are in the form of modified rhombohedra with an elongate A-axis and very curved faces. Others are in the form of pseudomorphs after three or four species of planktonic foraminifers, in which case coiling pattern and chamber arrangement are discernible but fine details such as apertural characteristics and wall structure are not. It is possible that the rhombohedra also represent pseudomorphs. With the limited information available, the pseudomorphs are consistent with species of late Eocene–early Oligocene age. They are present in concert with an enhanced glauconite content and a "dolomite"-glauconite intergrowth. They are thus from the same source, probably a Paleogene sequence in Prydz Bay or on the Mac. Robertson Shelf (Harris et al., 1997a; Quilty et al., 1999).

Below Sample 188-1165B-6H-5, 70–75 cm, no further planktonic species are documented until Sample 188-1165B-24X-CC, where planktonic forms constitute 65% of the assemblage, including *Globoturborotalita woodi* (Jenkins), *Globorotaloides variabilis, Globigerina bulloides* d'Orbigny, and *Globigerina praebulloides* Blow. This sample is tentatively placed in Zone AN5, even though the nominate zone

marker (*Neogloboquadrina nympha*) is absent. The reason for the absence is not clear, but this location is several degrees farther south than Berggren's (1992) study area; the reference taxon may not have reached this far south.

Well-preserved *Catapsydrax unicavus* Bolli, Loeblich, and Tappan is present in Sample 188-1165B-74X-1, 26 cm, and indicates that this sample is no younger than 17.3 Ma and is in Zone AN3 or older in the scheme of Berggren (1992).

A single poorly preserved specimen of *Catapsydrax dissimilis* (Cushman and Bermudez) was recovered from Sample 188-1165B-74X-CC and is consistent with the early Miocene age assigned by other fossil groups.

Hole 1165C

The richest pre-Pliocene planktonic fauna in Hole 1165C was recovered from Sample 188-1165C-2R-CC. It contains two genera (*Globorotalita* of the *woodi* group and *Catapsydrax* sp.), but no specimens are well enough preserved for identification to the species level. This level marks a dramatic change in the preservation of planktonic foraminifers. *C. unicavus* in Sample 188-1165B-74X-1, 26 cm, was well preserved, and *C. dissimilis* in the same sample was uncrushed and identifiable. Below this depth, planktonic species are severely crushed and unidentifiable. In contrast, benthic species are often very well preserved, even if the test seems delicate (e.g., those identified as *Eponides* sp. 1 and sp. 2).

Despite crushing, a few specimens identifiable to generic level were recovered from Sample 188-1165C-2R-CC, and *C. dissimilis* is present in Sample 188-1165C-11R-CC.

Benthic Foraminifers

Benthic foraminifers are present in many samples at Site 1165, but there is no obvious pattern to their stratigraphic location. Dissolution is expected at these water depths, and the sporadic presence of *Cyclammina incisa* throughout the sequence is consistent with this generalization. Even where faunas are present, they have little in common in structure or species composition. Thus, it is difficult to comment about their significance. Below Core 188-1165B-20X, evidence of dissolution is not prominent, and faunas from below that depth seem complete.

The few faunas that yielded calcareous benthic faunas at Site 1165 contain very little evidence of infaunal species (e.g., buliminid species are virtually absent); thus, the waters where these faunas accumulated were fully oxygenated. *Cyclammina* as an epifaunal genus (e.g., Gooday, 1990) supports this interpretation.

Epistominella vitrea is present in two samples at Site 1165 and appears to be roughly equally divided into dextrally and sinistrally coiled types.

Samples 188-1165A-1H-CC, 188-1165B-1H-CC, and 188-1165B-2H-CC contain a few calcareous benthic species that are outnumbered by the planktonic content. They are well preserved and probably in situ.

Sample 188-1165B-14H-CC yielded an abundant and diverse benthic foraminiferal fauna, containing both simple agglutinated and common calcareous forms and showing only minor evidence of dissolution. Planktonic species are absent. The dominant benthic form is *Oridorsalis umbonatus* (Reuss) (~50%), which van Morkhoven et al. (1986) regard as indicative of a mid-lower neritic depth. This suggests that the fauna, which shows no evidence of dissolution effects, probably originated on

the nearby continental shelf and made its way to the present site by mass movement.

Between Samples 188-1165C-12R-CC and 22R-CC, there is an association of agglutinated species that have many characteristics in common. Samples almost routinely yield fragments of more than one species, but the remains are poorly preserved because the tests are poorly cemented and do not survive processing well. They are clear in hand-specimen examination and consist of flattened white tubes or fragments parallel to bedding. Some may not be foraminifers, but they are included here. If foraminifers, they are astrorhizid/allogromiid or simple ammodiscid species lacking chamber partitions and thus referable to *Bathysiphon* in most instances. Two species can be recognized. One (*Bathysiphon* sp. 1, present throughout the section) is large and robust, up to 7–8 mm long, and straight or slightly meandrine. The other (*Bathysiphon* sp. 2) is soft, small (to ~1 mm), thin walled, and usually in fragments.

Another fauna, with both benthic and planktonic species, is present in Sample 188-1165B-24H-CC, and again there is no evidence of dissolution. The benthic component of this fauna is dominated by *Epistominella exigua* (Brady), accompanied by *Cibicidoides mundulus* (Brady, Parker, and Jones), *Cibicidoides subhaidingeri* (Parr), and *Hanzawaia mantaensis* (Galloway and Wissler), which suggests that the fauna is from a bathyal environment and is thus in situ. Also present are several species each of *Lagena, Fissurina,* and miliolid foraminifers.

A small, well-preserved fauna of two species, *Pullenia* cf. *subcarinata* and *E. vitrea,* is present in Sample 188-1165B-26H-CC.

Sample 188-1165B-58X-1, 134–136 cm, contains a diverse agglutinated/calcareous benthic-only fauna, dominated by *C. subhaidingeri* (Parr). This fauna has a few specimens (*Stilostomella* and *Virgulina*) that may represent some infauna and is accompanied by echinoid spines.

The labyrinthine agglutinated taxon *C. incisa* (Stache) is found in many samples in Holes 1165B and 1165C and is the most commonly present benthic species at this site. Deeper in the section, *C. incisa,* in addition to *Bathysiphon* sp. 1, is interpreted to constitute an assemblage found sporadically higher in the section, for example, in Samples 188-1165C-2R-CC and 3R-CC. In Samples 188-1165C-2R-1, 37 cm; 3R-4, 67–101 cm; 15R-2, 41 cm; and many levels in Cores 188-1165C-29R and 30R, there are zones in which these two species are clearly visible with a hand lens and sometimes are quite abundant (up to eight specimens of *Cyclammina* on one side of a "biscuit" of core). They are more likely to be found through hand-specimen examination than after vigorous processing. In some of these co-occurrences, they are accompanied by coarse sand detritus, in marked contrast to the dark gray siltstone above and below. *C. incisa* is also present deeper in Hole 1165C in association with a variety of other foraminifers.

Below Sample 188-1165C-58X-1, 134–136 cm, no other benthic species are recorded until Sample 188-1165B-74X-CC, which contains a crushed and unidentifiable specimen of *Trochammina.* At this depth (~660 mbsf), preservation changes and the tests assume a yellowish color that contrasts with the gray of the enclosing sediment, thus making separation easier. A few benthic species (normally one to three specimens per sample) are identified in Samples 188-1165C-3R-CC; 4R-CC; 17R-CC; 18R-2, 56–58 cm; and 18R-CC.

Sample 188-1165C-30R-3, 142–144 cm, contains *Repmanina* (formerly *Glomospira charoides*), known commonly from bathyal and abys-

sal assemblages, but in contrast to other assemblages, indicates the existence of an infaunal mode of life (Gooday, 1990).

Faunal Assemblages

Because of the erratic nature of faunas downhole, it is difficult to identify meaningful faunal assemblages from the foraminifers. Two agglutinated assemblages, however, seem to be recognizable: a *Cyclammina/Bathysiphon* sp. 1-dominated assemblage and a less well-constrained *Bathysiphon* assemblage. Both assemblages seem to imply that the sediment containing them has not moved more than a few tens of meters.

The *Cyclammina/Bathysiphon* sp. 1 assemblage is well defined and recurrent. It is present sporadically throughout the section (see preceding paragraph) but is best established in the lower cores of Hole 1165C, where it is apparent with the use of a hand lens. The large (to ~3-mm diameter) tests of *C. incisa* stand out because they are lenticular in vertical section and because the labyrinthine wall is clear. *Bathysiphon* sp. 1 (perhaps other nomenclature will evolve with more work) is normally present with *C. incisa*. It is a robust, thick-walled form ~1 mm in diameter, as long as 7–8 mm, and normally is present as flattened ovoids with a dark center. Usually there is no calcareous component of this assemblage, although *Cyclammina* does occur sporadically in association with other faunas. This assemblage is best developed in a distinctive lithofacies consisting of units as thick as 20 cm that are coarser grained than the black siltstone/shale prevalent in the sequence.

The *Bathysiphon* assemblage is present particularly in Cores 188-1165C-12R through 22R. It is not as well characterized as the *Cyclammina/Bathysiphon* sp. 1 assemblage. Two species of *Bathysiphon* are present in this assemblage and may be accompanied by others (e.g., *Psammosphaera* sp. 1 and rarely by a calcareous species). These are common in the sandstone beds in the lower part of the dark gray shale prevalent in the hole. The larger, more robust species has roughly the same size characteristics as *Bathysiphon* sp. 1, but it is much less robust but visible in the unprocessed rock. The second species (very tentatively placed in *Bathysiphon*) is much smaller, up to ~1–2 mm long and 0.3–0.5 mm in diameter. It is present in processed residues as fragments, and complete specimens are found only in the unprocessed rock. Because these specimens are so delicate, they probably can be found only where the sequence is in situ. They are accompanied by horizontal burrows (some of which, on further examination, may be placed in foraminiferal genera), and all are classic examples of the question of what constitutes a foraminifer. This assemblage is found where the prevailing black shale/siltstone contains abundant coarser, thin, white siltstone lenses and interbeds.

Sources of Faunas

It is clear that some of the faunas have arrived at their resting place by transport and are not in situ. That is, they are thanatocoenoses (death assemblages) instead of biocoenoses (life assemblages). If so, where did they originate, and how did they reach their current site? For most faunas, no answer can be given because of the small, unrepresentative faunal content, but an attempt is possible for those from Samples 188-1165B-14H-CC, 24X-CC, and 58X-1, 134–136 cm. In two of these cases, however, there is an inconsistency between planktonic percentage and benthic content.

Sample 188-1165B-14H-CC

The fauna present in this sample probably slumped to its present site or was carried in some form of turbidity current. It contains *O. umbonatus* (dominant: >40%), *Eggerella bradyi, Karreriella bradyi,* and *Laticarinina pauperata*. Knowledge of the global distribution of these species (van Morkhoven et al., 1986) suggests an outer neritic to mid-bathyal source, well above the CCD. As noted above (see "Benthic Foraminifers," p. 23), the absence of planktonic species is a puzzle and could be used to indicate a much shallower source, which would be in conflict with the species composition.

Sample 188-1165B-24X-CC

The fauna present in Sample 188-1165B-24X-CC has a planktonic component of ~65%, which in other environments would indicate an outer shelf/upper slope depth. Because it is a single sample and not part of a sequence with the same characteristics, use of planktonic percentage as an indicator of depth of deposition must be used with caution. Other features include the presence of *E. bradyi, C. subhaidingeri,* and dominant (30%) *E. vitrea*. These suggest an upper depth limit of ~600 m, although the upper depth limit of *E. vitrea* is considerably shallower than this estimate. A mid- to lower bathyal depth is therefore interpreted.

Sample 188-1165B-58X-1, 134–136 cm

C. subhaidingeri is dominant (45%), *L. pauperata* is present, and there are no planktonic foraminifers in this sample. Although in conflict with the absence of planktonic species, the benthic fauna indicates a mid-lower bathyal source.

Calcareous Nannofossils

Introduction

Calcareous nannofossils are present sporadically throughout Holes 1165A, 1165B, and 1165C, with moderate preservation and high abundance in only a few samples. Dissolution at this site is prevalent, which is consistent with a corrosive deeper water environment. Where nannofossils are present, the assemblages are characterized by low diversity with one or two dominant taxa and lack the usual age-diagnostic marker species. Assemblages are comparable to those previously described from Prydz Bay and other Southern Ocean drill sites (Wise, 1983; Wei and Wise, 1990; Wei and Thierstein, 1991; Wei and Wise, 1992a, 1992b). A detailed nannofossil biostratigraphy was not achieved for these drillcores. Nannofossil-bearing samples, however, could be assigned to rough zonal combinations and broad age designations (Figs. F28A, F28B, F29).

Hole 1165A

One core was taken in Hole 1165A in order to recover Pleistocene–Holocene sediments for high-resolution study. The core is tentatively assigned to the late Pliocene–Quaternary nannofossil Zones CN12–CN15 of Okada and Bukry (1980). No nannofossils were noted in a sample from the core catcher, but few to common specimens were noted

from discrete samples within the core. Sample 188-1165A-1H-1, 20–21 cm, contains few to common, poor to moderately preserved nannofossil specimens possibly assignable to the Pleistocene to Holocene species *Emiliania huxleyi,* the first occurrence (FO) of which marks the base of Zone CN15. Because of the small size of this taxon and less than ideal preservation, this assignment is only tentative and must be confirmed with scanning electron microscopic analysis. Additional species present show affinities to *Gephyrocapsa;* however, no specimens were noted with a bar spanning the central area, as is characteristic of this genus and as was noted in Hole 1165B (see **"Hole 1165B,"** p. 27). Sample 188-1165A-1H-8, 17–18 cm, contains moderately preserved but rare *Coccolithus pelagicus, Calcidiscus leptoporus,* and possible *Gephyrocapsa* sp. (no central bar). *E. huxleyi* may also be present in this sample but could not be confirmed aboard ship.

Hole 1165B

Early Miocene- to Pleistocene-age sediments were recovered in Hole 1165B with sporadic calcareous nannofossil recovery. Only general zonal age assignments were possible. Overall, nannofossils are poorly to moderately preserved with etching and dissolution of specimens reflecting deposition in deep corrosive waters.

Sample 188-1165B-1H-CC contains etched nannofossils dominated by common *C. pelagicus* with few specimens of *C. leptoporus* and *Gephyrocapsa* sp. (no central bar preserved). Specimens of *Gephyrocapsa caribbeanica* with a central bar intact are present in the upper two sections of Core 2H, which is indicative of an age of late Pliocene–Pleistocene. Questionable specimens of a smaller oval morphotype of *Pseudoemiliania lacunosa* were also noted in this core. According to Perch-Nielsen (1985), the smaller morphotype is more prevalent in the higher latitudes. If these specimens are the cold-water variety of *P. lacunosa,* then the bottom of this first core can be assigned to Zones CN12–CN14a of late Pliocene to mid-Pleistocene age.

Core-catcher samples from Cores 2H through 13H are barren of calcareous nannofossils. Sample 188-1165B-14H-CC, however, contains abundant moderately preserved specimens. The assemblage is dominated by *R. perplexa* (syn. *Dictyococcites antarcticus*) and *Reticulofenestra producta*. *C. pelagicus* and several varieties of small- and medium-sized *Reticulofenestra* spp. are few to common. The latter have been variably assigned by previous authors to a number of species including *Reticulofenestra haqii, Reticulofenestra minuta,* medium and small *Reticulofenestra gelida,* and *Reticulofenestra minutula*. Very rare *Reticulofenestra pseudoumbilica* and large *R. gelida* are also present. A surprise in this sample was the presence of rare specimens of *Minylitha convallis,* which is noted from Zones CN8 to CN9 of the late Miocene. Single specimens of the warmer-water taxa *Sphenolithus abies* and *Discoaster* sp. cf. *D. variabilis* were also noted. To our knowledge, these species, including *M. convallis,* have not been observed in upper Miocene sediments from the high austral latitudes, and in particular, the Antarctic margin.

Core-catcher samples from Cores 15H through 23X are also barren of calcareous nannofossils, but very abundant specimens were noted from a thin chalky layer within the core catcher of Core 24X. This sample contains an assemblage completely dominated by *R. perplexa* with fewer *R. producta, Reticulofenestra* spp., and rare *C. pelagicus*. The assemblage is characteristic of middle to late Miocene of the higher latitudes and can be roughly assigned to Zones CN5 to CN11. A single specimen of a

Reticulofenestra hesslandii was noted, which, if not reworked, suggests an age of middle Miocene for the assemblage. Samples 188-1165B-26X-CC and 27X-CC contained similar but less abundant assemblages. Unfortunately, Core 25X was not recovered from within this relatively nannofossil-rich interval of an otherwise barren section. Core catchers from Cores 28X through 57X are barren of nannofossils.

Cores 58X and 59X contain several intervals of common to abundant nannofossils. The presence of *Cyclicargolithus floridanus,* whose last occurrence (LO) roughly corresponds to the top of Zone CN4, along with abundant *R. hesslandii* and *Reticulofenestra* spp., is indicative of the lower to middle Miocene of the austral high latitudes (e.g., Wei and Wise, 1992a). Rare *Cyclicargolithus abisectus* suggests an age of early Miocene. In light of the diatom data, in addition to the absence of *C. leptoporus,* an age of late early Miocene is probable (nannofossil Zones CN2–CN3). Rare reworked Oligocene specimens of *Chiasmolithus* sp., *Dictyococcites bisectus, Reticulofenestra daviesii,* and *Reticulofenestra samodurovii* were noted in Sample 188-1165B-58X-2, 34–35 cm.

Below Core 59X down to Core 76X (674.96 mbsf), nannofossils are very rare with sporadic occurrences of *R. hesslandii, C. floridanus,* and small species of *Reticulofenestra.* Assemblages are generally in agreement with diatom stratigraphy, which places the section in the lower Miocene.

Hole 1165C

Calcareous nannofossils are moderately preserved but few and sporadic in the predominantly dark brown to gray-green mudstones of Hole 1165C. A good biostratigraphy could not be achieved, but assemblages recovered are indicative of an early Miocene age for the hole, most likely encompassing nannofossil Zones CN2 to CN1 (Fig. **F29**).

Nannofossils, where present in Hole 1165C, are dominated by small and medium-sized nondescript species of *Reticulofenestra* (*R. haqii, R. minuta,* and *R. producta*) and *C. pelagicus*. Few *R. hesslandii* are present down through Core 14R and questionably below that. Very rare and sporadic *C. floridanus* are found throughout, and rare to few *C. abisectus* are present in Core 29R and below. Very rare non–age diagnostic *Sphenolithus* spp. are present in Samples 188-1165C-12R-4, 24–26 cm, and 18R-CC. A single poorly preserved specimen of *Discoaster* sp. aff. *D. deflandrei* was also noted in Sample 188-1165C-12R-4, 24–26 cm, and very rare specimens of the early- to mid-Miocene age taxa *Coccolithus miopelagicus* are present in Samples 188-1165C-18R-CC and 22R-CC.

The bottom core, Sample 188-1165C-35R-1, 19–20 cm, contains few to common specimens of a relatively rich nannoflora (>6 species) that includes common *Reticulofenestra* spp., few *C. pelagicus,* rare *C. abisectus,* and single specimens of *Helicosphaera* sp. cf. *H. paleocarteri, Helicosphaera* sp., and *Umbilicosphaera jafarii*. The latter is only known from Miocene and younger strata, whereas the remaining assemblage is generally assignable to the lower Miocene (nannofossil Zones CP19b–CN3).

Bottom-Hole Age

When compared to previously drilled sections at nearby Kerguelen Plateau and elsewhere in the Southern Ocean, the overall assemblages noted in discrete samples of Hole 1165C are consistent with an early Miocene age (Wei and Wise, 1990; Wei and Thierstein, 1991; Wei and Wise, 1992a). The presence of *C. abisectus* in Core 188-1165C-29R and

below broadly limits the section to the late Oligocene–early Miocene age interval. However, in Southern Ocean sections, the uppermost Oligocene is characterized by few to common *D. bisectus,* whose LO marks the top of the Oligocene, and abundant *R. daviesii,* which actually ranges just into the lower Miocene. *D. bisectus* specimens were not observed in bottom assemblages, and only questionable (overgrown?) specimens of *R. daviesii* were noted. These species were reported in Antarctic margin sections such as nearby Prydz Bay, Site 739 (Wei and Thierstein, 1991), and in Cape Roberts cores (Watkins and Villa, in press). Thus, it would be reasonable to assume their presence at this site if Oligocene sediments were reached. Poor preservation is ruled out as a potential cause of the absence of *D. bisectus* because it is more robust (8–10 µm for smaller morphotypes) than most of the species observed in these samples. In addition, reworked specimens were noted upsection, which further indicates their presence in the region and supports the interpretation that the Oligocene was not cored at Site 1165.

Nannofossil Environmental Significance

Because of the sporadic presence of nannofossils, little paleoenvironmental interpretation is possible beyond speculation. Nannofossil abundance at this site may be a factor of several processes or a combination of processes. High nannofloral productivity in surface waters around Prydz Bay (associated with warmer intervals?) perhaps periodically depressed the CCD and permitted the preservation of nannofossils, whereas under conditions of normal production, dissolution was prevalent. Occurrences can also be attributed to rapid downslope transport, burial, and preservation of nannofossils. Two examples of this latter process are evident at Site 1165. In Sample 188-1165B-14H-CC, nannofossils are abundant and fairly well preserved, along with a well-developed fauna of neritic benthic foraminifers, which were obviously brought downslope. Similarly, in Sample 188-1165C-12R-4, 24–26 cm, nannofossils are abundant in a carbonate-rich interval that sedimentologists have interpreted as a distal mud-flow deposit. Further corroborating this interpretation is the presence of rare reworked Oligocene–Eocene nannofossils in this sample.

Interpreting the lack of nannofossils throughout most of the section is difficult. As cited above, dissolution below the CCD is likely and/or nannoplankton surface productivity was low due to cool surface-water temperatures—or it may simply be a result of dilution of an already low number of nannofossils by a copious supply of terrigenous sediment. Intervals of higher nannofossil abundance may be merely the result of a diminishing terrigenous supply, possibly associated with interglacial periods.

As previously mentioned, assemblages recovered at Site 1165 are comparable to those of equivalent age found elsewhere in the high austral latitudes, particularly in Prydz Bay and on the Kerguelen Plateau (Wei and Thierstein, 1991; Wei and Wise, 1992a). These assemblages are composed of a typical cold-water nannofossil flora. An example is *R. perplexa,* which achieves very high abundances and comprises almost 100% of the assemblage at various intervals in upper Miocene to lower Pliocene austral sections (Wei and Wise, 1992b). A nearly monospecific assemblage of very abundant *R. perplexa* is present at Site 1165 in Sample 188-1165B-24X-CC and may represent a period of extremely high nannofossil productivity (depressing the paleo-CCD and allowing carbonate deposition?; see Wei and Wise, 1992b). It is also possible to infer

warmer intervals from abundance increases of *C. pelagicus* (Wei and Wise, 1992b). At Site 1165, a few intervals of *C. pelagicus* relative abundance increase are noted in Core 188-1165B-2H (7.1 mbsf); Samples 188-1165B-14H-CC (124.51 mbsf); 58X-2, 34.5 cm (512.85 mbsf); 188-1165C-18R-CC (829.57 mbsf); and to a lesser extent, 35R, 19–20 cm (989.69 mbsf). These intervals are generally characterized by overall nannofossil abundance increase as well, so it remains speculative at this time as to whether increases in *C. pelagicus* is a significant warm-water proxy at Site 1165.

Diatoms

Introduction

Neogene sediments recovered at Site 1165 contain rich diatom assemblages, although in variable states of abundance and preservation. Poorly preserved diatoms are present in one sample at the base of Hole 1165A (5.33 mbsf) and indicate a Quaternary age for this core. In Hole 1165B, an expanded upper Pliocene to lower Miocene section is present from ~9 to ~650 mbsf and is disconformably overlain by a thin upper Pleistocene section. An excellent diatom record is represented in the upper Pliocene to lower Miocene cores of Hole 1165B, which provides for detailed biostratigraphic analysis. Cores recovered in Hole 1165C were barren of diatoms, except for one sample recovered from a burrow at ~754 mbsf. This sample is assigned an age of early Miocene.

The diatom zonation of Harwood and Maruyama (1992) was applied to Neogene cores of Holes 1165B and 1165C (see **"Biostratigraphy and Sedimentation Rates,"** p. 9, in the "Explanatory Notes" chapter). Diatom zonal datums recognized in Holes 1165B and 1165C are listed in Table **T5.** Lower Miocene to upper Pliocene zones are well represented in these cores, although some zones were combined because of the absence of marker taxa or apparent juxtaposition of datum events. Initial biostratigraphic "reconnaissance" of core-catcher samples also suggests that a few zones may be absent in the section. Further work with narrow sample spacing is required to identify whether these zones are present or are missing as a result of hiatuses. Contamination of core-catcher samples from the drilling slurry may also be a problem in some samples, and examination of discrete core samples will provide clarification on the stratigraphic ranges of specific taxa.

T5. Summary of diatom datums identified, Holes 1165B and 1165C, p. 177.

Hole 1165A

One piston core was taken in Hole 1165A, and a diatom sample from the base of the core at 5.33 mbsf (Sample 188-1165A-1H-CC) was examined. The presence of *Thalassiosira elliptipora* (FO = 2.2 Ma) indicates the section is Quaternary in age, and the presence of Neogene and Paleogene taxa, including *Denticulopsis praedimorpha* (LO = 11.5 Ma) and *Pyxilla reticulata* (LO = 30.7 Ma), indicates Oligocene and Miocene reworking. Apparent reworking in this sample prohibits the use of Quaternary LO datums (e.g., the LO of *Actinocyclus ingens* at 0.66 Ma); as a result, this section has been left unzoned.

Hole 1165B

Poorly preserved diatom assemblages are present above ~17 mbsf in Hole 1165B, with the interval above 1.70 mbsf representing a thin up-

per Pleistocene section. Moderately to well-preserved diatom assemblages were recovered from ~17 to ~606 mbsf through a succession of lower Pleistocene to lower Miocene strata. Initial zonal assignment and age interpretation were carried out using core-catcher samples. In some sections, additional core samples have been examined to further constrain the depth of zonal boundaries. A summary of diatom zonal assignments for Hole 1165B is shown in Figure **F28A** and **F28B,** and a summary of datums applied to designate zonal boundaries is presented in Table **T5.**

Diatom abundance varied from absent to very abundant throughout Hole 1165B. In general, diatom preservation and abundance were best in lower Pliocene sediments (~30 to ~50 mbsf). Preservation and abundance varied with lithology in the Miocene section, where preservation appears to be best and abundance highest in light green rather than in gray-green to gray-black claystones. Barren samples were predominantly recovered below ~606 mbsf (Sample 188-1165B-67X-CC), except for a few carbonate-cemented horizons and burrows where diatoms were preserved. Samples at 646.10 mbsf (Sample 188-1165B-73X-1, 30–32 cm) and 753.77 mbsf (Sample 188-1165B-10H-3, 127–129 cm), for example, contain poorly preserved siliceous microfossil assemblages. Barren and poorly preserved samples below ~606 mbsf indicate that the hole reached the level of complete opal-A dissolution at this depth.

Neritic diatoms associated with shallow-euphotic water depths (<100 m) are noted throughout diatom-rich intervals of Hole 1165B. Many intervals contain low abundances of *Cocconeis* spp., *Paralia sulcata, Rhabdonema* spp., *Grammatophora* spp., and *Entopyla* spp. These taxa maintained a benthic or tychopelagic habitat within the photic zone and are interpreted to indicate reworking from a continental shelf source during deposition of the sequence.

Numerous samples were examined from Cores 1H and 2H. Most samples in this interval contain very poorly preserved diatom assemblages with many reworked taxa. Moderately preserved assemblages, however, were noted in Samples 188-1165B-1H-1, 20–21 cm; 1H-5, 20–21 cm; and 2H-2, 95–96 cm. The highest occurrence of *A. ingens* is noted between Samples 188-1165B-1H-2, 20–21 cm (1.70 mbsf), and 1H-5, 20–21 cm (6.20 mbsf), placing the base of the *Thalassiosira lentiginosa* Zone between these samples. An interval of poor preservation between these samples inhibits the accurate placement of this zonal boundary, as this taxon can be easily reworked into overlying sediments. An age of <0.66 Ma is therefore interpreted for sediments above 1.70 mbsf.

The interval between 1.70 and 9.25 mbsf is presently left unzoned because of poor diatom preservation and the presence of *Fragilariopsis* sp. cf. *barronii,* as opposed to the zonal datum *Fragilariopsis barronii.* Taxonomic problems associated with the identification of the LO of *F. barronii* have been noted by several workers (e.g., Gersonde and Bárcena, 1998). Lower Pleistocene assemblages documented in several Southern Ocean drill cores contain transitional forms of *F. barronii* that are difficult to distinguish from early forms of *Fragilariopsis ritscherii* or *Fragilariopsis kerguelensis,* thereby limiting the use of the LO datum of *F. barronii* as a zonal marker.

The highest occurrence of *Thalassiosira kolbei* is noted between Samples 188-1165B-2H-2, 95–96 cm (9.25 mbsf), and 3H-1, 95–96 cm (17.25 mbsf), which serves as a rough estimation of the Pliocene/Pleistocene boundary. Again, this datum cannot be constrained to a narrow depth interval because of poor preservation between these samples. The presence of *F. barronii sensu stricto* at 9.25 mbsf (Sample 188-1165B-2H-2,

95–96 cm), however, places the sample at this level within the *F. kerguelensis* Zone (1.35 to 1.8–2.0 Ma).

The absence of *A. ingens* (LO = 0.66 Ma) at 1.70 mbsf and the presence of *F. barronii* (LO = 1.35 Ma) at 9.25 mbsf indicates an ~1-m.y. hiatus within this interval. Numerous short hiatuses may exist between 1.70 and 9.25 mbsf but presently cannot be resolved from the diatom data.

Sample 188-1165B-3H-1, 95–96 cm (17.25 mbsf), is placed within the *T. kolbei* Zone (1.8–2.0 to 2.2–2.3 Ma). *T. kolbei* is present within this sample, and the highest occurrence of *Thalassiosira vulnifica* is recognized below this level between Samples 188-1165B-3H-1, 95–96 cm (17.25 mbsf), and 3H-2, 20–21 cm (18.00 mbsf).

The highest occurrence of *Thalassiosira insigna* is between Samples 188-1165B-3H-3, 20–21 cm (19.50 mbsf), and 3H-2, 20–21 cm (18.00 mbsf). The overlying interval, which includes Sample 188-1165B-3H-2, 20–21 cm (18.00 mbsf), is therefore placed in the *T. vulnifica* Zone (2.2–2.3 to 2.5–2.6 Ma), based on the presence of *T. vulnifica* and the absence of *T. insigna*.

Samples 188-1165B-3H-3, 20–21 cm (19.50 mbsf), through 3H-CC (25.01 mbsf) are assigned to the *T. insigna–T. vulnifica* Zone (2.5–2.6 to 2.8–3.2 Ma). This zone is constrained by the combined presence of *T. vulnifica* and *T. insigna* through the section. The lowest occurrence of *T. vulnifica* is identified between Samples 188-1165B-3H-CC (25.01 mbsf) and 4H-1, 20–21 cm (26.00 mbsf).

The highest occurrence of *Fragilariopsis weaveri* in Sample 188-1165B-3H-5, 95–96 cm (23.25 mbsf), may allow the *T. insigna–T. vulnifica* Zone to be further subdivided into Subzones "a" and "b." Several rare specimens of *F. weaveri,* however, were noted above this level. These occurrences may represent reworking, but further work is required to validate its use as a subzonal marker.

The lowest occurrence of *Fragilariopsis interfrigidaria* is noted between Samples 188-1165B-5H-1, 127–128 cm (36.57 mbsf), and 5H-2, 127–128 cm (38.07 mbsf). The *F. interfrigidaria* Zone (2.8–3.2 to 3.7–3.8 Ma) is therefore identified between Samples 188-1165B-4H-1, 20–21 cm (26.00 mbsf), and 5H-1, 127–128 cm (36.57 mbsf), based on the presence of *F. interfrigidaria* and the absence of *T. vulnifica* throughout this interval. The boundary between the upper and lower Pliocene lies within the *F. interfrigidaria* Zone and is roughly placed at ~30 mbsf.

The lowest occurrence of *F. barronii* is identified between Samples 188-1165B-5H-4, 95–96 cm (40.75 mbsf), and 5H-5, 60–61 (41.90 mbsf). Accordingly, the interval between 38.07 and 40.75 mbsf is placed within the *F. barronii* Zone (3.7–3.8 to 4.2–4.4 Ma), which is constrained by the presence of *F. barronii* and the absence of *F. interfrigidaria*. The highest occurrence of *Rhizosolenia costata* between Samples 188-1165B-5H-3, 95–96 cm (39.25 mbsf), and 5H-4, 95–96 cm (40.75 mbsf), may allow this zone to be further subdivided into Subzones "a" and "b," as defined by Harwood and Maruyama (1992).

The lowest occurrence of *Thalassiosira inura* is documented between Samples 188-1165B-6H-3, 95–96 cm (48.75 mbsf), and 6H-4, 59–60 cm (49.89 mbsf). The interval between 41.90 and 48.75 mbsf is placed within the *T. inura* Zone (4.2–4.4 to 4.8–4.9 Ma), as indicated by the presence of *T. inura* and the absence of *F. barronii*. It should be noted that morphologies taxonomically similar to *T. inura* are found below the lowest occurrence of *T. inura* presently identified here. These forms have a reduced central hyaline area and are tentatively identified as *Thalassiosira jacksonii*. In the present study, *T. inura* is limited to speci-

mens with a central hyaline patch that spans at least one-fourth of the valve diameter.

The lowest occurrence of *Fragilariopsis praeinterfrigidaria* in Sample 188-1165B-8H-CC (73.61 mbsf) lies well below the lowest occurrence of *T. inura* at ~49.89 mbsf. Previously, the FOs of both taxa were considered to be contemporaneous (Harwood and Maruyama, 1992). Recovery of an expanded upper Miocene section at Site 1165 will allow refinement of a number of secondary datums, such as the FO of *F. praeinterfrigidaria*.

Within some intervals of the *T. inura* Zone, the occurrence of silicoflagellates and diatoms with a subantarctic affinity is noted. Sample 188-1165B-5H-CC (44.08 mbsf), for example, contains a high abundance of *Dictyocha* spp. silicoflagellates (relative to *Distephanus* spp.). Future work on this interval will possibly allow early Pliocene warming and cooling phases to be identified from both diatom and silicoflagellate assemblage data.

Below the lowest occurrence of *T. inura* (~49.89 mbsf), the *Thalassiosira oestrupii* to *Nitzschia reinholdii* Zones (4.8–4.9 to ~6.4 Ma) are represented, as indicated by the presence of *Thalassiosira oliverana* (FO = 6.4 Ma). The position of the base of the *N. reinholdii* Zone is approximated in Hole 1165B by the lowest occurrence of *Hemidiscus triangularus* (FO = 6.2 Ma) between Samples 188-1165B-9H-CC (81.39 mbsf) and 10H-1, 20–21 cm (83.00 mbsf), which places the *T. oestrupii* to *N. reinholdii* Zones in the interval from 48.75 to 81.39 mbsf. It is noteworthy that *H. triangularus* (FO = 6.2 Ma, calibrated from Leg 120 data) is used here as a substitute datum for the FO of *Thalassiosira miocenica*. The usefulness of the FOs of *T. oestrupii* and *T. miocenica* as zonal datums requires investigation, as these datums could not be identified at Site 1165. *T. oestrupii* was only observed in the *T. inura* Zone, which may indicate the presence of a disconformity below this zone or that the FO of *T. oestrupii* is unreliable as a high southern latitude marker datum.

In the Southern Ocean diatom zonation of Harwood and Maruyama (1992), the Pliocene and Miocene boundary is placed within the *T. oestrupii* Zone; no datums, however, recognized in Hole 1165B distinctly identify this boundary. The Miocene/Pliocene boundary is therefore tentatively placed between the lower part of Cores 6H and 9H, within the *T. oestrupii* to *N. reinholdii* Zones.

The section between Samples 188-1165B-10H-1, 20–21 cm (83.00 mbsf), and 11H-CC (100.32 mbsf) is assigned to the *Hemidiscus ovalis* Zone (~6.4 to ~8.7 Ma). The base of this zone is identified by the lowest occurrence of *H. ovalis,* which lies between Samples 188-1165B-11H-CC (100.32 mbsf) and 12H-CC (101.80 mbsf). As noted above, the top of the *H. ovalis* Zone is identified by the lowest occurrence of *H. triangularus* between 81.39 and 83.00 mbsf.

Sample 188-1165B-12H-CC (101.80 mbsf) is assigned to the *Thalassiosira torokina* Zone (~8.7 to ~8.5–9.0 Ma), as indicated by the presence of *T. torokina* and the absence of *H. ovalis*. The use of the lowest occurrence of *H. ovalis* as the top of this zone is tentative, as morphologies similar to *H. ovalis* were observed below this level. These forms may only represent slightly oval-shaped specimens of *A. ingens* and will be further investigated in postcruise work.

The section between Samples 188-1165B-13H-CC (116.02 mbsf) and 23H-CC (194.70 mbsf) is placed within the *Asteromphalus kennettii* to *Denticulopsis simonsenii* Zones (8.5–10.0 to 11.0–11.1 Ma). These zones are identified by the occasional presence of *A. kennettii,* with an acme in Samples 188-1165B-13H-CC (116.02 mbsf) and 22X-CC (185.08 mbsf);

the absence of *T. torokina;* and the infrequent occurrence of *Denticulopsis dimorpha*. The inconsistent occurrence of *A. kennettii* prevented the separation of the *A. kennettii* and *D. simonsenii* Zones, which are divided by the FO of *A. kennettii*. The presence of *A. kennettii* in Sample 188-1165B-22X-CC may represent downhole contamination because this taxon was not observed below Sample 188-1165B-13H-CC.

The *D. dimorpha* to *D. praedimorpha–Nitzschia denticuloides* Zones (11.0–11.1 to 12.2–12.8 Ma) are recognized from Samples 188-1165B-23X-CC (194.70 mbsf) to 27X-CC (231.69 mbsf) between the highest common occurrence and lowest occurrence of *D. dimorpha*. The stratigraphic position of the highest occurrence of *N. denticuloides* could not be identified during shipboard investigations and prevents the separation of the *D. dimorpha* and *D. praedimorpha–N. denticuloides* Zones.

The upper to middle Miocene boundary is within the *D. dimorpha* Zone in the Southern Ocean diatom zonation. In Leg 120 cores, the full range of *Denticulopsis meridionalis* is recorded only in the upper *D. dimorpha* Zone; as a result, the lowest occurrence of *D. meridionalis* is used here to approximate the position of this boundary. This datum occurs between Samples 188-1165B-24X-CC (199.15 mbsf) and 26X-CC (213.90 mbsf).

Sample 188-1165B-28X-CC (242.68 mbsf) is assigned to the *D. praedimorpha* Zone (12.2–12.8 to 12.8–13.1 Ma), as indicated by the presence of *D. praedimorpha* and the absence of *D. dimorpha*.

The section from Samples 188-1165B-30X-CC (253.71 mbsf) through 33X-CC (281.33 mbsf) is placed within the *N. denticuloides* Zone (12.8–13.1 to 13.5–13.8 Ma), as marked by the presence of *N. denticuloides* and the absence of *D. praedimorpha*. The lowest occurrence of *N. denticuloides* is recorded between Samples 188-1165B-33X-CC (281.33) and 34X-CC (290.89 mbsf). Rare occurrences of *N.* cf. *denticuloides,* however, were noted below this level, which may represent transitional forms between *Denticulopsis maccollumii* and *N. denticuloides*. The lower range of *N. denticuloides,* therefore, remains uncertain.

The interval from Samples 188-1165B-34X-CC (290.89 mbsf) through 35X-CC (298.38 mbsf) is assigned to the *D. simonsenii–Nitzschia grossepunctata* Zone (13.5–13.8 to 14.1–14.6 Ma), as indicated by the absence of *N. denticuloides* and the lowest common occurrence of *D. simonsenii* in Sample 35X-CC.

The *A. ingens* var. *nodus* Zone (14.1–14.6 to 14.5–14.7 Ma) is identified in the interval between Samples 188-1165B-36X-CC (309.52 mbsf) and 38X-CC (327.78 mbsf), based on the absence of *D. simonsenii* and the presence of *A. ingens* var. *nodus*. The lowest occurrence of *A. ingens* var. *nodus* is noted in Sample 188-1165B-38X-CC (327.78 mbsf) but was rare in all samples examined, except for Sample 188-1165B-34X-6, 20–21 cm (288.90 mbsf).

The interval between Samples 188-1165B-39X-CC (336.89 mbsf) and 50X-CC (443.99 mbsf) is placed within the *N. grossepunctata* to *A. ingens–D. maccollumii* Zones (14.5–14.7 to 15.9–16.4 Ma). This assignment is based on the absence of *A. ingens* var. *nodus* and the common occurrence of *A. ingens*. The boundary between the *N. grossepunctata* and *A. ingens–D. maccollumii* Zones was not determined because of the similarities between *N. grossepunctata* and *Nitzschia* sp. 17 (of Schrader, 1976), as the latter species extends into the underlying *D. maccollumii* Zone (e.g., in Holes 747A and 751A on the Kerguelen Plateau [Harwood and Maruyama, 1992]).

The *D. maccollumii* Zone (15.9–16.4 to 16.7–17.3 Ma) is recognized between Samples 188-1165B-51X-CC (449.80 mbsf) and 55X-CC

(487.52 mbsf). The top of this interval is marked by the lowest common occurrence of *A. ingens,* and the base is identified by the lowest occurrence of *D. maccollumii.*

The lowest occurrence of *Crucidenticula kanayae* is noted in Sample 188-1165B-55X-CC (487.52 mbsf), in addition to the lowest occurrence of *D. maccollumii.* In the Southern Ocean zonal scheme, the FO of *C. kanayae* (17.5–17.7 Ma) and the FO of *D. maccollumii* (16.7–17.0 Ma) define the *C. kanayae* Zone. The lowest occurrence of these two taxa in the same sample possibly indicates the presence of a hiatus between Samples 188-1165B-55X-CC and 56X-CC. Calibrated ages from Hole 744B for the FO of *C. kanayae* and *D. maccollumii* and the first common occurrence (FCO) of *A. ingens* suggest that this hiatus is ~0.7–1.4 m.y. in duration.

The middle to lower Miocene boundary is placed within the *D. maccollumii* Zone in the Southern Ocean zonal scheme of Harwood and Maruyama (1992). As noted above, Samples 188-1165B-51X-CC (449.80 mbsf) through 55X-CC (487.52 mbsf) are assigned to combined zones (*D. maccollumii* to *C. kanayae*) because of uncertainty in the level of the lowest occurrence of *D. maccollumii.* The middle/lower Miocene boundary is therefore placed between ~450 and ~487 mbsf.

The *Thalassiosira praefraga* "c" Subzone (17.5–17.7 to 18.3–19.1 Ma) is identified between Samples 188-1165B-56X-CC (495.81 mbsf) and 59X-CC (527.92 mbsf). This section represents an interval zone between the lowest occurrence of *D. maccollumii* and the highest occurrence of *T. praefraga.*

The section from Sample 188-1165B-60X-CC (534.60 mbsf) to the bottom of Hole 1165B (Sample 188-1165B-76X-CC) is assigned to the *T. praefraga* "a" to "b" Subzones (18.3–19.1 to 19.9–20.8 Ma). Subzones "a" and "b" are constrained by the full biostratigraphic range of *T. praefraga. T. praefraga* is frequent to common in Samples 188-1165B-60X-CC through 67X-CC. Below this level (~606 mbsf), all samples are poorly preserved to barren of diatoms, which indicates complete opal-A dissolution below this level. *T. praefraga,* however, is present in one sample from Hole 1165C, stratigraphically below the bottom of Hole 1165B (see **"Hole 1165C,"** p. 35, in "Diatoms"), allowing the entire lower section of Hole 1165B to be placed in the *T. praefraga* "a" and "b" Subzones. The absence of *Rossiella symmetrica* (LO = 19.4 Ma) may place the lowermost section of Hole 1165B in the *T. praefraga* Subzone "b." Its absence, however, may merely represent biogeographical exclusion from the high southern latitudes.

Hole 1165C

Core 1R was recovered to complete the missing section that resulted from the failed retrieval of Core 188-1165B-7H. A distinct color change is noted in Core 1R, from dark tan at the top to gray green at the bottom. Samples were taken across this contact, but no distinct differences in the diatom assemblages were observed. With further work, the presence of a disconformity may be discerned from detailed analysis of multiple samples above and below this level, but a hiatus is not presently identified. Samples from Core 1R are assigned to a combined *T. oestrupii* to *N. reinholdii* Zone (4.8–4.9 to ~6.4 Ma), as was the bottom of Core 188-1165B-6H-CC (54.39 mbsf) to the top of Core 8H-1, 95-96 cm (64.75 mbsf). This zonal assignment is based on the absence of *T. inura* and the presence of *H. triangularus* lower down in the section (see **"Hole 1165B,"** p. 30, in "Diatoms").

Rotary drill core retrieval from Hole 1165C recommenced at a depth of ~673 mbsf, stratigraphically below Hole 1165B. Diatom recovery was marginal and patchy, with most samples barren of diatoms or containing only traces of recrystallized diatoms. Moderately preserved diatom assemblages were recovered from only one carbonate-cemented burrow in Sample 188-1165C-10R-3, 127–129 cm (753.77 mbsf). The presence of *T. praefraga* in this sample indicates an age <20.8 Ma and places the interval above this level in the *T. praefraga* "a" and "b" Subzones. This age assignment is corroborated by the presence of *Dactyliosolen antarcticus,* which has a FO at ~21 Ma in the CRP-2A drill core in the southern Ross Sea (Scherer et al., in press).

Radiolarians

Introduction

Radiolarian faunas were recovered from both Holes l165B and 1165C. Well-preserved and age-diagnostic radiolarian samples were limited to 487.5 mbsf and above in Hole 1165B.

The radiolarian zones proposed by Lazarus (1990, 1992) and Abelmann (1990, 1992) for high-latitude Pliocene and Miocene radiolarians are summarized in Table **T2,** p. 63, in the "Explanatory Notes" chapter. Several of these Neogene zones were recognized in Holes 1165B and 1165C (Figs. **F28A, F28B, F29**).

Discussion of unconformities or hiatuses in the stratigraphy of Holes 1165B and 1165C, based on missing radiolarian zones, is premature because this initial work on the radiolarian fauna has been based entirely on core-catcher samples. In addition, there are numerous sections barren of radiolarians (Figs. **F28A, F28B, F29**). Final conclusions regarding zonal determinations and hiatuses in Holes 1165B and 1165C will be postponed until all the individual core samples are processed and analyzed. The following zones were recognized on initial examination of samples from Holes 1165B and 1165C.

Upsilon Zone

Samples 188-1165B-3H-CC, 4H-CC, and 5H-CC are assigned to the Upsilon Zone (Lazarus, 1992). The base of the this zone is marked by the first appearance of *Helotholus vema* Hays (Table **T6**), which is present in all these samples. Samples 188-1165B-4H-CC and 5H-CC may represent the lower part of the Upsilon Zone, as *Prunopyle titan* Campbell and Clark is present in those samples. The last appearance of *P. titan* is noted in Sample 188-1165B-4H-CC (Table **T6**) and represents the top of the middle Upsilon Zone (Lazarus, 1992). Additional samples from the core will be processed postcruise to determine more precise boundaries between the lower and upper Upsilon Zone.

T6. Summary of diatom and radiolarian biostratigraphic datums recognized in Holes 1165B and 1165C, p. 178.

Tau Zone

Samples 188-1165B-6H-CC and 188-1165C-1R-CC are tentatively assigned to the Tau Zone (Lazarus, 1992). The base of this zone is marked by the last appearance of the species *Amphymenium challengerae* Weaver. This taxa, however, was not seen in any of the samples from Holes 1165B or 1165C. The top of the Tau Zone is marked by the first appearance of *H. vema,* which is not present in Samples 188-1165B-6H-CC or 188-1165C-1R-CC but does appear in the overlying Sample 188-1165B-

5H-CC (Table T6). Sample 188-1165C-1R-CC may represent the lower part of the Tau Zone because *Lynocanoma grande* Campbell and Clark (Table T6) is very abundant in this sample. Lazarus (1992) defined the lower part of the Tau Zone by the last common occurrence of *L. grande*.

The *A. challengerae* Zone was not recognized in the core-catcher samples, but the processing of additional samples from Cores 188-1165C-1R and 188-1165B-8H may result in the identification of this very short zone (6.1 to 6.6 Ma).

Acrosphaera? *labrata* Zone

Samples 188-1165B-8H-CC, 9H-CC, 10H-CC, and 12H-CC were assigned to the *Acrosphaera*? *labrata* Zone of Lazarus (1992). The base of this zone is marked by the FO of *A.*? *labrata* in Sample 188-1165B-11H-CC (Table T6), and this species is present in all the above samples.

The *Siphonosphaera vesuvius* Zone (Lazarus, 1992) has not been identified in Hole 1165B during shipboard investigations but may be recognized with more detailed sampling of Cores 188-1165B-13H, 14H, and 15H.

Acrosphaera australis Zone

Samples 188-1165B-13H-CC, 14H-CC, 15H-CC, 16H-CC, 17H-CC, 18H-CC, and 19X-CC were assigned to the *Acrosphaera australis* Zone of Lazarus (1992), based on the presence of *A. australis* Lazarus. The base of the *A. australis* Zone is marked by the evolutionary transition from *Acrosphaera murrayana* (Haeckel) Strelkov and Reshetnyak to *A. australis* (Table T6). Also present in these samples is *Cycladophora spongothorax* (Chen), which has its LO at the top of the *A. australis* Zone (Table T6). *Ceratocyrtis stigi* Nigrini and Lombari is also present in Sample 188-1165B-16H-CC, which supports assignment of this sample to the *A. australis* Zone.

Cycladophora spongothorax Zone

Samples 188-1165B-22X, 24X-CC, 34X-CC, 38X-CC, and 39X-CC are assigned to the *C. spongothorax* Zone. The base of this zone is marked by the first appearance of *C. spongothorax* in Sample 188-1165B-38X (Table T6). This species is present in all samples assigned to this zone. The top of this zone is represented by the evolutionary transition from *A. murrayana* to *A. australis*. *A. australis* is present in Sample 188-1165B-19X-CC, which has been assigned to the *A. australis* Zone. Sample 188-1165B-22X-CC may represent the top of the *C. spongothorax* Zone and the bottom of the *A. australis* Zone, as there are rare specimens of *A. australis* in the sample. *Actinomma golownini* is present in Sample 188-1165B-24X-CC (Table T6) and is reported to have its last appearance near the top of the *C. spongothorax* Zone.

The *A. golownini, Cycladophora humerus,* and *Eucyrtidium punctatum* Zones of Abelmann (1992) have not been recognized in samples from Holes 1165B or 1165C. It is not likely that these zones will be identified in these holes even with postcruise work because Samples 188-1165B-40X-CC (347.04 mbsf) through 54X-CC (479.50 mbsf) are barren of radiolarians (Figs. F28A, F28B, F29).

Cycladophora golli regipileus Zone

Sample 188-1165B-55X-CC is assigned to the *Cycladophora golli regipileus* Zone of Abelmann (1992). The base of this zone is defined by the FO of *C. golli regipileus* (Table T6), which was identified in Sample 188-1165B-55X-CC.

Paleontological Summary of Site 1165

Drilling at Site 1165 yielded a composite sedimentary section of ~999 m through Pleistocene to lower Miocene strata with only a few minor disconformities (i.e., ≤2 m.y. in duration). An excellent record of siliceous microfossils is present in Hole 1165B, allowing the application of the Neogene high-latitude zonal schemes for both diatoms and radiolarians (Fig. F28A, F28B). Twenty diatom biostratigraphic datums and 12 radiolarian datums were identified in Miocene to Pleistocene cores of Holes 1165B and 1165C from initial analysis of siliceous microfossil assemblages (Table T6). These datums are used to construct an initial age-depth model for Holes 1165B and 1165C (see "Sedimentation Rates," p. 39).

Diatoms are well preserved and abundant down to ~500 mbsf and absent below ~606 mbsf in Hole 1165B, except for two deeper horizons cemented by carbonate. Diatom assemblages are predominantly oceanic planktonic in character. The low abundance of neritic benthic diatoms recorded throughout the section indicates a fraction of "background" recycled biosiliceous sedimentation derived from areas within the photic zone on the continental shelf.

Well-preserved radiolarian assemblages are identified down to ~488 mbsf in Hole 1165B. Six radiolarian zones are currently identified, providing a well-defined upper Miocene to lower Pliocene biostratigraphy.

Nannofossils are generally rare and sporadic at Site 1165, with only a few discrete intervals of higher abundance and moderate to good preservation. Assemblages are characterized by low diversity and are comparable to those previously described from Prydz Bay and other Southern Ocean drill sites. Because of the inconsistent occurrences, a detailed nannofossil biostratigraphy could not be achieved. However, broad age assignments are possible and indicate that Pleistocene to lowermost Miocene sediments were recovered.

Fossil recovery in Hole 1165C was very poor, and diatoms, radiolarians, and planktonic foraminifers are very rare to absent. A burrow with poor to moderately preserved diatoms at ~754 mbsf indicates an age of <21 Ma. Biostratigraphic age control otherwise is provided primarily by calcareous nannofossils in this section. A lowermost Miocene position for the base of Hole 1165C is interpreted from nannofossil data (CN1 to CN2 Zones).

Planktonic foraminifers provide little assistance in chronostratigraphy at Site 1165 but place upper limits on the age of a few samples. Postcruise Sr dating of Pliocene–Pleistocene planktonics may clarify some apparent anomalies. Benthic foraminifers are noted more commonly than planktonics throughout the section recovered at Site 1165. Benthic foraminifer assemblages and accessory components noted in foraminiferal residues provide useful paleoenvironmental information on the source of some sediment units and help identify times at which major environmental changes occurred. Several faunas in the upper levels of Hole 1165B show evidence of being derived from shallower waters.

Sedimentation Rates

Figure F27 is a plot of age vs. depth for the composite section of Holes 1165B and 1165C. Approximately 20 diatom and 12 radiolarian FO and LO datums were used (Table T6) along with magnetostratigraphic data to construct this age model and to estimate sedimentation rates for the section. Good age control is available down through middle Miocene sediments to ~600 mbsf, at which point siliceous-microfossil dissolution is prevalent. In general, calcareous nannofossil and planktonic foraminifers are too sporadic to provide reliable datum events. Below 600 mbsf, magnetostratigraphic chron designations are based mainly on extrapolation of sedimentation rates from limited diatom and nannofossil biostratigraphic data. These data suggest that the lower part of the hole is of early Miocene age.

Biostratigraphic data were used to obtain a fit for the observed paleomagnetic reversal stratigraphy. This fit yields a set of dates with several constraints at certain depths (see "Paleomagnetism," p. 39). In Figure F30, paleomagnetic and biostratigraphic data are combined to constrain an age-depth plot. For this purpose, we assume the errors on depth and age of the paleomagnetic datums are negligible and take the most conservative estimate within the range of the biostratigraphic datums. This defines an age-depth "envelope;" for a given depth, the age is constrained to lie within the gray box.

Three lithologic units represented in Figure F27 have been identified (see "Lithostratigraphy," p. 11), which very roughly correspond to major shifts in sedimentation rates. An overall trend of decreasing sedimentation rates throughout the Neogene is noted. Sedimentation estimated for the lower Miocene is fairly high at ~110–130 m/m.y. (lithologic Unit III) and drops to ~50 m/m.y. through the middle and upper Miocene (lithologic Unit II). Uppermost Miocene to Pleistocene rates during the deposition of Unit I are even less and average ~15 m/m.y. Accumulation of sediment at Site 1165 appears to have been fairly continuous, as few disconformities were noted. Preliminary radiolarian data suggest a possible hiatus of ~2 m.y. within the middle Miocene lithologic Unit III at ~328 mbsf. An additional disconformity (~1 m.y.) is tentatively noted from diatom data at ~485–495 mbsf in the same unit.

F30. Age-depth model, p. 112.

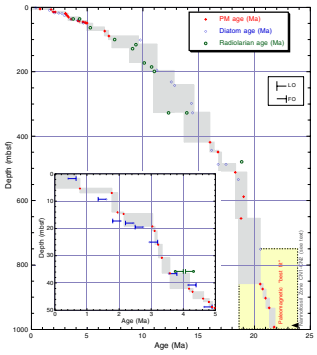

PALEOMAGNETISM

Methods

Magnetostratigraphy

For the purpose of developing a magnetic polarity stratigraphy at Site 1165, the archive halves from Holes 1165A, 1165B, and 1165C were measured with the shipboard pass-through cryogenic magnetometer. Natural remanent magnetization (NRM) and remanent magnetization after alternating field (AF) demagnetization were measured at 4-cm intervals. Time constraints and the need to keep pace with core flow permitted only two AF steps for the majority of core sections, with an additional step (30 mT) in the lower half of the core. The presence of a strong rock-saw overprint (potentially induced by the splitting saw) between ~860 and 880 mbsf necessitated progressive demagnetization of the archive halves up to 80 mT.

A total of 614 oriented discrete samples (standard 8-cm^3 plastic cubes) were also collected from the working halves. Most discrete samples were AF demagnetized at successive peak fields of 10, 20, 30, 40, 50, 60, 70, and 80 mT to verify the reliability of the whole-core measurements. Three hundred eighty-nine of these samples yielded good principal component analysis (PCA) (Kirschvink, 1980) fits. Six discrete samples were progressively thermally demagnetized at temperatures of 100°, 200°, 300°, 330°, 360°, 400°, 400°, 500°, 550°, 600°, 650°, and 700°C. The magnetic susceptibility was measured after each step to monitor thermal alteration of the magnetic mineralogy.

The lack of azimuthal orientation of the cores does not pose a problem for magnetostratigraphic studies because the geomagnetic field at the latitude of Site 1165 (64.4°S) has a steep inclination (±76.5°, assuming a geocentric axial dipole model). Consequently, the paleomagnetic inclinations, which were determined from the 20–30 mT AF steps from the long-core measurements and from PCA of characteristic remanence components of discrete samples, are sufficient to determine polarity. In the Southern Hemisphere, negative (upward) inclinations correspond to normal polarity and positive (downward) inclinations correspond to reversed polarity.

Rock Magnetism

Mineral magnetic analyses were performed on a set of discrete samples after they had been subjected to AF demagnetization. The low-field magnetic susceptibility (k) was routinely measured for each sample, and the data were compared with the whole-core susceptibility log (see **"Physical Properties,"** p. 54). The frequency-dependent susceptibility, *fd*(%), of 338 selected discrete samples was monitored. An anhysteretic remanent magnetization (ARM) was imparted on 135 samples using a 100-mT alternating field and a 0.05-mT bias field. An isothermal remanent magnetization (IRM) was imparted on 334 samples in a direct-current (DC) magnetic field of 1.3 T. The IRM was then demagnetized by inverting the sample and applying a backfield of 300 mT to determine the S-ratio ($-IRM_{-0.3T}/IRM_{1.3T}$) (e.g., Verosub and Roberts, 1995). Moreover, on selected samples we investigated the following:

1. The progressive acquisition of the IRM up to 1.3 T,
2. The coercivity of remanence (B_{cr}) determined by progressively increasing backfield to the maximum IRM, and
3. Stepwise thermal demagnetization of a composite IRM (Lowrie, 1990). Fields of 1.3, 0.5, and 0.12 T were applied to distinguish between high-, intermediate-, and low-coercivity magnetic phases, respectively.

Results

Rock Magnetism

Based on magnetic properties and behavior during demagnetization treatment, the drilled sedimentary sequence can be divided into three main intervals that are not directly related to lithologic variations in the core. The downcore variations of k, ARM, and IRM are shown in Figure **F31.** The highest values of these magnetic concentration–dependent parameters are recorded in the upper 94 mbsf of the core. In this interval, preliminary analyses of magnetic mineralogy-dependent pa-

F31. Downcore variation of concentration-dependent parameters, p. 113.

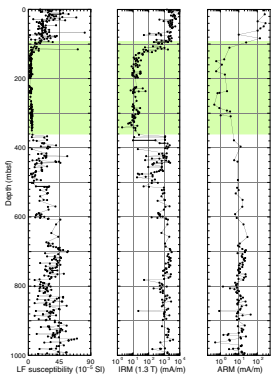

rameters (e.g., B_{cr} and S-ratio) and thermal unblocking characteristics are consistent with a magnetite-dominated magnetic mineralogy. During thermal demagnetization of the three orthogonal IRMs, the intensity decays in a quasi-linear fashion from room temperature to the Curie temperature of magnetite (580°C), with a weak inflection point between 320° and 350°C (Fig. F32). Several magnetic minerals experience thermal unblocking at these temperatures, including titanomagnetite (Hunt et al., 1995), iron sulfides such as greigite (Roberts, 1995), and pyrrhotite (Dekkers, 1989). Shipboard investigations did not yield enough evidence to distinguish between these possibilities. The significance of these phases becomes progressively more pronounced in the lower parts of the succession (Figs. F31, F32). The interval between 94 and 130 mbsf is a transition zone where the magnetic concentration–dependent parameters decrease significantly. Below this interval, between 130 and 362 mbsf, very low concentration-dependent values are present. For example, IRM decreases from an average of 2943 mA/m between 0 and 130 mbsf to ~17 mA/m between 130 and 362 mbsf. High coercivity values (Fig. F33) and Curie temperatures of >650°C indicate the presence of hematite in addition to minor magnetite contributions in this interval. Corresponding to this interval of low-magnetic mineral concentrations, geochemical analyses show the presence of a particularly high broad peak in silica concentration (see "Inorganic Geochemistry," p. 43). We suggest that in the presence of an amorphous silica-saturated environment, magnetite was unstable and consequently was consumed by chemical processes. Such processes would preferentially remove "free" small grains with large surface area/volume ratio, leaving inclusions of magnetite in other mineral phases unaffected. The stable iron-rich solid phases expected under such conditions are iron silicates and hematite (Garrells and Christ, 1965). The presence of a low-coercivity drilling overprint suggests that a limited amount of coarse-grained, multidomain magnetite remains in this zone.

The interval between 362 and 512 mbsf is a transitional zone and is characterized by parameters that indicate frequently changing high and low magnetic mineral concentrations. The lower section, between 512 and 999 mbsf, contains almost the same high ferrimagnetic concentrations as encountered in the uppermost 94 m.

Magnetostratigraphy

In the following section, we describe the magnetic polarity stratigraphy above 94 and below 362 mbsf. The decreased abundance of ferrimagnetic minerals between 94 and 362 mbsf coincides with a poor-quality paleomagnetic signal that prohibited the determination of a reliable magnetic polarity stratigraphy (Fig. F34). Most of the samples analyzed suggest the presence of a nearly vertical reversed polarity overprint (Weeks et al., 1995). This overprint is soft and is always removed at peak fields of 10 mT. After overprint removal, a stable characteristic remanence component is evident for a large proportion of the analyzed samples (Fig. F35). In a few cases (samples between 860 and 880 mbsf), an additional overprint—stronger than the drilling-induced overprint—is present. This overprint has a nearly horizontal inclination and is probably related to contamination introduced by cutting the sections. In most cases, this component is parallel to the splitting plane (i.e., in sample coordinates, the overprint is in the y-z plane with x = 0) and in a few cases, is perpendicular to it (the overprint is in the x-z plane with

F32. Thermal demagnetization of a composite three-axis IRM for two representative samples, p. 114.

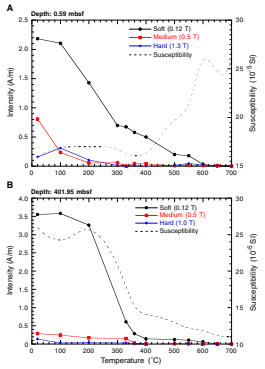

F33. Plot of IRM acquisition and DC demagnetization of seven representative samples, p. 115.

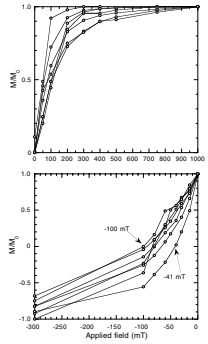

F34. Inclination record (0–999.1 mbsf) after demagnetization at 20–30 mT, p. 116.

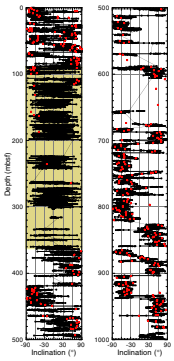

F35. Vector component diagram of demagnetization (AF) behavior of representative samples, p. 117.

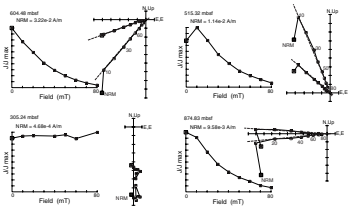

y = 0). When present, this overprint could only be partially removed even after demagnetization to peak fields of 60–80 mT.

The preliminary magnetostratigraphic interpretation of the top 50 mbsf is well constrained by diatom datums derived from initial analysis of core-catcher samples (Fig. **F36;** see **"Biostratigraphy and Sedimentation Rates,"** p. 21). The inclination record for this interval, when compared with the geomagnetic polarity time scale (GPTS) (Cande and Kent, 1992, 1995; Berggren et al., 1995), provides a near-complete record of the Pliocene–Pleistocene polarity intervals from the Brunhes Chron (C1n) to the Thvera Subchron (C3n.4n), with the Pliocene/Pleistocene boundary at 6.97 mbsf. Correlation with the GPTS suggests disconformities at ~6, 14.4, 15.6, and ~16 mbsf. Corresponding to the stratigraphical break at ~6 mbsf, the Jaramillo Subchron (C1r.1n) is missing. From this correlation, the relatively reduced thickness of the Brunhes Chron can be explained by the presence of one or more disconformities. Also, if the present correlation is correct, a new reversed polarity event is recognized within Subchron C2An.3n (at ~32.64 mbsf).

The polarity record from 50 to 94 mbsf is constrained by limited biostratigraphic control, which makes correlation with the GPTS more difficult (Fig. **F37**); however, following the pattern recorded in the upper 50 mbsf, the four recorded reversals can be matched with the lower part of the Thvera Subchron (C3n.4n), C3r, C3An.2n, C3Ar, and the upper part of Chron C3.Bn. In this context, the Miocene/Pliocene boundary lies at ~54.60 mbsf. The sharp polarity change at ~67 mbsf suggests a disconformity with a significant amount of missing time, including Subchrons C3An.1n and C3An.1r. Several small variations in the magnetic polarity between 69 and 100 mbsf correspond with the presence of metamorphic and/or igneous pebbles.

Some segments within the transitional band between ~94 and ~130 mbsf show changes in magnetic intensity and polarity corresponding to the alternation between black and gray horizons (Fig. **F38**). This provides further evidence that variations in magnetic properties below ~94.0 mbsf are related to variations in redox conditions, resulting in partial dissolution of the detrital magnetic minerals and formation of secondary magnetic phases (e.g., Florindo and Sagnotti, 1995).

The polarity pattern is obscure between 94.0 and 362.0 mbsf, which renders delineation of any magnetic polarity interval impossible. A good magnetostratigraphic signal, however, is recorded in the sediments between 362.0 and 999.1 mbsf (Figs. **F39, F40**). Unfortunately, it proved difficult to fit this record to the GPTS because of the scarcity of biostratigraphical datums. Four taxa, including the FCO of *A. ingens* (<15.9–16.4 Ma), the FO of *C. kanayae* (<17.5–17.7 Ma), the LO of *T. praefraga* (>18.3–19.1 Ma), and the FO of *T. praefraga* (<19.9–20.8 Ma; see **"Biostratigraphy and Sedimentation Rates,"** p. 21), are identified in this interval. Starting from these tie points, a magnetostratigraphic correlation was attempted; however, the limited biostratigraphic control and the complex nature of the paleomagnetic signal mean that this interpretation is preliminary and its validity needs to be tested through shore-based studies. By approximating the sedimentation rate from the available biostatigraphic data, the expected lengths of chrons were calculated and an iterative approach was taken to achieve a fit. Between ~350.0 and ~419.0 mbsf, polarity is mostly reversed and is followed by a normal polarity interval characterized at the bottom (449.4 mbsf) by a sharp magnetic polarity boundary. The presence of the FCO of *A. ingens* (<15.9–16.4 Ma) constrains these two magnetozones to the C5Br and

F36. Magnetostratigraphic record (0–50 mbsf), p. 118.

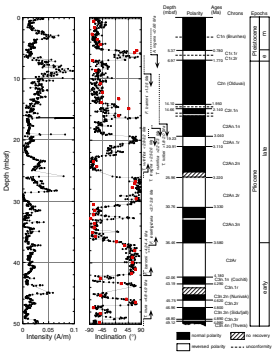

F37. Magnetostratigraphic record (50–100 mbsf), p. 119.

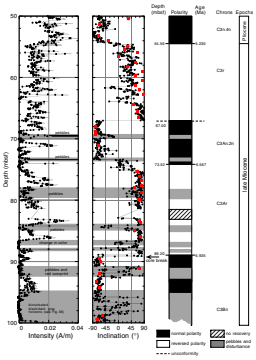

F38. Coincidence between the intensity of remanence and polarity changes with lithology changes in Core 188-1165B-11H, p. 120.

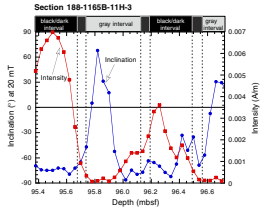

F39. Magnetostratigraphic record (350–650 mbsf), p. 121.

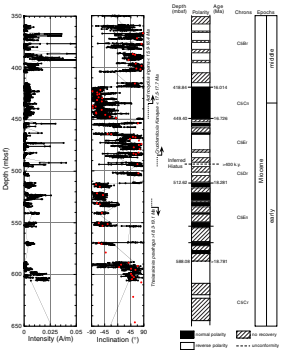

C5Cn Chrons. The thick interval of normal polarity between 718.4 and ~824.0 mbsf contains the FO of *T. praefraga* (<19.9–20.8 Ma) and is correlated with Chron C6n. Consequently, the sequence of magnetozones below 824 mbsf are correlated with Chrons C6r, C6An, and C6Ar, respectively.

Biostratigraphic data indicate a disconformity between 487 and 497 mbsf with a duration of ~1 m.y. Several sharp changes in magnetic polarity (e.g., at 718.4 and 746.4 mbsf) suggest the presence of more than one disconformity surface with a significant interval of time missing.

Relative Paleointensity

The ideal sediment characteristic for relative paleointensity determination is one in which the remanence is a detrital remanent magnetization determined by pseudo–single domain (PSD) magnetite, the concentration does not vary by more than a factor of 10 (King et al., 1983; Tauxe, 1993; Jacobs, 1998), and there is no correlation between normalized NRM and the concentration-dependent magnetic parameters such as k, IRM, and ARM (Tauxe, 1993).

In the uppermost part of Hole 1165B (0–94 mbsf), rock magnetic analyses demonstrate that the sediment satisfies the criteria for relative paleointensity determination. Magnetite, probably in the PSD state, is the primary magnetic carrier. Variation of bulk magnetic parameters (k, ARM, and IRM) shows that its concentration does not vary by more than one order of magnitude. Furthermore, a significant correlation between the NRM/k ratio and the normalizing factor k does not exist.

The NRM intensity record, demagnetized at 20 mT to eliminate the drilling-induced overprint, was normalized with low-field magnetic susceptibility in the uppermost 100 mbsf of Hole 1165B (Fig. **F41**). The NRM_{20mT}/k ratio vs. depth shows a series of high and low values. Polarity boundaries are characterized by low NRM_{20mT}/k ratios that recover immediately after the termination of the polarity boundary. This is consistent with published paleointensity records and current geodynamo models. These results indicate that a relative paleointensity record can be established in the uppermost 100 m of Hole 1165B and that comparison with previously published data sets might improve the stratigraphic resolution of the Pliocene–Pleistocene part of the section.

INORGANIC GEOCHEMISTRY

Shipboard chemical analyses of the interstitial water samples from Site 1165 followed the procedures outlined in **"Inorganic Geochemistry,"** p. 19, in the "Explanatory Notes" chapter. Sixty-nine 10- to 20-cm-long whole-round core samples from 0.45 to 995.30 mbsf were squeezed for interstitial water. Samples were taken at 50-cm intervals from Hole 1165A. Samples were taken from Hole 1165B at 1.5-m intervals to ~60 mbsf, every ~10 m to 100 mbsf, and then every ~30 m to 636 mbsf. Samples were taken from Hole 1165C every ~30 m from 636 to 995 mbsf. Results from all three holes are considered to represent a single continuous profile and are presented in Table **T7** and Figures **F42** and **F43.**

Chlorinity decreases slightly downhole, from 555 mM near the seafloor to 531 mM at 995.30 mbsf. A local maximum of ~573 mM, between 30 and 50 mbsf, represents an increase of ~3% over seafloor values (Fig. **F42**). This increase is significant relative to the measure-

F40. Magnetostratigraphic record (500.0–999.1 mbsf), p. 122.

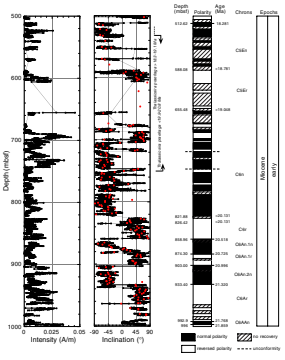

F41. The relative paleointensity record (susceptibility normalization) for the uppermost 100 m, p. 123.

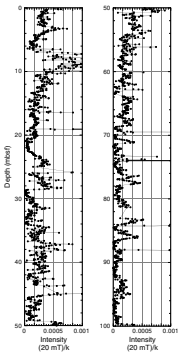

T7. Interstitial water chemistry from shipboard measurements, p. 179.

F42. Selected high-resolution interstitial water chemistry profiles vs. depth, p. 124.

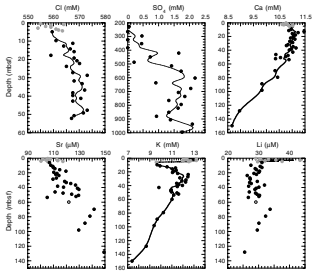

ment precision (<0.3%) and likely reflects the global increase in ocean salinity during the last glaciation. The increase is not observed in the salinity measurements (Fig. F43), probably because of the relatively low resolution of the optical refractometer. The irregular downhole trend toward lower chlorinity values (564.5–531.0 mM; ~6%) shows no clear evidence of simple linear mixing between two separate water masses. The profile likely reflects diagenetic reactions within the core such as increasing clay mineral dehydration with increasing depth.

The pore-water profiles at Site 1165 may be referenced to three dominant chemical reactions: sulfate reduction, carbon dioxide reduction (methanic), and inorganic diagenesis. Although the first two reactions are largely exclusive, inorganic diagenesis occurs throughout the core.

F43. Full interstitial water chemistry profiles vs. depth, p. 125.

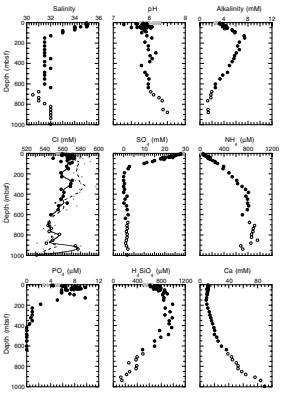

Sulfate Reduction Zone (Seafloor to ~150 mbsf)

The uppermost sediments at Site 1165 are strongly reducing, reflecting the active diagenesis of buried organic matter (see "Organic Geochemistry," p. 47). Dissolved sulfate (SO_4^{2-}) decreases linearly (R^2 = 0.984) downhole from seafloor values of 29 to 2 mM at 150 mbsf (Fig. F43). Sulfate depletion is highly negatively correlated (R^2 = 0.964) with a corresponding linear downhole increase in dissolved ammonium (NH_4^+) (Fig. F43). Other key byproducts of organic matter decay increase roughly threefold through the sulfate reduction zone (SRZ), namely alkalinity (3–8 mM; derived from the oxidation of carbon in organic matter) and phosphate (HPO_4^{2-} = 3–10 µM; derived from the remineralization of organic phosphorous) (Fig. F43). In theory, the oxidation of organic matter during sulfate reduction follows the simplified stoichiometric form:

$$2CH_2O\ (\text{organic matter}) + SO_4^{2-} = H_2S + 2HCO_3^-\ (\text{alkalinity})$$

or the full redfield ratio sulfate reduction reaction:

$$53SO_4^{2-} + C_{106}H_{263}O_{110}N_{16}P = 39CO_2^- + 67HCO_3^- + 16NH_4^+ + 53HS^- + 39H_2O + HPO_4^{2-}$$

or

$$53SO_4^{2-} + (CH_2O)_{106}(NH_3)_{16}H_3PO_4 + 39H_2O = 106HCO_3^- + 16NH_4^+ + 53HS^- + 39H_2O + HPO_4^{2-},$$

wherein 2 mM of alkalinity are produced for each millimole of sulfate reduced. At Site 1165, significantly less alkalinity (and phosphate) are produced for each millimole of sulfate reduced (see "Conclusions," p. 47).

The profile of dissolved manganese (Mn^{2+}) within the SRZ is characteristic of the reduction of manganese oxides during the oxidation of organic carbon. Manganese concentrations remain below analytical resolution from the seafloor to 10 mbsf (Fig. F43). From 10 to 32 mbsf, manganese increases rapidly to 168 µM before dropping to ~8 µM at the base of the SRZ (~150 mbsf).

The interstitial water profiles of dissolved calcium (Ca^{2+}), magnesium (Mg^{2+}), and potassium (K^+) (Fig. F43) all display marked inflections at 150 mbsf. Calcium shows a small but measurable downhole increase over 15 samples between the seafloor (10.8 mM) and 15 mbsf (11.2

mM). Calcium values then decrease nonlinearly downhole to 8.7 mM at 150 mbsf (Fig. F42). Magnesium concentrations decrease linearly (R^2 = 0.956) downhole, from the modern seawater value (~54 mM) near the seafloor to 37 mM at 150 mbsf. Dissolved strontium (Sr^{2+}) increases downhole, from 106 µM at the seafloor to ~150 µM at 150 mbsf. The detailed profile shows repeated high-frequency excursions of ~10%, which remain unexplained (Fig. F42). The variations are unlikely to represent analytical drift because each excursion is characterized by four or more discrete analyses run in random order.

Dissolved lithium (Li^+) approximates seawater concentrations immediately below the seafloor (29 µM at 0.45 mbsf) but increases rapidly to 43 µM at ~3 mbsf before dropping back to seawater values between 5 and ~150 mbsf. Lithium also shows the unexplained high-frequency excursions observed for strontium. Interstitial water potassium levels are enriched by ~3 mM over standard seawater potassium in the top 4.45 m of Hole 1165A (Fig. F42). These high pore-water potassium concentrations coincide with traces of reworked glauconite (see "Lithostratigraphy," p. 11), which suggests that active dissolution of the grains is taking place. Between 4.45 and 4.95 mbsf, interstitial potassium values drop sharply to 9.6 mM and increase again to 12.4 mM at 22 mbsf before beginning a gradual downhole decrease to 7 mM at the base of the SRZ. Dissolved sodium concentrations are within ~1% of the modern seawater value (~480 mM) to the base of the SRZ (Fig. F43).

Near the seafloor, the interstitial water silica (H_4SiO_4) concentration of 522 µM is significantly enriched relative to modern deep-ocean water (typically <200 µM). Continuing dissolution of abundant siliceous microplankton within the near-surface sediments produces an exponential increase in dissolved silica to ~850 µM at 100 mbsf (Fig. F43).

CO_2 Reduction (Methanic) Zone (~150 to ~400 mbsf)

When sulfate is depleted, CO_2-utilizing methanogenic Archaea bacteria rapidly take over as the dominant life form within the sediment (Fig. F44). In the presence of excess organic matter, the theoretical reaction follows the form:

$$(CH_2O)_{106}(NH_3)_{16}(H_3PO_4) = 53CO_2 + 53CH_4 + 16NH_3 + H_3PO_4.$$

F44. Downhole profiles of dissolved sulfate and headspace methane for the upper 400 m, p. 127.

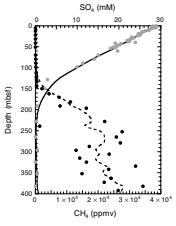

At Site 1165, headspace methane concentrations increase rapidly below 150 mbsf, marking the top of the CO_2 reduction zone (CRZ) (see "Organic Geochemistry," p. 47). The base of the active reaction zone is more diffuse and is therefore identified at ~400 mbsf on the basis of changes in pore-water ammonium and phosphate profiles (Fig. F43). Dissolved ammonium increases linearly downhole, from 400 µM at 150 mbsf to 800 µM at 400 mbsf, approximating the ammonium gradient measured in the overlying SRZ. The alkalinity profile deflects sharply at 150 mbsf (Fig. F43) and steadily decreases to the base of the hole. The 30% decline in alkalinity observed between 150 and 400 mbsf signifies the large-scale removal of HCO_3^- from the system. Phosphate decreases sharply to <2 µM between 150–200 mbsf and finally disappears from the interstitial waters below 400 mbsf.

Dissolved manganese shows a small increase from 7 to 23 µM between 191 and 265 mbsf, before decreasing to ~14 µM at the base of the CRZ. The dissolved calcium concentration increases linearly (11–19 mM; R^2 = 0.997) through the CRZ, reversing the trend observed in the

overlying SRZ. Magnesium decreases nonlinearly downhole, from 32 to 30 mM, through the same interval. Dissolved strontium increases nonlinearly, from 160 µM at 150 mbsf to ~247 µM at ~400 mbsf. There is a sublinear correlation ($R^2 \approx 0.8$) between calcium/strontium gain and magnesium loss through the CRZ.

Interstitial water lithium concentration increases sublinearly ($R^2 = 0.819$) downhole, from 28 µM at 191 mbsf to 59 µM at 382 mbsf. Dissolved potassium decreases linearly ($R^2 = 0.984$) to 2.8 mM at 487 mbsf. The dissolved sodium concentration begins a slow linear ($R^2 = 0.937$) downhole decline, from 483 mM at 265 mbsf to 399 mM at 880 mbsf. The dissolved silica concentration remains constant at ~1000 µM, approaching the solubility limit of opal-A.

Rock-Water Reaction Zone (~400 to 995 mbsf)

Below ~400 mbsf, the fermentation processes driving active methanogenesis appear to decrease and inorganic reactions become more significant. Chloride and salinity both record low values between 600 and 800 mbsf (543 mM and 30.5, respectively, at ~700 mbsf). Ammonium approaches steady state below 400 mbsf, averaging ~800 µM to the base of the hole. The small change in the ammonium profile between Holes 1165B and 1165C may be an artifact of different sample batches. The sulfate profile shows a small downhole increase from ~0 to 2.2 mM between ~400 and 995 mbsf (Fig. **F42**). Alkalinity continues to decrease linearly ($R^2 = 0.980$) downhole to ~800 mbsf (1.26 mM). The lowermost two samples analyzed (851 and 880 mbsf) show indications that alkalinity may be increasing again, but the sample resolution is too low to draw any firm conclusions.

Dissolved manganese shows no clear trend between 400 and 600 mbsf, with values ranging from 11 to 23 µM. Two minor downhole-decreasing trends are apparent between 677 and 765 mbsf (25–18 µM) and from 794 to 995 mbsf (26–5 µM). Dissolved calcium increases exponentially below the CRZ ($R^2 = 0.986$), reaching a maximum of 89 mM at 995 mbsf. The magnesium profile is significantly more complex. An upper reaction zone, from ~400 to ~600 mbsf, shows a continuation of the nonlinear gradient observed in the overlying CRZ. The lower two reaction zones, from ~600 to 800 mbsf and ~800 to 937 mbsf, show distinct nonlinear gradients. Magnesium concentrations reach a low of 6.6 mM near the base of the hole. Dissolved strontium increases exponentially downhole, from 217 µM at 421 mbsf to 764 µM at 995 mbsf. The 250% downhole increase in strontium compares to a 367% increase in calcium and a 78% decrease in magnesium concentrations over the same interval.

The dissolved lithium profile appears to show marked inflections at ~600 and 880 mbsf. Lithium shows significant scatter between 400 and 600 mbsf, but the dominant trend is toward higher values downhole (50 to ~80 µM). The lithium profile then decreases linearly (79–21 µM; $R^2 = 0.964$) to 880 mbsf before increasing linearly (21–41 µM; $R^2 = 0.987$) to the base of the hole. The dissolved potassium profile from 487 to 937 mbsf shows minor variations in concentration, although the overall downhole trend is toward lower values (1.3 mM at 937 mbsf). Sodium decreases sublinearly ($R^2 = 0.924$) downhole, from 467 mM at 420 mbsf to 399 mM at 880 mbsf. Dissolved silica declines steadily below 420 mbsf, decreasing from ~972 to ~130 µM at 938 mbsf.

Conclusions

Interstitial water chemistry at Site 1165 reveals three distinct reaction zones within the sedimentary section. The SRZ shows the expected depletion of dissolved sulfate and salinity, with associated increases in ammonium, phosphate, alkalinity, and silica. In theory, 2 mM of alkalinity are produced for each 1 mM of sulfate reduced. Within the SRZ, alkalinity increases by <0.2 mM/mM sulfate reduced (Fig. F45), indicating rapid removal of bicarbonate from the system. Likely mechanisms for this reaction are calcium carbonate precipitation or silicate reactions. If the alkalinity deficit is assumed to be caused solely by carbonate precipitation, preliminary saturation-state calculations predict a decrease of 5.5 mM calcium in the interstitial waters at the base of the Site 1165 SRZ. This compares to the observed calcium decrease of only 1.9 mM between the seafloor and ~150 mbsf (Fig. F46). Associated sediment calcium carbonate values are generally <1 wt% (see "Organic Geochemistry," p. 47), further confirming that calcite precipitation is not the principle mechanism involved in the alkalinity removal. It should be noted that this simplified mass-balance approach ignores the possible role of advective and diffuse transport in controlling element distribution.

Below 150 mbsf, the CRZ shows the expected increases in methane and ammonium. Removal of dissolved CO_2 by methano-bacteria lowers alkalinity, raises pH, and accelerates carbonate precipitation. The decrease in dissolved phosphate within the CRZ is likely due to the precipitation of authigenic phases such as $Ca_3(PO_4)_2$, $Fe_3(PO_4)_3$, $MgNH_4PO_4$, or $Ca_5(PO_4)_3F$.

Calcium and magnesium are inversely correlated through much of the sedimentary section (Fig. F47). The correlation is mostly nonlinear, suggesting independent diagenetic reactions are responsible for the profile variations. No firm conclusions can be drawn from the available data; however the following may be considered: although diagenetic rather than diffusive reactions appear to dominate throughout much of the core, calcite or dolomite dissolution/precipitation alone cannot explain the observations. Clay mineral reactions, such as smectite formation, could produce the observed downhole decrease in dissolved magnesium and alkalinity. Dissolution of calcium-rich plagioclase may account for part of the exponential downhole increase in dissolved calcium, although no clear correlation is evident from comparison with plagioclase estimates from XRD analyses (see "Lithostratigraphy," p. 11). The sharp downhole decline in dissolved potassium is closely matched by a relative increase in K-feldspar within the sediment (Fig. F48). It seems likely that much of the K-feldspar observed at Site 1165 is authigenic in origin.

F45. Sulfate vs. alkalinity, p. 128.

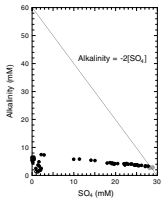

F46. Observed calcium depletion vs. predicted calcium depletion within the SRZ, p. 129.

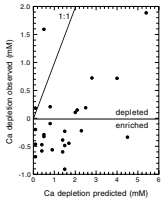

F47. Calcium vs. magnesium, p. 130.

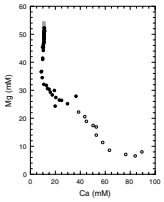

F48. Interstitial water potassium concentrations vs. semiquantitative K-feldspar distribution from XRD analyses, p. 131.

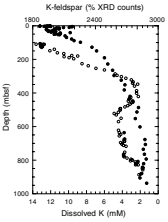

ORGANIC GEOCHEMISTRY

Shipboard organic geochemical studies of cores from Holes 1165B and 1165C included monitoring of hydrocarbon gases, carbonate and organic carbon, total sulfur and total nitrogen content, and Rock-Eval pyrolysis characterization of organic matter. Procedures are summarized in "Organic Geochemistry," p. 20 in the "Explanatory Notes" chapter.

Hydrocarbon Gases

Hydrocarbon gas measurements by the headspace method are reported in Table T8. Results are reported in parts per million by volume (ppmv) of methane (C_1), ethane (C_2), and propane (C_3) in the air headspace of a 20-cm³ vial containing a nominal 5-cm³ sediment sample. Results are plotted as parts per million by volume of hydrocarbon gas component vs. depth in Figure F49. Methane content increases slowly from background levels (4 ppmv) to 400 ppmv in the cored interval between 30 and 150 mbsf and increases rapidly (400–20,000 ppmv) over the interval from 150 to 230 mbsf. Methane levels remain within a relatively uniform range (20,000–40,000 ppmv) down to 700 mbsf and then increase again to the 40,000–80,000 ppmv range in the deepest part of Hole 1165C (700–980 mbsf). The linear dissolved sulfate gradient above 130 mbsf projects to 0 mM concentration at a depth of 147 mbsf (see "Inorganic Geochemistry," p. 43), where the sulfate-free sediments inevitably result in the onset of methanogenesis and the presence of abundant methane in deeper cores (Claypool and Kaplan, 1974). It is unusual to have small but significant levels of headspace methane (50–400 ppmv) present within the sediment depth interval in which dissolved sulfate is present (seafloor to 147 mbsf). Usually methane is maintained at background levels by microbial methane oxidation within the zone of sulfate reduction. Such methane oxidation may not be occurring in Site 1165 sediments.

Ethane and propane make consistent downhole appearances below 150 and 820 mbsf, respectively. Gas composition as expressed by the C_1/C_2 value of headspace gas is plotted vs. depth in Figure F50 and vs. estimated sediment temperature (assuming an average geothermal gradient of 48°C/km) in Figure F51. The C_1/C_2 value shows the usual exponential increase in ethane content relative to methane with increasing depth. When C_1/C_2 is plotted vs. temperature (Fig. F51), the C_1/C_2 trend falls within the normal range associated with in situ low-temperature ethane generation and well to the right of the "Anomalous" field that would indicate migrating thermogenic hydrocarbons (JOIDES Safety Manual, 1992).

Headspace methane values above ~10,000 ppmv are residual concentrations, representing only that gas retained by sediments after outgassing has taken place during core retrieval to the surface (Kvenvolden and Lorenson, 2000). Moreover, there is some variability in the results of the headspace technique due to nonuniform sample size. Additionally, when cores become lithified it is more difficult to obtain reproducible sample volumes. Typically, indurated core pieces are broken into fragments <1 cm and the headspace vial is filled about one-half full. To investigate the possible effect of variable sample size on headspace gas concentration, all of the analyzed sample-filled headspace vials were weighed to an accuracy of ~0.1 g on a mechanical triple-beam laboratory balance. Sample net weights reported in Table T9 are after subtracting the average tare weight (16.6 g) of an empty—but labeled, crimped, and septum capped—headspace vial. Sample weights were converted to sample volume using a bulk density vs. depth relationship (see "Physical Properties," p. 54). Calculated sample volumes were used to estimate effective headspace volumes for each analysis and are presented in Table T9. Note that sample volumes varied between 2.8 and 7.9 cm³. Kvenvolden et al. (1989) give the equations for converting from parts per million by volume in headspace concentration units to absolute volume of gas per volume of sediment using sample volumes. The re-

T8. Headspace gas concentrations of C_1, C_2, and C_3, p. 180.

F49. C_1, C_2, and C_3 vs. depth, p. 132.

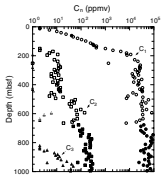

F50. C_1/C_2 values of headspace gas vs. depth, p. 133.

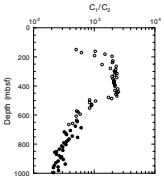

F51. C_1/C_2 values of headspace gas vs. sediment temperature, p. 134.

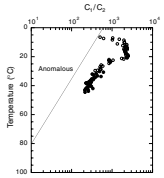

T9. Recalculation of headspace gas CH_4 concentrations, p. 181.

sulting methane concentrations, expressed in microliters of CH_4 per liter of wet sediment, are listed in Table T9. Further evaluation of the quantity of methane present in cores is possible if the methane concentration is expressed relative to the volume of pore water that originally contained most of the gas. An average porosity vs. depth function (see "Physical Properties," p. 54) was used to convert from a volume of sediment to volume of water basis. Gas concentrations expressed in millimoles of methane per liter of water (mM), are also shown in Table T9 and plotted in Figure F52. Also shown on Figure F52 is the solubility of methane in seawater at 0°C and 1 atmosphere pressure (2.3 mM). Below ~175 mbsf, the residual dissolved CH_4 content in pore water is supersaturated with respect to surface solubility but unsaturated relative to estimated subsurface methane solubility.

Site survey data show a bottom-simulating reflector (BSR) on a seismic line located ~62 nmi from Site 1165. Although there is no BSR at Site 1165, with the appearance of methane in the cores, a protocol was established for examining and possibly sampling any methane hydrate occurrences. No evidence for gas hydrate was present in the cores. Moreover, there was insufficient gas to cause voids or gas pockets within the core liner. It is likely that the pore waters at Site 1165 lacked the minimum dissolved methane concentration required for the stabilization of methane hydrate. Under the pressure and temperature conditions at Site 1165 (see "In Situ Temperatures," p. 62), the minimum dissolved methane concentration required for the stabilization of methane hydrate is ~80–90 mM near the seafloor, rising rapidly to ~180–200 mM at the base of the methane hydrate stability zone. The depth of the theoretical base of methane hydrate stability at Site 1165 is ~460 mbsf.

F52. Recalculated concentration of methane dissolved in pore water, p. 135.

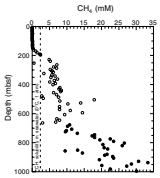

Carbon and Elemental Analyses

A total of 172 sediment samples (one to two samples per core) were analyzed for carbonate carbon, and 47 selected (darker colored) samples from Holes 1165B and 1165C were analyzed for total carbon, OC (by difference), total nitrogen (TN), and total sulfur (TS). The results are reported in Table T10. Inorganic carbon (IC) content is plotted against depth of burial in Figure F53A. Carbonate content is uniformly very low (0.01–0.1 wt% IC), with the exception of scattered beds at the base of the section with between 0.1 and 1 wt% IC and 12 samples throughout the cored section with higher carbonate content (1–7.5 wt% IC).

T10. Carbon, nitrogen, and sulfur analyses of sediments, p. 182.

F53. Weight percent of inorganic carbon (carbonate carbon) and organic carbon in sediments, p. 136.

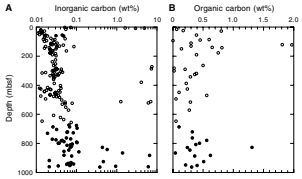

OC content of sampled intervals (Table T10; Fig. F53B) ranges from 0 to 1.97 wt%, with most samples between 0.1 and 0.5 wt%. The highest OC contents (1.81 and 1.97 wt%) are in the depth interval from 110 to 112 mbsf. Only one other sample, at 823 mbsf, exceeds the 1 wt% carbon level (1.31 wt% OC).

TN content is generally between 0 and 0.13 wt% but with values as low as 0 wt% (Table T10). The TN data show no apparent trends vs. either depth or OC content. TS contents are similarly scattered, with many analyzed samples showing sulfur below detectable limits (Table T10). Whereas marine sediments generally show a consistent relationship between TS and OC content (TS = 0.36 × OC) (Goldhaber and Kaplan, 1974), samples from Site 1165 tend to have more variability. Site 1165 sediments generally contain excess sulfur relative to carbon in the interval from 0 to 350 mbsf and are more sulfur deficient in the lower part.

Organic Matter Characterization

Eleven samples from Holes 1165B and 1165C were characterized by Rock-Eval pyrolysis (Table T11). Samples with >0.5 wt% OC were selected for analysis. All samples have low pyrolyzable carbon contents, with S_2 yields ranging from 0.1 to 0.7 mg of hydrocarbon per gram of sediment. The T_{max} values and the broad S_2 peak shapes in the pyrograms (not shown) indicate that most samples contain mixtures of small amounts of primary marine organic matter with variable amounts of possibly recycled and degraded thermally mature organic matter. The shallowest samples, at 27.9 and 76.7 mbsf, have the highest T_{max} values (479° and 540°C, respectively), indicating the highest proportions of recycled organic matter. The two samples (110.2 and 111.7 mbsf) with the highest OC content (1.81 and 1.97 wt%) have broad pyrograms and T_{max} values of 434° and 439°C. If the primary organic matter in these samples is thermally immature (T_{max} < 420°C), then a significant proportion (10%–20%) of recycled, high-maturity (T_{max} > 500°C) organic matter could be present. Alternatively, the two organic-rich samples from the 110–112 mbsf interval could also contain even larger proportions (50%?) of less mature (T_{max} = 460°C) recycled organic matter.

T11. Organic carbon and Rock-Eval pyrolysis on selected samples, p. 183.

COLOR ALTERNATIONS IN CORES

The following section describes the preliminary shipboard analysis of color alternations (cyclicity) that are observed in cores from Site 1165. This work will be the basis for postcruise studies to more thoroughly explain the observations and processes involved.

Observations

As part of standard laboratory operations, cores from Site 1165 were analyzed with the Minolta CM-2002 spectrophotometer for color variations (see "Lithostratigraphy," p. 11; Fig. F6) and were photographed in color and black and white (see the "Core Descriptions" contents list). The cores were also analyzed for density and magnetic susceptibility variations using the multisensor track (MST) system.

Upon visual inspection, systematic color variations, or color cyclicity, is apparent in the cores from Site 1165. The visual variations are also observed as cyclicity in the lightness factor values from the spectrophotometer (Fig. F54). The L* values show that there is a general downhole darkening of the core that is evidenced by the decreasing trend of the lightness values (see "Lithostratigraphy," p. 11; Fig. F6). Superimposed on this trend are variations with many wavelengths ranging from centimeter to decimeter size.

In general, the short-wavelength (<3–4 m) lightness variations are caused by cycles between a green to greenish gray facies (lighter, with larger L* values) and a gray to dark gray facies (darker, with smaller L* values; Fig. F55). The greenish facies are structureless diatom-bearing clay with higher biogenic content, dispersed clasts, and lonestones than the dark gray facies, which are mostly clay with some silt laminations (see "Lithostratigraphy," p. 11). Greenish facies generally have lower bulk-density, magnetic susceptibility, and organic carbon values.

The lightness cycles occur throughout the hole but are more evident in the upper ~400 mbsf (i.e., green/gray cycles are more evident) than in the lower part of the hole, where rocks are darker and harder with lo-

F54. Example showing color cycles, p. 137.

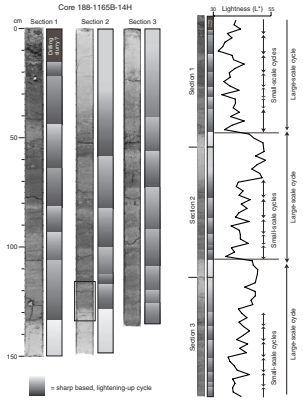

F55. Example of the boundary of a large-scale cycle, p. 138.

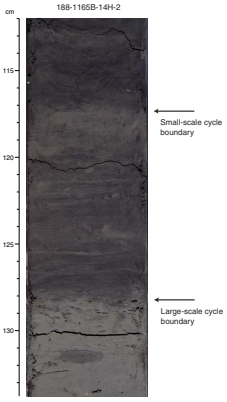

cal diagenetic cementation (e.g., opaline silica and carbonate). The ratio of the thickness of the dark to light facies increases with depth downhole (as sedimentation rates also increase; see "Biostratigraphy and Sedimentation Rates," p. 21). The cycles can also be seen in the color and black and white core photographs, mostly above ~400 mbsf.

Background

Studies on cores with color variations have been done previously for carbonate-rich sections (e.g., Nobes et al., 1991; Harris et al., 1997; Balsam et al., 1997; Grützner et al., 1997; Kegwin, Rio, Acton, et al., 1998; Ortiz et al., 1999) and have shown that climatic cyclicities (i.e., Milankovitch periodicities) appear in the carbonate and terrigeneous input. In general, climatic cycles are reflected by changes in biogenic productivity and dissolution and by variations in terrigenous sediment fluxes. In low-latitude studies, variations in terrigenous input are caused by changes in sea level and erosion of the continental shelves at times of low sea level. Around the Antarctic margin, carbonate nannofossils and foraminfers are generally uncommon, and the biogenic component consists largely of silicious microfossils. Terrigeneous input variations come largely from glacier erosion and transport of sediments to the continental shelf edge and uppermost continental slope (and then beyond by deep-ocean processes such as turbidity flows and contour currents) during sea-level lowstands when grounded glaciers advance to the continental shelf edge.

Antarctic margin drilling has shown that Milankovitch cyclicities may exist in sediment cores. Upper Miocene and younger sediment drift deposits off the Antarctic Peninsula were drilled during ODP Leg 178 (Site 1095), and color variations were observed, with darker-colored units containing larger amounts of terrigenous debris and lighter-colored beds having more biogenic material. It was noted that "...pronounced cyclicity of the depositional record is evident in visual core descriptions and is recorded to date in color scanner, magnetic susceptibility, gamma-ray attenuation porosity evaluator (GRAPE), and downhole magnetic (GHMT) logging records, as well as (probably) in clay content. Preliminary shipboard analysis has shown this record to contain Milankovitch orbital frequencies [unspecified]...." (Shipboard Scientific Party, 1999, p. 7). At Site 1095, the color and other variations were related to fluctuations of the West Antarctic Ice Sheet. Milankovitch cyclicity has also been reported from drilling activities in front of the Transantarctic Mountains and East Antarctic Ice Sheet in the western Ross Sea by the Cape Roberts Project, Site CRP-2/2A (CRST, 1999; Claps et al., in press; Woolfe et al., unpubl. data). At Site CRP-2/2A, the cyclicites are seen in upper Oligocene/lower Miocene nearshore glaciomarine strata as variations in mean grain size, sand abundance, neutron porosity/density, GRA bulk density, coarse fraction clast abundance, and magnetic susceptibility.

Site 1165 is on the flank of a drift deposit, analogous to ODP Site 1095, but unlike Site 1095, the sedimentation cyclicity is responding to changes in nearby East Antarctica. Additionally, the cyclic green and gray color bands at Site 1165 are of slightly different color than at Site 1095, where brown and gray intervals are present; however, the slight difference may be due to different sediment provenances and geochemical settings of the two sites, in particular the amounts and types of clay and OC present (see "Organic Carbon and Iron," p. 53).

Spectral Analysis

In order to investigate cyclic changes in sedimentation within lithostratigraphic Units I and II (i.e., above 305 mbsf) of Site 1165, spectral analyses of spectrophotometer color parameter L* were performed in the depth domain for two separate intervals spanning 83–100 mbsf (Fig. F56A) and 107–123 mbsf (Fig. F57A), respectively. For these intervals, almost continuous color (5-cm sampling interval) and GRA bulk-density records (4-cm sampling interval) of high quality were obtained. The spectra were calculated using the Blackman-Tuckey (BT) spectrum algorithm with 50% lags ("Analyseries" program; Paillard et al., 1996). This algorithm (Blackman and Tuckey, 1958) estimates the autocorrelation function from equally spaced data series, weighted by specifically designed windows to discard possible bias, and computes the Fourier transform to obtain the power spectrum. Coherency between lightness and bulk density was obtained by running the program in the cross-spectrum mode. The same data sets were also analyzed with two additional spectral methods. The first (Scargle, 1982) does not require equally spaced series ("Spectrum" program; Schultz and Stattegger, 1997), and the second is a maximum entropy technique (Burg, 1978; see below). The spectra calculated with the three different methods gave similar results for both of the investigated time series.

For the upper interval, significant spectral density peaks in lightness (only BT results are shown) are found at periods of 3.28, 1.45, 1.08, 0.73, and 0.64 m (Fig. F56B). Based on relatively good magnetostratigraphic and biostratigraphic age control, the average sedimentation rate over the interval is 3.5 cm/k.y. Assuming that the sedimentation rate has not changed dramatically over the investigated interval, the cyclicities in depth can be converted to time and the above periods are equal to 93.7, 41.4, 30.9, 20.9, and 18.3 k.y. The 1.45-m period could be suspect because it is close to the section length of 1.5 m, but visual examination of the core photographs confirms distinct color changes that are spaced at ~1.5 m, indicating that the computed cyclicity of 1.45 m is real. The fact that four spectral peaks (93.7, 41.5, 20.8, and 18.2 k.y.) are close to the Milankovitch cycles of 100 k.y. (eccentricity), 41 k.y. (obliquity), 23, and 19 k.y. (precession) suggests an orbital origin of the cyclicity. Although some of the spectral peaks in the gamma-ray attenuation bulk-density spectrum appear shifted when compared to the lightness spectrum, the two records are highly coherent (>90%) in all three orbital frequency bands.

Between 107 and 123 mbsf, significant spectral density peaks were found at 4.27, 1.55, 0.95, and 0.72 m (Fig. F57B). L* and GRA bulk density show a very similar spectral character in this interval, resulting in high coherencies at the significant variance density maxima. Unfortunately, the sedimentation rate for this interval can only be roughly estimated because of the limited resolution of biostratigraphic and magnetostratigraphic dating techniques. The procedure for the detection of orbital cyclicity used for the upper interval is not applicable in this case, but since the Milankovitch cycles are always characterized by a similar hierarchy of periods (although their periods cannot be assumed to be absolutely constant through time) the numerical ratios of the detected peaks can provide indications for orbital control (e.g., Hinnov and Goldhammer, 1991; Fischer et al., 1991). Normalized to the 19-k.y. precessional cycle, the Milankovitch periods have ratios of 1.00:1.21:2.16:5.26. The periods of the above spectral density peaks found in the lightness record of Site 1165 exhibit very similar ratios of

F56. Lightness and GRA bulk density and a cross spectra of the L* and density measurements for 83–100 mbsf, p. 139.

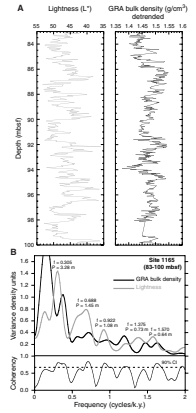

F57. Lightness and GRA bulk density and a cross spectra of the L* and density measurements for 107–123 mbsf, p. 140.

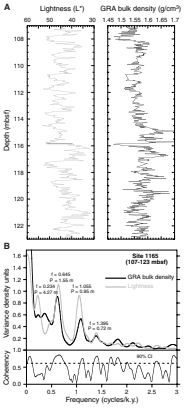

1.00:1.32:2.15:5.93, suggesting an orbital origin for the observed color and density changes. A similar approach has recently been used to detect orbital signals in sedimentary sequences drilled by the Cape Robert Project (Claps et al., in press). Assuming that the 1.55-, 0.95-, and 0.72-m cycles are of orbital origin and are equivalent to the 41-, 23-, and 19-k.y. Milankovitch cycles, refined sedimentation rates can be calculated to be in the range of 3.78–4.13 cm/k.y. for the depth interval from 107 to 123 mbsf.

The variation in the cyclicity with depth was tested for the interval 78–125 mbsf by performing evolutionary spectral analyses over 10-m intervals every 2 m downcore (Fig. **F58**). The maximum entropy method (MEM) (Burg, 1978) was used with software available from **http://www.atmos.ucla.edu/tcd/ssa/.** The MEM was chosen because it produces sharp spectral peaks that are easily identified, although the significance of the amplitude values for the peaks is not known.

In the interval between 78 and 100 mbsf, a shift in the spectral peaks can be seen at ~92 mbsf and may be due to a small change in the sedimentation rate. The interval between 107 and 127 mbsf has a consistent spectral pattern that indicates stable sedimentation rates. The correlation of spectral peaks across the core break between 100 and 107 mbsf is difficult to trace because the peak spacing changes, which suggests that sedimentation rate may vary in this interval; however, spectra from around 120 mbsf are quite similar to those from ~98 mbsf, indicating similar periodicities.

Spectral analysis of the lightness and bulk-density measurements demonstrates that the detected frequencies show good consistency with the frequencies predicted by the Milankovitch theory and are reasonably consistent down the section of core examined. The correlation of lightness, GRA bulk density, and magnetic susceptibility (see **"Physical Properties,"** p. 54) indicates that the color (lightness) data most likely document orbital-driven changes in the marine depositional environment.

F58. Spectral analyses on lightness values, p. 141.

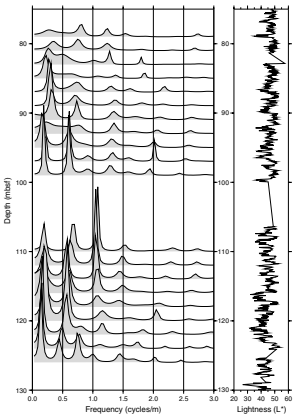

Organic Carbon and Iron

Color (lightness) cyclicity appears throughout the hole, although the cyclicity is highly subdued in the darker-shaded rocks of lithostratigraphic Unit III (i.e., below ~305 mbsf) and in the light brown sediments of lithostratigraphic Unit I (i.e., above 63 mbsf). The cyclicity is most apparent in lithostratigraphic Unit II, where biogenic silica concentration of the green beds are >15%–20% (see **"Lithostratigraphy,"** p. 11; Fig. **F6**), OC values in dark-colored beds are generally >0.4 wt% (see **"Organic Geochemistry,"** p. 47; Fig. **F53B**), and average sedimentation rates are ~3–5 cm/k.y. (see **"Biostratigraphy and Sedimentation Rates,"** p. 21; Fig. **F27**). In this depth range (i.e., 63–305 mbsf), the green and gray sediment color-(lightness) may be related to the oxidation state of iron (Fe^{2+}, green) and OC content (>0.3 wt%, gray) (Potter et al., 1980, p. 55). The same relation may hold for the green to gray color- (lightness) banded interval at 20–30 mbsf, which has relatively high OC (0.8 wt%) content and lies within the otherwise uniform brown sediments of Unit I.

Paleomagnetic analyses show that the magnetic intensity is much lower in the gray-green sediments than in the dark-colored beds and that in some intervals of lithologic Units I and II paleomagnetic inclination covaries with the green to dark alternations, especially from ~90 to 130 mbsf. These observations suggest that the variations in the mag-

netic properties for some intervals are also related to variations in redox conditions, causing partial dissolution of the detrital magnetic minerals and formation of secondary magnetic phases (see "Paleomagnetism," p. 39; Fig. F38).

At Site 1165, OC values greater than ~0.3 wt% seem to enhance the color (lightness) contrasts but do not alter the location of boundaries for the color (lightness) cycles. Further assessment of the causes of color (lightness) banding is planned for postcruise studies.

Summary

The initial identification and evaluation of the cyclicity in color (lightness) of biogenic-rich (greenish gray) and terrigenous (dark gray) intervals suggests that these depositional facies are influenced by Milankovitch periodicities of 100, 41, 23, and 19 k.y. The analysis was done for only two sections of the hole, for late Miocene and early Pliocene times. Similar cyclicities are observed throughout the hole back to early Miocene time, but uncertainties in sedimentation rates for the lower part of the hole at this time preclude determining the times for the cycles. Site 1165 lies in front of the outlet for the Lambert glacier–Amery Ice Shelf system that now drains 22% of East Antarctica with ice and entrained sediment. The color (lightness) cycles at Site 1165 are likely linked to the depositional processes of the onshore glacier system (sediment source) and ocean current system (sediment distribution), which in turn are strongly controlled by climate variations that are driven in part by long-term orbital variations (Milankovitch cycles). Postcruise sedimentological analyses of the cored intervals will supply further fundamental information on compositional and textural variations associated with the observed cylicities.

PHYSICAL PROPERTIES

Multisensor Track

Measurements with the MST have been obtained at 2-cm intervals for GRA bulk densiometer measurements and *P*-wave velocity, at 4-cm intervals for magnetic susceptibility, and at 12-cm intervals for NGR. Below 290 mbsf, the sampling interval for GRA bulk density and *P*-wave velocity has been changed to 4 cm. *P*-wave velocity was not measured on RCB cores. MST results in XCB and RCB cores were degraded in quality because of drilling disturbance associated with coring and the smaller diameter of the core relative to that of the core liner. This disturbance is illustrated by a comparison of GRA bulk densities with discrete density determinations (see "Moisture and Density Measurements," p. 56). In Figure F59, we present edited MST data from Hole 1165B measured on APC cores (0–150 mbsf). Measurements from deeper intervals may be also useful to identify lithologic changes but need more extensive postcruise editing. All MST measurements (raw data) are available and can be downloaded from the ODP Janus database (see the "Related Leg Data" contents list).

The general trend in magnetic susceptibility shows a decrease from average values of 80 × 10^{-5} SI at 0.3 mbsf to 10 × 10^{-5} SI at 145 mbsf. Superimposed on this trend, the smoothed susceptibility record displays meter-scale variability, which is most likely related to variations in the relative amount of biogenous and terrigenous sediment components.

F59. MS, GRA bulk density, *P*-wave velocity, and NGR measurements from Hole 1165B, p. 142.

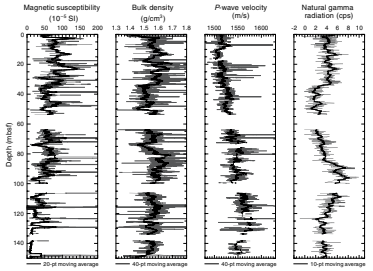

Susceptibility (maxima) of >200 × 10^{-5} SI can be correlated with the presence of lonestones.

GRA bulk densities show no significant trend in the upper 150 mbsf and display meter-scale variability around an average value of 1.56 g/cm³. A covariation of GRA bulk density and magnetic susceptibility is observed throughout the upper 150 mbsf. An interval of lower density (~1.50 g/cm³) possibly stretches from 35 to 85 mbsf (gap from 53 to 63 mbsf), most likely indicating a zone of higher biosiliceous content. IRD (lonestones) can be identified by high-density spikes.

P-wave velocities measured with the *P*-wave logger (PWL) in soft sediments from directly below the seafloor (i.e., 0–5 mbsf) appear to be too high by ~5% when compared to data from other areas (e.g., Barker, Camerlenghi, Acton, et al., 1999). This might be caused by an incorrect calibration of the distance transducers. A comparison of the PWL measurements with discrete velocity data obtained from split cores (*P*-wave sensor [PWS]) shows a consistent offset of 70 m/s throughout the upper 150 mbsf (Fig. **F60**). This offset has been subtracted from the raw velocity data obtained with the PWL. In general, *P*-wave velocity increases from 1510 m/s close to the seafloor to 1580 m/s at 130 mbsf. Meter-scale variability is also seen in the velocity data but shows no consistent correlation with GRA bulk density and magnetic susceptibility. Although some intervals show a positive correlation between density and velocity (e.g., 105–120 mbsf), others are characterized by an inverse relationship (e.g., 20–40 mbsf), which indicates a complex sedimentological control mechanism on velocity changes. Lonestones appear as high-velocity spikes in the record.

In Figure **F61**, NGR data from Holes 1165B and 1165C are combined and compared to the bulk mineralogy derived from XRD measurements. For Hole 1165B, whole-core NGR emissions were counted for 10 s with a constant background correction of 10.36 counts per second (cps) being subtracted automatically from the values measured by the MST. For Hole 1165C, a constant background correction of 6.28 cps was used. This induces an apparent mismatch between the corrected, but not the measured, values between Holes 1165B and 1165C (see the **"Related Leg Data"** contents list). In Figure **F61**, the different backgrounds were taken into account by adding 4.08 cps to the values for Hole 1165B before plotting. Variations in NGR emissions are caused by changes in the composition of the sediment, usually the content of clays and K-feldspars. Similar trends are observed in both the total clay mineral content of the bulk mineralogy (**"Lithostratigraphy,"** p. 11) and the NGR data.

Energy spectra from the radioactive elements potassium (^{40}K), uranium (^{238}U series, mainly ^{214}Bi), and thorium (^{232}Th series, mainly ^{228}Ac) have characteristic energies. Spectra of detector channels 100 to 248 (1.16 to 2.99 MeV) of the NGR system were binned for different depth intervals. These intervals were chosen to improve counting statistics because they had differing NGR intensities (Fig. **F61**) and to trace the shifts in the peak intensities of the potassium, uranium, and thorium series. Such shifts would indicate mineralogical changes. The spectral results indicate that the ^{238}U and ^{232}Th peaks are not present or are poorly defined throughout the hole. The absence of the ^{238}U and ^{232}Th peaks may either result from insufficient total measuring time for the individual bins or indicate a mineralogy with an abundance of potassium-rich minerals such as illite and K-feldspars. The presence of these potassium-rich minerals is supported by clay and bulk mineralogical

F60. PWL and PWS velocity data vs. depth, p. 143.

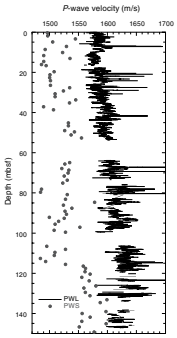

F61. Bulk mineralogy from XRD, NGR, and binned natural gamma spectra vs. depth, p. 144.

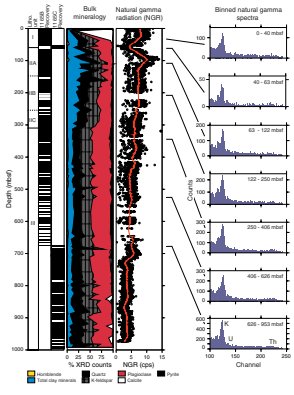

analyses (see "Lithostratigraphy," p. 11). Kaolinite, which is also a major component of the clay-sized fraction (see "Lithostratigraphy," p. 11), has a relatively greater content of Th than illite. The relatively low total clay content may result in the small magnitude of the Th peak.

Lithostratigraphic Unit I (0–63.8 mbsf) is characterized in its upper part (0–40 mbsf) by an increasing NGR intensity (~5–6 cps) above an interval of decreasing intensities. The Unit I/Unit II boundary is at the minimum in the NGR curve. Only two XRD samples were analyzed from the upper 40 m of Unit I, one of which was from a layer of foraminifer-rich clay. The NGR increases in Subunit IIA (63.8–160.1 mbsf) to a maximum at ~100 mbsf with an underlying decline to a constant value of ~6 cps, with a similar trend in the total clay mineral plus K-feldspar content. The uniform NGR values between 160.1 and 254.4 mbsf characterize Subunit IIB, whereas the drop to ~5 cps with the associated decrease in total clay mineral content and K-feldspars marks Subunit IIC (254.4–307 mbsf).

Unit III constitutes the remainder of the hole. There is a general slow decrease in the NGR values downcore, interrupted by higher levels at ~700 m. These higher NGR values may be attributed to an increase in the K-feldspar content, but this relationship is not clear. The NGR data combined with the bulk mineralogy, therefore, indicate that the most prominent compositional change—possibly the most prominent change in depositional environment—occurred during the transition from Unit III to Unit II at 307 mbsf.

Decimeter- to meter-scale changes in sediment color from greenish gray to dark gray intervals in lithostratigraphic Unit II are characterized by L* variations (see "Lithostratigraphy," p. 11). Plotting L* vs. magnetic susceptibility and bulk density for Cores 188-1165B-14H and 15H (Fig. F62) demonstrates that these lightness variations closely covary with changes in GRA bulk density and magnetic susceptibility. Darker intervals have higher densities and susceptibilities. This suggests that the color changes are at least partly caused by changes in the sediment composition.

F62. MS, GRA bulk density, and lightness measurements on Cores 188-1165B-14H and 15H, p. 145.

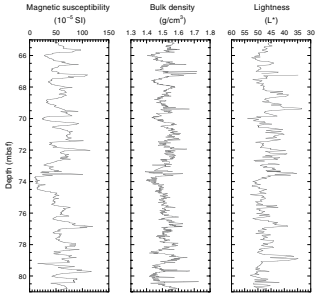

Moisture and Density Measurements

Gravimetric and volumetric determinations of moisture and density (MAD) were made for 353 samples from Hole 1165B (Cores 188-1165B-1H through 74X) and 187 samples from Hole 1165C (Cores 188-1165C-1R through 35R). Two samples were taken, where possible, from each section of Cores 188-1165B-1H through 21X and from Core 188-1165C-1R. For the remaining cores, one sample was taken per section where possible. Samples were not taken from the disturbed sediment surrounding the "biscuits" in the XCB cores or in flow-in regions of APC cores. No moisture and density samples were taken from Hole 1165A. Wet mass, dry mass, and dry volume were measured, and from these measurements, percentage water weight, porosity, dry density, bulk density, and grain density were calculated (see "Physical Properties," p. 21, in the "Explanatory Notes" chapter; also see the "Related Leg Data" contents list).

The grain densities measured at Site 1165 are shown in Figure F63A. Eighty determinations of grain density were made in lithostratigraphic Unit I (0–63.8 mbsf), giving an average value of 2.61 g/cm³, with a range of 2.37–2.74 g/cm³. The measured values show a decrease from top to bottom of the unit, with values on the order of 2.7 g/cm³ near

F63. Grain density and porosity from discrete measurements, p. 146.

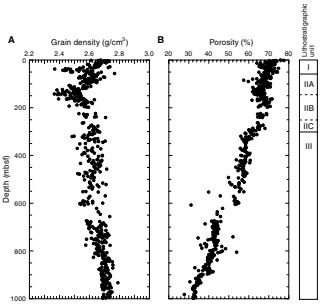

the seafloor and decreasing to 2.5 g/cm³ and lower near the base of the unit.

A total of 163 determinations of grain density were made in lithostratigraphic Unit II (~63.8 to ~305 mbsf). In Subunit IIA, the mean value is 2.54 g/cm³, with a range of 2.37–2.70 g/cm³. Similar to Unit I, the measured values show a decrease from top to bottom of Subunit IIA, with values on the order of 2.65 g/cm³ near the top of the subunit and decreasing to 2.5 g/cm³ or lower near the base of the subunit at 160.1 mbsf. In Subunit IIB, the mean value is 2.56 g/cm³, with a range of 2.39–2.71 g/cm³. In Subunit IIC, the mean value is 2.62 g/cm³, with a range of 2.55–2.67 g/cm³. Subunits IIB and IIC show an increase in grain density from top to bottom.

Within lithostratigraphic Unit III (305–998.27 mbsf), 292 determinations of grain density were made, giving an average value of 2.66 g/cm³, with a range of 2.49–3.14 g/cm³. The measured values show an increase from top to bottom of the unit, with values around 2.62 g/cm³ near the top of the unit and increasing to 2.72 g/cm³ near the bottom of the hole.

The two zones of low grain density, one in lithostratigraphic Unit I (36–50 mbsf) and one in Unit II (120–160 mbsf), appear to be associated with diatomaceous material in those units (see **"Lithostratigraphy,"** p. 11). Siliceous tests of diatoms have a density of 2.0–2.25 g/cm³ (Klein and Hurlbut, 1977). If the lower grain density measured in these zones is due solely to such diatom tests and the remaining material within these zones has a grain density of ~2.65 g/cm³, then diatom tests would make up 40%–50% of the mass of the sediment. The zone of low grain density at 140 mbsf occurs at the same depth where a loss of the magnetic signal is observed (see **"Paleomagnetism,"** p. 39).

The porosities measured at Site 1165 are shown in Figure **F63B.** A total of 243 determinations of porosity were calculated in lithostratigraphic Units I and II (0 to ~305 mbsf). Within Unit I, the average value of porosity is 70%, with a range of 64%–77%. Within Unit II, the average value of porosity is 67%, with a range of 57%–72%. Both Units I and II show a gradual decrease in porosity with increasing depth and overburden pressure.

Within lithostratigraphic Unit III, 292 determinations of porosity were made. The porosity generally decreases with depth and increasing overburden pressure (Fig. **F63B**). There are two significant features in the porosity plot of Unit III, the first at ~620 mbsf and the second at ~800 mbsf. An abrupt decrease in porosity from 54% to 44% occurs at 620 mbsf. This decrease correlates with an increase in velocity and density (see below) but does not coincide with an identified lithostratigraphic boundary. Below 620 mbsf, the porosity remains essentially constant until the second feature, a change of the slope of the plot, is reached. Within the uppermost portion of Unit III (305–620 mbsf), the mean value is 57%, with a range of 31%–64%. From 620 to 800 mbsf, the mean porosity is 43%, with a range of 35%–52%. From 800 mbsf to the bottom of Hole 1165C, the mean value of porosity is 37%, with a range of 28%–54%.

Other parameters that are derived from the measured data include bulk density, dry density, water content, and void ratio. Bulk density and dry density values are presented in Figure **F64.** A total of 535 determinations of bulk and dry density were made on samples from Holes 1165B and 1165C. Bulk density shows only a slight increase with depth from the surface to ~200 mbsf (0.000117 g/cm³/m), and then a more

F64. Bulk density and dry density from discrete measurements, p. 147.

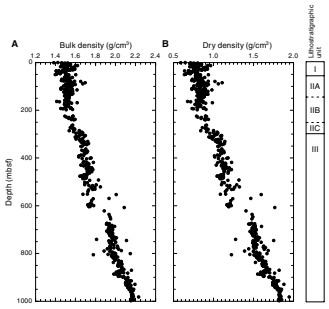

rapid increase below that depth to the termination of Hole 1165C at 998.27 mbsf (0.000811 g/cm³/m). Dry density reveals a similar trend, with an increase of 0.000371 g/cm³/m from the surface to 200 mbsf and an increase of 0.001271 g/cm³/m from 200 mbsf to the termination of the hole.

Water content (as a percentage of dry mass corrected for salt content) and void ratio are presented in Figure F65. These plots show trends similar to those observed in the porosity data.

A common feature of density, porosity, and water content records of Site 1165 is the change to higher gradients below 200 mbsf that occurs within lithostratigraphic Unit II. Whereas the gradient observed below 200 mbsf is expected for a normal compaction of clay-rich sediments, the almost constant porosity in the upper part is uncommon. A possible explanation is the higher biogenic silica content in the upper 200 mbsf, which could inhibit compaction as described by Bryant and Rack (1990).

As described previously in this section, bulk-density data were also obtained from the GRA bulk densiometer in addition to the discrete MAD measurements. To compare the GRA bulk-density data to the discrete MAD measurements, the GRA data set was cleaned by first removing the data points at the top and bottom of each core section. Examination of the remaining data set showed that ~25% of data points lay outside the modal trend. The points outside the modal trend were biased to low bulk-density values, caused by voids in the core and gaps between the core and the core liner. This was especially apparent in the RCB cores. The outlier points were removed from the data set if they exceeded a critical range. The critical range was determined at each depth interval by computing the average and standard deviation for 50 data points on either side of the depth interval. The critical range for the depth interval was then taken as the average value ±0.75 of the standard deviation. The cleaning procedure removed 5962 data points from the data set, or 27% of the raw data. The trend line through the resulting cleaned data set was calculated using an exponential smoothing routine.

Figure F66A presents the GRA bulk-density trend line described above, superimposed on the bulk densities computed from the discrete MAD measurements. The plot demonstrates that there is good agreement between the two measurement methods to ~500 mbsf; below this depth, the discrete measurements are consistently higher than the GRA bulk-density measurements. The ratio of the discrete bulk-density measurements to the GRA bulk-density measurements for corresponding depths (Fig. F66B) is relatively constant and equal to 0.97 for APC cores (0–147 mbsf), 1.04 for XCB cores (147–673 mbsf), and 1.16 for RCB cores (673 mbsf to the termination of the hole at 998.27 mbsf). This indicates that different calibration constants should be used for the GRA depending on the coring method being employed or that GRA measurements on different core types using the same GRA calibration should be scaled to correct the measurements.

Figure F67 illustrates the calculated effective overburden pressure (total overburden pressure minus hydrostatic pressure) using the two data sets. The two curves are in good agreement to 500 mbsf, but by the bottom of the hole, the cumulative error in the GRA-based curve is on the order of 1440 kPa. This error results from the systematic error in the GRA measurements described above.

F65. Water content and void ratio from discrete measurements, p. 148.

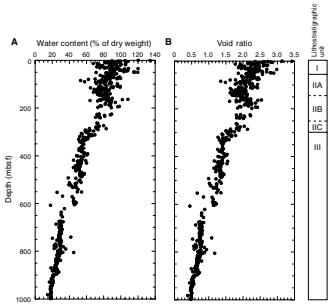

F66. GRA bulk-density data vs. bulk density from discrete measurements and ratio of discrete measurement of bulk density to bulk density from GRA measurements, p. 149.

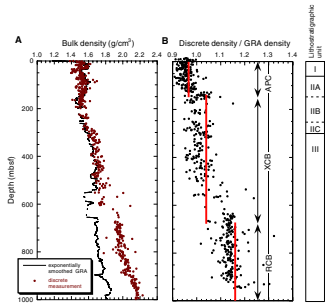

F67. Calculated overburden pressure based on discrete measurements vs. that from GRA data, p. 150.

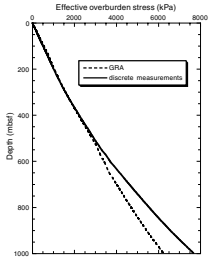

Velocimetry

At Site 1165, *P*-wave velocities on split cores were measured at a frequency of one measurement per section. In soft sediments, the velocity probes PWS1 and PWS2 were inserted into sediments allowing measurements in z- and y-directions. Below 114 mbsf, the sediments became too stiff to insert the probes, and *P*-wave velocities were only measured in the x-direction (through the core liner) by using probe PWS3. Below 607 mbsf, the sediments became lithified enough to cut out blocks and measure the *P*-wave velocity in x-, y-, and z-directions by using PWS3. The laboratory velocity measurements presented here were not corrected to in situ temperature and pressure conditions. Velocity data are compiled in Table T12 (also see the "Related Leg Data" contents list).

Acoustic velocities generally increase with depth below seafloor as consolidation increases (Fig. F68). In lithostratigraphic Unit I, *P*-wave velocities range between 1500 and 1545 m/s and are superimposed on a trend of increasing velocities from ~1500 m/s at the seafloor to ~1535 m/s at 64 mbsf. The top of lithostratigraphic Unit II (64–114 mbsf) has more uniform velocities, around 1535 m/s, compared to Unit I. In the uppermost 114 mbsf, horizontal (y-direction) and vertical (z-direction) velocity values have nearly the same magnitudes, indicating that the sediments are acoustically isotropic. An abrupt change in *P*-wave velocities is observed at 114 mbsf (within lithostratigraphic Subunit IIA), where horizontal velocities (x-direction) increase from ~1535 to ~1575 m/s. From 114 to 603 mbsf, horizontal *P*-wave velocities show an increase from 1575 to 1820 m/s, resulting in a depth gradient of 0.5/s. In this interval, no significant velocity changes are observed at the lithostratigraphic boundaries.

From 492 down to 800 mbsf (within lithostratigraphic Unit III), abundant high-velocity spikes (up to 5098 m/s) characterize local lithified calcareous and siliceous (chert nodule) beds. An abrupt increase from 1820 to 2120 m/s in the general velocity trend (x-direction) occurs at 620 mbsf and correlates with changes in density and porosity. There is no obvious lithologic change described for this interval. A possible (at this stage, speculative) explanation for the velocity increase could be an enhanced silica diagenesis below this depth (see "Inorganic Geochemistry," p. 43) or an increase in the amount of chert. Close to the base of Site 1165, high-velocity zones of ~2660 m/s and ~2840 m/s occur at 880 mbsf and 960 mbsf, respectively, which may explain strong seismic reflectors observed at this depth. Velocities measured in the x- and y- (horizontal) directions in claystones of lithostratigraphic Unit III are 100 to 300 m/s higher than the corresponding velocities in the z-direction. Below 620 mbsf, the acoustic anisotropy increases with depth and is most likely caused by the alignment of clay minerals parallel to the bedding plane.

Undrained Shear Strength

A total of 237 shear strength measurements were taken using three different instruments (automated vane shear [AVS], fall cone [FC], and pocket penetrometer [PP]). The strength of the sediment determined which instruments could be used. The ranges used were 0–165 kPa, 0–370 kPa, and 66–800 kPa for the AVS, FC, and PP, respectively. The measured undrained shear strengths are tabulated in Table T13 and plotted in Figure F69. The strength of clays normally increases as a function of depth (Brooker and Ireland, 1965; Andresen et al., 1979) because of

T12. Discrete *P*-wave measurements, p. 184.

F68. Discrete velocity measurements obtained with the PWS, p. 151.

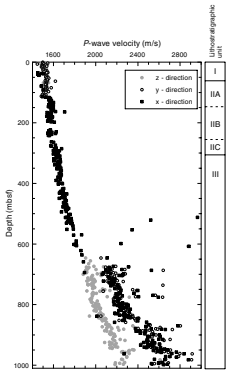

T13. Undrained shear strength measurements, p. 185.

F69. Measurements of undrained shear strength using the AVS, FC, and PP, p. 152.

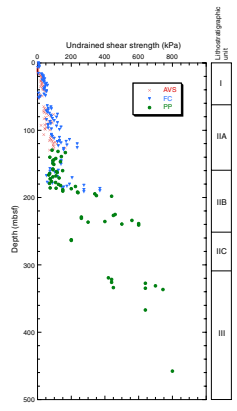

consolidation caused by the increase of the effective overburden stress (p'_o). Figure **F70** shows the ratio of undrained shear strength values and the calculated effective overburden stress values derived from the discrete bulk-density data (Fig. **F64A**). These data were used for the calculation because they are not affected by voids between the core liner and sample, as are the density measurements from the MST. It is usually expected that the ratio of undrained shear strength to effective overburden stress (C_u/p'_o) will be between 0.25 and 0.35 for normally consolidated clays of medium plasticity (Brooker and Ireland, 1965; Andresen et al., 1979). Ratios below this range indicate that the clays may have been remolded during the drilling and sampling process. An alternative explanation is that the clay content and plasticity of these sediments are too low for shear strength measurements to be meaningful. The FC values are roughly 50% higher than the AVS results. Cracks that formed in the sediments during AVS measurements are the most likely explanation for the lower values. The FC and PP values are similar in the 130–190 mbsf interval where both methods were used.

Lithostratigraphic Unit I (0–63.8 mbsf) appears to be normally consolidated with undrained shear strengths increasing from close to 0 near the seafloor to ~50 kPa at the base of the unit. Low C_u/p'_o ratios between 40 and 60 mbsf indicate that Core 188-1165B-6H may have been remolded during the drilling and sampling process.

The interval between ~125 and ~180 mbsf, spanning the bottom part of lithostratigraphic Subunit IIA and the top of Subunit IIB, may also be disturbed and corresponds to the last cores taken with the APC and the first cores taken with the XCB. The lithologic change from Subunit IIA to Subunit IIB is gradational (see **"Lithostratigraphy,"** p. 11) with a downward decrease in biosiliceous components. Because small deformation or disturbance of the core can decrease the undrained shear strength of the sediment, alterations in the measured shear strengths may represent a change from a sediment from which it is difficult to retrieve geotechnically undisturbed samples to one in which this is easier. In other words, the change may be an artifact of the sampling process. Alternatively, the change of strength may be a direct function of the change of the lithology. Care was taken to measure within biscuits and not to sample the drilling slurry between the biscuits in the XCB cores. The presence of biscuits shows that the sediments have been subjected to remolding that can influence the geotechnical parameters. As the sediments become stronger, they probably become more resistant to remolding. The general trend of the shear strength vs. depth plot (Fig. **F69**) indicates that the shear strength in lithostratigraphic Subunit IIA (63.8–160.1 mbsf) increases from ~50 to ~300 kPa; in Subunit IIB (160.1–254.4 mbsf), the increase is from ~300 to ~500 kPa.

Pocket penetrometer measurements were made only in Unit III down to 457.75 mbsf using a small point as an extension to the tool. Below this depth, the sediment became too hard to be measured. Other shear strength measurements were not possible. The strength of Unit III at 500 mbsf is ~900 kPa.

The shear strength measurements indicate that the sediment column is normally consolidated in the upper 500 m of Hole 1165B and does not have over- or undercompacted layers within this interval. This is shown by the ratio of C_u/p'_o (Fig. **F70**), which generally lies in or below the expected range of 0.25–0.35 (Brooker and Ireland, 1965; Andresen et al., 1979).

F70. Normalization of undrained shear strength with respect to effective overburden pressure, p. 153.

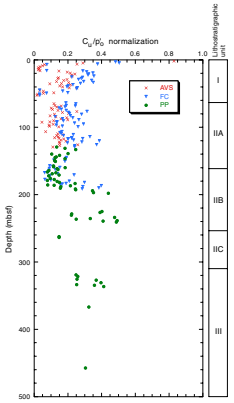

Thermal Conductivity

Thermal conductivity was measured using both a full-space and a half-space needle probe, as appropriate to the strength of the core recovered (see "Physical Properties," p. 21, in the "Explanatory Notes" chapter; also see the "Related Leg Data" contents list). Where possible, thermal conductivity was measured twice per core using the full-space probe on APC and XCB cores, usually near the middle of sections. On RCB cores, it was frequently not possible to measure thermal conductivity because there were no pieces in the core long enough to use the half-space needle probe, and the core was too strong to insert the full-space needle probe. Consequently, only a limited number of thermal conductivity measurements were made on cores from below 500 mbsf.

Tables T14 and T15 present the thermal conductivity measurements made at Site 1165. Figure F71 shows the data with a trend line that best represents in situ conditions. The trend line has been intentionally biased toward the higher measurements in the interval 150–500 mbsf for the reasons described below.

The section of the sedimentary column from which XCB cores were taken (147–673 mbsf) was heavily biscuited. Because the full-space needle was inserted into cores before splitting, it was impossible to avoid inserting the needle into the drilling slurry between biscuits. Upon splitting, it was observed not only that the sediment between biscuits was disturbed but also that the water content was often higher than the undisturbed biscuits, the result of the introduction of drilling fluids into the core. Thermal conductivity in fine-grained sediments is, as a first approximation, a linear combination of the conductivities of the grains and the interstitial water. It therefore depends upon porosity or water content and lithology. The thermal conductivity of water is ~0.6 W/(m·°C), whereas the thermal conductivity of most sediment-forming minerals is much higher. Thus, lithology aside, thermal conductivity should decrease as water content increases. The lower values of thermal conductivity measured from 150 to 500 mbsf have been attributed to measurements made in drilling slurry between biscuits and to splitting biscuits during insertion of the needle, allowing the crack to fill with water or air.

Below 500 mbsf, two values at ~700 mbsf (from Sections 188-1165C-3R-4 and 6R-3) represent thin chert layers and lie well above the trend line for the sediment section.

T14. Thermal conductivity measurements for APC and XCB cores using full-space needle, p. 186.

T15. Thermal conductivity measurements for RCB cores using half-space needle, p. 187.

F71. Measurements of thermal conductivity, p. 154.

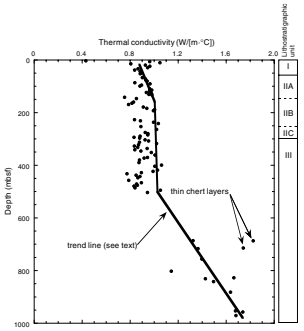

Summary

Physical properties generally change at the identified lithostratigraphic boundaries. The physical properties measurements, however, also show a change at 620 mbsf, at which depth there is no identified lithostratigraphic boundary. The change is particularly apparent as a sharp decrease in the porosity from 54% to 44% at 620 mbsf (Fig. F63B) and as an abrupt increase in the *P*-wave velocity from 1820 to 2120 m/s (Fig. F68). Similar changes are seen at this depth in the downhole logs for natural gamma ray, bulk density, porosity, and photoelectric effect (see "Downhole Measurements," p. 62). A reason for this change in the physical properties but not in the lithology may be silica diagenesis (see "Inorganic Geochemistry," p. 43).

IN SITU TEMPERATURES

Temperature measurements were made at three subbottom depths in Hole 1165B from Cores 188-1165B-4H, 10H, and 14H using the Adara temperature tool. A fourth temperature measurement was attempted for Core 188-1165B-7H; however, because of the failure of the Adara tool, no data could be obtained for this depth. Using the TFIT software package, measured temperature data were extrapolated to a stabilized sediment temperature (Table T16; Figs. F72, F73, F74) for each APC deployment of the Adara temperature tool. The seafloor temperature was determined as the lowest mudline temperature from each measurement before probe penetration. The measured temperatures are plotted against depth in Figure F75.

A straight line was plotted through the data to determine an average thermal gradient of 53.4°C/km for the uppermost 126 m of sedimentary section. A mean measured thermal conductivity of 0.915 W/(m·°C) (see "Physical Properties," p. 54) was multiplied by the thermal gradient to provide an estimated heat flow of 51.4 mW/m². Assuming a conductive steady-state system and constant heat flow in the sedimentary section, measured conductivities from the needle probe (see "Physical Properties," p. 21, in the "Explanatory Notes" chapter) were used to provide estimated downhole temperatures (Fig. F75). The deepest temperature estimate at 970.5 mbsf was 43.6°C, which is ~10°C less than the linearly extrapolated temperature value. Using the conductivity-estimated temperature profile, a secant thermal gradient of 45.2°C/km was determined. Both the heat flow and secant thermal gradient lie within normal thermal ranges for postrift passive margin regions (Allen and Allen, 1990).

Depths to the base of the gas hydrate stability zone (GHSZ) were determined using the ODP Pollution Prevention and Safety Panel (PPSP) hydrate stability equation (PPSP, 1992), which was modified for seawater. Using the linearly extrapolated thermal gradient of 53.4°C/km, the depth to the base of the GHSZ was determined to be 440 mbsf. However, using variable interval thermal gradients from Table T16, the depth to the base of the GHSZ was estimated to be 460 mbsf.

DOWNHOLE MEASUREMENTS

Downhole measurements in Hole 1165C were made after completion of RCB coring to a total depth of 999.10 mbsf. Prior to logging, Hole 1165C was filled with sepiolite mud, reamed, and flushed of debris. In addition, five round trips of the BHA had been made in the borehole while we waited on icebergs. During each round trip, the condition of the borehole was assessed for collapse and deterioration. Apart from a number of ledges, the borehole was in fairly good shape for the logging runs. Two tool strings were run: the triple combo and the FMS-Sonic (see "Downhole Measurements," p. 25, in the "Explanatory Notes" chapter; Fig. F76; Table T17).

The triple-combo tool string (porosity, density, resistivity, and natural gamma-ray emissions) was successfully lowered to 995.5 mbsf, within 5 m of the total hole depth, and logged up to the base of the pipe at 174 mbsf. This logging run had initially encountered sticking problems caused by a ledge or bridge at 119 mbsf, just beneath the base of the pipe. To overcome this problem, the tools were partially rigged

T16. Measured and estimated temperatures, geothermal gradients, and heat-flow estimations, p. 188.

F72. Measured temperature vs. time from deployment of the Adara tool for Core 188-1165B-4H, p. 155.

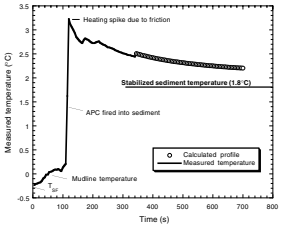

F73. Measured temperature vs. time from deployment of the Adara tool for Core 188-1165B-10H, p. 156.

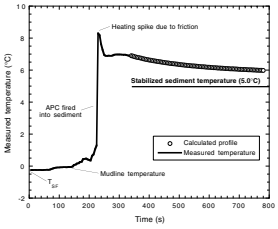

F74. Measured temperature vs. time from deployment of the Adara tool for Core 188-1165B-14H, p. 157.

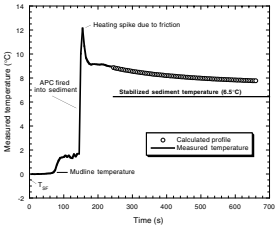

F75. Measured and estimated temperature vs. depth profile, p. 158.

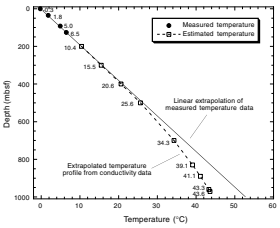

down and three stands of drill pipe were added to push through the obstruction, putting the base of the drill pipe at 174 mbsf, where it remained throughout the logging operations. During logging, the tool string was trapped under a ledge at 303 mbsf for a short time, affecting the logs at this point. The tools provided continuous and high-quality log data. The borehole diameter averaged ~15 in, increasing to a maximum of 18 in toward the top of the logged section. Occasional ledges were encountered, although on the whole the borehole walls remained fairly smooth.

The FMS-Sonic tool string (microresistivity [FMS], seismic velocity, and natural gamma-ray emissions) was lowered without difficulty to 584.8 mbsf, where a bridge that had been encountered during the previous run prevented access to the lower reaches of the hole. A failure of the z-axis accelerometer on the general purpose inclinometer tool just before logging was followed by a general software communication failure to the FMS tool after only 50 m of FMS data were recorded. The DSI sonic tool was run in the *P* and *S* and dipole shear data acquisition modes. The shear wave slowness log was good, but the compressional wave slowness log contained several intervals of anomalously slow values. (The DSI results are not as good where formation velocities are generally slow).

The wireline depth to seafloor was determined from the step increase in gamma-ray values at the sediment water interface to be at 3546.5 mbrf; the driller's mudline depth used for establishing core depth was 3548.7 mbrf.

Logging Units

The sedimentary sequence was divided into three log units on the basis of changes in the character of the downhole logs (Figs. F77, F78).

Unit 1 (174 [Base of Pipe]–608 mbsf)

Logging Unit 1 is characterized by its large-scale uniformity, showing only small variations about the compaction trend. Porosity (density and core) ranges from 65% at the top to 50% at the bottom, and compressional *P*-wave velocity ranges from 1550 to 1775 m/s. Isolated highly resistive and lower-porosity beds are present, having a greater amplitude in Subunit 1c than in 1a or 1b.

Subunit 1a (174–304 mbsf)

This subunit has, on average, slightly lower natural gamma-ray (HSGR) and photoelectric effect (PEF) values than deeper subunits. In this unit, the HSGR baseline value increases slightly at 210 mbsf. Similar abrupt changes are not observed in the other logs, suggesting that the HSGR shift may reflect a mineralogy change.

Subunit 1b (304–480 mbsf)

This subunit is distinguished from Subunit 1a by initially lower values of the natural gamma-ray emission followed by a rapid increase. This feature, however, may be due partially to the tool string becoming stuck at this location. Correlation between core (MST) and log gamma-ray values is difficult, and MST gamma-ray values do not decrease at this depth. Tentative correlation between the two records indicates that the decrease may occur in a break between Cores 188-1165C-35X and 36X at a log depth of 308 mbsf (Fig. F79). The ledge at this depth, ap-

F76. Logging summary diagram, p. 159.

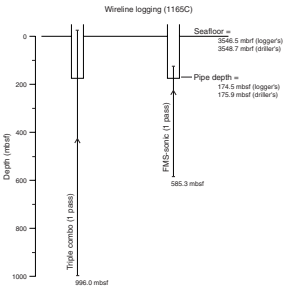

T17. Logging operations summary, Hole 1165C, p. 189.

F77. Gamma-ray, density, porosity, resistivity, and sonic velocity logs, p. 160.

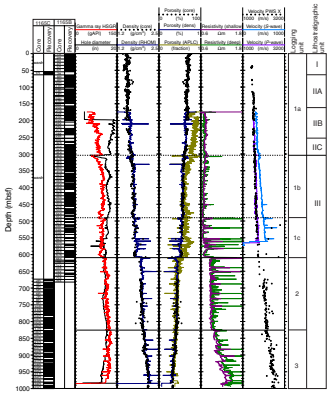

F78. HSGR, uranium, thorium, potassium, and PEF logs, p. 161.

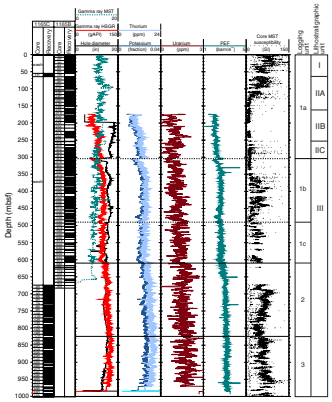

parent in the caliper log, is possibly a result of swelling clay. Isolated small-amplitude spikes in resistivity (e.g., at 452 mbsf) indicate that harder, likely calcareous, beds are present within the claystones of lithologic Unit III (see "Lithostratigraphy," p. 11). Pervasive small-scale lows in density (porosity highs) correlate with lows in natural gamma. These are interpreted to correspond to intervals richer in diatoms: the microfossil framework provides the extra porosity and the reduced clay fraction lowers the natural gamma.

Subunit 1c (480–608 mbsf)

A very resistive bed between 480 and 482 mbsf is the first of several that distinguish the subunit. The interval between 550 and 585 mbsf contains many resistive beds and has a higher background resistivity than the rest of the subunit.

Unit 2 (608–824 mbsf)

The top of logging Unit 2 is marked by a step decrease in porosity from 55% to 45% and step increases in density and resistivity. The coincident step increase in natural gamma-ray emission can be accounted for by the decreased porosity; therefore, the change from Unit 1 to Unit 2 is more likely to be petrophysical (e.g., cementation) than lithologic. The isolated harder beds with resistivity spikes seen in Unit 1 continue into Units 2 and 3, and they can be correlated with thin calcareous intervals observed in the cores (Table T18). The PEF log also has spikes at the calcareous intervals because calcium carbonate has a higher PEF than most other common rock-forming minerals.

Unit 3 (825–993 mbsf [Base of Logs])

Unit 3 has a somewhat "sawtooth" pattern to the resistivity log—it consists of a series of intervals in each of which the resistivity increases downhole, but the bases have abrupt decreases in resistivity. The overall trend is a porosity decrease downhole, from 40% at the top to around 30% near the base of the hole. The isolated resistivity spikes continue in this unit and sometimes mark the boundaries of the porosity intervals.

Core-Log Natural Gamma Comparison

There is no strong similarity between the natural gamma-ray values measured on the MST track and the gamma-ray values (HSGR) measured downhole (Fig. F77). Differences are due in part to the variable diameter of the core, especially the XCB cores. Greater porosity will decrease the natural gamma-ray values; however, porosity will be similar in core and log values, except in the drilling slurry between the biscuits. The effect of variance in borehole diameter is corrected for in the HNGS tool during logging; however, even given the above sources of error, the mismatches between core and log values are still larger than may be expected from measuring the same property on the same formation.

Another difference between the core and log measurement lies in the width of the gamma radiation energy spectrum windowed in the measurement: the MST gives the total gamma counts in all parts of the spectrum, whereas the HSGR is more discriminating, including only the gamma-ray energies above 1100 eV—the region covering the main potassium, uranium, and thorium peaks. The MST records data in 250 sep-

F79. Comparison of HSGR log (downhole) and core gamma-ray values (adjusted), p. 162.

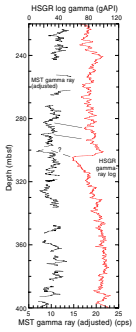

T18. Correlation of density, resistivity, and PEF peaks observed in the downhole logs to carbonate-cemented intervals in the cores, p. 190.

arate energy windows, so in an effort to compare like parts of the energy spectrum between the MST and the log, the MST range above 1100 eV was used for the comparison (Fig. F79). However, the match remains poor both in terms of the shapes of the cores and in the amplitude of the variations.

Log Signature of the Calcified Beds

The thin, resistive, dense, low-porosity beds observed in the logs correlate well with calcified beds, or intervals containing carbonate nodules, observed in the core (Table T18). As an example, the 24-cm-thick bed at 731 mbsf gives responses in all the logs (Fig. F77, F80). High porosity, density, and resistivity reflect the porosity decrease that accompanies carbonate cementation. The PEF peak reflects an increase in the proportion of calcium carbonate (PEF ~5 barn/e⁻), and the concurrent drop in natural gamma likely reflects a decrease in the proportion of clays.

In addition to these clear large log spikes, the sediment between them contains smaller, regularly spaced log peaks, or cycles (Fig. F80). To determine the average cycle thickness, resistivity peaks were counted in two intervals, one in logging Unit 1 and the other in Unit 2. Resistivity appears to be the log most sensitive to cementation and is relatively insensitive to borehole effects, so it was chosen for this exercise. Counting gamma-ray or density peaks would lead to slightly different results, but those results would be in the same ballpark as that derived from resistivity. In logging Unit 1, between 307 and 470 mbsf, there are about 90 resistivity peaks with an average cycle thickness of 1.81 m. The dating of this part of the hole is poor, but the sedimentation rate is roughly 8 cm/k.y. At this rate, the cycle duration is roughly 22.6 k.y., close to the precessional periodicity. In logging Unit 2, between 612 and 867 mbsf, there are about 140 resistivity peaks with an average cycle thickness of 1.82 m. There is only one date in this part of the section, but it is thought that the Oligocene was not reached. A reasonable estimate for the sedimentation rate is 11 cm/k.y., giving it an average cycle duration of 16.5 k.y. The smaller log peaks may be caused by minor calcification (or silicification), though at a level too subtle to be observed in the cores. They may also result from cyclic sedimentation processes similar to those described in "Color Alternations in Cores," p. 50.

Synthetic Seismogram

A composite synthetic seismogram was created from a combination of core-based *P*-wave velocities and log-based porosities. Sonic log data were not used to calculate the synthetic trace because only a short log was recorded as the result of an obstruction in the hole at ~580 mbsf and because sections of the data were unreliable. The bulk-density log was used to calculate a density-based porosity, and that porosity was in turn used to create a pseudo-sonic log for the logged interval. The synthetic seismogram was calculated from the pseudo-sonic and bulk-density logs, with the core-based *P*-wave velocities and bulk densities filling in the unlogged interval above 178 mbsf.

The bulk-density log was converted to density-porosity using the grain densities from the core (see "Physical Properties," p. 54) and a seawater density of 1.03 g/cm³. Rather than using a single average grain density for the entire log, grain densities were matched depth for depth with the log data because of variations caused by diatom abundance.

F80. Expanded sections from logging Units 2 and 3, p. 163.

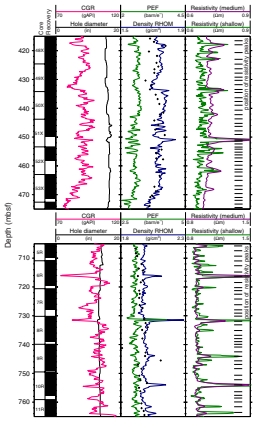

The density-porosity was converted to velocity using the global porosity-velocity model for siliciclastic sediments of Erickson and Jarrard (1998). This model proposes an empirical relationship covering the entire range of possible porosities for both normally compacted and highly compacted sediments, derived from an analysis of 23 wide ranging, mostly marine data sets. The bulk-density log was compared to the MAD bulk-density data (see **"Physical Properties,"** p. 54) for compatibility (Fig. **F81**) and the core *P*-wave velocities were likewise compared to the pseudo-velocities derived from the model (Fig. **F82**) as well as the sonic log data. The pseudo-sonic and real-sonic logs indicated that a 7% in situ correction of the core velocities was needed. Seven percent seemed a bit too much of a correction for the MAD bulk-density data, but for compatibility, both velocity and density were corrected by the same amount.

Porosity is the dominant control on velocity for sediments, including clays, with >40% porosity; velocity does not become lithology dependent until below this threshold (Erickson and Jarrard, 1998). A highly consolidated sediment tends to have a slightly higher velocity at a given porosity than a normally consolidated sediment because of an overall stiffening of the sediment (Erickson and Jarrard, 1998). For the upper half of the hole, the empirical relationship for highly consolidated sediments gave a better match to the discrete core-based *P*-wave velocities (see **"Physical Properties,"** p. 54) than the relationship for normally consolidated sediments. Consequently, the empirical relationship relating porosity to velocity in highly consolidated sediments was used throughout.

For the lower half of the hole, core velocities were measured on three orthogonal axes. The x- and y-directions are across the core, with the x-direction value taken through the radius of the split core and the y-direction value across the diameter. The z-direction is down the length of the core (see **"Physical Properties,"** p. 54). It was originally thought that the x-direction would be the most representative for in situ conditions because core expansion caused by degassing and lithostatic unloading would part horizontal bedding planes resulting in anomalously low z-direction velocities. The velocities derived from the model, however, greatly underestimated the x-direction core measurements in the lower part of the hole. On the other hand, porosity-velocity estimates are very close to the z-direction measurements, indicating that perhaps the z-direction core measurements are more representative of the true seismic velocities in the core than originally thought and that post-recovery fracturing of the contourite beds and fissile texture of the cores caused less velocity change than expected.

For the lower 100 mbsf of the hole, the porosities are <40%, the z-direction core velocities are lithology dependent, with a shale fraction of 0.9, giving the best estimate to the porosity-velocity model values (Fig. **F83**).

The source wavelet of the water gun was extracted by digitizing the seafloor reflection of trace 1191 (i.e., shotpoint 1191) from the site survey, near the position of the hole. The wavelet is ~85 ms long (170 ms two-way traveltime), with a 15 ms (30 ms two-way traveltime) precursor arrival before a two-lobed main impulse (Fig. **F84**). Convolution of this wavelet with a reflection coefficient log derived from the pseudo-sonic and bulk-density data produced the resultant synthetic trace that matches the seismic section quite well in the upper part, but that overshoots the basal reflection (5–83 s) by ~0.2 s (synthesis not shown).

F81. Comparison of MAD bulk density and log bulk density, p. 164.

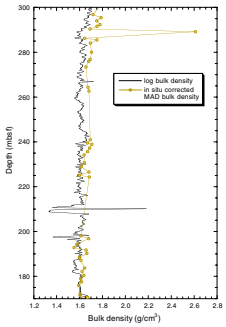

F82. Comparison of z-direction core *P*-wave velocity measurements and log *P*-wave velocity, p. 165.

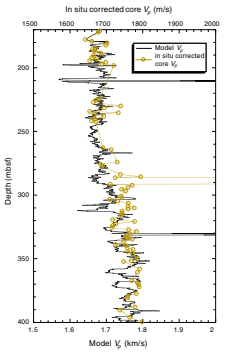

F83. Comparison of z-direction core *P*-wave velocities and *P*-wave velocity derived from the density-porosity log values, p. 166.

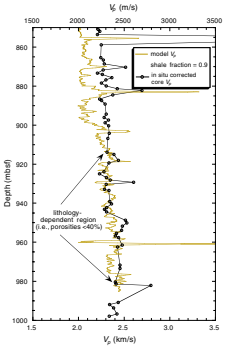

Changing the shale fraction in the model of Erickson and Jarrard (1998) from 0.9 to 0.5 shifts this reflection up to match the reflection without adversely shifting the data above 5.6 s (Fig. F85), although some change in the character of the synthetic is observed. This change to a shale fraction of 0.5 overestimates the z-direction core velocities by ~400 m/s, but improves the match between model velocities and the x- and y-direction core velocities (Fig. F86).

The synthetic seismogram and depth-time models are preliminary, and postcruise work is expected to improve them. Several factors are responsible for mismatches between the synthetic and the seismic. First, the bulk-density data were not edited for any but the most egregious outlying data points even though there are places where hole conditions were rough. Further editing of the log should improve the character match. Second, the synthetic seismogram does not include the loss of signal caused by spherical divergence of the original seismic input and does not contain any automatic gain control. This might explain differences in the visual importance of certain reflections at depth, such as the packet of strong reflectors ending at 800 ms and their equivalents in the synthetic seismogram. Third, the wavelet used to generate the synthetic section is not a completely accurate representation of the original water-gun signature because it was manually extracted from the seismogram based on the seafloor reflection. The presence of any reflections close to the seafloor will have distorted the original wavelet. For example, the base of lithostratigraphic Unit I is at 63 mbsf (see "Lithostratigraphy," p. 11), within a wavelet's length of the seafloor, and the reflection from the transition of Unit I to Unit II, if any, is included in the wavelet. Fourth, alternative velocity logs can be derived from the porosity.

Origin of Seismic Reflectors

The synthetic seismogram was created to put a depth scale on the seismic data and determine the likely position of lithostratigraphic units on the seismic section (Fig. F87). Since the wavelet response to a distinct geologic horizon is a series of impulses over an 85 ms interval, 15 ms of which is a precursor to the main impulse, it is difficult—even on the synthetic seismogram—to identify the precise depth of the horizon that leads to a reflector. The best way to pick depths is to refer to the reflection coefficient log (Fig. F88) that was created to generate the synthetic seismogram.

Six prominent reflections other than the seafloor reflection were identified and their likely origins were identified from the cores.

Reflector 1 (~0.25 s two-way traveltime below seafloor) was identified as a >40-cm-thick nannofossil chalk at 210 mbsf in Cores 188-1165B-24X-3 and 24X-CC. Reflector 2 (~0.44 s) is at the top of a zone of poor recovery at 330 mbsf, around Core 188-1165B-40X, at a depth containing chalk nodules. Reflector 3 (~0.6 s) is the uppermost strongly cherty/calcified bed seen in the hole at ~490 mbsf. Reflector 4 (~0.65 s) is the top of another zone of poor recovery in Core 188-1165B-63X at ~550 mbsf, in an area with much harder calcified beds and claystones. The central zone of reflectors between Reflectors 4 and 5 (~0.82 s) appears to be caused by multiple closely spaced hard calcified beds. Reflector 5 is at a depth of 710 mbsf on the depth-time model. Because of the many closely spaced reflectors in the overlying reflector zone, the wavelet becomes quite distorted, and in fact the impedance contrast that represents the end of this zone is at 650 mbsf (the opal-A/opal-CT

F84. Wavelet used to produce a synthetic seismogram, p. 167.

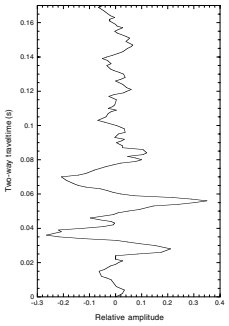

F85. Synthetic seismogram for shale fraction = 0.5, overlain on the site survey profile, p. 168.

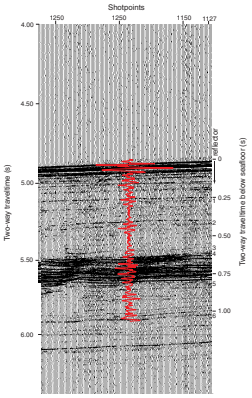

F86. Comparison of x-direction core *P*-wave velocities and *P*-wave velocity derived from the density-derived porosity, p. 169.

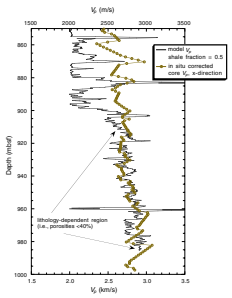

transition), with the wavelet trailing out another 60 m. Furthermore, there is a change in Core 188-1165B-74X at the same depth, from a cemented siliceous bed >25 cm thick to a softer claystone. The basal target Reflector 6 (~1.06 s) is found at ~960 mbsf in Core 188-1165C-32R and is a thick calcite-cemented horizon. In general, most strong reflectors are caused by relatively thin single or multiple intervals of calcified or silicified beds with high acoustic impedance.

Temperature Log

The Lamont-Doherty temperature-acceleration-pressure tool recorded the temperature of the fluid in Hole 1065C during the first pass of the triple-combo tool string (Fig. F89). These measurements underestimate the formation temperature, as the fluid temperature does not have time to equilibrate to the formation temperature. A temperature of 36°C was recorded at the bottom of the hole (993 m), so the temperature gradient is at least 36°C/km. The downgoing and upgoing curves have an offset of ~5°C, owing to borehole reequilibration during acquisition.

F87. Synthetic seismogram wave trace placed on a depth axis, p. 170.

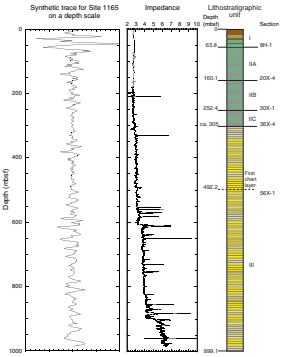

F88. Reflection coefficient log on both traveltime and depth axes, p. 171.

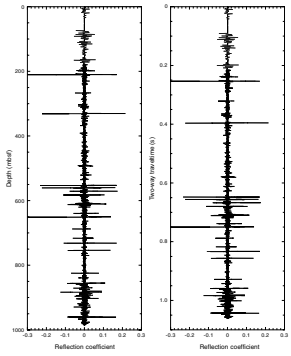

F89. Downhole temperature from the TAP tool, p. 172.

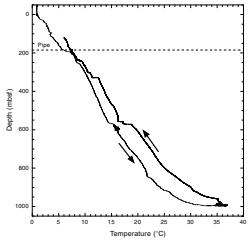

REFERENCES

Abelmann, A., 1990. Oligocene to middle Miocene radiolarian stratigraphy of southern high latitudes from Leg 113, Sites 689–690, Maud Rise. *In* Barker, P.F., Kennett, J.P., et al., *Proc. ODP, Sci. Results,* 113: College Station, TX (Ocean Drilling Program), 675–708.

————, 1992. Early to middle Miocene radiolarian stratigraphy of the Kerguelen Plateau, Leg 120. *In* Wise, S.W., Jr., Schlich, R., et al., *Proc. ODP, Sci. Results,* 120: College Station, TX (Ocean Drilling Program), 757–783.

Allen, P.A., and Allen, J.R., 1990. *Basin Analysis: Principles and Applications:* Oxford (Blackwell Sci. Publ.).

Andresen, A., Berre, T., Kleven, A., and Lunne, T., 1979. Procedures used to obtain soil parameters for foundation engineering in the North Sea. *Norw. Geotech. Inst. Publ.,* 129:1–18.

Balsam, W.L., Damuth, J.E., and Schneider, R.R., 1997. Comparison of shipboard vs. shore-based spectral data from Amazon Fan cores: implications for interpreting sediment composition. *In* Flood, R.D., Piper, D.J.W., Klaus, A., and Peterson, L.C. (Eds.), *Proc. ODP, Sci. Results,* 155: College Station, TX (Ocean Drilling Program), 193–215.

Barker, P.F., Camerlenghi, A., Acton, G.D., et al., 1999. *Proc. ODP, Init. Repts.* [CD-ROM], 178: College Station, TX (Ocean Drilling Program).

Berggren, W.A., 1992. Neogene planktonic foraminifer magnetobiostratigraphy of the southern Kerguelen Plateau (Sites 747, 748, and 751). *In* Wise, S.W., Jr., Schlich, R., et al., *Proc. ODP, Sci. Results,* 120 (Pt. 2): College Station, TX (Ocean Drilling Program), 631–647.

Berggren, W.A., Kent, D.V., Swisher, C.C., III, and Aubry, M.-P., 1995. A revised Cenozoic geochronology and chronostratigraphy. *In* Berggren, W.A., Kent, D.V., Aubry, M.-P., and Hardenbol, J. (Eds.), *Geochronology, Time Scales and Global Stratigraphic Correlation.* Spec. Publ.—Soc. Econ. Paleontol. Mineral. (Soc. Sediment. Geol.), 54:129–212.

Blackman, R.B., and Tukey, J.W., 1958. *The Measurement of Power Spectra From the Point of View of Communication Engineering:* Mineok, NY (Dover).

Brooker, E.W., and Ireland, H.O., 1965. Earth pressures at rest related to stress history. *Can. Geotech. J.,* 2:1–15.

Bryant, W.R., and Rack, F.R., 1990. Consolidation characteristics of Weddell Sea sediments: results of ODP Leg 113. *In* Barker, P.F., Kennett, J.P., et al., *Proc. ODP, Sci. Results,* 113: College Station, TX (Ocean Drilling Program), 211–223.

Burg, J.P., 1978. A new technique for time series data. *In* Childers, D.G. (Ed.), *Modern Spectrum Analysis:* New York (IEEE Press), 42–48.

Cande, S.C., and Kent, D.V., 1992. A new geomagnetic polarity time scale for the Late Cretaceous and Cenozoic. *J. Geophys. Res.,* 97:13917–13951.

————, 1995. Revised calibration of the geomagnetic polarity timescale for the Late Cretaceous and Cenozoic. *J. Geophys. Res.,* 100:6093–6095.

Claps, M., Niessen, F., and Florindo, F., in press. High-frequency analysis of physical properties from CRP-2/2A and implication for sedimentation rate. *Terra Antart.*

Claypool, G.E., and Kaplan, I.R., 1974. The origin and distribution of methane in marine sediments. *In* Kaplan, I.R. (Ed.), *Natural Gases in Marine Sediments:* New York (Plenum), 99–139.

Cape Roberts Science Team (CRST), 1999. Initial reports on CRP 2/2A. *Terra Antart.,* 6(1/2).

Dekkers, M.J., 1989. Magnetic properties of natural pyrrhotite, Part II. High- and low-temperature behavior of J_{rs} and TRM as function of grain size. *Phys. Earth Planet. Inter.,* 57:266–283.

Erickson, S.N., and Jarrard, R.D., 1998. Velocity-porosity relationships for water-saturated siliciclastic sediments. *J. Geophys. Res.,* 103:30385–30406.

Fischer, A.G., Herbert, T.D., Napoleone, G., Premoli Silva, I., and Ripepe, M., 1991. Albian pelagic rhythms (Piobbico Core). *J. Sediment. Petrol.,* 6:1164–1172.

Florindo, F., and Sagnotti, L., 1995. Palaeomagnetism and rock magnetism at the upper Pliocene Valle Ricca (Rome, Italy) section. *Geophys. J. Int.,* 123:340–354.

Forsberg, C.F., Solheim, A., Elverhøi, A., Jansen, E., Channell, J.E.T., and Andersen, E.S., 1999. The depositional environment of the western Svalbard margin during the late Pliocene and the Pleistocene: sedimentary facies changes at Site 986. *In* Raymo, M.E., Jansen, E., Blum, P., and Herbert, T.D. (Eds.), *Proc. ODP, Sci. Results,* 162: College Station, TX (Ocean Drilling Program), 233–246.

Garrels, R.M., and Christ, C.L., 1965. *Solutions, Minerals and Equilibria:* San Francisco (Freeman, Cooper & Company).

Gersonde, R., and Bárcena, M.A., 1998. Revision of the late Pliocene-Pleistocene diatom biostratigraphy for the northern belt of the Southern Ocean. *Micropaleontology,* 44:84–98.

Goldhaber, M.B., and Kaplan, I.R., 1974. The sulfur cycle. *In* Goldberg, E.D. (Ed.), *The Sea* (Vol. 5): *Marine Chemistry: The Sedimentary Cycle:* New York (Wiley-Interscience), 569–655.

Gonthier, E.G., Faugeres, J.C., and Stow, D.A.V., 1984. Contourite facies of the Faro Drift, Gulf of Cadiz. *In* Stow, D.A.V., and Piper, D.J.W. (Eds.), *Fine-grained Sediments: Deep Water Processes and Facies*. Geol. Soc. Spec. Publ. London, 15:275–292.

Gooday, A.J., 1990. Recent deep-sea agglutinated foraminifera: a brief review. *In* Hemleben, C., Kaminski, M.A., Kuhnt, W., and Scott, D.B. (Eds.), *Paleoecology, Biostratigraphy, Paleoceanography and Taxonomy of Agglutinated Foraminifera*. NATO ASI Ser., 327:271–304.

Grützner, J., Bassinot, F.C., and Mienert, J., 1997. High-resolution compressional-wave velocity measurements in Pleistocene sediments of the Ceara Rise (western equatorial Atlantic): implications for orbital driven sedimentary cycles. *In* Shackleton, N.J., Curry, W.B., Richter, C., and Bralower, T.J. (Eds.), *Proc. ODP, Sci. Results,* 154: College Station, TX (Ocean Drilling Program), 135–149.

Harris, P.T., O'Brien, P.E., Quilty, P.G., Taylor, F., Domack, E., De Santis, L., and Raker, B., 1997a. Post-cruise report, Antarctic CRC Marine Geoscience: Vincennes Bay, Prydz Bay and Mac.Robertson Shelf, AGSO Cruise 186, ANARE Voyage 5, 1996/97. *Aust. Geol. Surv. Org. Rec.,* 1997/51.

Harris, S.E., Mix, A.C., and King, T., 1997b. Biogenic and terrigenous sedimentation at Ceara Rise, western tropical Atlantic, supports Pliocene–Pleistocene deep-water linkage between hemispheres. *In* Shackleton, N.J., Curry, W.B., Richter, C., and Bralower, T.J. (Eds.), *Proc. ODP, Sci. Results,* 154: College Station, TX (Ocean Drilling Program), 331–345.

Harwood, D.M., Lazarus, D.B., Abelmann, A., Aubry, M.-P., Berggren, W.A., Heider, F., Inokuchi, H., Maruyama, T., McCartney, K., Wei, W., and Wise, S.W., Jr., 1992. Neogene integrated magnetobiostratigraphy of the central Kerguelen Plateau, Leg 120. *In* Wise, S.W., Jr., Schlich, R., et al., *Proc. ODP, Sci. Results,* 120: College Station, TX (Ocean Drilling Program), 1031–1052.

Harwood, D.M., and Maruyama, T., 1992. Middle Eocene to Pleistocene diatom biostratigraphy of Southern Ocean sediments from the Kerguelen Plateau, Leg 120. *In* Wise, S.W., Jr., Schlich, R., et al., *Proc. ODP, Sci. Results,* 120: College Station, TX (Ocean Drilling Program), 683–733.

Heezen, B.C., Hollister, C.D., and Ruddiman, W.F., 1966. Shaping of the continental rise by deep geostrophic contour currents. *Science,* 152:502–508.

Hinnov, L.A., and Goldhammer, R.K., 1991. Spectral analysis of the Middle Triassic Latemar limestone. *J. Sediment. Petrol.,* 61:1173–1193.

Hunt, C.P., Moskowitz, B.M., and Banerjee, S.K., 1995. Magnetic properties of rocks and minerals. *In* Rock Physics and Phase Relations. *AGU Reference Shelf,* 3:189–204.

Jacobs, J.A., 1998. Variations in the field intensity of the Earth's magnetic field. *Surv. Geophys.,* 19:39–187.

JOIDES PPSP, 1992. Ocean Drilling Program guidelines for pollution prevention and safety. *JOIDES J.,* 18.

Keigwin, L.D., Rio, D., Acton, G.D., et al., 1998. *Proc. ODP, Init. Repts.,* 172: College Station, TX (Ocean Drilling Program).

King, J.W., Banerjee, S.K., and Marvin, J., 1983. A new rock-magnetic approach to selecting sediments for geomagnetic paleointensity studies: application to paleointensity for the last 4000 years. *J. Geophys. Res.,* 88:5911–5921.

Kirschvink, J.L., 1980. The least-squares line and plane and the analysis of palaeomagnetic data. *Geophys. J. R. Astron. Soc.,* 62:699–718.

Klein, C., and Hurlbut, C.S., Jr., 1977. *Manual of Mineralogy, after James D. Dana:* New York (John Wiley & Sons).

Kuvaas, B., and Leitchenkov, G., 1992. Glaciomarine turbidite and current-controlled deposits in Prydz Bay, Antarctica. *Mar. Geol.,* 108:365–381.

Kvenvolden, K.A., Golan-Bac, M., McDonald, T.J., Pflaum, R.C., and Brooks, J.M., 1989. Hydrocarbon gases in sediment of the Vøring Plateau, Norwegian Sea. *In* Eldholm, O., Thiede, J., Taylor, E., et al., *Proc. ODP, Sci. Results,* 104: College Station, TX (Ocean Drilling Program), 319–326.

Kvenvolden, K.A., and Lorenson, T.D., 2000. Methane and other hydrocarbon gases in sediment from the southeastern North American continental margin. *In* Paull, C.K., Matsumoto, R., Wallace, P.J., and Dillon, W.P. (Eds.), *Proc. ODP, Sci. Results,* 164: College Station, TX (Ocean Drilling Program), 29–36.

Lazarus, D., 1990. Middle Miocene to Recent radiolarians from the Weddell Sea, Antarctica, ODP Leg 113. *In* Barker, P.F., Kennett, J.P., et al., *Proc. ODP, Sci. Results,* 113: College Station, TX (Ocean Drilling Program), 709–727.

————, 1992. Antarctic Neogene radiolarians from the Kerguelen Plateau, Legs 119 and 120. *In* Wise, S.W., Jr., Schlich, R., et al., *Proc. ODP, Sci. Results,* 120: College Station, TX (Ocean Drilling Program), 785–809.

Lowrie, W., 1990. Identification of ferromagnetic minerals in a rock by coercivity and unblocking temperature properties. *Geophys. Res. Lett.,* 17:159–162.

Mizukoshi, I., Sunouchi, H., Saki, T., Sato, S., and Tanahashi, M., 1986. Preliminary report of geological and geophysical surveys off Amery Ice Shelf, East Antarctica. *Mem. Nat. Inst. Polar Res. Spec. Iss. Jpn.,* 43:48–61.

Nobes, D.C., Bloomer, S.F., Mienert, J., and Westall, F., 1991. Milankovitch cycles and nonlinear response in the Quaternary record in the Atlantic sector of the Southern Oceans. *In* Ciesielski, P.F., Kristoffersen, Y., et al., *Proc. ODP, Sci. Results,* 114: College Station, TX (Ocean Drilling Program), 551–576.

Okada, H., and Bukry, D., 1980. Supplementary modification and introduction of code numbers to the low-latitude coccolith biostratigraphic zonation (Bukry, 1973; 1975). *Mar. Micropaleontol.,* 5:321–325.

Ortiz, J., Mix, A., and O'Connell, S., 1999. Diffuse spectral reflectance as a proxy for percent carbonate content in North Atlantic sediments. *Paleoceanography,* 14:171–186.

Paillard, D., Labeyrie, L., and. Yiou, P., 1996. Macintosh program performs time-series analysis. *Eos,* 77:379.

Perch-Nielsen, K., 1985. Mesozoic calcareous nannofossils. *In* Bolli, H.M., Saunders, J.B., and Perch-Nielsen, K. (Eds.), *Plankton Stratigraphy:* Cambridge (Cambridge Univ. Press), 329–426.

Pollution Prevention and Safety Panel, 1992. Ocean Drilling Program guidelines for pollution prevention and safety. *JOIDES J.,* 18:1–24.

Potter, P.E., Maynard, J.B., and Pryor, W.A., 1980. *Sedimentology of Shale:* Berlin (Springer-Verlag).

Quilty, P.G., 1985. Distribution of foraminiferids in sediments of Prydz Bay, Antarctica. *Spec. Publ. S. Aust. Dep. Mines Energy,* 5:329–340.

Quilty, P.G., Truswell, E.M., O'Brien, P.E., and Taylor, F., 1999. Paleocene-Eocene biostratigraphy and palaeoenvironment of East Antarctica: new data from Mac. Robertson Shelf and western Prydz Bay. *AGSO J. Aust. Geol Geophys.,* 17:133–143.

Rebesco, M., Larter, R.D., Barker, P.F., Camerlenghi, A., and Vanneste, L.E., 1997. The history of sedimentation on the continental rise west of the Antarctic Peninsula. *In* Barker, P.F., and Cooper, A.K. (Eds.), *Geology and Seismic Stratigraphy of the Antarctic Margin* (Pt. 2). Am. Geophys. Union, Antarctic Res. Ser., 71:29–50.

Roberts, A.P., 1995. Magnetic properties of sedimentary greigite (Fe_3S_4). *Earth Planet. Sci. Lett.,* 134:227–236.

Scargle, J.D., 1982. Aspects of spectral analysis of unevenly spaced data. *Astrophys. J.,* 263:835–853.

Scherer, R.P., Bohaty, S.M., and Harwood, D.M., in press. Oligocene and lower Miocene siliceous microfossil biostratigraphy of Cape Roberts Project core CRP-2/2A, Victoria Land Basin, Antarctica. *Terra Antart.*

Schrader, H.-J., 1976. Cenozoic planktonic diatom biostratigraphy of the Southern Pacific Ocean. *In* Hollister, C.D., Craddock, C., et al., *Init. Repts. DSDP,* 35: Washington (U.S. Govt. Printing Office), 605–671.

Schultz, M., and Stattegger, K., 1997. Spectral analysis of unevenly spaced paleoclimatic time series. *Comput. Geosci.,* 23:929–945.

Shipboard Scientific Party, 1999. Leg 178 summary: Antarctic glacial history and sea-level change. *In* Barker, P.F., Camerlenghi, A., Acton, G.D., et al., *Proc. ODP, Init. Repts.,* 178: College Station TX (Ocean Drilling Program), 1–58.

Stow, D.A.V., and Holbrook, J.A., 1984. North Atlantic contourites: an overview. *In* Stow, D.A.V., and Piper, D.J.W. (Eds.), *Fine-Grained Sediments: Deep Water Processes and Facies.* Geol. Soc. Spec. Publ. London, 15:245–256.

Stow, D.A.V., and Piper, D.J.W., 1984. Deep-water fine-grained sediments: facies models. *In* Stow, D.A.V., and Piper, D.J.W. (Eds.), *Fine-Grained Sediments: Deep-Water Processes and Facies.* Geol. Soc. Spec. Publ. London, 15:611–645.

Tauxe, L., 1993. Sedimentary records of relative paleointensity of the geomagnetic field: theory and practice. *Rev. Geophys.,* 31:319–354.

Tingey, R.J., 1991. The regional geology of Archean and Proterozoic rocks in Antarctica. *In* Tingey, R.J. (Ed.), *The Geology of Antarctica:* Oxford (Clarendon Press), 1–58.

van Morkhoven, F.P.C.M., Berggren, W.A., and Edwards, A.S., 1986. Cenozoic cosmopolitan deep-water benthic foraminifera. *Bull. Cent. Rech. Explor.—Prod. Elf-Aquitaine,* 11.

Verosub, K.L., and Roberts, A.P., 1995. Environmental magnetism: past, present, and future. *J. Geophys. Res.,* 100:2175–2192.

Watkins, D.K., and Villa, G., in press. Palaeogene calcareous nannofossils from Cape Roberts Project 2A. *Terra Antart.*

Weeks, R.J., Roberts, A.P., Verosub, K.L., Okada, M., and Dubuisson, G.J., 1995. Magnetostratigraphy of upper Cenozoic sediments from Leg 145, North Pacific Ocean. *In* Rea, D.K., Basov, I.A., Scholl, D.W., and Allan, J.F. (Eds.), *Proc. ODP, Sci. Results,* 145: College Station, TX (Ocean Drilling Program), 491–521.

Wei, W., and Thierstein, H.R., 1991. Upper Cretaceous and Cenozoic calcareous nannofossils of the Kerguelen Plateau (southern Indian Ocean) and Prydz Bay (East Antarctica). *In* Barron, J., Larsen, B., et al., *Proc. ODP, Sci. Results,* 119: College Station, TX (Ocean Drilling Program), 467–494.

Wei, W., and Wise, S.W., Jr., 1990. Middle Eocene to Pleistocene calcareous nannofossils recovered by Ocean Drilling Program Leg 113 in the Weddell Sea. *In* Barker, P.F., Kennett, J.P., et al., *Proc. ODP, Sci. Results,* 113: College Station, TX (Ocean Drilling Program), 639–666.

————, 1992a. Oligocene-Pleistocene calcareous nannofossils from Southern Ocean Sites 747, 748, and 751. *In* Wise, S.W., Jr., Schlich, R., et al., *Proc. ODP, Sci. Results,* 120: College Station, TX (Ocean Drilling Program), 509–521.

————, 1992b. Selected Neogene calcareous nannofossil index taxa of the Southern Ocean: biochronology, biometrics, and paleoceanography. *In* Wise, S.W., Jr., Schlich, R., et al., *Proc. ODP, Sci. Results,* 120: College Station, TX (Ocean Drilling Program), 523–537.

Wetzel, A., 1984. Bioturbation in deep-sea fine-grained sediments: influence of sediment texture, turbidite frequency and rates of environmental change. *In* Stow, D.A.V., and Piper, D.J.W. (Eds.), *Fine-Grained Sediments: Deep Water Processes and Facies*. Geol. Soc. Spec. Publ., 24:595–608.

Wise, S.W., Jr., 1983. Mesozoic and Cenozoic calcareous nannofossils recovered by Deep Sea Drilling Project Leg 71 in the Falkland Plateau region, Southwest Atlantic Ocean. *In* Ludwig, W.J., Krasheninnikov, V.A., et al., *Init. Repts. DSDP,* 71 (Pt. 2): Washington (U.S. Govt. Printing Office), 481–550.

APPENDIX

Accessory Components

During examination of residues of samples prepared for foraminifers, observations of other fossil groups and various lithologic characteristics of sediments were made. These observations are summarized in Table AT1.

The site was drilled on the continental rise; therefore, glauconite and well-rounded terrigenous grains found above Core 188-1165B-26X (which originated in shallow marine settings) were probably reworked from older sections on the continental shelf.

AT1. Accessory components identified in foraminiferal residues, p. 191.

Glauconite

Glauconite is a common component of Paleogene sediments on the Mac. Robertson Shelf (Quilty et al., 1999) and is unlikely to be forming in the modern shelf environment around Antarctica. It is present in sediments at Site 1165 in several forms: individual rounded grains or clusters of grains; elongate, curved "concertina" form; and in one instance, pseudomorphic after a foraminifer. It appears almost continuously above Core 188-1165B-26X but only rarely below that depth.

Volcanic Glass

Sample 188-1165B-2H-CC contains a notable quantity of volcanic glass shards in the 63- to 125-µm fraction. Possible sources include a South Sandwich Islands eruption (followed by transport to this site via currents south of the Antarctic Divergence), a local source from an unknown eruption (Gaussberg is only 800 km east of this site and has been active in the last 50 k.y.), or some other source such as the McDonald Islands west of Heard Island.

Smaller amounts of volcanic glass are present in several other samples and seem to represent three different types. No information is available on possible genetic relationships between the different types of glass. One is clear and consists of thin walled glass that surrounds bubbles. A second, widespread but rare form, is dark brown with fewer bubbles. Occasionally it appears to be solid. A third type is in the form of white grains, usually somewhat elongate, with highly parallel structure, probably resulting from flow of a viscous lava and elongation of bubbles.

Pyrite

Crystalline pyrite in small irregular clusters, or pseudomorphic after organic remains, is present in the interval from Samples 188-1165B-32X-CC through 45X-CC. It appears to be diagenetic and not detrital. In some samples (e.g., 188-1165B-37X-CC), it is in the form of simple rods (length:diameter = 5:1) but in others it is in the form of semicylinders, suggesting growth in the lower half of a horizontal cylindrical fossil on (or slightly under) the seafloor. This has been observed in modern samples in the vicinity of Prydz Bay (Harris et al., 1997a).

Larger cylindrical bodies of pyrite (up to 2.5 mm × 1.0 mm) are present in the form of framboidal aggregates in Sample 188-1165B-45X-CC. These are pseudomorphic after fossils, perhaps echinoid spines,

suggesting that calcite-secreting organisms lived on the seafloor but are not represented by fossils.

Bone and Teeth

Several samples yielded small amounts of unidentifiable fine bone fragments; however, each of those in Samples 188-1165B-38X-CC, 55X-CC, and especially 33R-CC also yielded several teeth that may be attributable to notothenioid fish, the only fish family now occupying the waters around Antarctica.

Chert

Chert is present in several samples in and below Sample 188-1165B-40X-CC. It is in the form of chert chips (probably from small nodules formed in situ) in samples such as 188-1165B-67X-CC and commonly in samples below that depth. In most shallower occurrences, it is found as partly chertified sediment with high organic silica content. This material seems to be in the early stages of formation. It appears to be restricted to a discrete depth range because it is absent from Hole 1165C cores, except for Sample 188-1165C-10R-CC, where it is in the form of partly chertified sediment rather than solid chert.

Residue Changes with Depth

Using the data tabulated in Table AT1, it is possible to identify a series of levels at which the paleoenvironment changed. These are indicated on the table. Horizons and events are discussed in an uphole (i.e., time) sequence.

Sample 188-1165B-56X-CC

Below this depth, residues contain no evidence of a terrigenous component nor of siliceous microfossils. The uniformity of the sequence is broken only by the occasional presence of chert, in the form of chips (in the residue) of dark gray chert, probably fragments of small diagenetic nodules, essentially in situ.

Sample 188-1165B-53X-CC

The interval between Samples 188-1165B-56X-CC and 53X-CC marks a transition from small chert-dominated residues to more terrigenous grains. Some samples contain residues of terrigenous and biogenic origin, including sponge spicules and minor amounts of bone.

Sample 188-1165B-46X-CC

This interval of six cores is barren of pyrite but contains minute residues, commonly dominated by terrigenous content, and may include minor incipient chert. The distinction between it and the interval below is the greater volume of residue.

Sample 188-1165B-32X-CC

Between this sample and 188-1165B-45X-CC, samples contain pyrite, orosphaerid radiolarians, and in one case, significant bone. The presence of pyrite indicates reducing conditions near the sediment surface (a seafloor feature), and the presence of the large (up to 2–3 mm) planktonic radiolarians suggests changes either in the planktonic realm or in preservation conditions on the seafloor.

Sample 188-1165B-27X-CC

Above this depth residues are generally larger, but the notable feature is the presence in most samples of glauconite—usually only in trace quantities, but in two samples (188-1165B-11H-CC and 12H-CC) in noteworthy amounts. The increase in glauconite at this level in the hole suggests a shift in sediment source to a Paleogene section. This increase may reflect a change in either source or transporting mechanism.

Sample 188-1165B-3H-CC

This level approximates the horizon above which abundant carbonate is present.

Other Noteworthy Horizons

In situ diagenetic chert is absent from samples above Sample 188-1165X-40X-CC, suggesting that this is an important horizon from a diagenetic perspective. Another significant level is at the base of Core 188-1165B-2H, where volcanic glass is notable. It coincides roughly with the base of abundant carbonate and, with the carbonate above, provides scope for dating from the surface to some level in Core 188-1165B-3H using radiometric and biochemical means.

Figure F1. Map showing bathymetry of the Prydz Bay region with location of drill sites and existing seismic lines. Sites PBD-13A and PDB-15A are alternate sites that were not drilled.

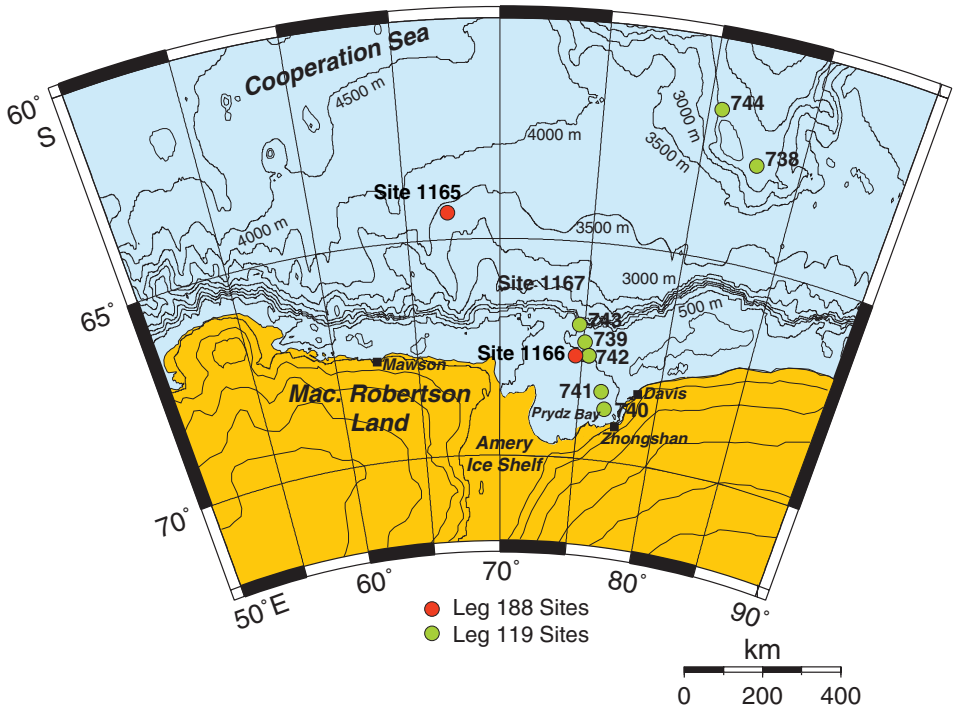

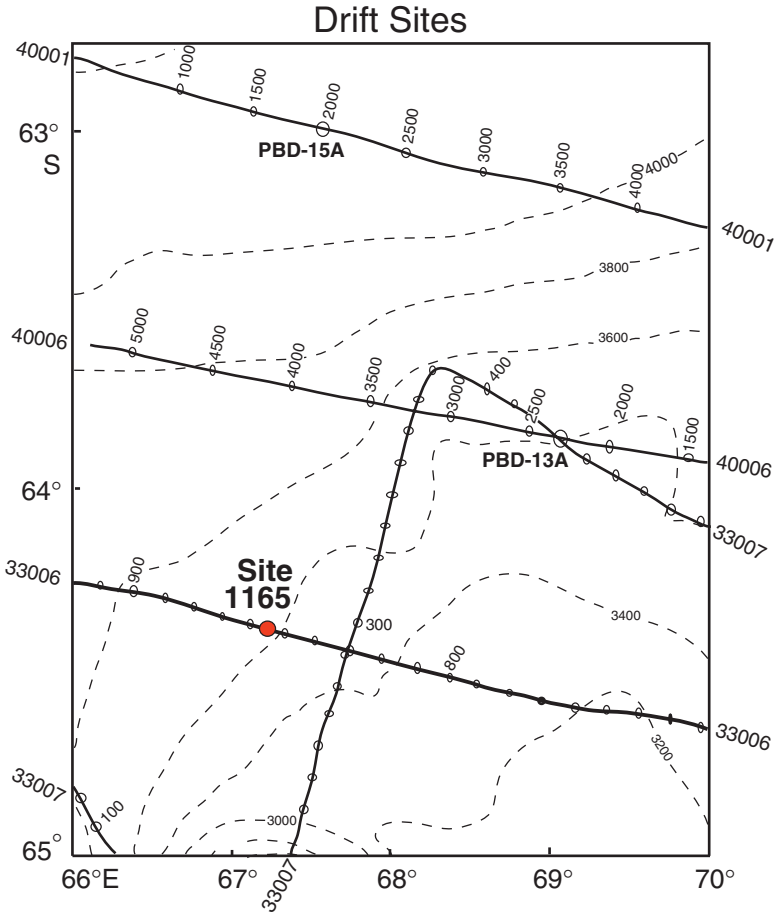

Figure F2. Seismic section through Site 1165 showing Reflectors PP12, P3, P2, and P1 (line SAE 33006).

Figure F3. Presite survey track line for Site 1165.

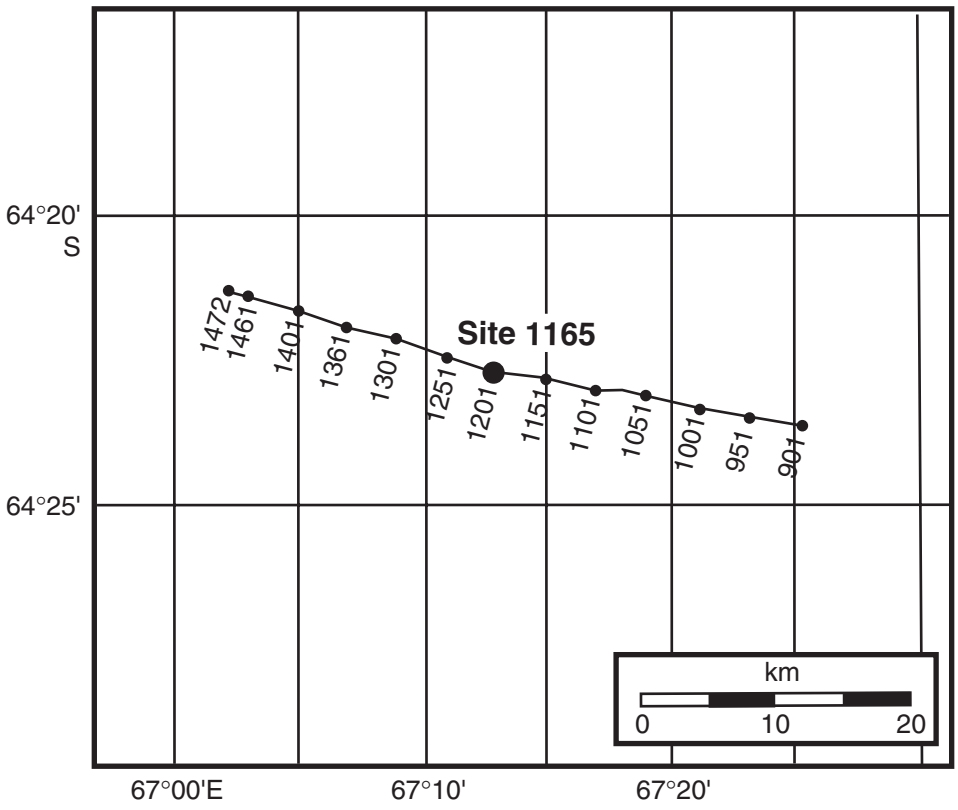

Figure F4. Predrilling seismic survey across Site 1165. SP = shotpoint.

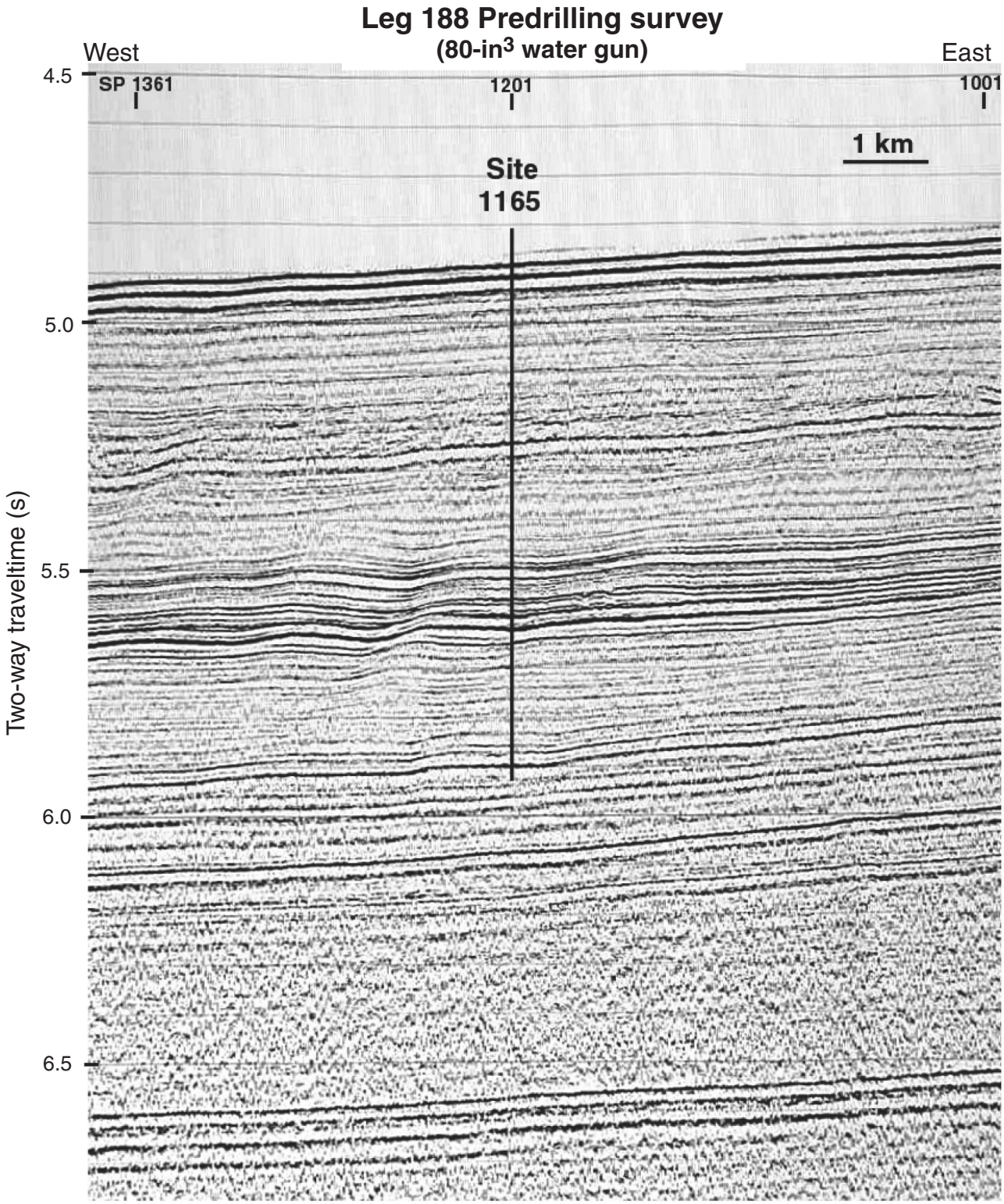

Figure F5. Lithostratigraphic subdivision of Site 1165.

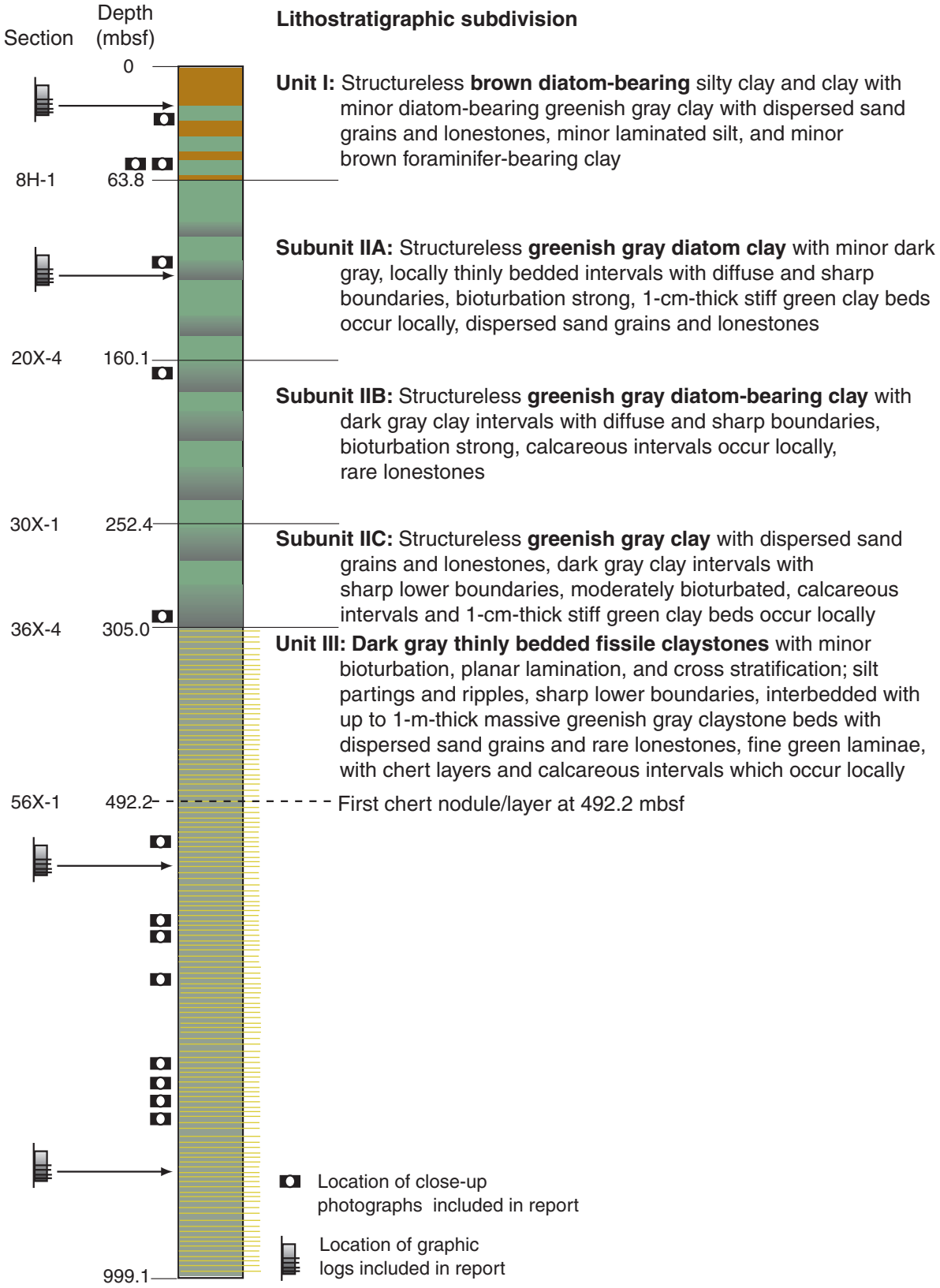

Figure F6. Composite stratigraphic section for Site 1165 showing core recovery, a simplified summary of lithology, lithostratigraphic unit boundaries, and age. Also shown are the distribution of lonestones and dispersed clasts, mineral abundances identified by XRD, the percentage of diatoms and sponge spicules from smear slides, and color reflectance. The bar graph shows the distribution of isolated lonestones (>5 mm) downhole. The vertical bars on the side of the column right show the distribution of dispersed grains and granules (<5 mm). XRD shows the percentage of most abundant minerals. This graph was plotted using the methods of Forsberg et al. (1999). In the smear slide graph, solid line = diatoms and dashed line = sponge spicules. The thin line in the color reflectance plot shows the percent light reflectance (L*) downhole. The thick line is a 200-point moving average. The spectrophotometer light-reflectance data were measured at 5-cm intervals for core from Hole 1165B and at higher resolution (2-cm intervals) for core from Hole 1165C to better characterize the highly fractured cores. The data illustrate several lithologic distinctions at Site 1165. A general trend of darkening with depth can be recognized, and light reflectance has higher variability in the upper 500 m. Lithologic symbols are explained in Figure F3, p. 42, in the "Explanatory Notes" chapter. (**Figure shown on next two pages.**)

Figure F6 (continued). (Caption shown on previous page.)

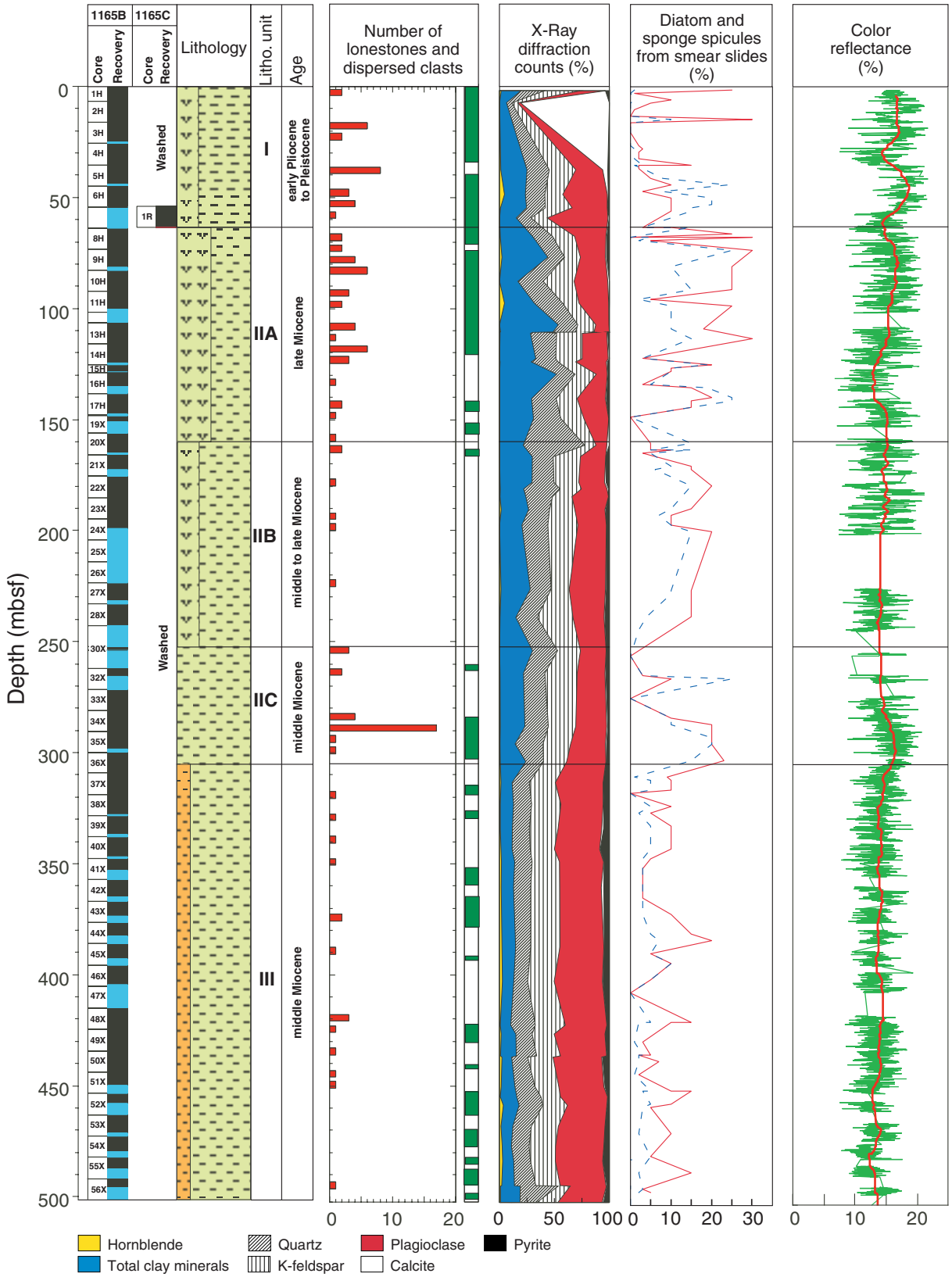

Figure F6 (continued).

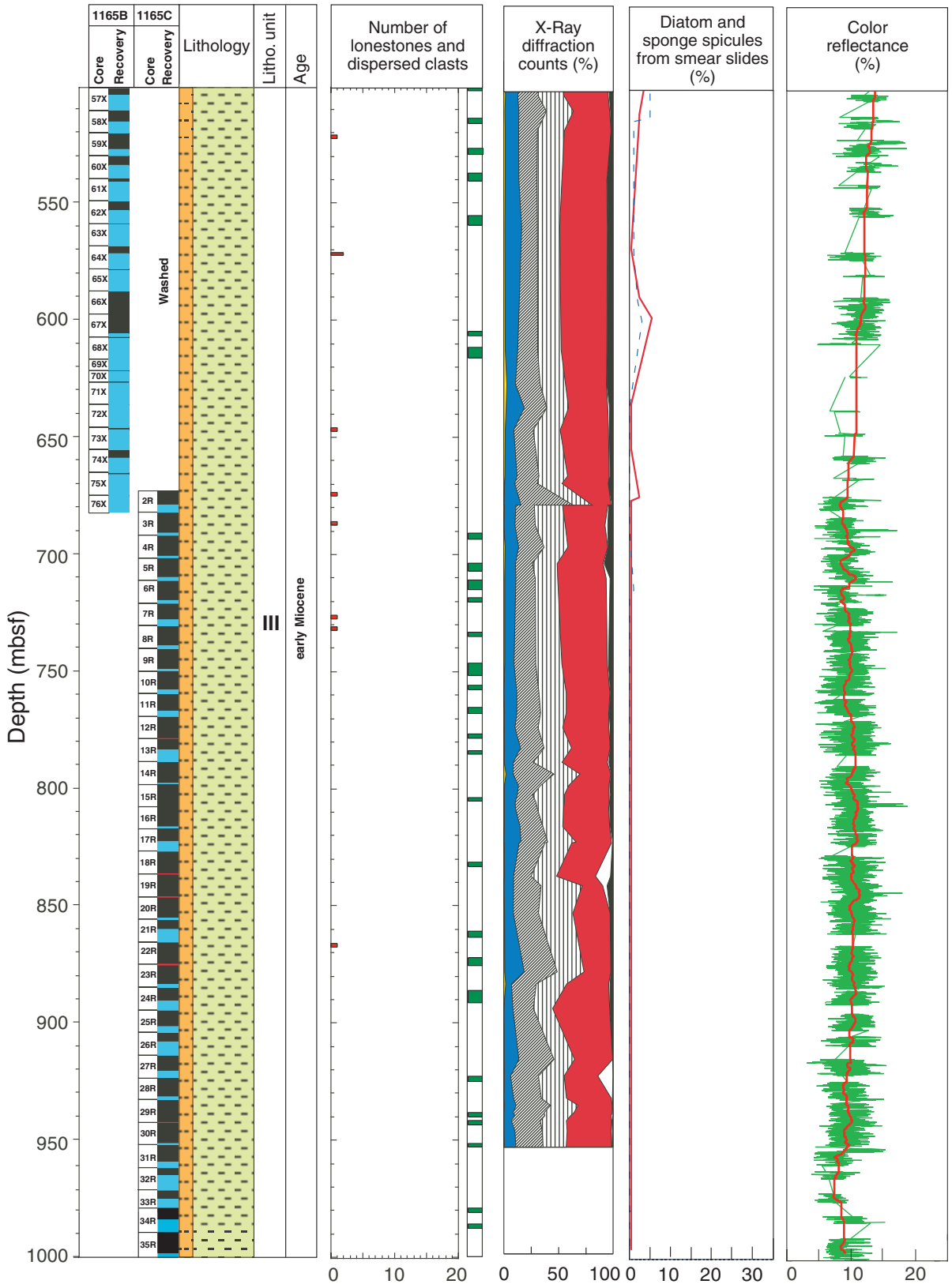

Figure F7. Graphic logs illustrating facies associations. The location is indicated in Figure F5. **A.** Graphic log for Core 188-1165B-4H. (Continued on next three pages.)

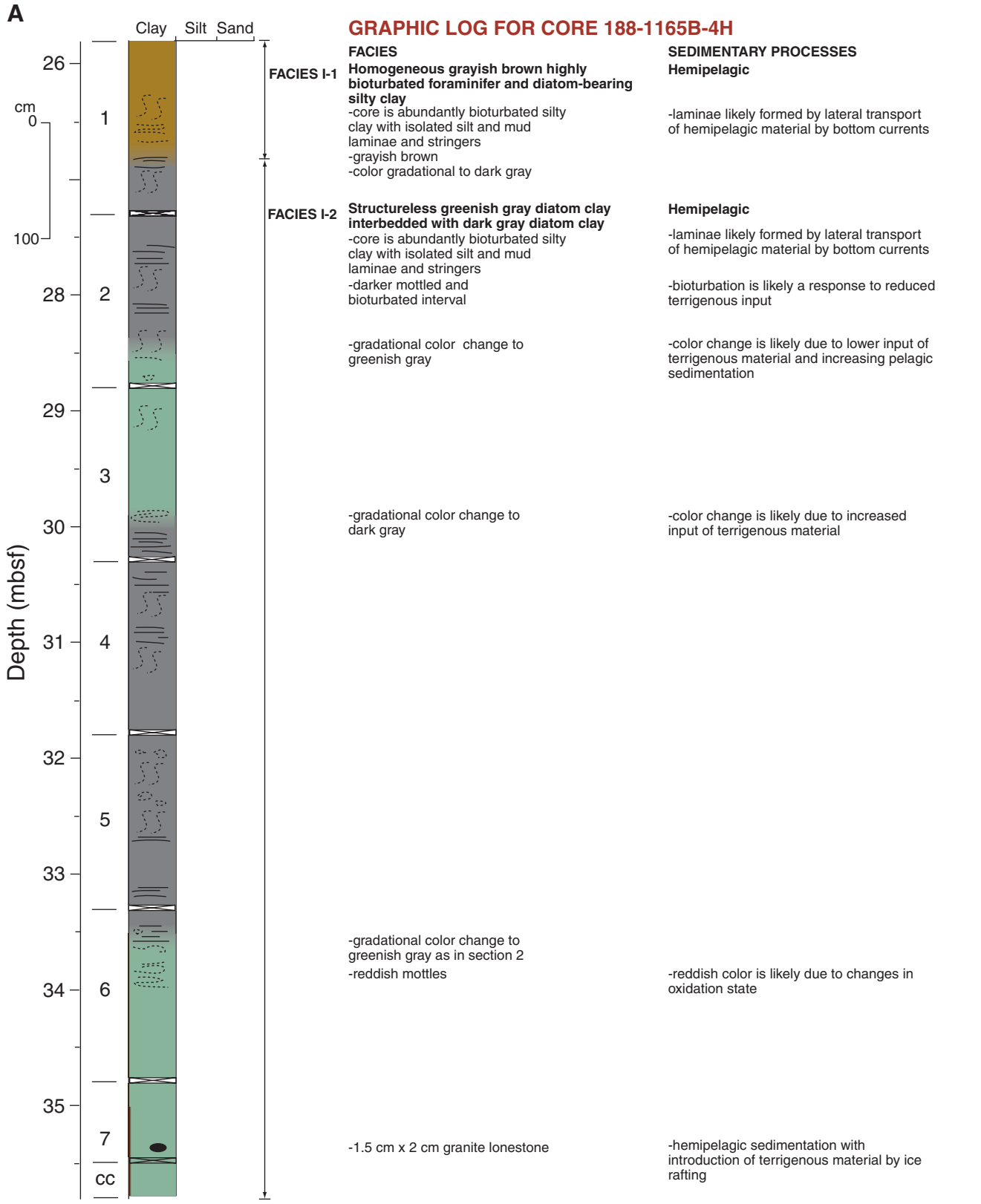

Figure F7 (continued). B. Graphic log for Core 188-1165B-14H.

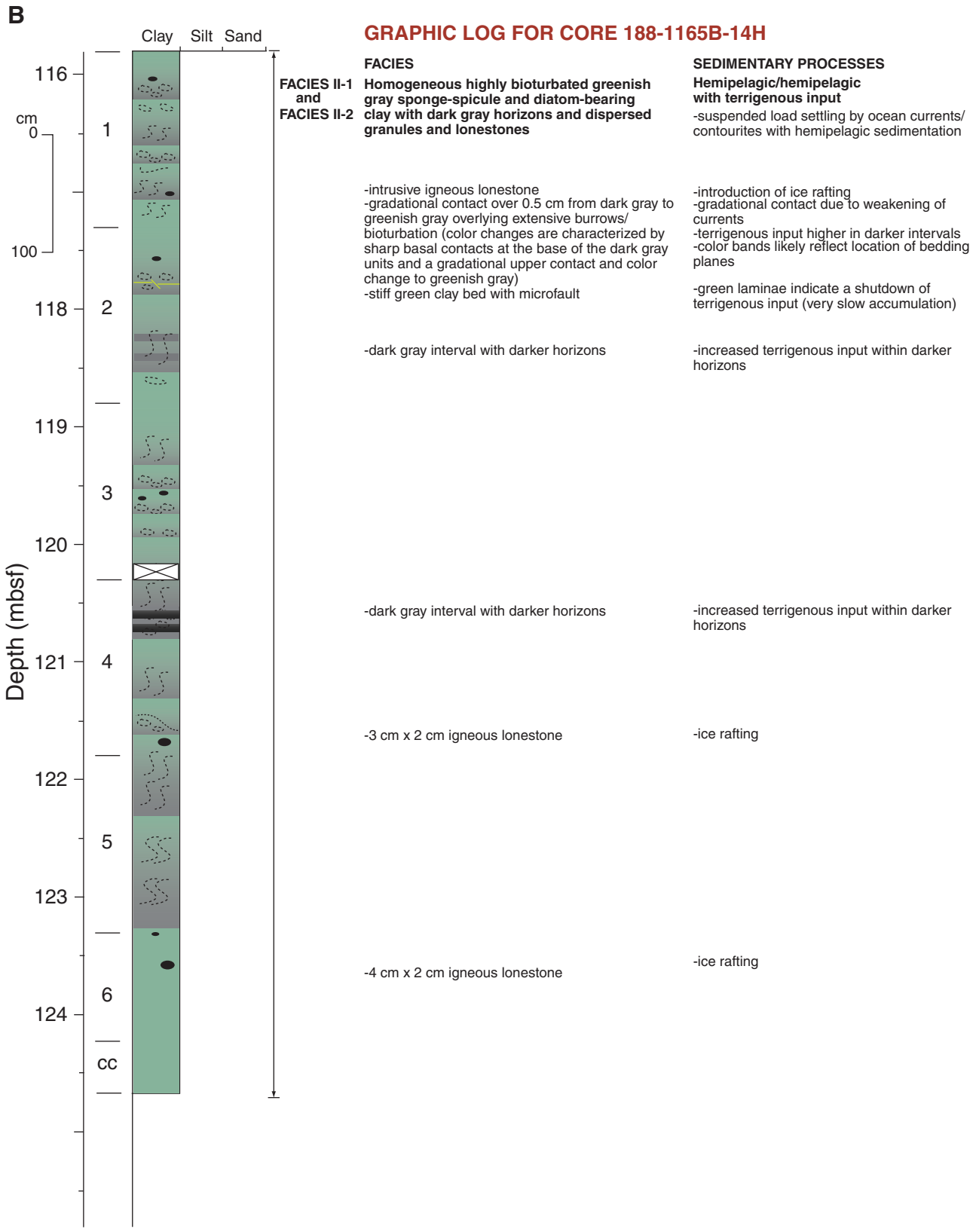

Figure F7 (continued). C. Graphic log for Core 188-1165B-59X.

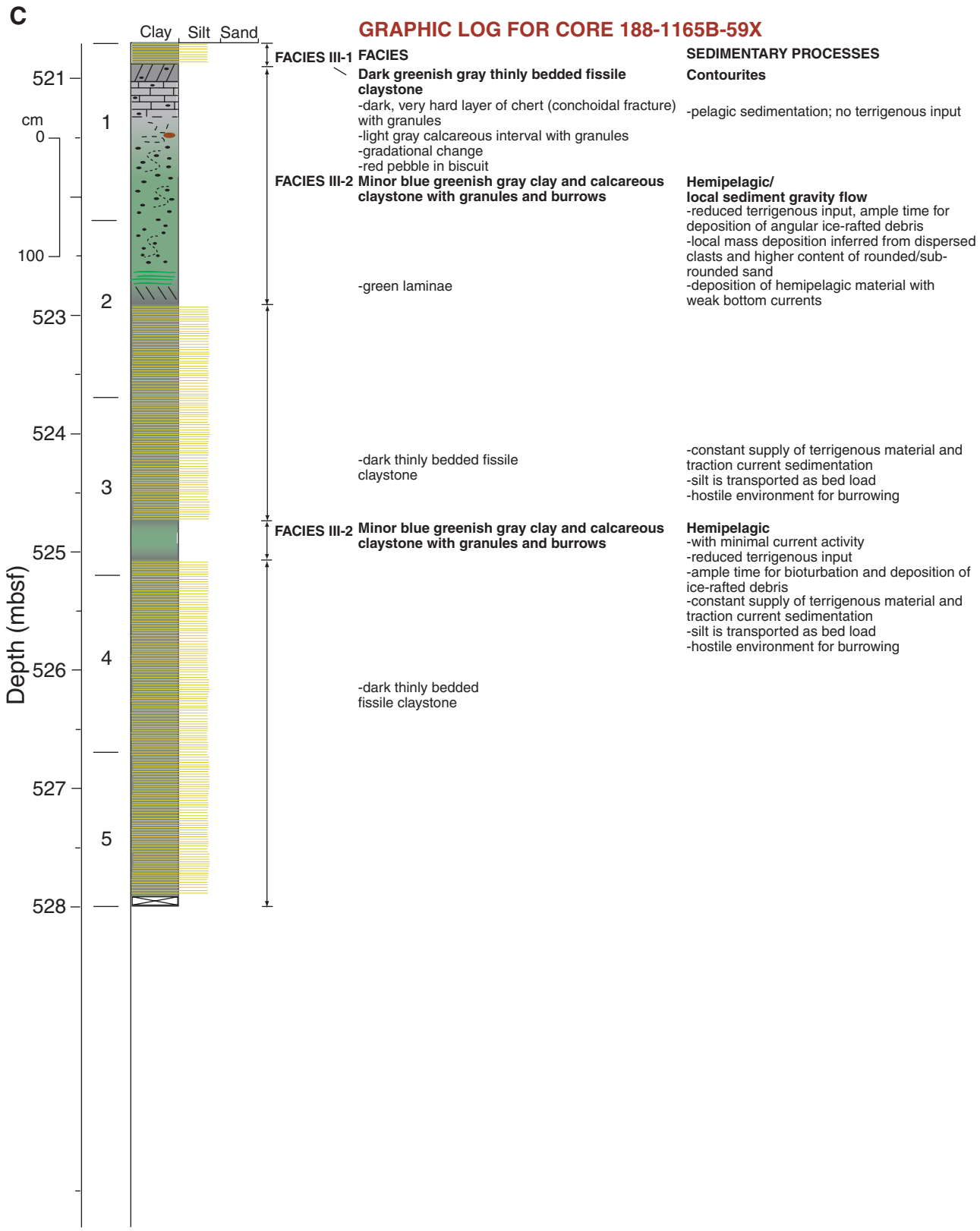

Figure F7 (continued). D. Graphic log for Core 188-1165C-27R.

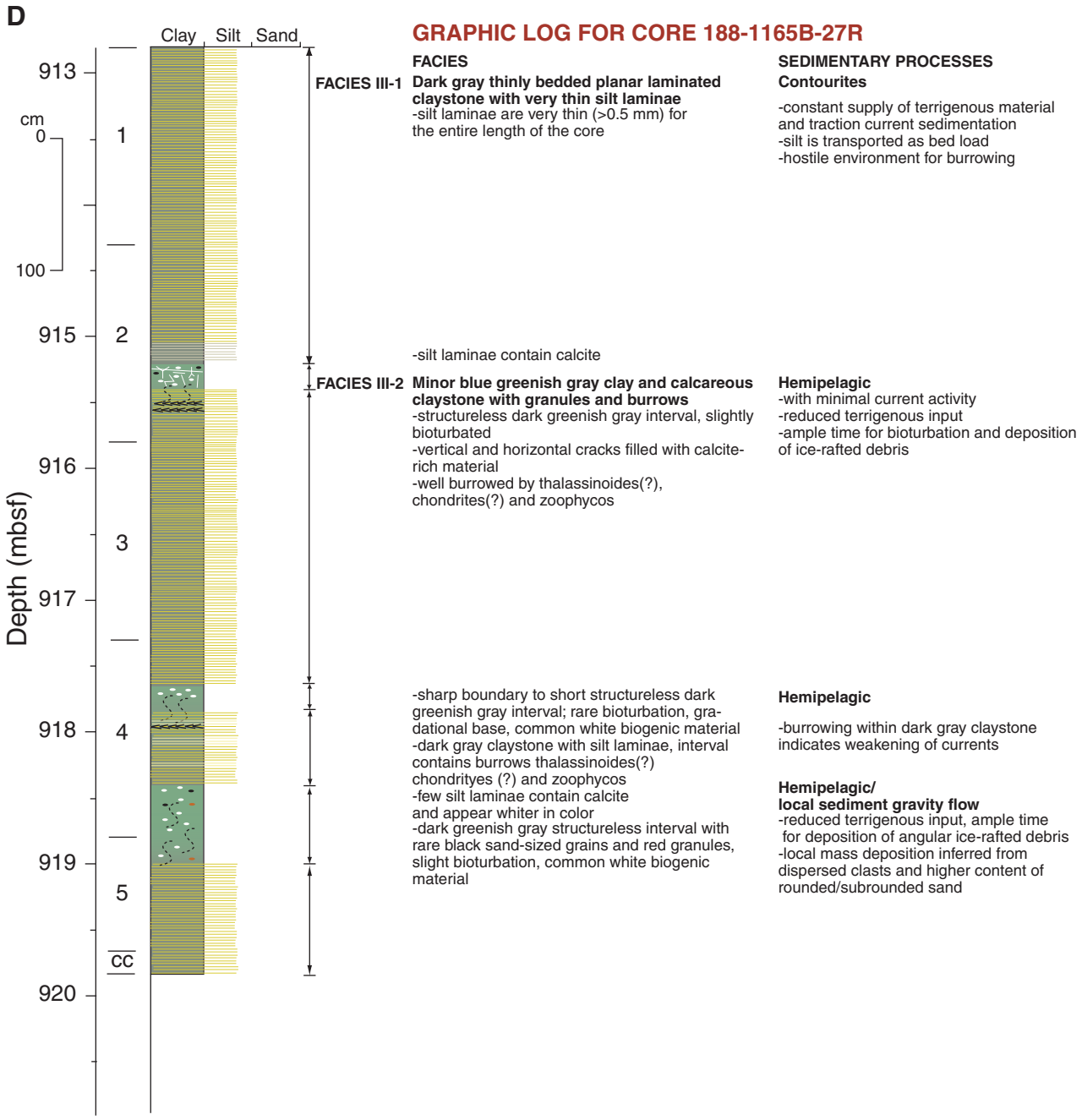

Figure F8. Structureless greenish gray diatom clay interbedded with dark grayish brown to dark gray diatom clay in Unit I (Facies I-2) (interval 188-1165C-1R-2, 15–35 cm).

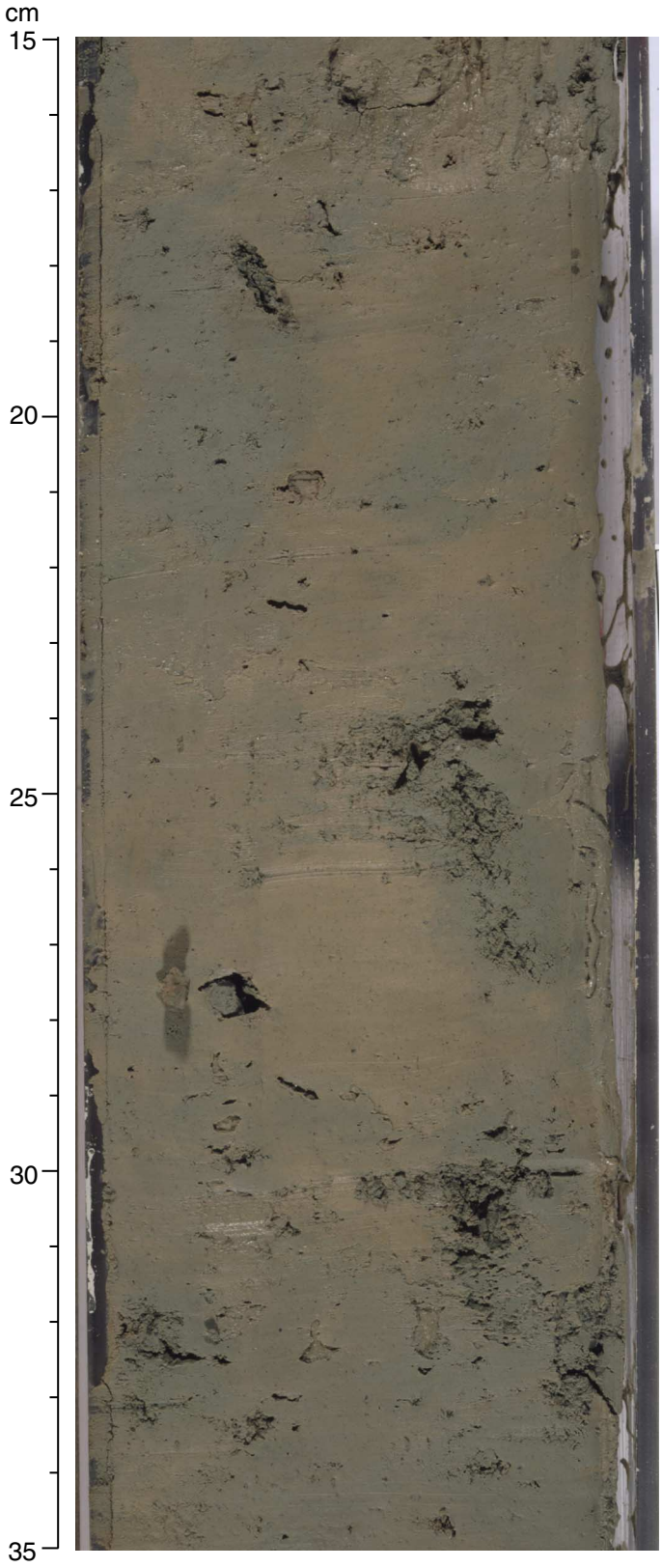

Figure F9. Silt laminae and stringers in Unit I (interval 188-1165B-4H-4, 10–25 cm).

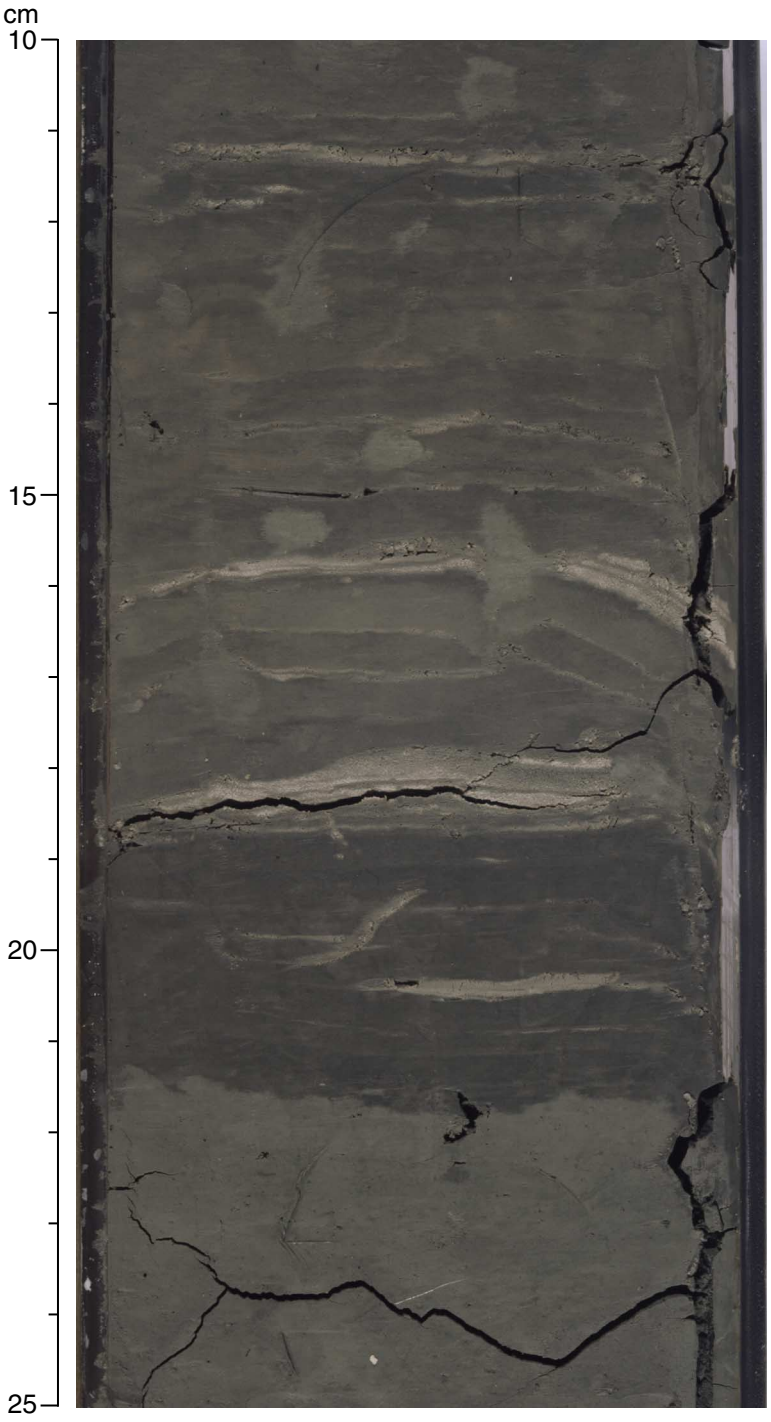

Figure F10. Injection structure and abrupt color changes in Unit I (interval 188-1165C-1R-4, 112–134 cm).

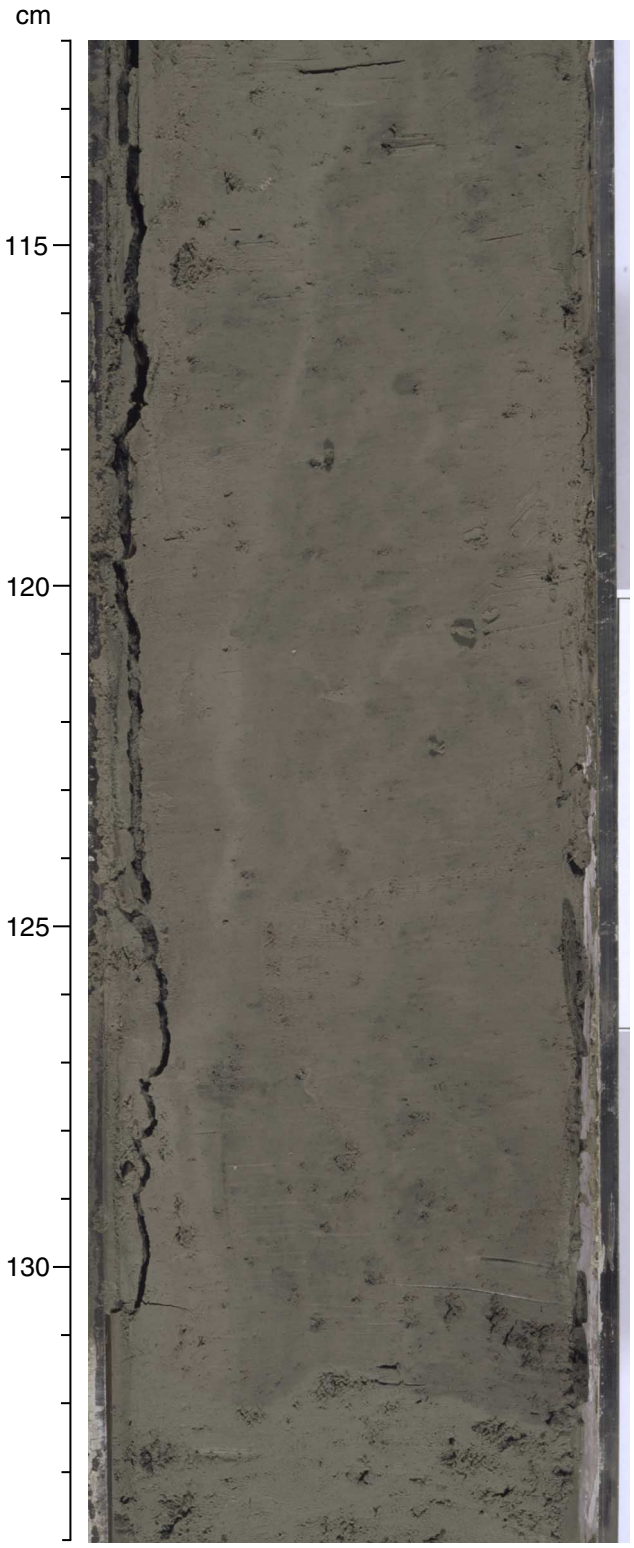

Figure F11. Color banding and planar lamination in dark gray diatom-bearing clay in Unit II (Facies II-2) (interval 188-1165B-13H-2, 50–85 cm).

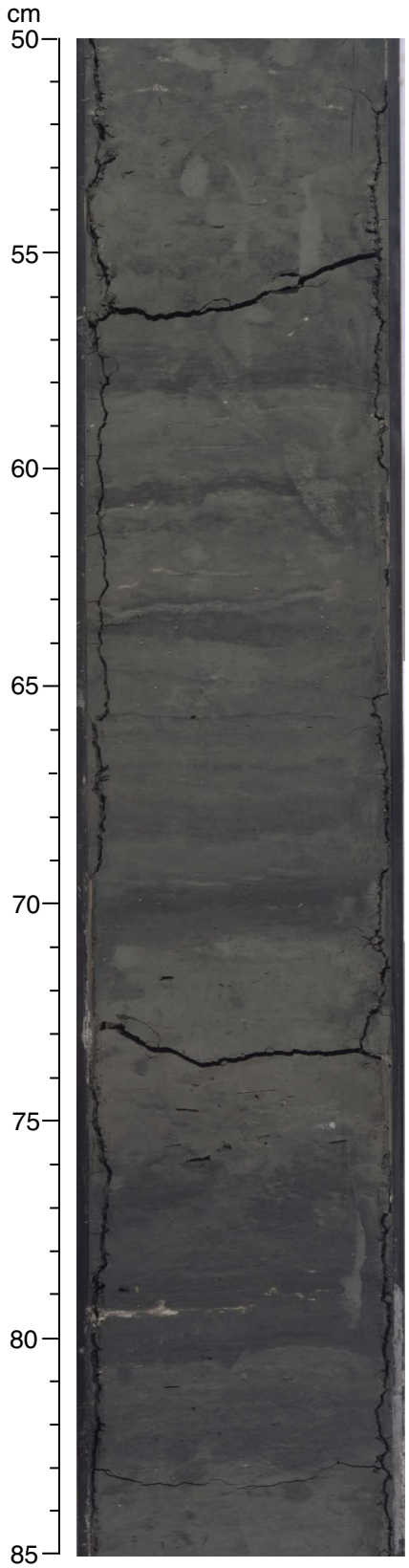

Figure F12. Photomicrographs of diatom clay and diatom-bearing clay. **A.** Dark gray diatom-bearing clay with iron sulfides (pyrite) giving a distinctive color to the sediment (Sample 188-1165B-14H-5, 40–42 cm). **B.** Greenish gray diatom clay showing well-preserved diatoms and sponge spicules with little quartz silt (Sample 188-1165B-14H-6, 60–62 cm).

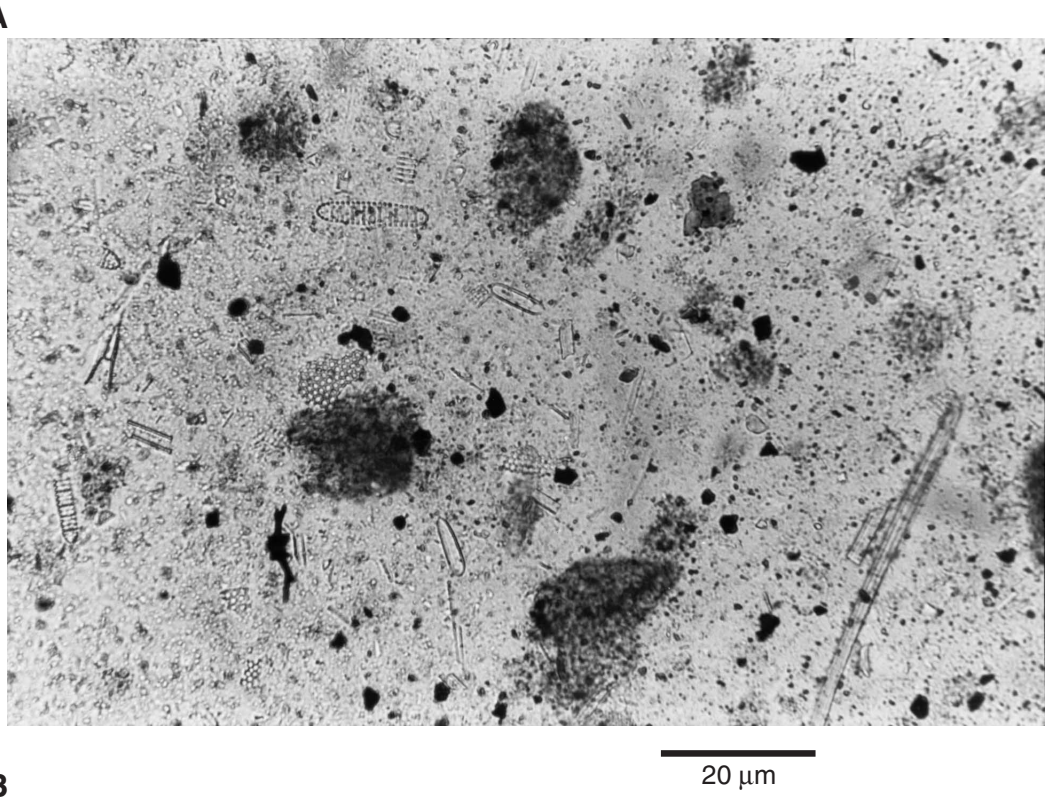

Figure F13. Thick calcareous bed (Facies II-3) within Subunit IIB (interval 188-1165B-20X-5, 110–140 cm).

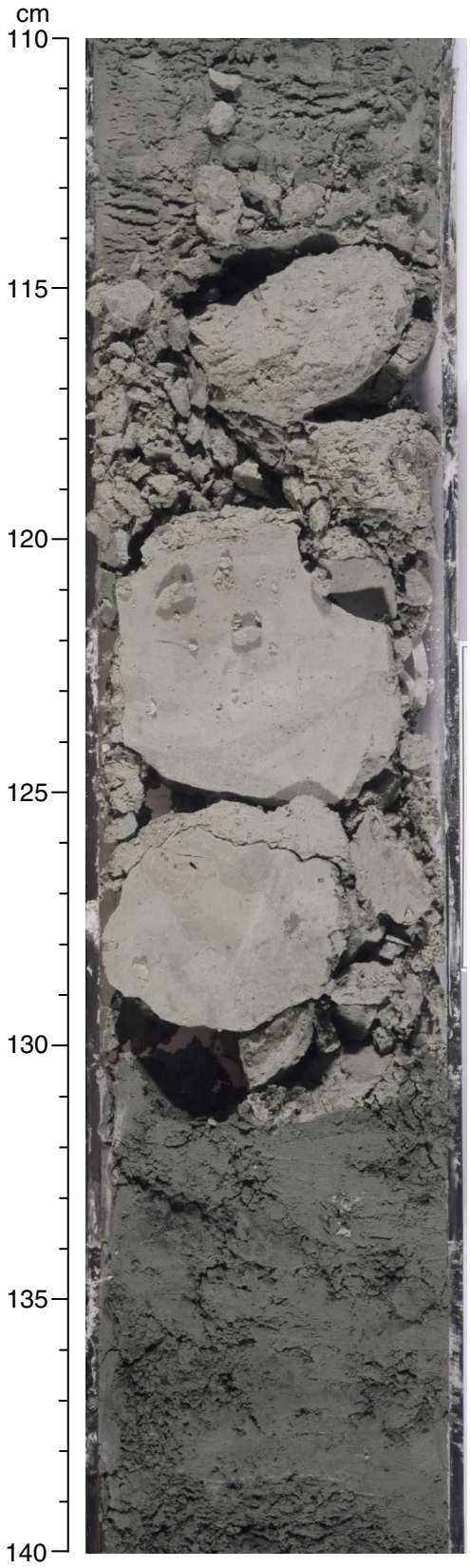

Figure F14. Planar silt laminae within Subunit IIIC (interval 188-1165B-35X-5, 44–54 cm).

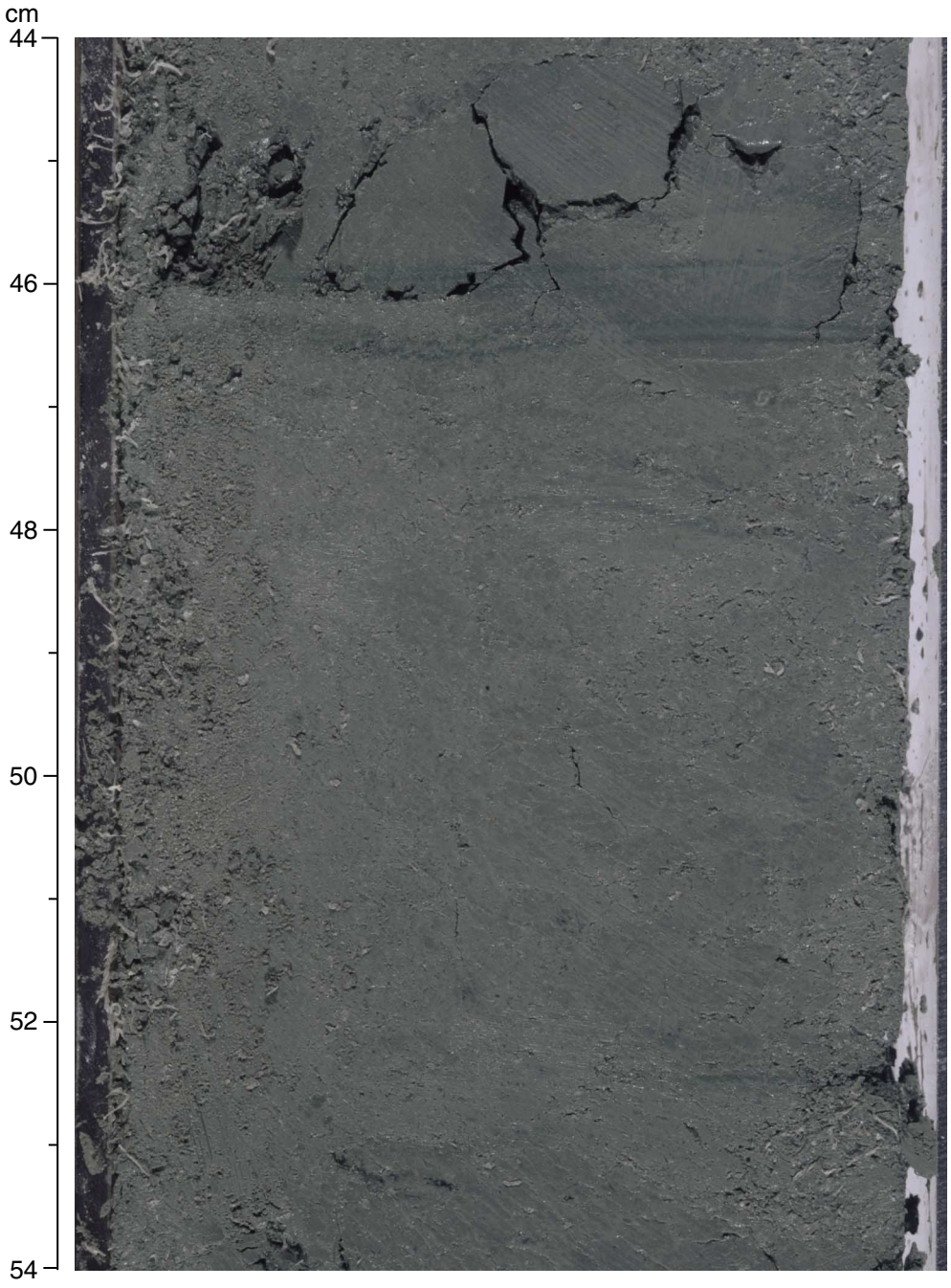

Figure F15. Greenish gray claystone facies (Facies III-2) of Unit III (interval 188-1165C-8R-1, 30–60 cm).

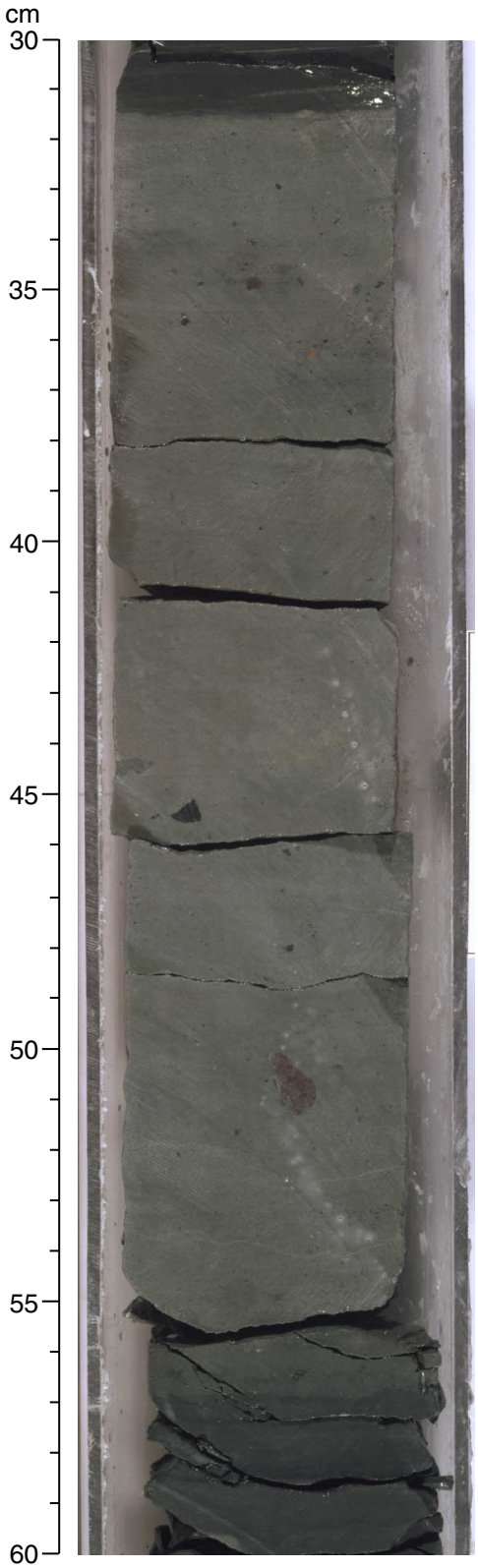

Figure F16. Dark gray claystone (Facies III-1) of Unit III with ~1-cm beds and silt partings along bedding planes (interval 188-1165C-3R-3, 55–75 cm).

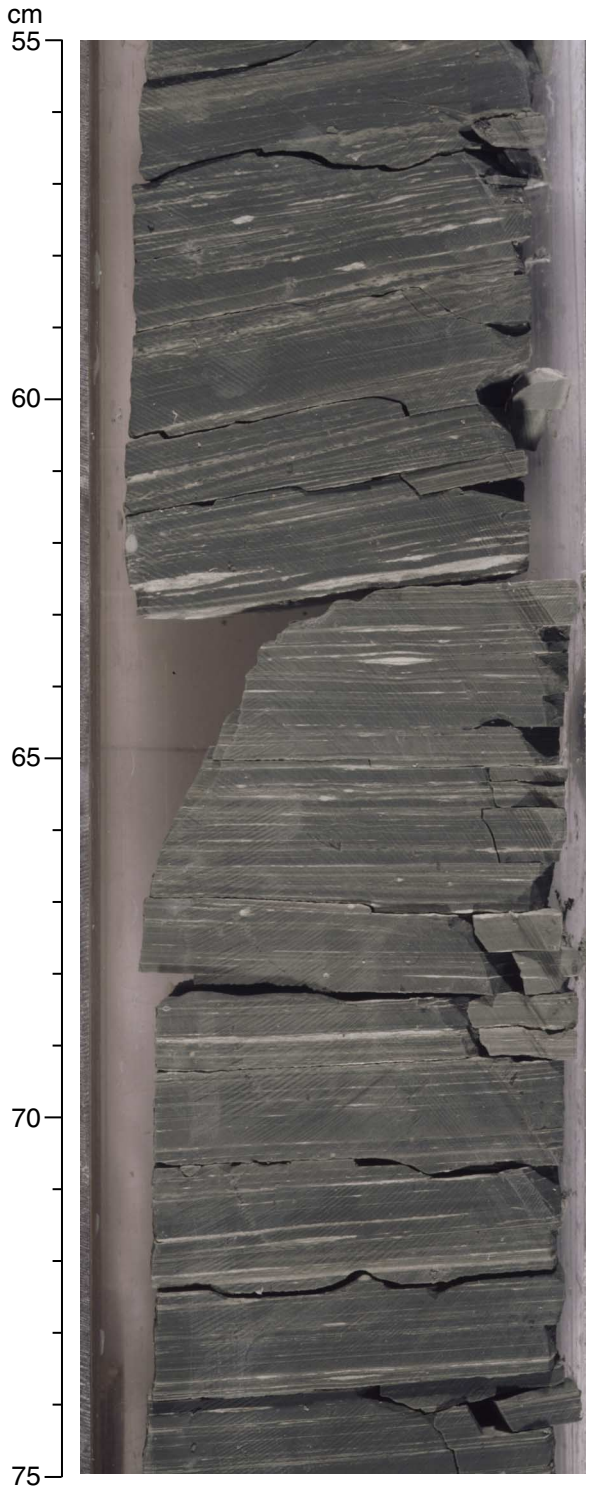

Figure F17. Silt ripple and cross-bedded silt within dark gray claystone (Facies III-1) of Unit III (interval 188-1165C-4R-4, 120–124 cm).

Figure F18. Deformed interval within Unit III (interval 188-1165C-19R-3, 101–121 cm).

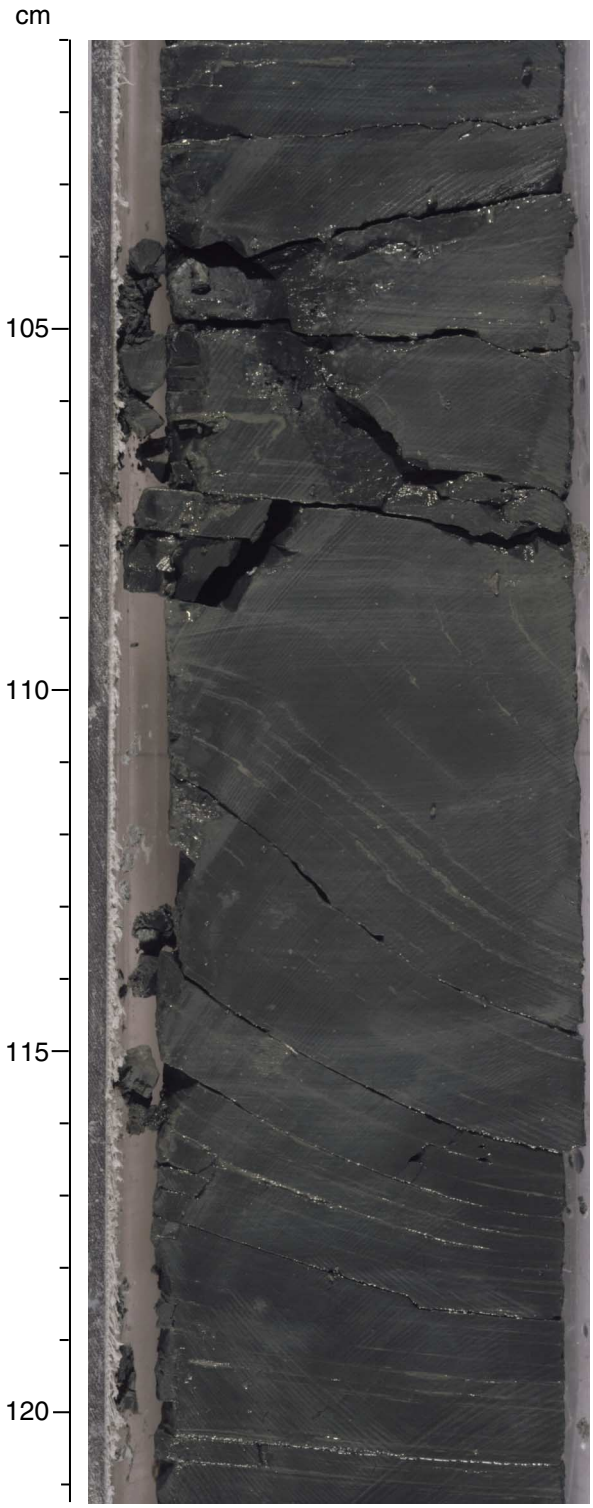

Figure F19. Benthic foraminifers and rip-up clasts (Facies III-2) of Unit III (interval 188-1165C-23R-6, 27–33 cm).

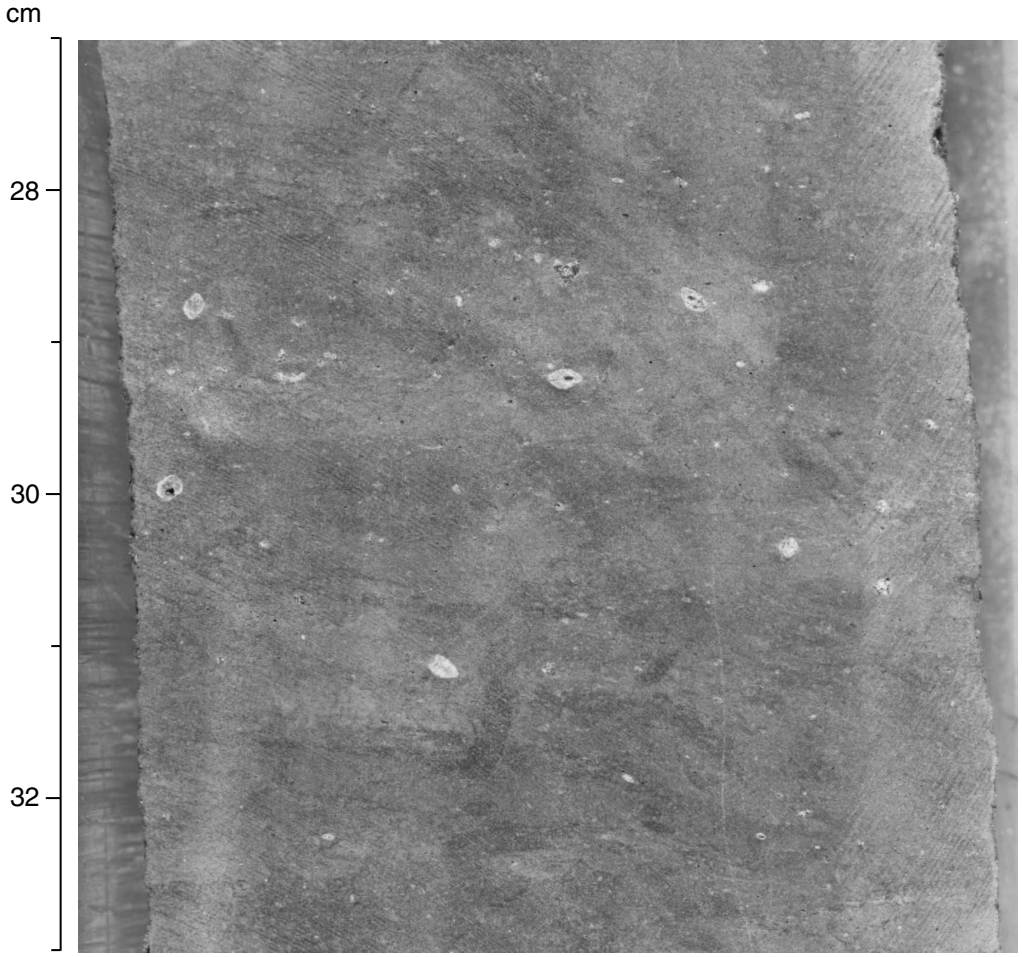

Figure F20. Well-preserved *Zoophycos*(?) trace fossil in bioturbated greenish gray claystone of Unit III (interval 188-1165B-58X-2, 65–90 cm).

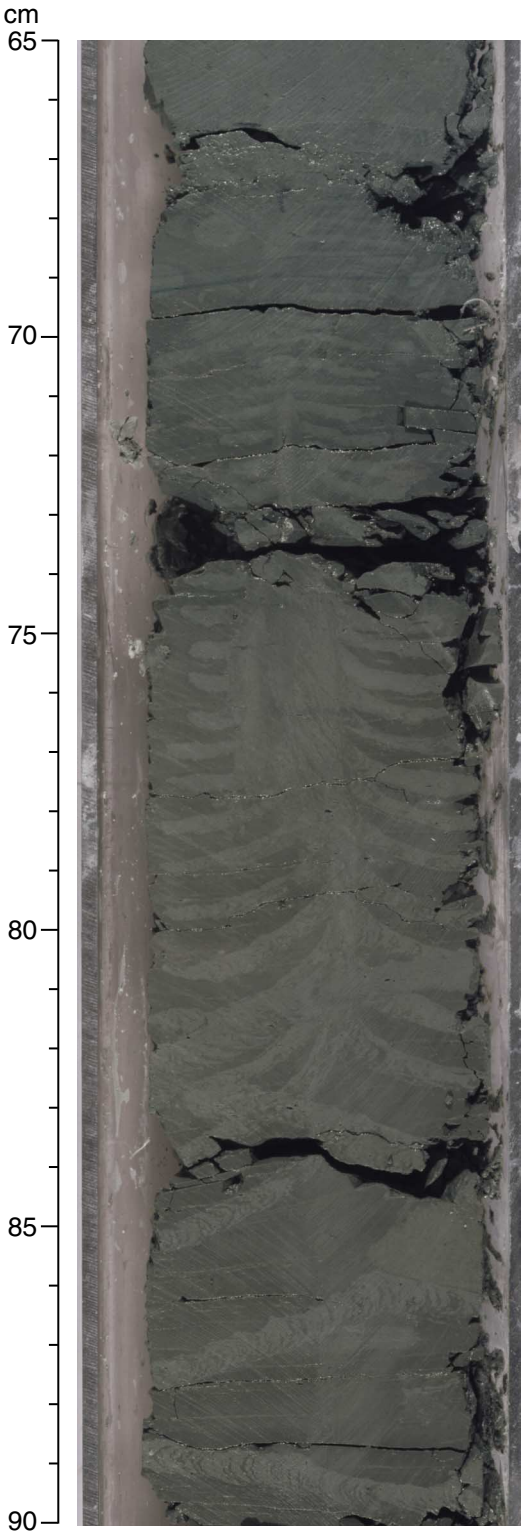

Figure F21. Burrows and *Zoophycos* trace fossils from Unit III (interval 188-1165C-24R-2, 2–22 cm).

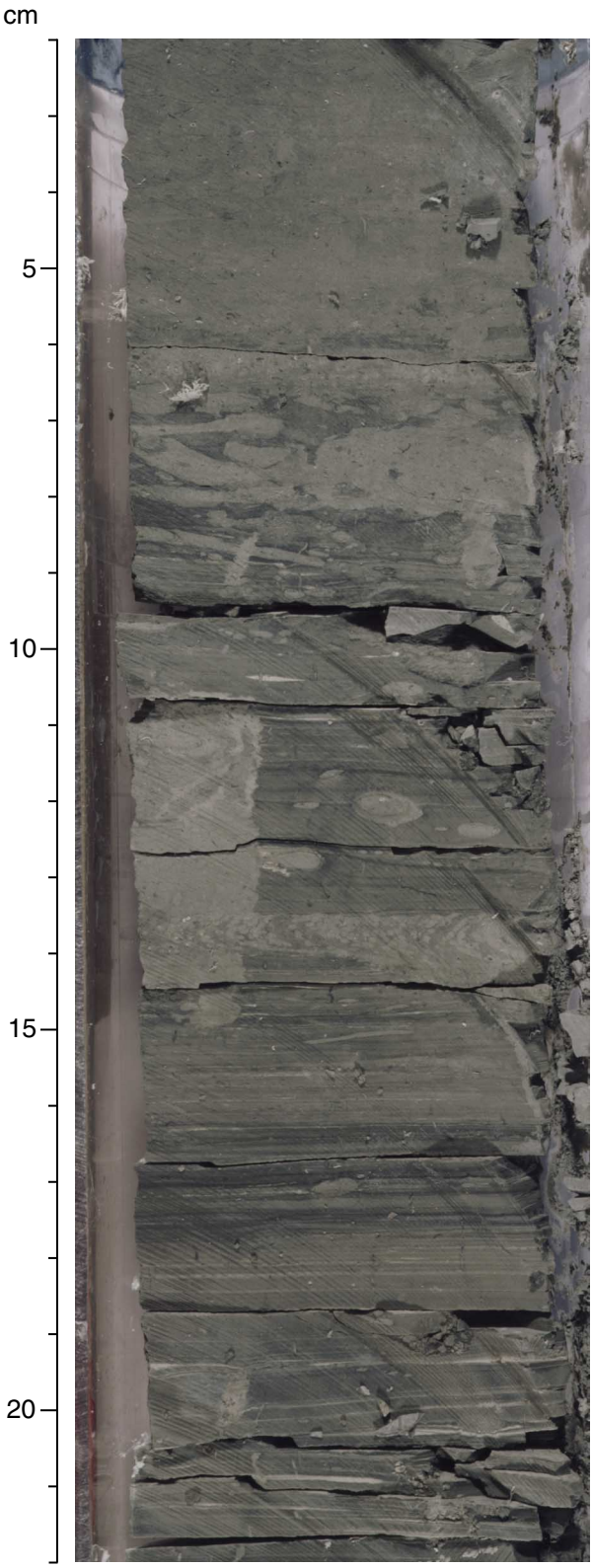

Figure F22. Photomicrograph of metamorphic rock fragments and very angular quartz grains in structureless calcite-cemented claystone in Unit III (Sample 188-1165B-73X-1, 30–32 cm).

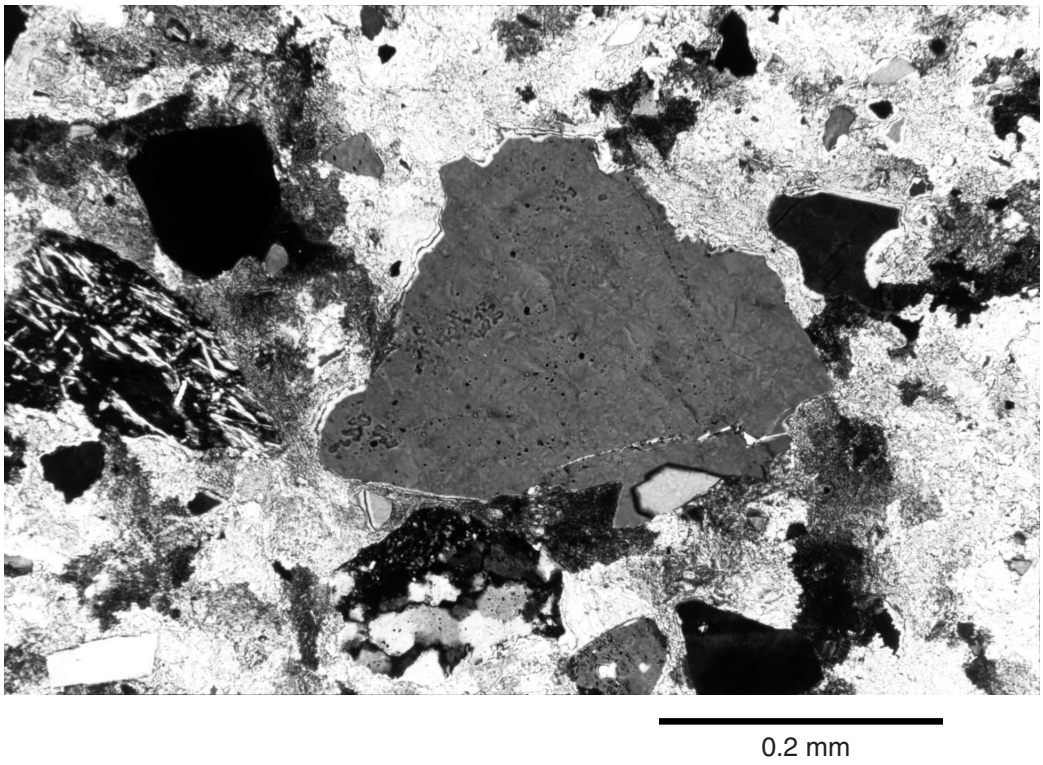

Figure F23. Lonestones within greenish gray beds (Facies III-2) of Unit III (interval 188-1165C-21R-3, 74–94 cm).

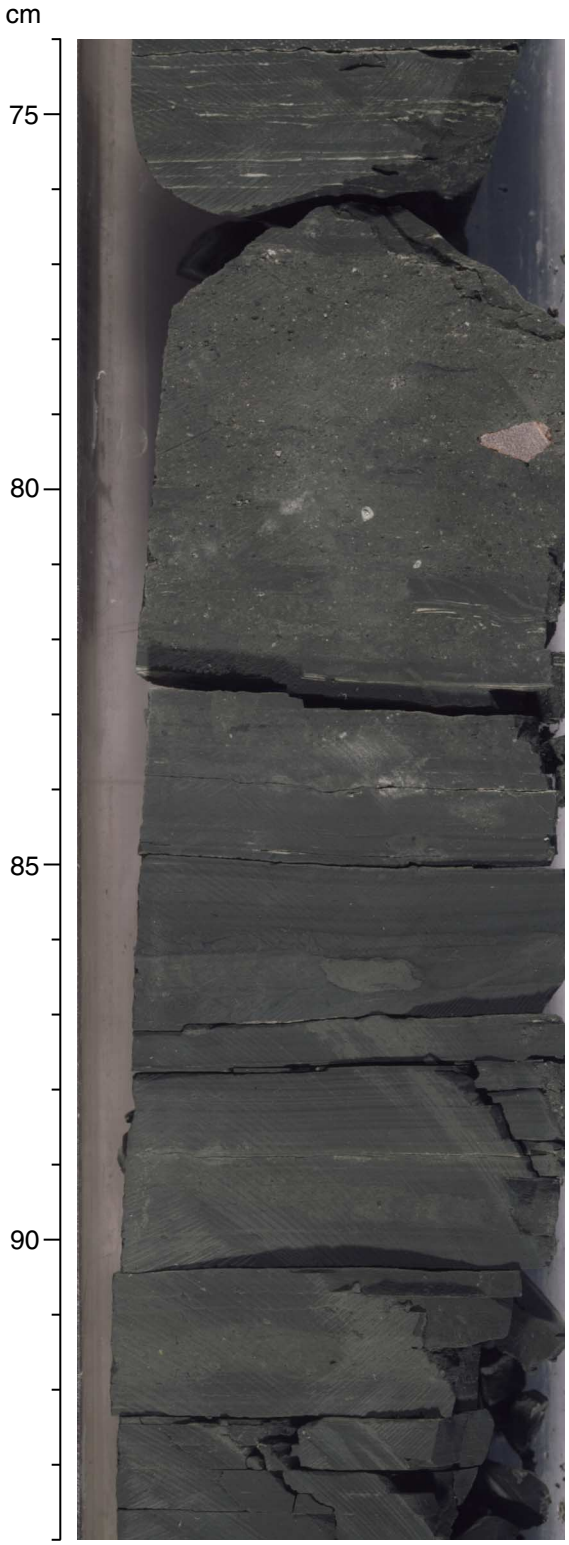

Figure F24. X-ray diffractograms of clay-sized fractions of sediment from Samples 188-1165B-14H-5, 36–38 cm (dark gray clay), and 55–57 cm (greenish gray clay).

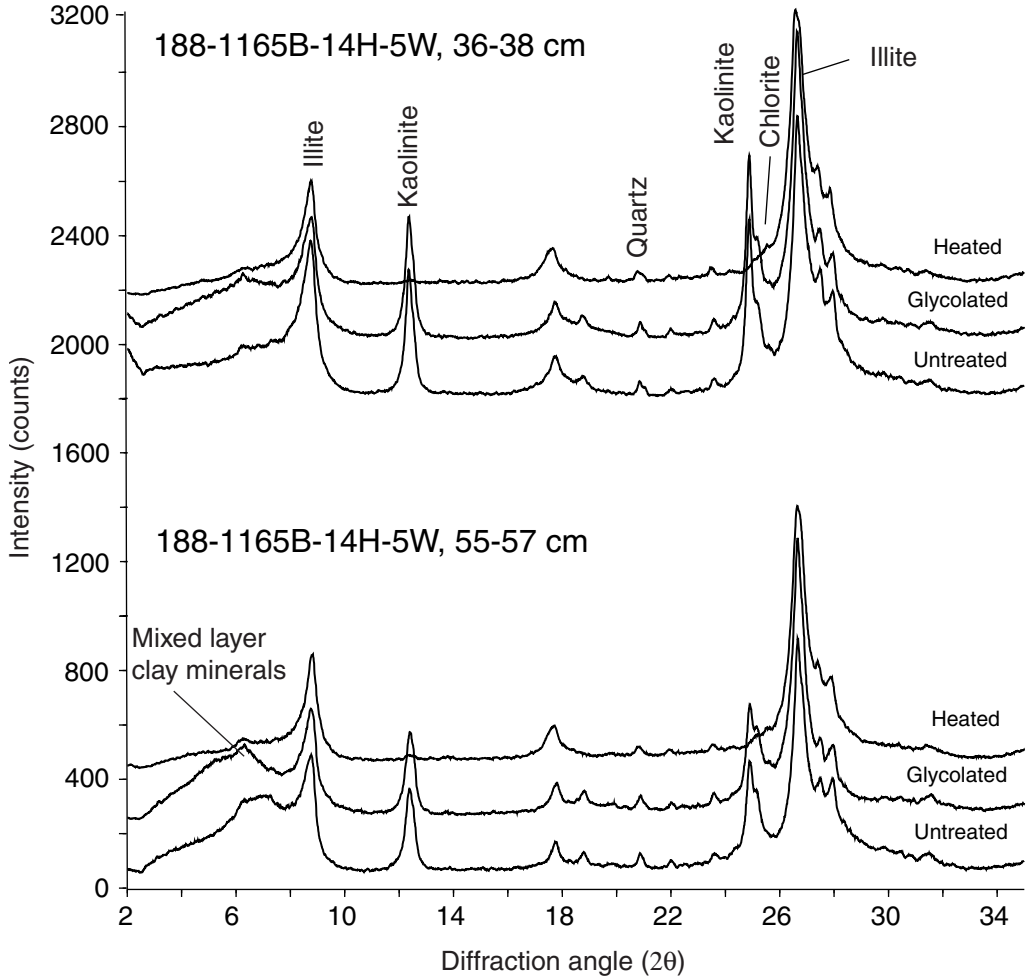

Figure F25. X-ray diffractograms of clay-sized fractions of sediment from Samples 188-1165C-37X-5, 41–43 cm (greenish gray clay), and 37X-6, 41–43 cm (dark gray clay).

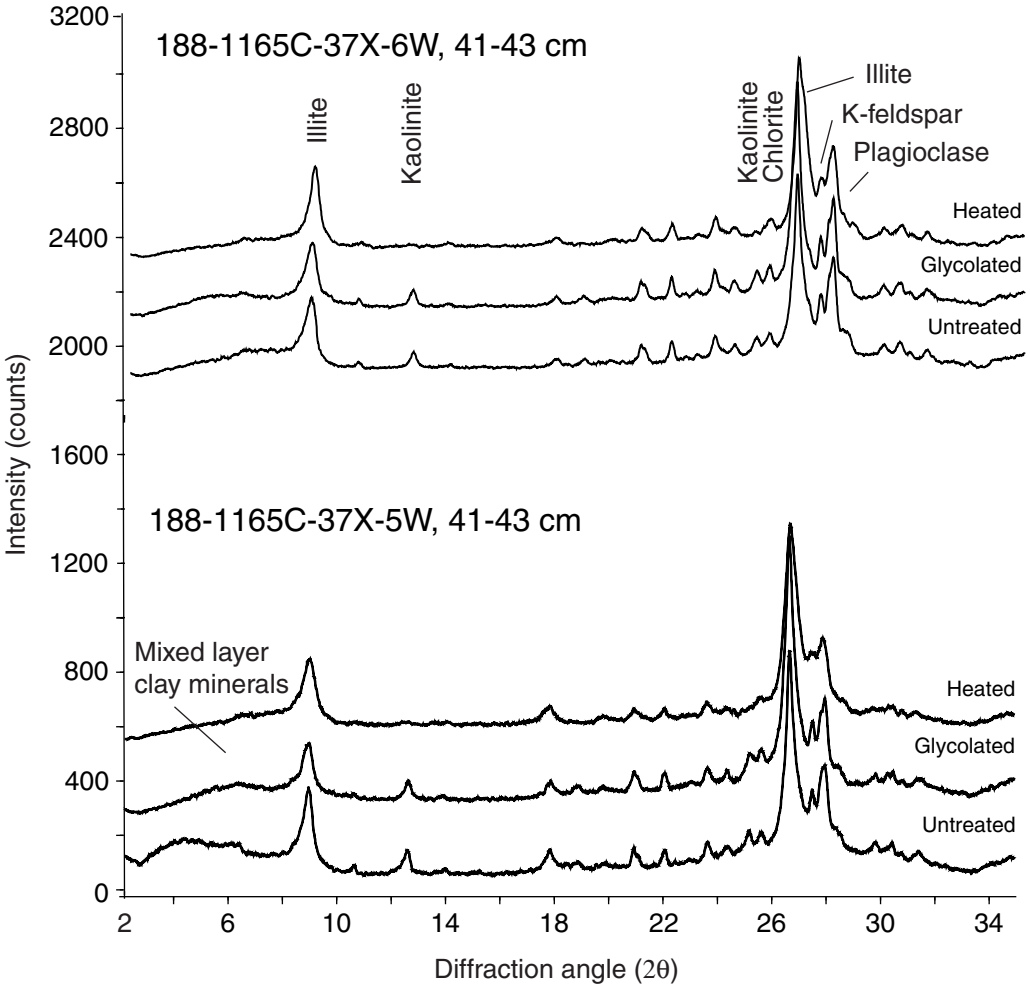

Figure F26. Downhole abundance of terrigenous debris in the >125-µm grain-size fraction.

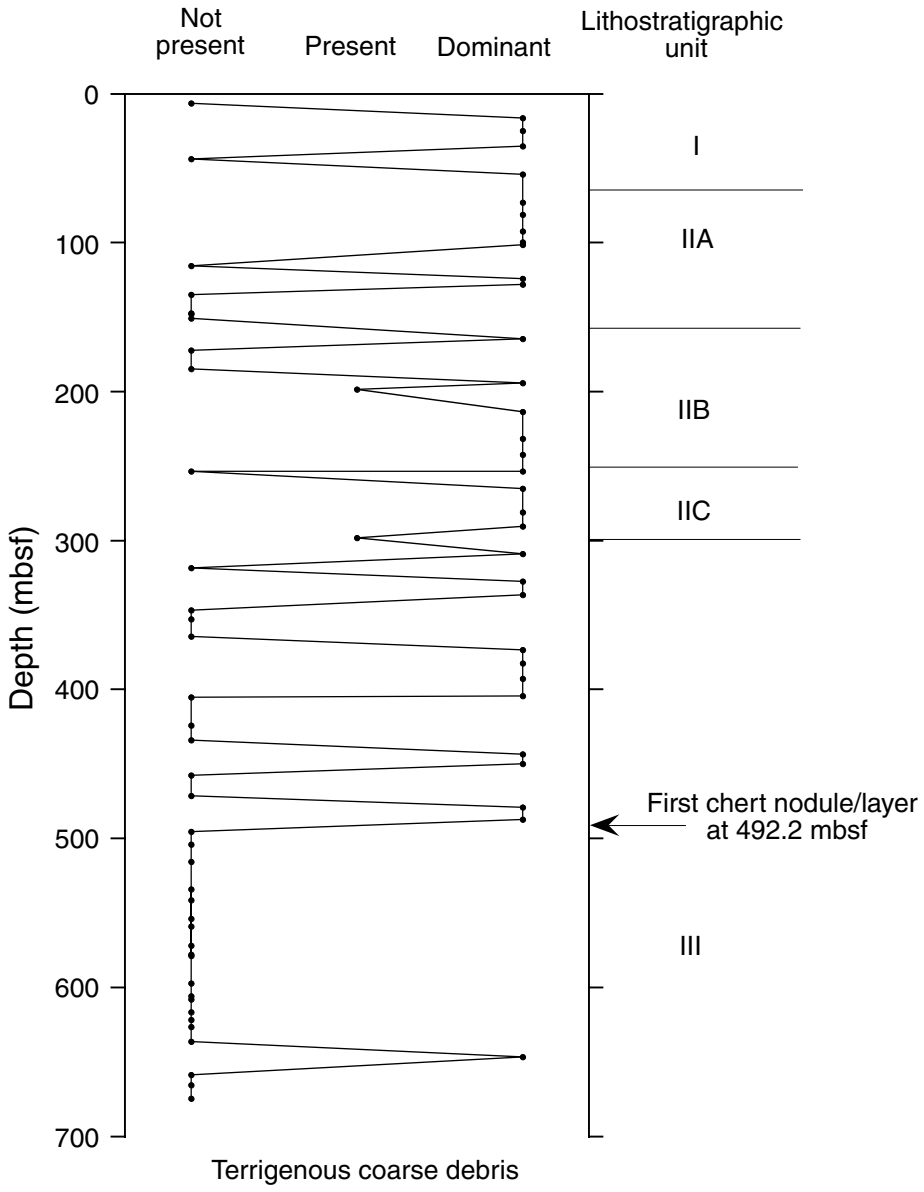

Figure F27. Age-depth plot for the composite section represented by Holes 1165B and 1165C. FO = first occurrence; LO = last occurrence.

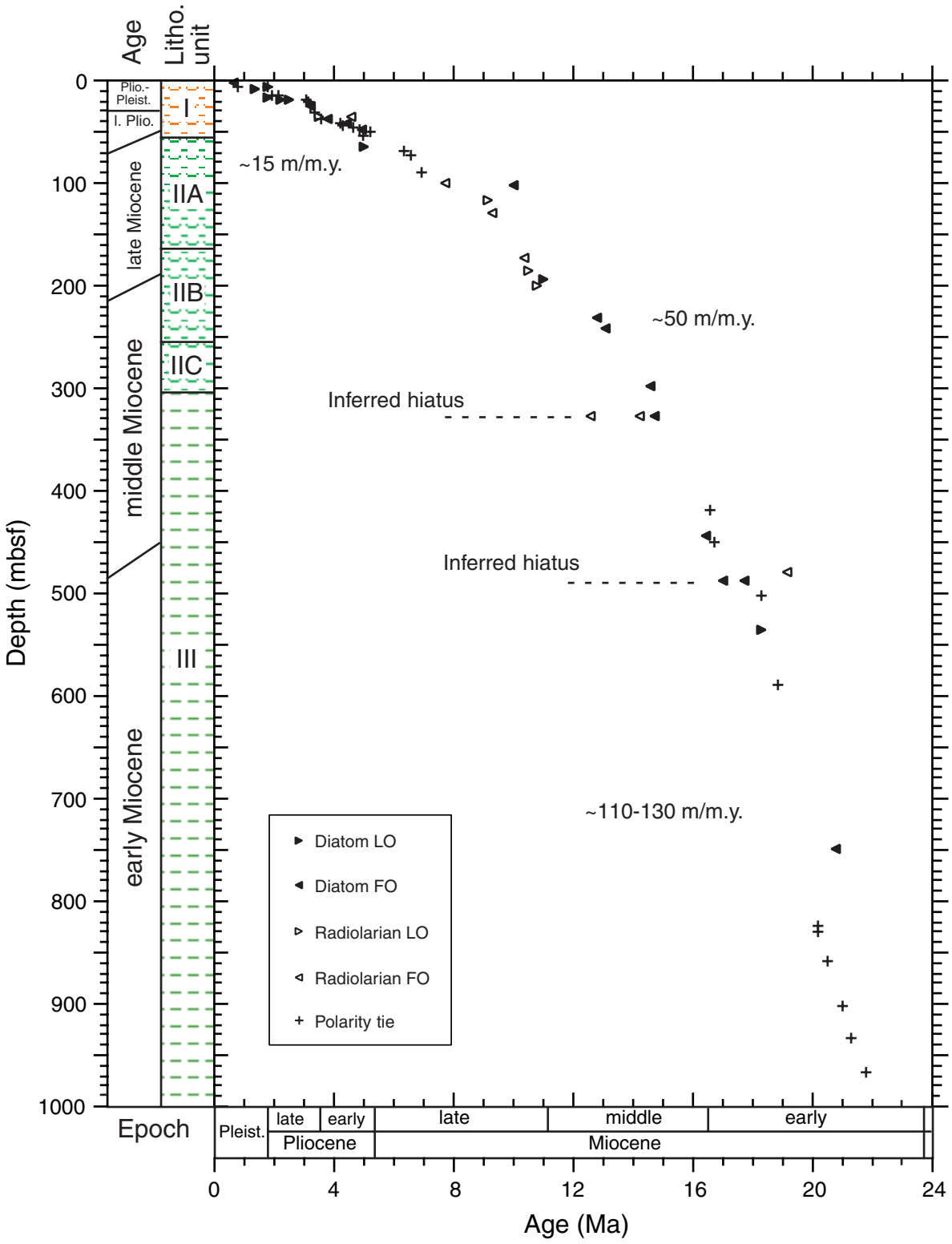

Figure F28. Graphical summary of core recovery, lithologic units, magnetostratigraphy, and biostratigraphic zones for Hole 1165B. (Continued on next page.)

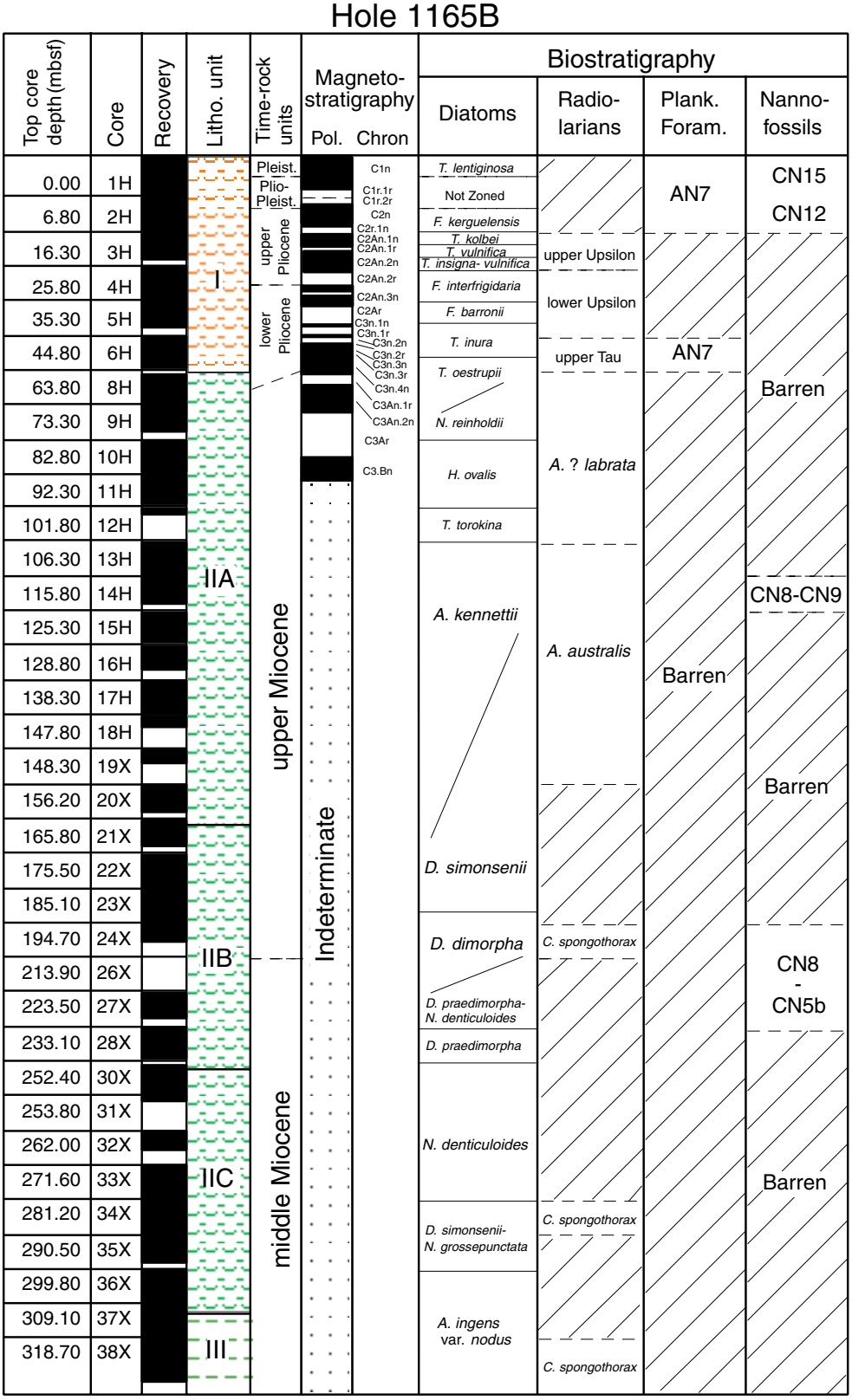

Figure F28 (continued).

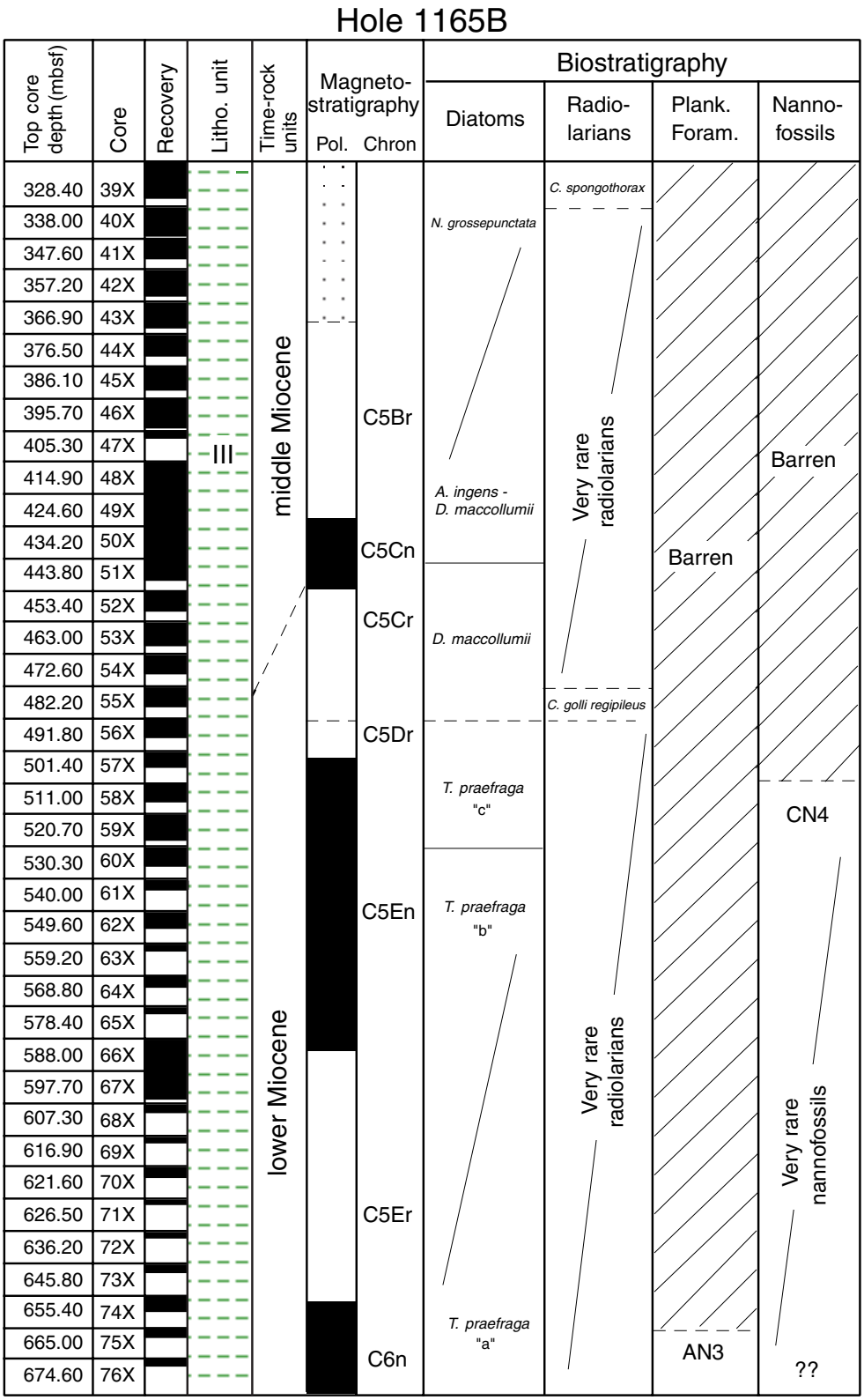

Figure F29. Graphical summary of core recovery, lithologic units, magnetostratigraphy, and biostratigraphic zones for Hole 1165C.

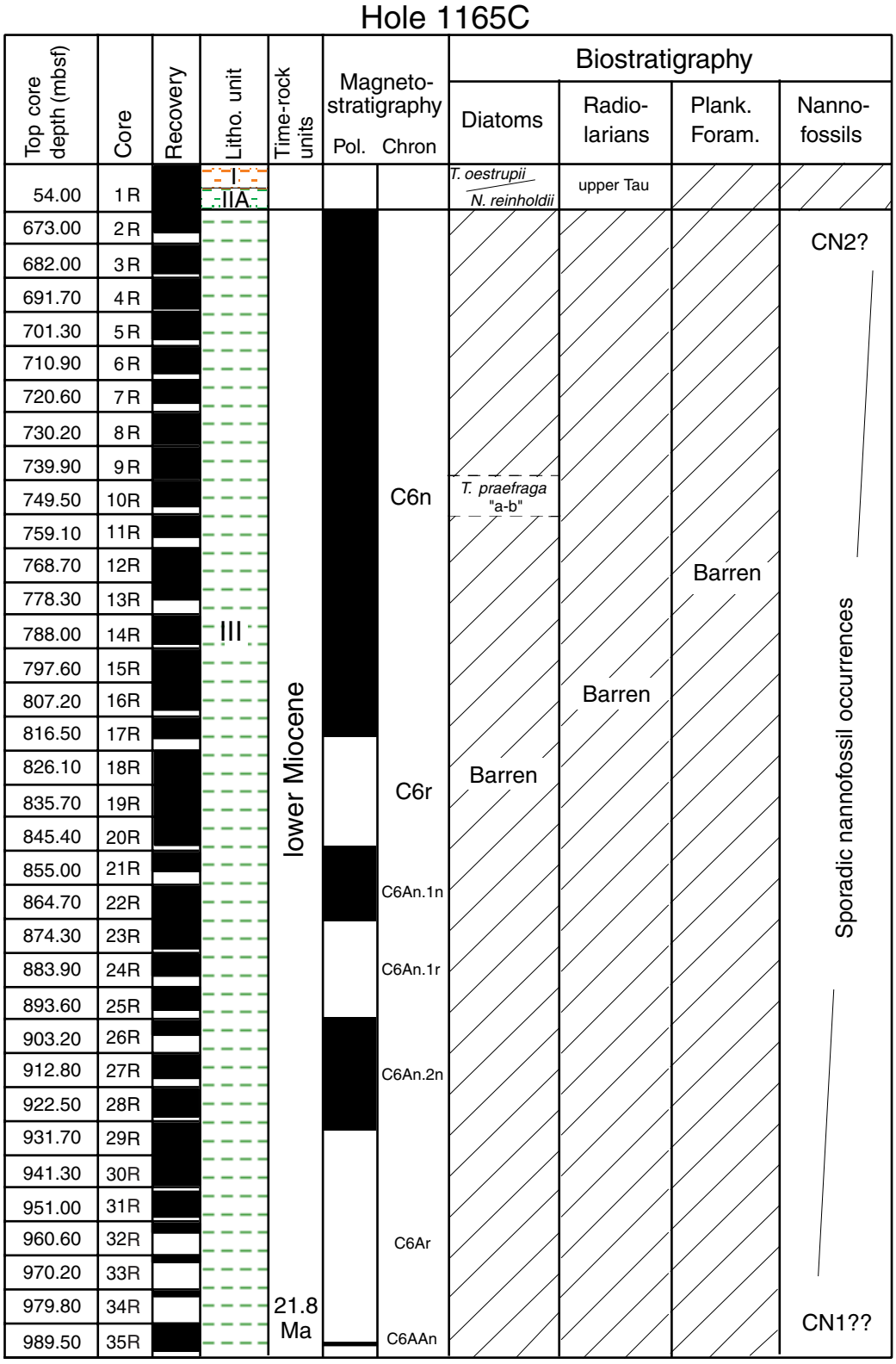

Figure F30. Age-depth model ("envelope") with errors on depth and age denoted by shaded boxes, Site 1165. FO = first occurrence; LO = last occurrence; and PM = paleomagnetic.

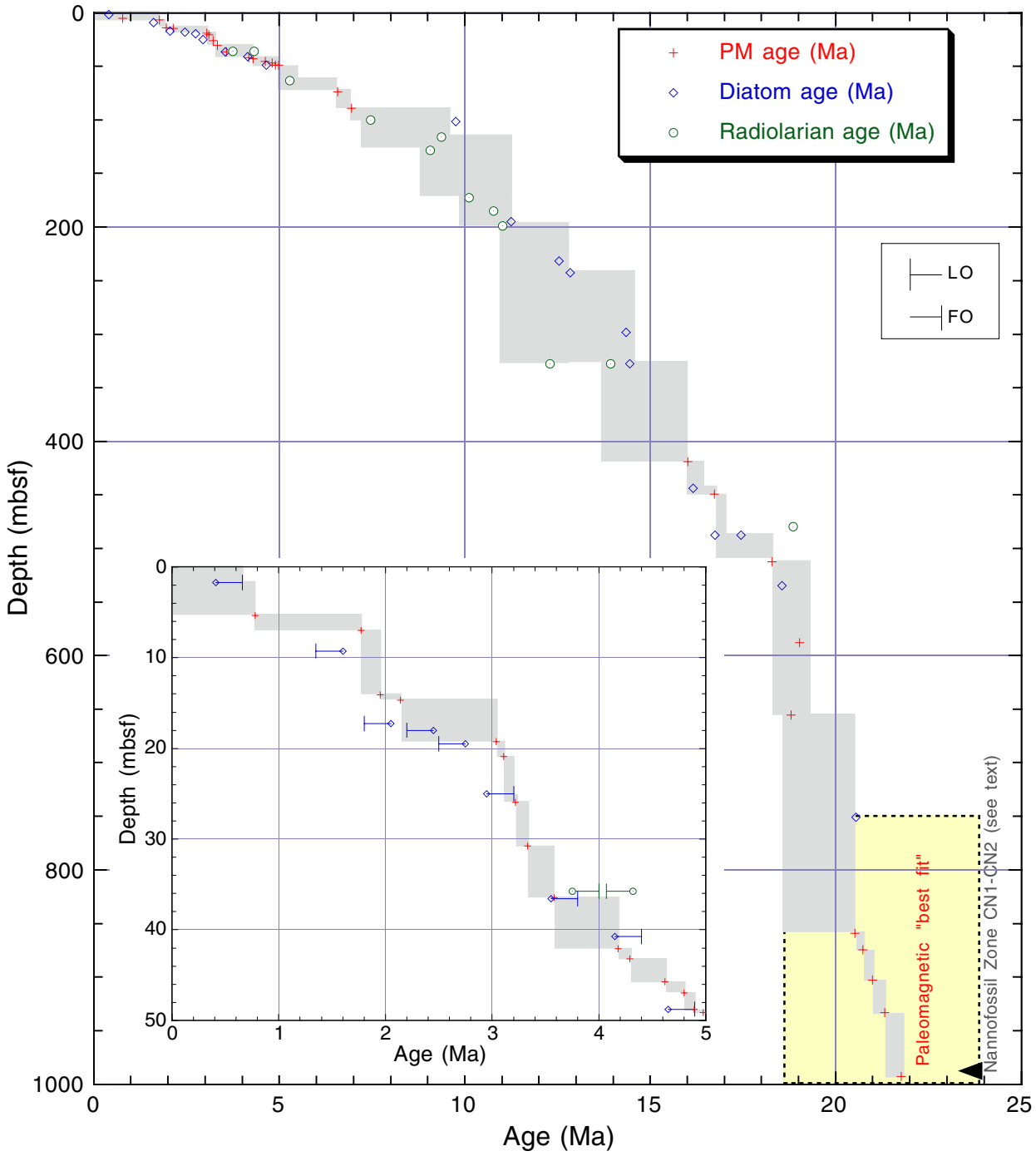

Figure F31. Downcore variation of concentration-dependent parameters (k, ARM, and IRM) at Site 1165. The shaded area represents the intervals (including transitional) between 94 and 362 mbsf that are depleted in magnetic minerals. IRM = isothermal remanent magnetization; ARM = anhysteretic remanent magnetization; and LF = low-field magnetic susceptibility.

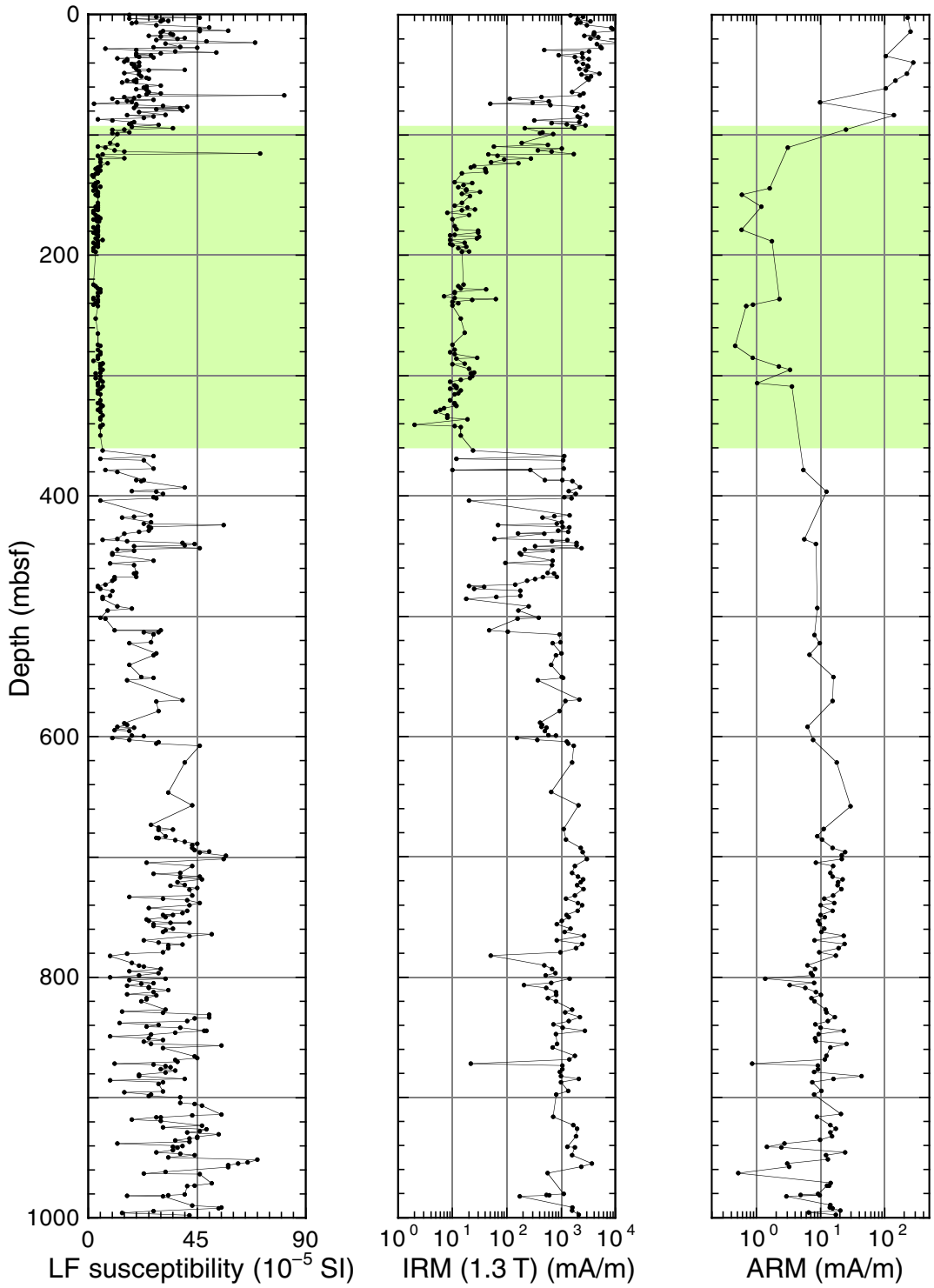

Figure F32. Thermal demagnetization of a composite three-axis IRM (Lowrie, 1990) for two representative samples from (**A**) 0.59 mbsf, which is dominated by magnetite, and (**B**) 401.95 mbsf, which contains evidence of a magnetic mineral (probably an iron sulfide) with thermal unblocking between 320° and 350°C.

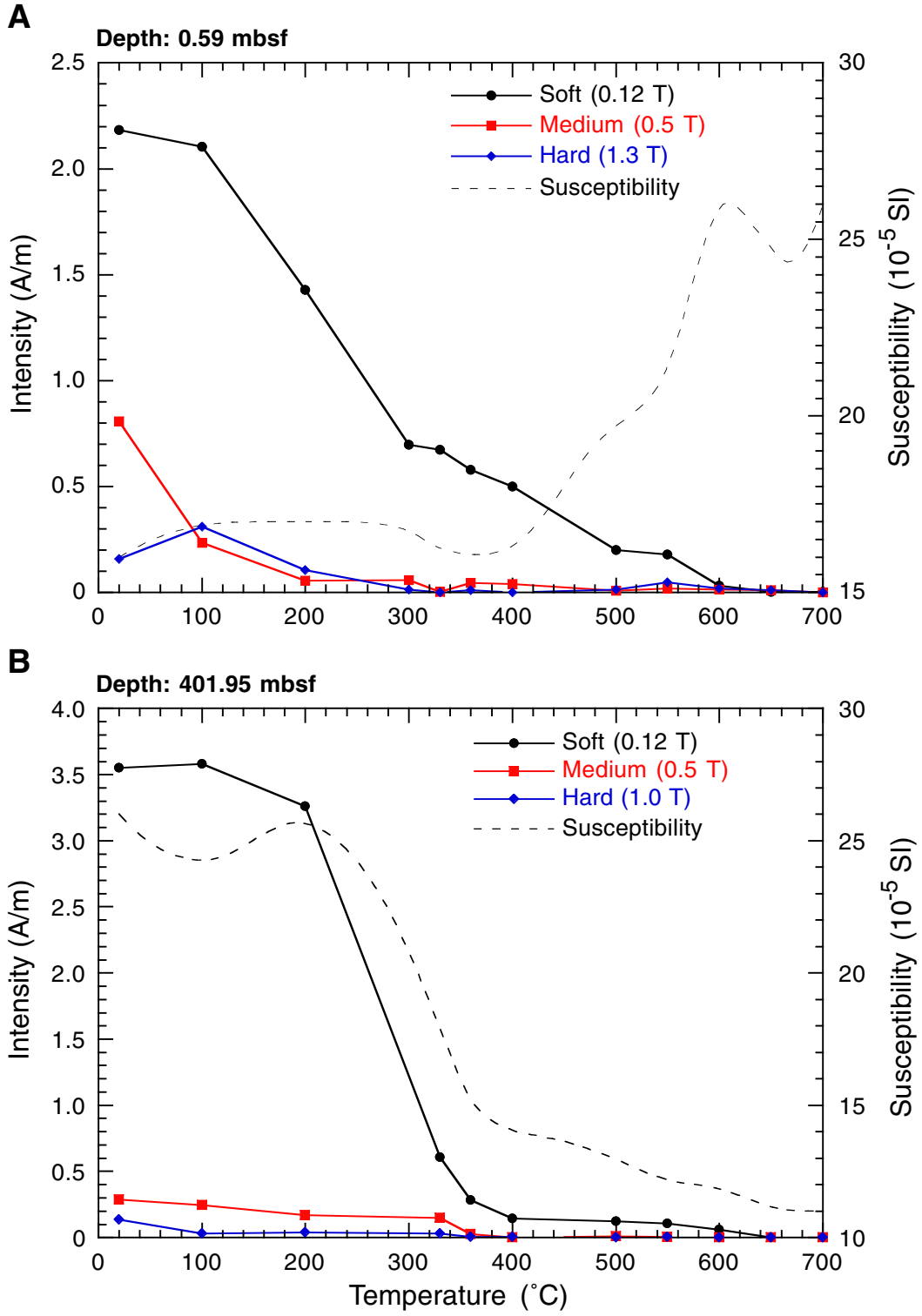

Figure F33. Plot of IRM acquisition and DC demagnetization of seven representative samples. Some samples have low coercivity (B_{cr} = <50 mT) and saturate rapidly (at ~300 mT), whereas other samples have high coercivity (B_{cr} = 60–100 mT) and saturate above 300 mT, which indicates the presence of significant amounts of high-coercivity phases.

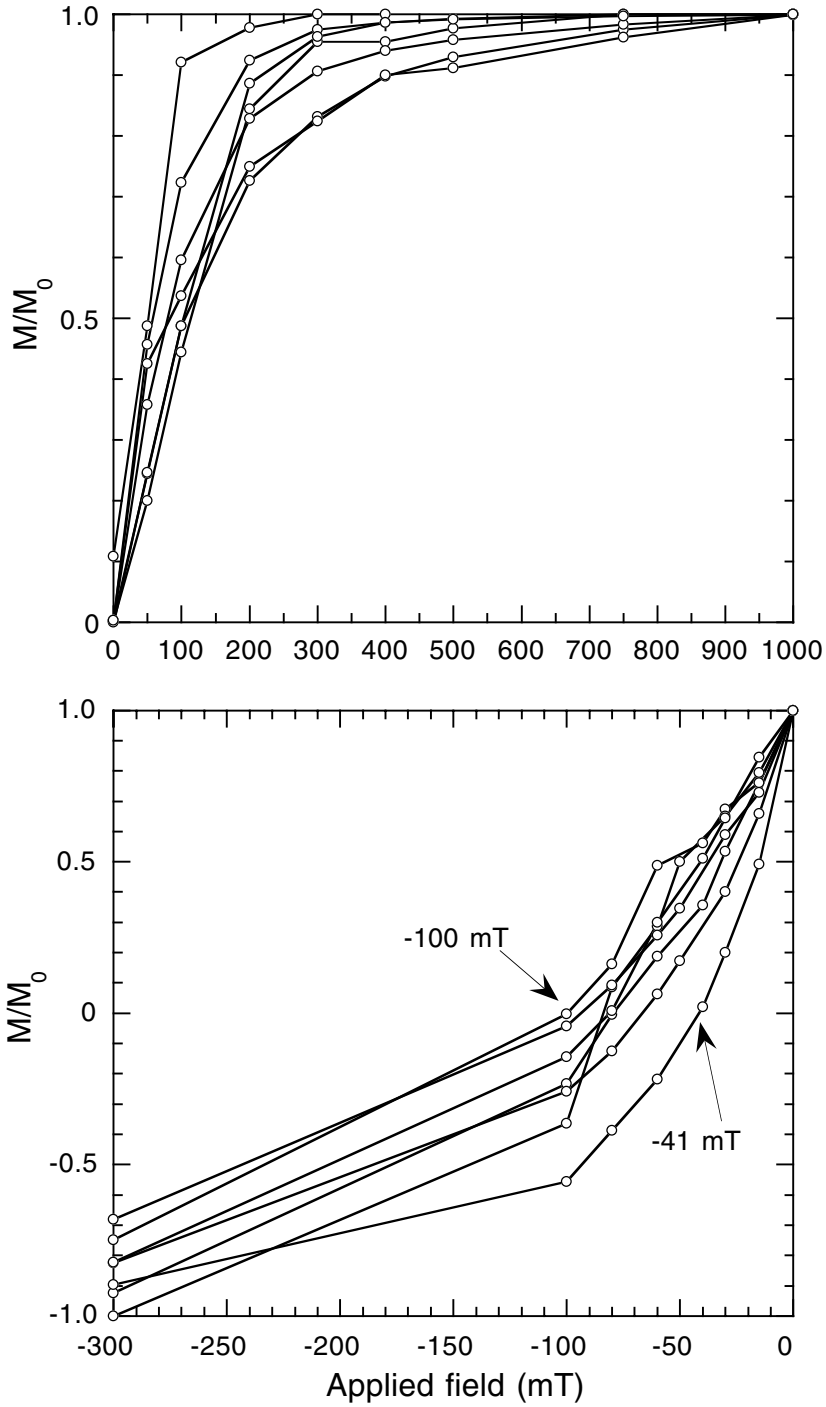

Figure F34. Inclination record for the composite section of Holes 1165B and 1165C (0–999.1 mbsf) after demagnetization at 20–30 mT. The inclinations from split-core measurements (solid circles) are compared to inclinations from stepwise-demagnetized discrete samples (solid squares). Inclinations for discrete samples were determined by linear regression fits to multiple demagnetization steps. The shaded area represents the interval (94–362 mbsf) depleted in magnetic minerals.

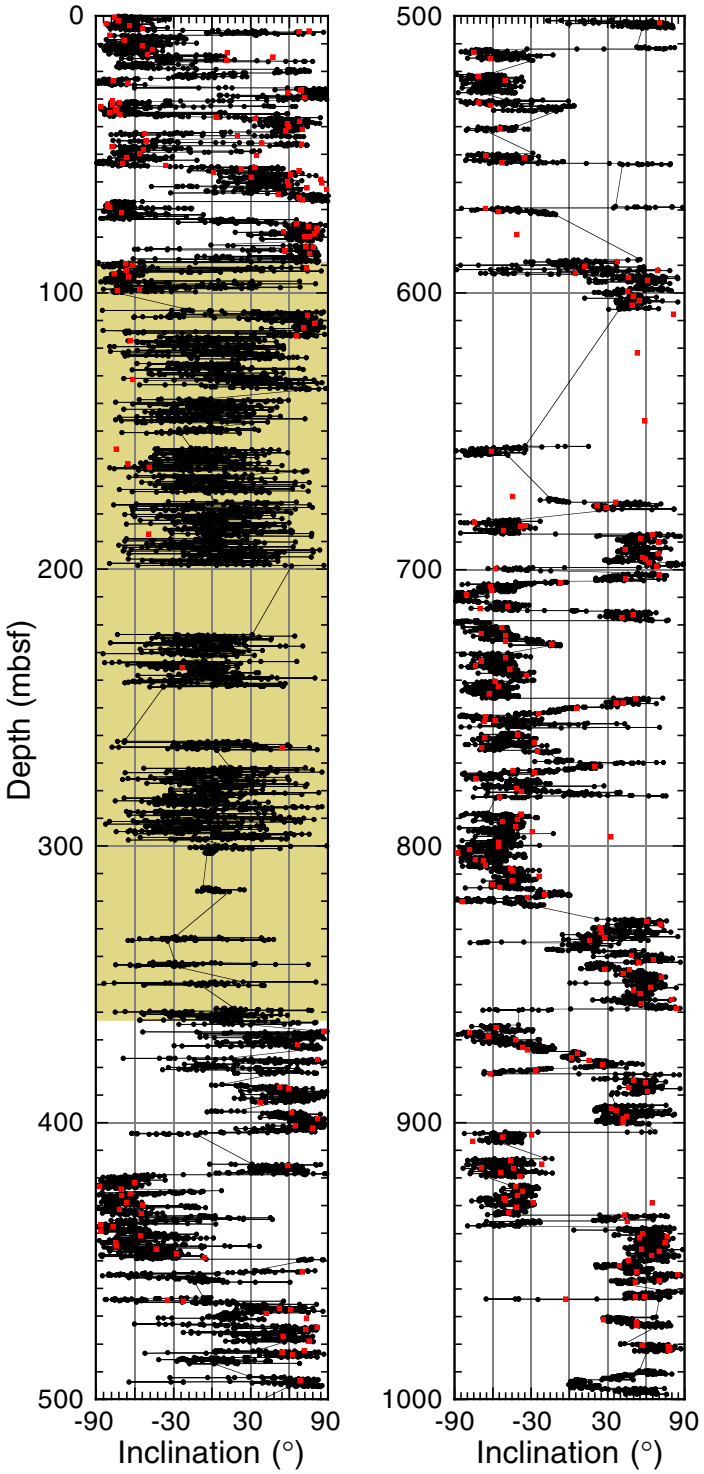

Figure F35. Vector component diagram (with normalized intensity decay plots) of demagnetization (AF) behavior of representative samples from Site 1165. Open symbols = projections onto the vertical plane; closed symbols = projections onto the horizontal plane. The dashed lines represent linear regression fits that indicate the characteristic remanence component for each sample. The core is not azimuthally oriented; therefore, declination values are not meaningful. NRM = natural remanent magnetization.

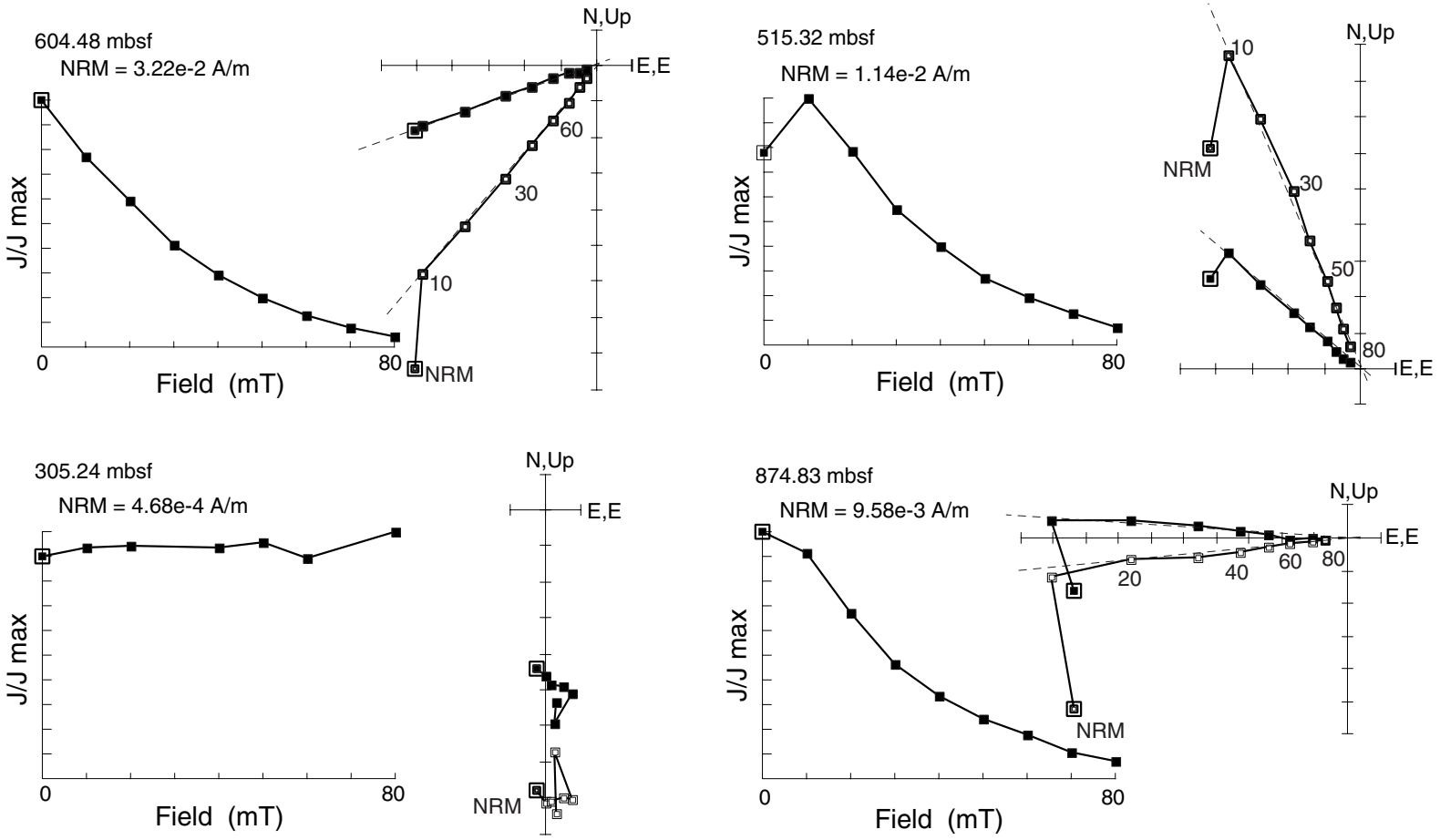

Figure F36. Magnetostratigraphic record from Site 1165 (0–50 mbsf). Plot of NRM intensity and inclination after demagnetization at 20–30 mT. The inclinations obtained from split cores for the top 50 mbsf are compared to inclinations from stepwise-demagnetized discrete samples (solid squares). Inclinations for discrete samples were determined by linear regression fits to multiple demagnetization steps. Polarity is shown on the log to the right. Chron ages for polarity reversal boundaries are from Berggren et al. (1995).

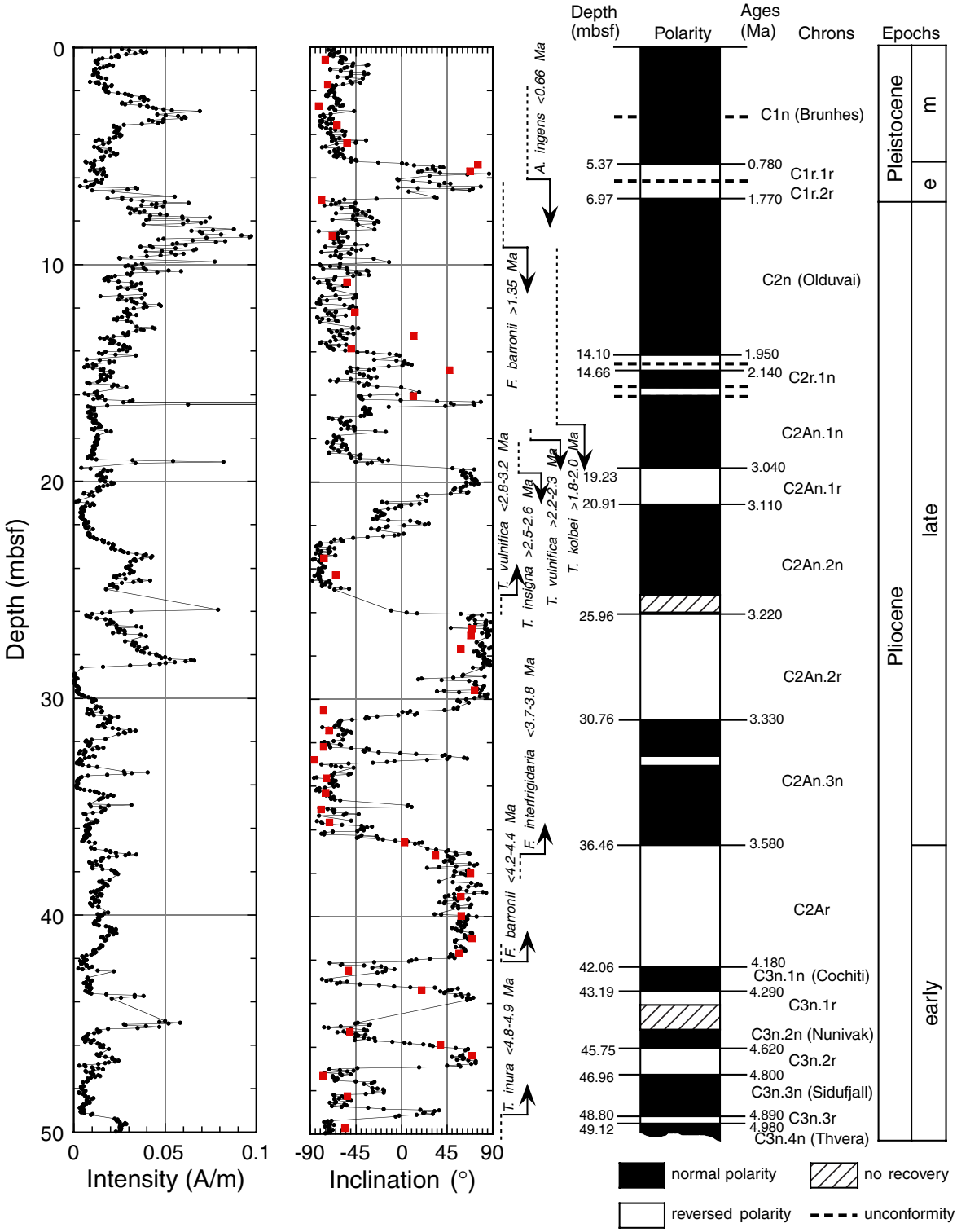

Figure F37. Magnetostratigraphic record from Site 1165 (50–100 mbsf). Plot of NRM intensity and inclination after demagnetization at 20–30 mT. The inclinations obtained from split cores are compared to inclinations from stepwise-demagnetized discrete samples (solid squares) Inclinations for discrete samples were determined by linear regression fits to multiple demagnetization steps. Polarity is shown on the log to the right. Chron ages for polarity reversal boundaries are from Cande and Kent (1992, 1995) and Berggren et al. (1995).

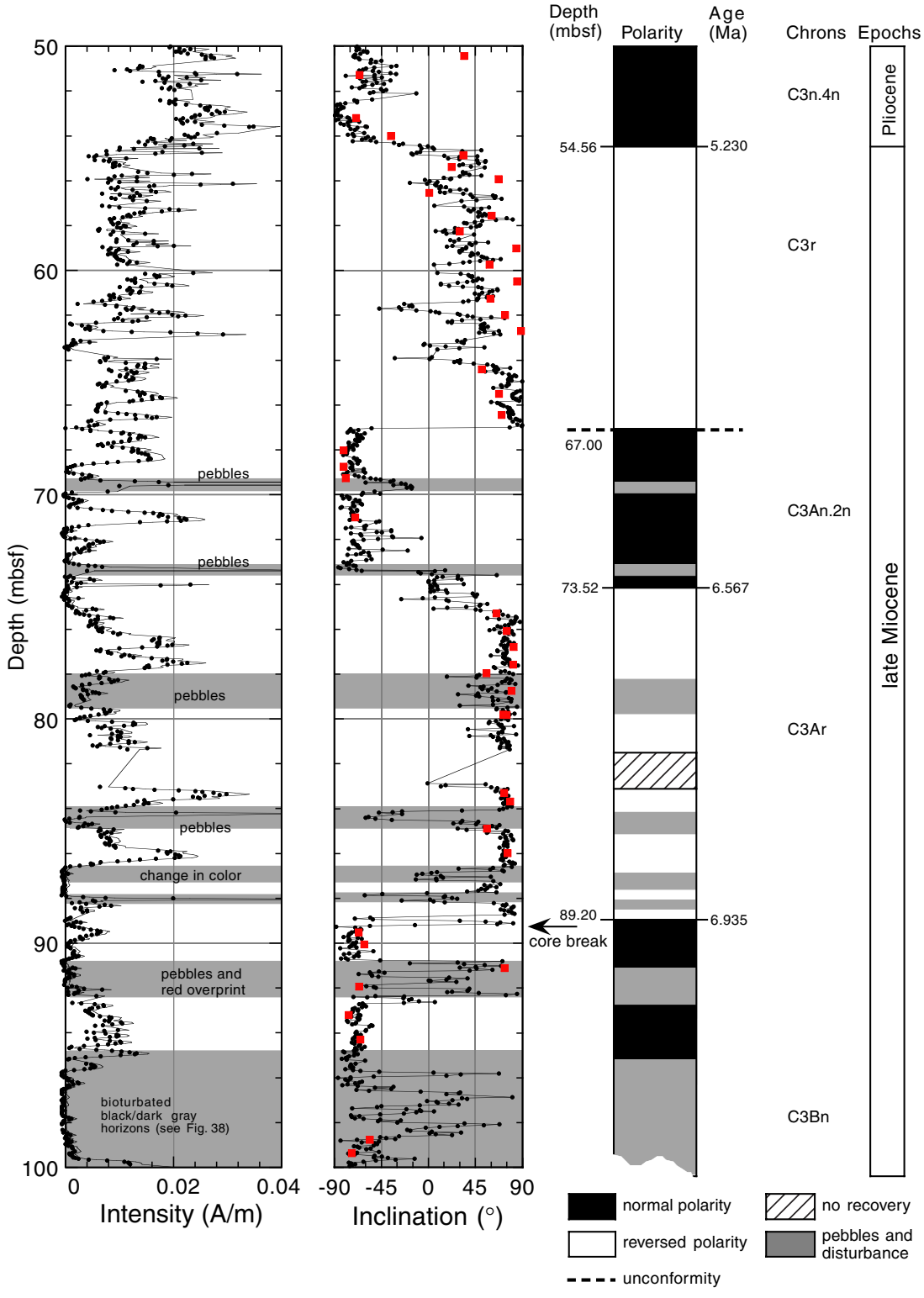

Figure F38. Plot showing the coincidence between the intensity of remanence and polarity changes (after demagnetization to peak AF of 20 mT) with the alternation between black/dark and gray horizons in Core 188-1165B-11H.

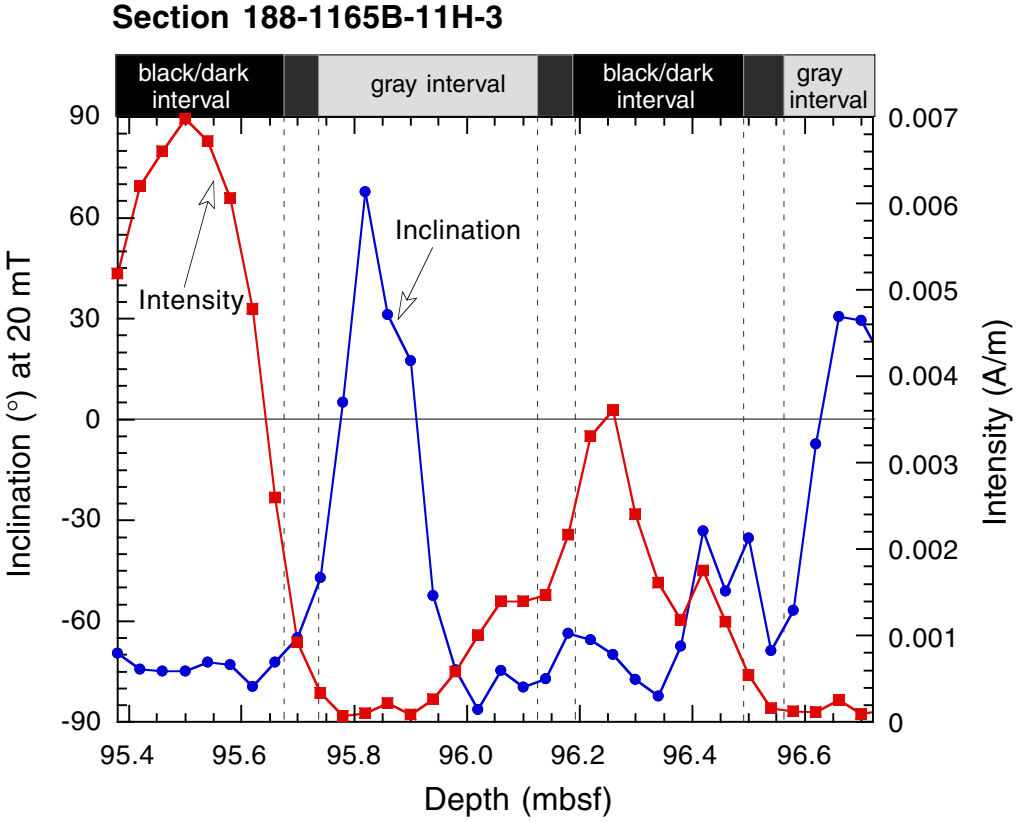

Figure F39. Magnetostratigraphic record from Site 1165 (350–650 mbsf). Plot of NRM intensity and inclination after demagnetization at 20–30 mT. The inclinations obtained from split cores are compared to inclinations from stepwise-demagnetized discrete samples (solid circles). Inclinations for discrete samples were determined by linear regression fits to multiple demagnetization steps. Polarity is shown on the log to the right. Chron ages for polarity reversal boundaries are from Berggren et al. (1995). Striped intervals indicate no recovery.

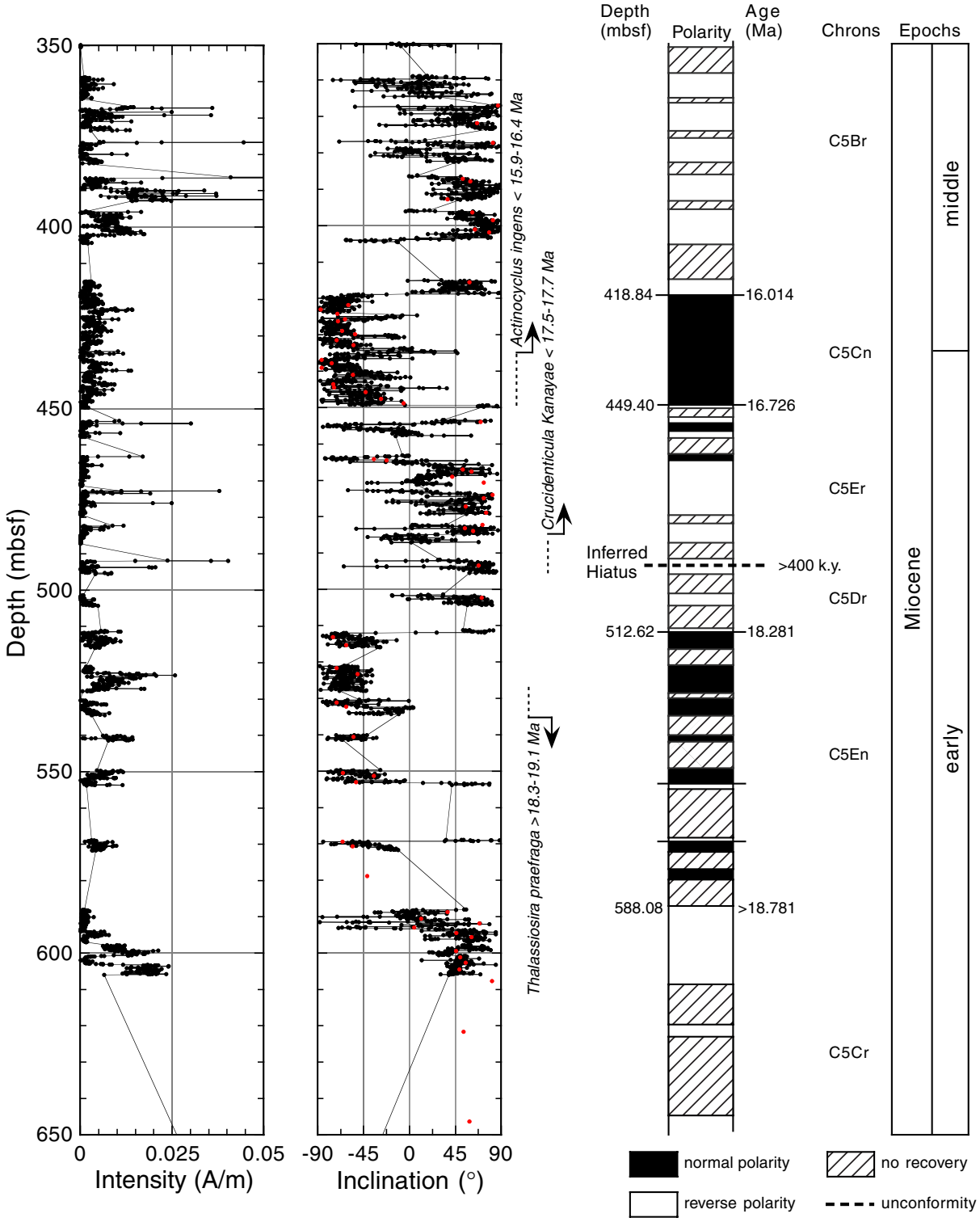

Figure F40. Magnetostratigraphic record from Site 1165 (500.0–999.1 mbsf). Plot of NRM intensity and inclination after demagnetization at 20–30 mT. The inclinations obtained from split cores are compared to inclinations from stepwise-demagnetized discrete samples (solid circles). Inclinations for discrete samples were determined by linear regression fits to multiple demagnetization steps. Polarity is shown on the log to the right. Chron ages for polarity reversal boundaries are from Cande and Kent (1992, 1995) and Berggren et al. (1995).

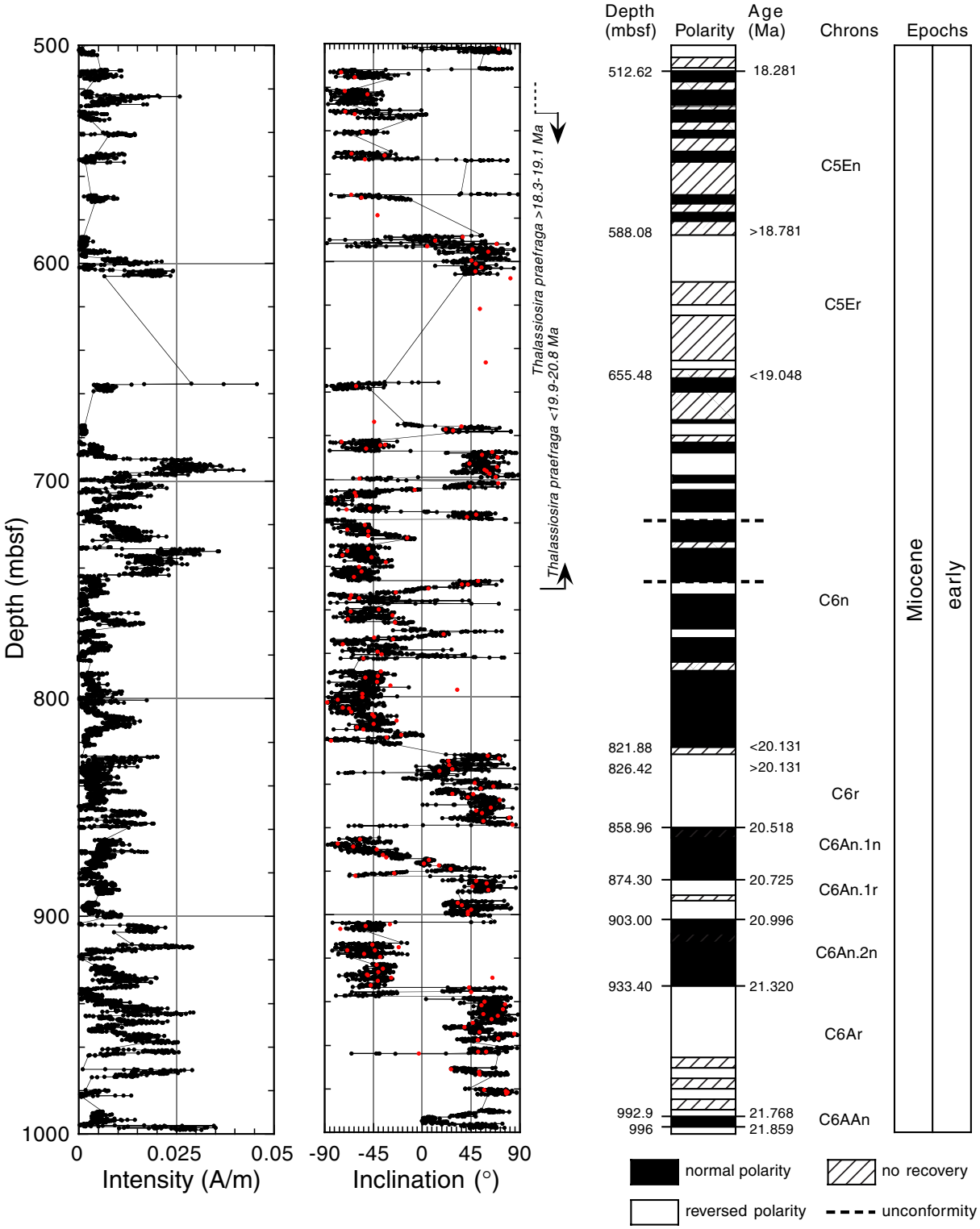

Figure F41. The relative paleointensity record (susceptibility normalization) for the uppermost 100 m at Site 1165.

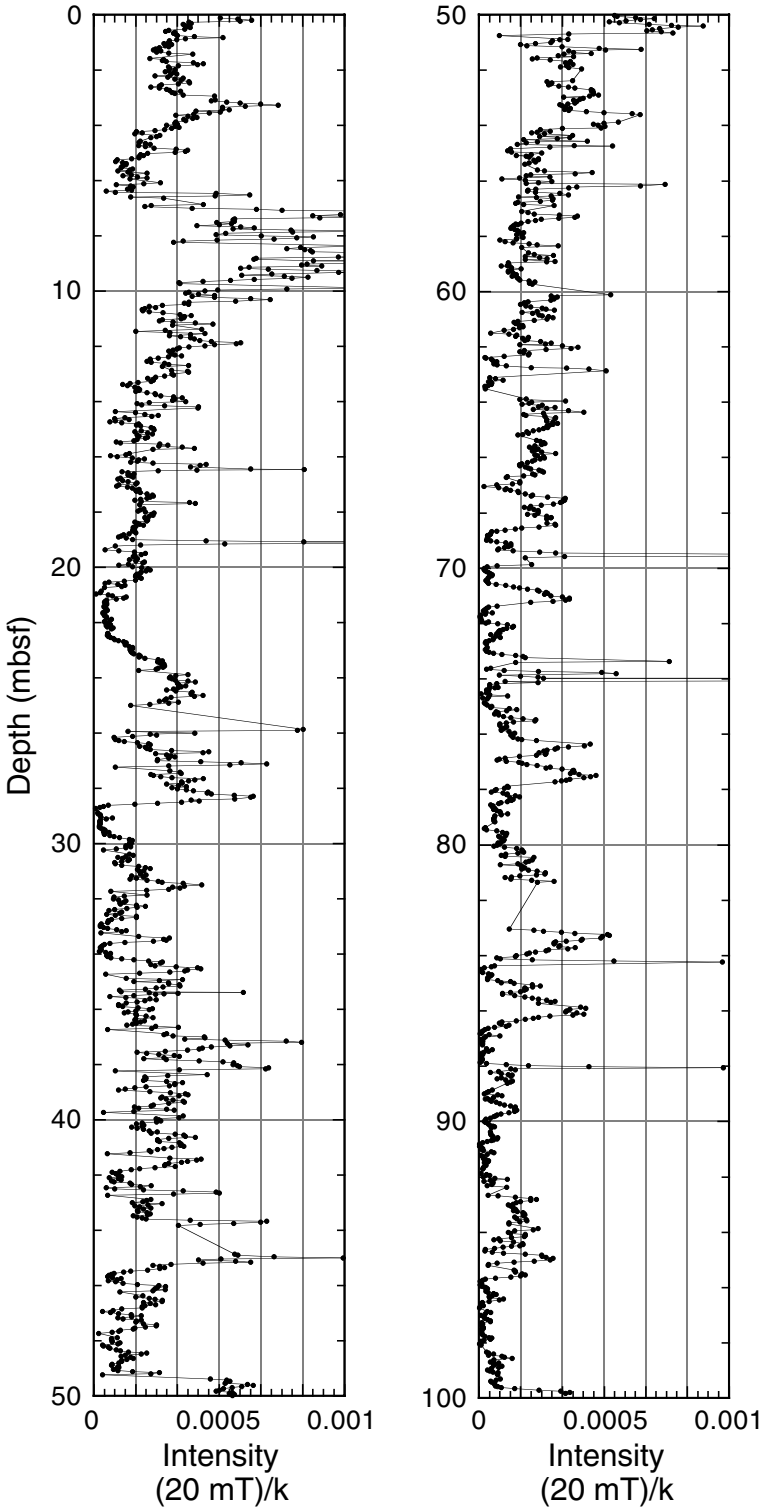

Figure F42. Selected high-resolution interstitial water chemistry profiles vs. depth for chlorinity, sulfate, calcium, strontium, potassium, and lithium. Shaded circles = Hole 1165A; solid circles = Hole 1165B; and open circles = Hole 1165C. Data are reported in Table T7, p. 179.

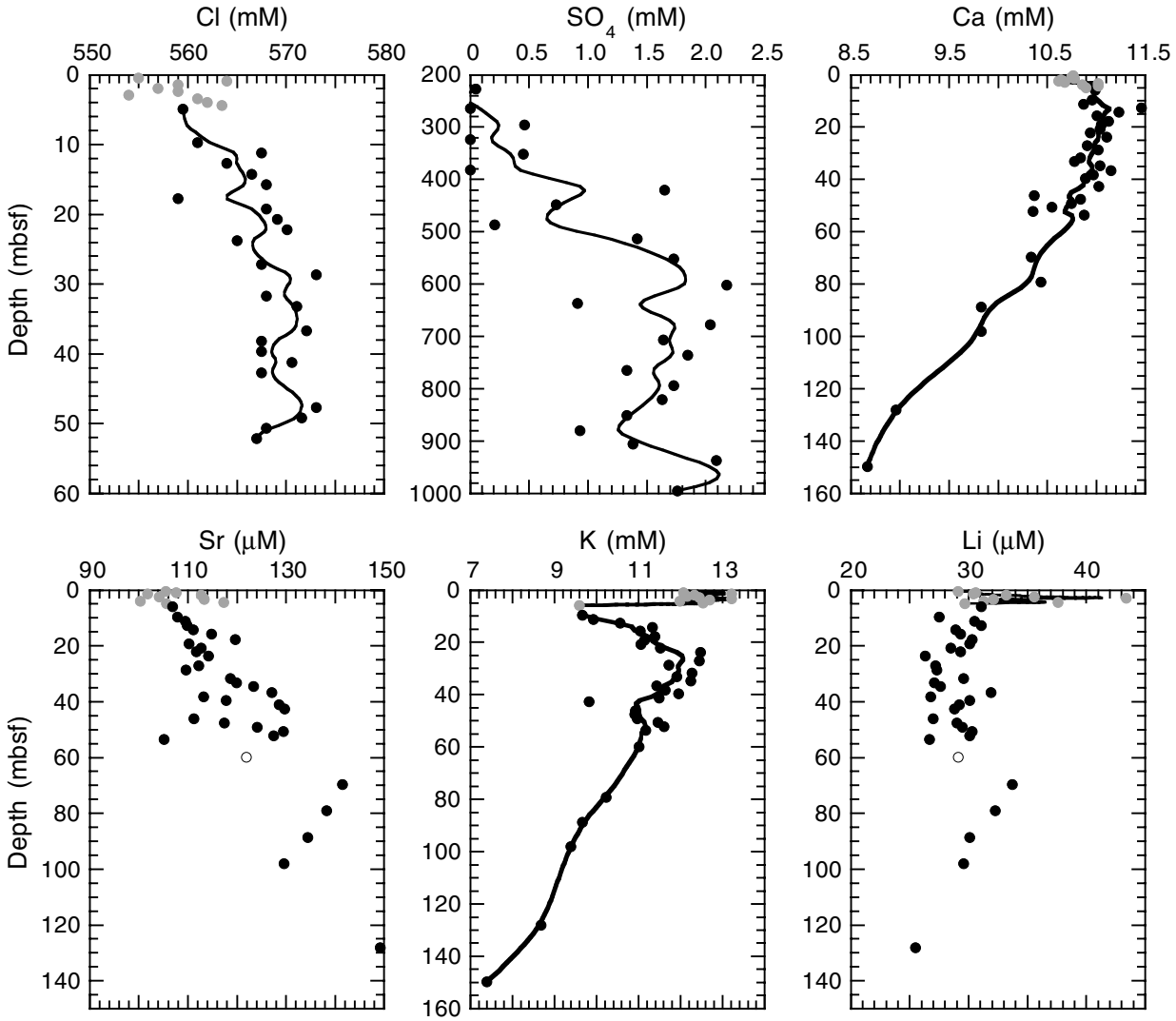

Figure F43. Full interstitial water chemistry profiles vs. depth for salinity, pH, alkalinity, chlorinity (solid line = titration analyses; dashed line = ion chromatography analyses), sulfate, ammonium, phosphate, silica, calcium, magnesium, strontium, potassium, sodium, lithium, and manganese at Site 1165. Shaded circles = Hole 1165A; solid circles = Hole 1165B; and open circles = Hole 1165C. Data are reported in Table T7, p. 179. (Continued on next page.)

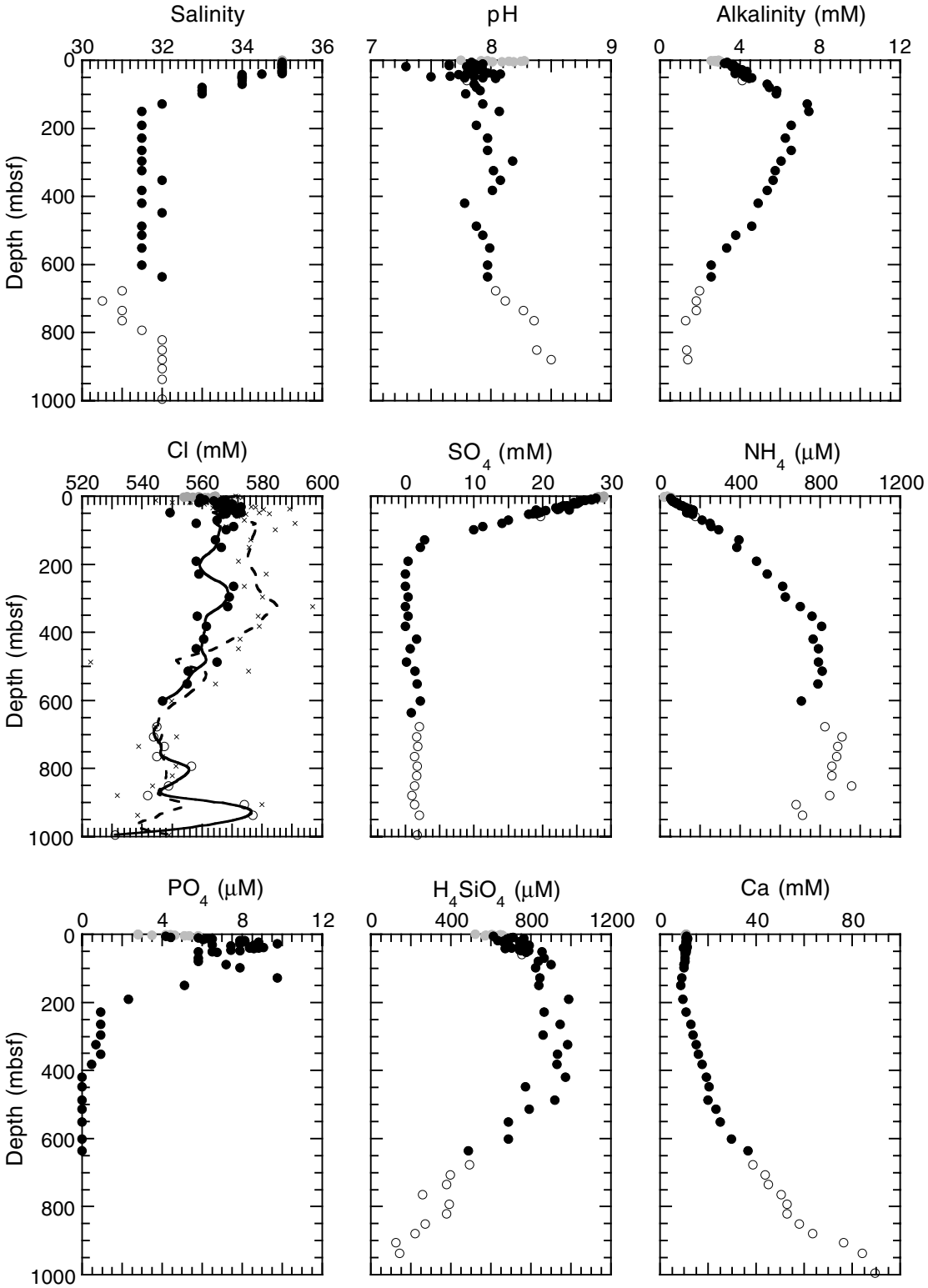

Figure F43 (continued).

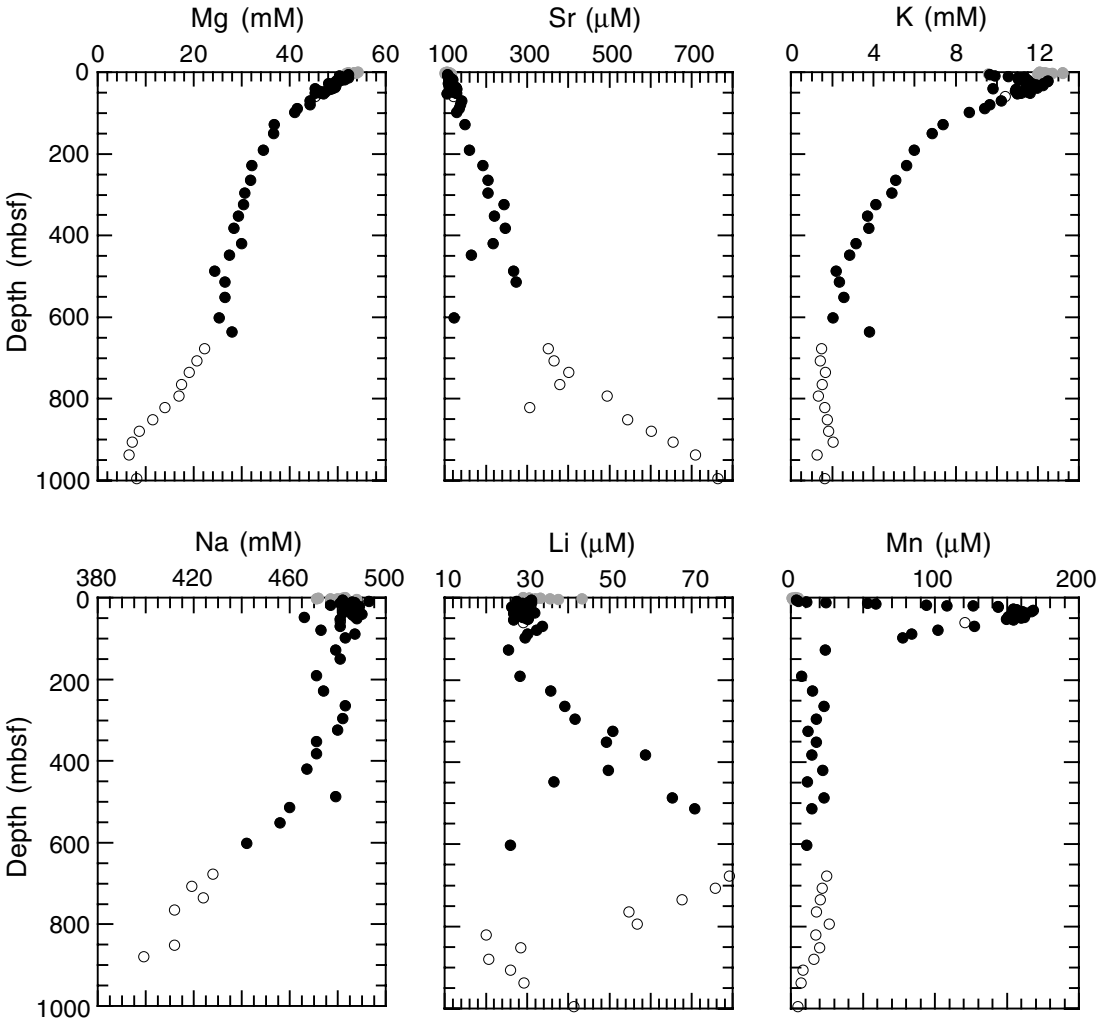

Figure F44. Downhole profiles of dissolved sulfate (shaded circles) and headspace methane (solid circles) for the upper 400 m of Site 1165. The downhole shift from SO_4 reduction to CO_2 reduction is evident at ~150 mbsf. Data are reported in Table T7, p. 179, and Table T8, p. 180.

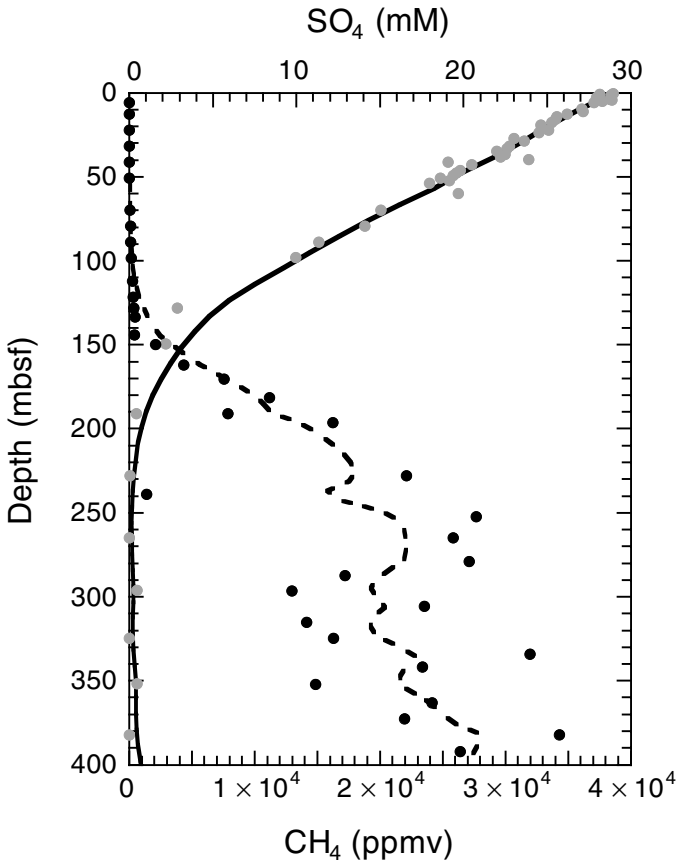

Figure F45. Sulfate vs. alkalinity within the SRZ (0–150 mbsf) at Site 1165. The correlation line shows the theoretical relationship: $1 \times SO_4^{2-} = 2 \times HCO_3^-$ expected if sulfate behaves conservatively. Shaded circles = Hole 1165A; solid circles = Hole 1165B; and open circles = Hole 1165C.

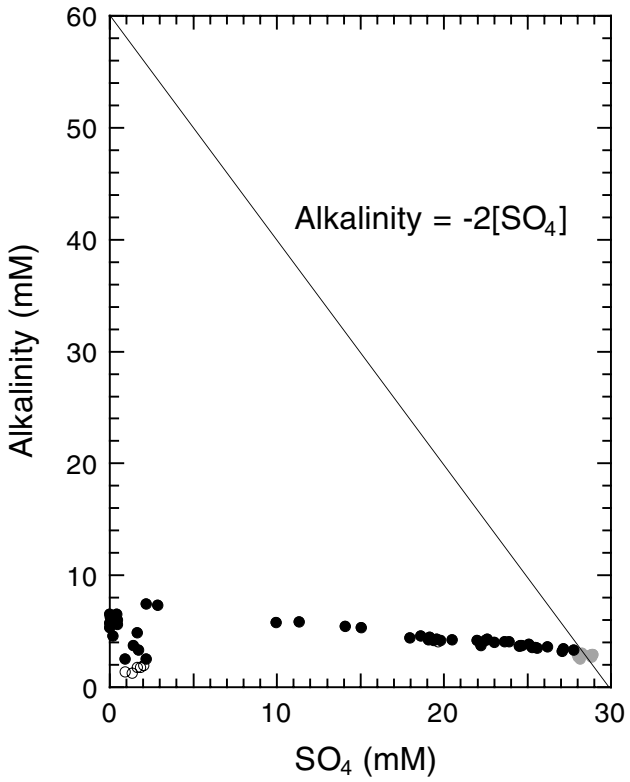

Figure F46. Observed calcium depletion vs. predicted calcium depletion within the SRZ (0–150 mbsf) at Site 1165, assuming that all of the alkalinity deficiency shown in Fig. F45, p. 128, is lost as $CaCO_3$ precipitation.

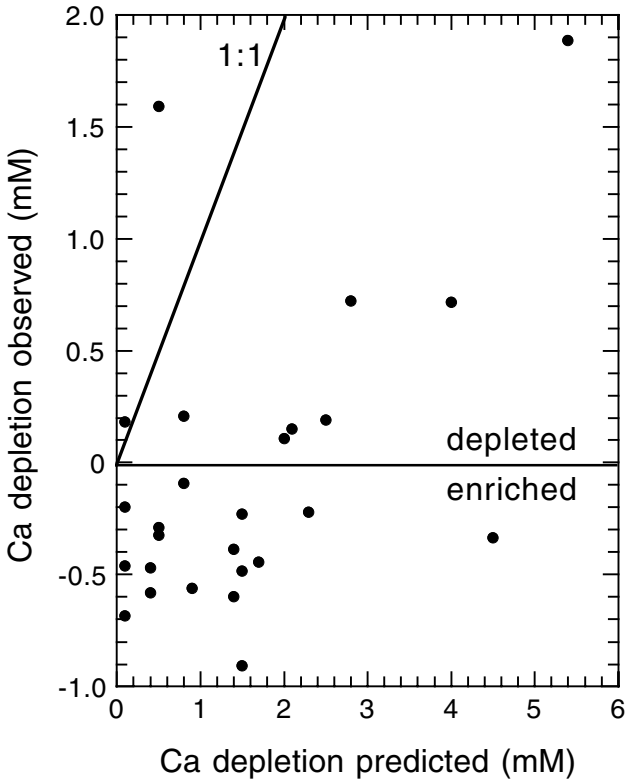

Figure F47. Calcium vs. magnesium at Site 1165. Shaded circles = Hole 1165A; solid circles = Hole 1165B; and open circles = 1165C.

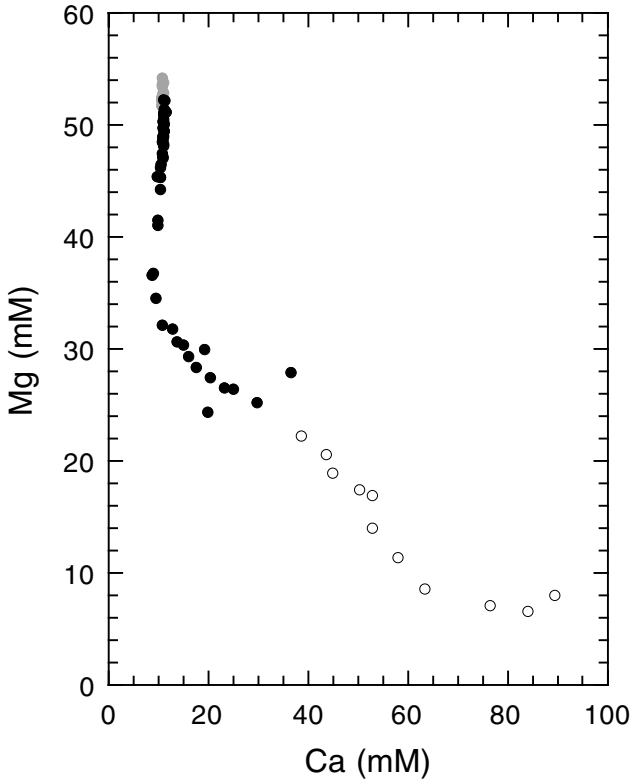

Figure F48. Interstitial water potassium concentrations vs. semiquantitative K-feldspar distribution from XRD analyses. Solid circles = dissolved potassium in interstitial waters; open circles = K-feldspar counts.

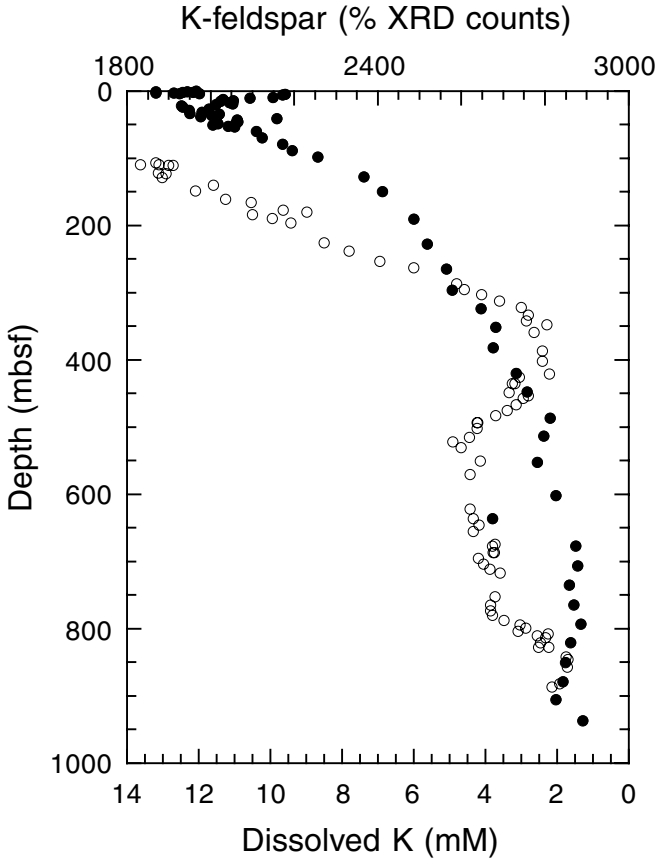

Figure F49. C_1, C_2, and C_3 vs. depth for Holes 1165B (open symbols) and 1165C (solid symbols). Circles = C_1; squares = C_2; and triangles = C_3.

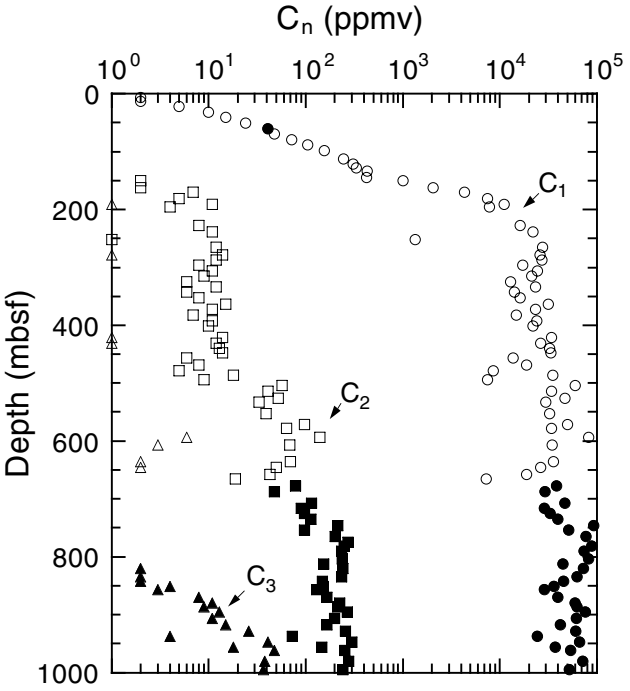

Figure F50. C_1/C_2 values of headspace gas vs. depth for Holes 1165B (open symbols) and 1165C (solid symbols).

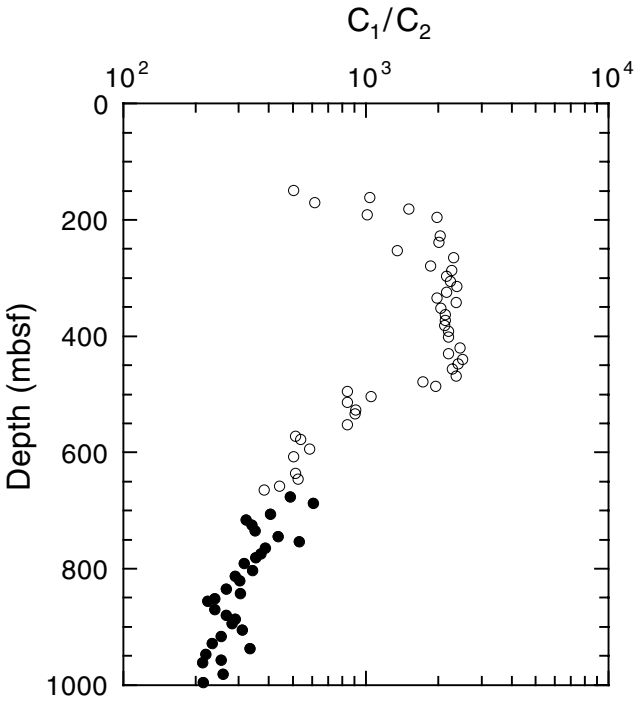

Figure F51. C_1/C_2 values of headspace gas vs. sediment temperature for Holes 1165B (open symbols) and 1165C (solid symbols).

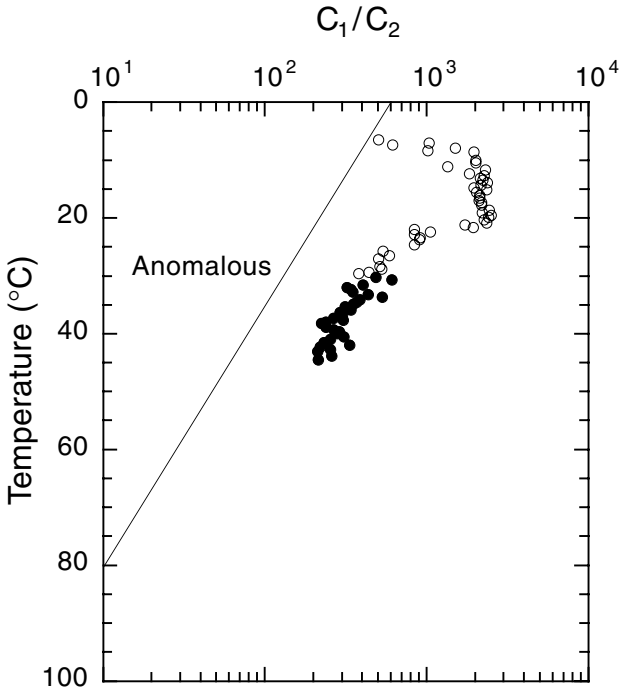

Figure F52. Recalculated concentration of methane (CH_4) dissolved in pore water for Holes 1165B (open symbols) and 1165C (solid symbols).

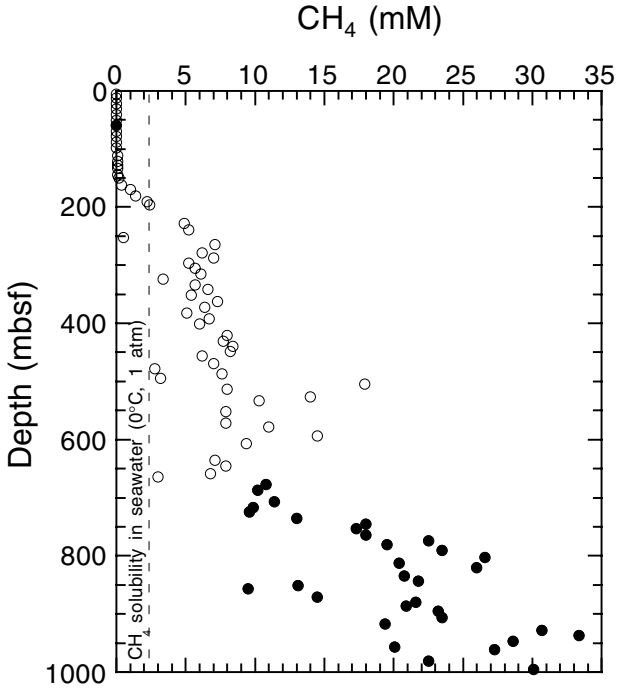

Figure F53. Weight percent of (**A**) inorganic carbon (carbonate carbon) and (**B**) organic carbon in sediments from Holes 1165B (open symbols) and 1165C (solid symbols).

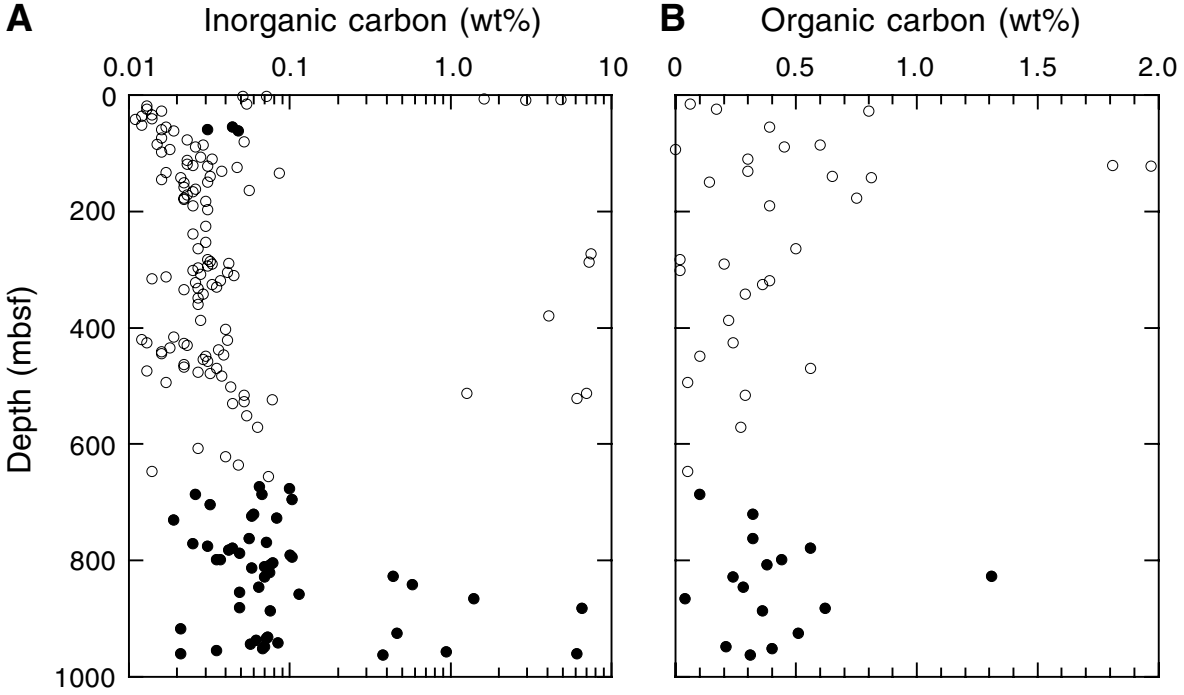

Figure F54. Example from Core 188-1165B-14H showing color cycles (i.e., dark to light couplet). There are large-scale cycles—here ~1.5 m—and small-scale cycles that are shorter and generally lie in the darker areas of the core. The curve on the right shows lightness values measured by the spectrophotometer.

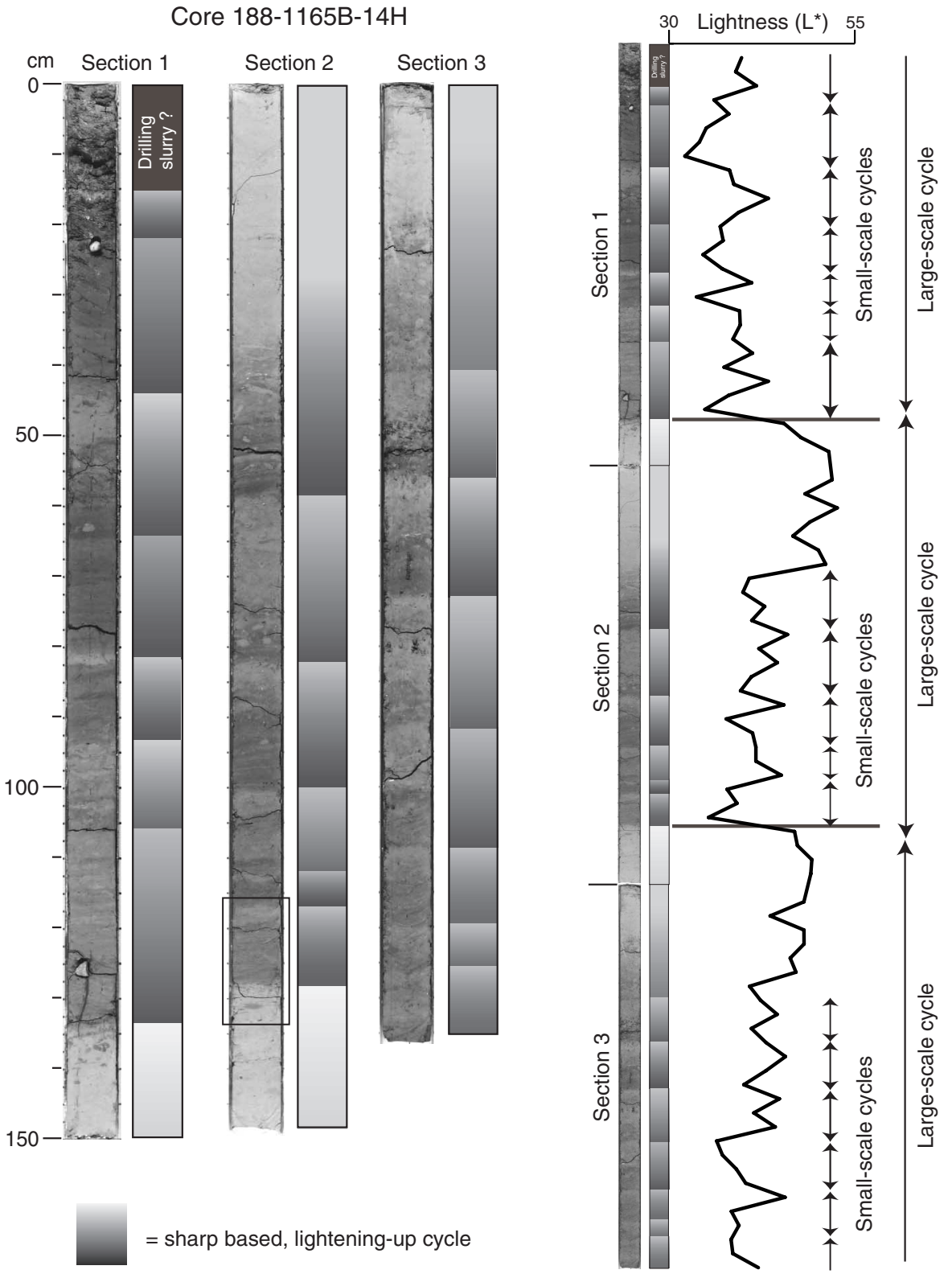

Figure F55. Example from Section 188-1165B-14H-2 of the boundary of a large-scale cycle (i.e., light to dark facies). The boundary has some bioturbation, and a small-scale cycle lies directly above the large-cycle boundary. See Figure **F54,** p. 137, for the location.

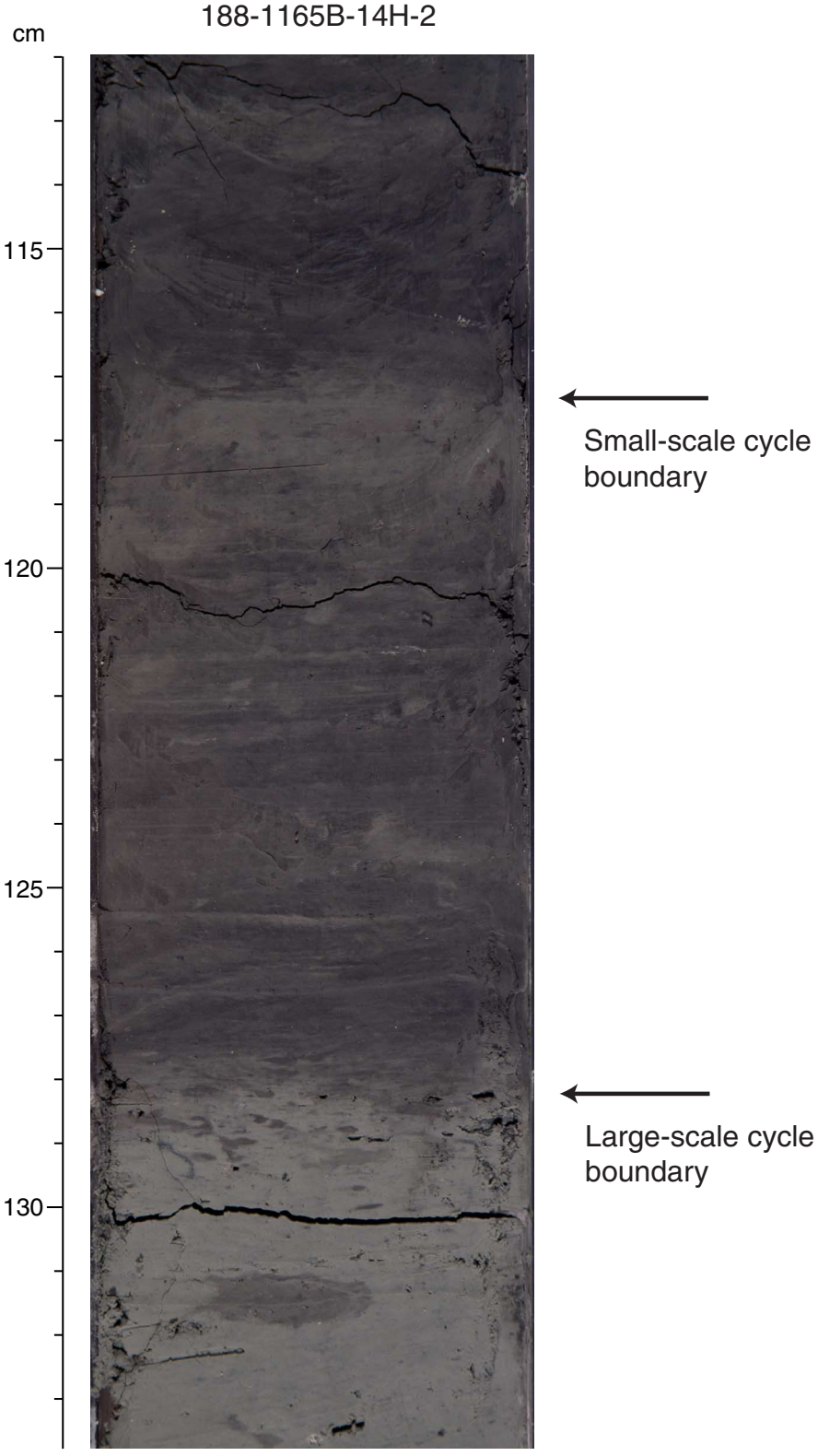

Figure F56. A. Lightness (L*) and GRA bulk density for the interval between 83 and 100 mbsf. The compaction trend has been removed from the density curve. **B.** Cross spectra (Blackman-Tuckey method) of the L* and density measurements calculated in the depth domain. CI = confidence interval.

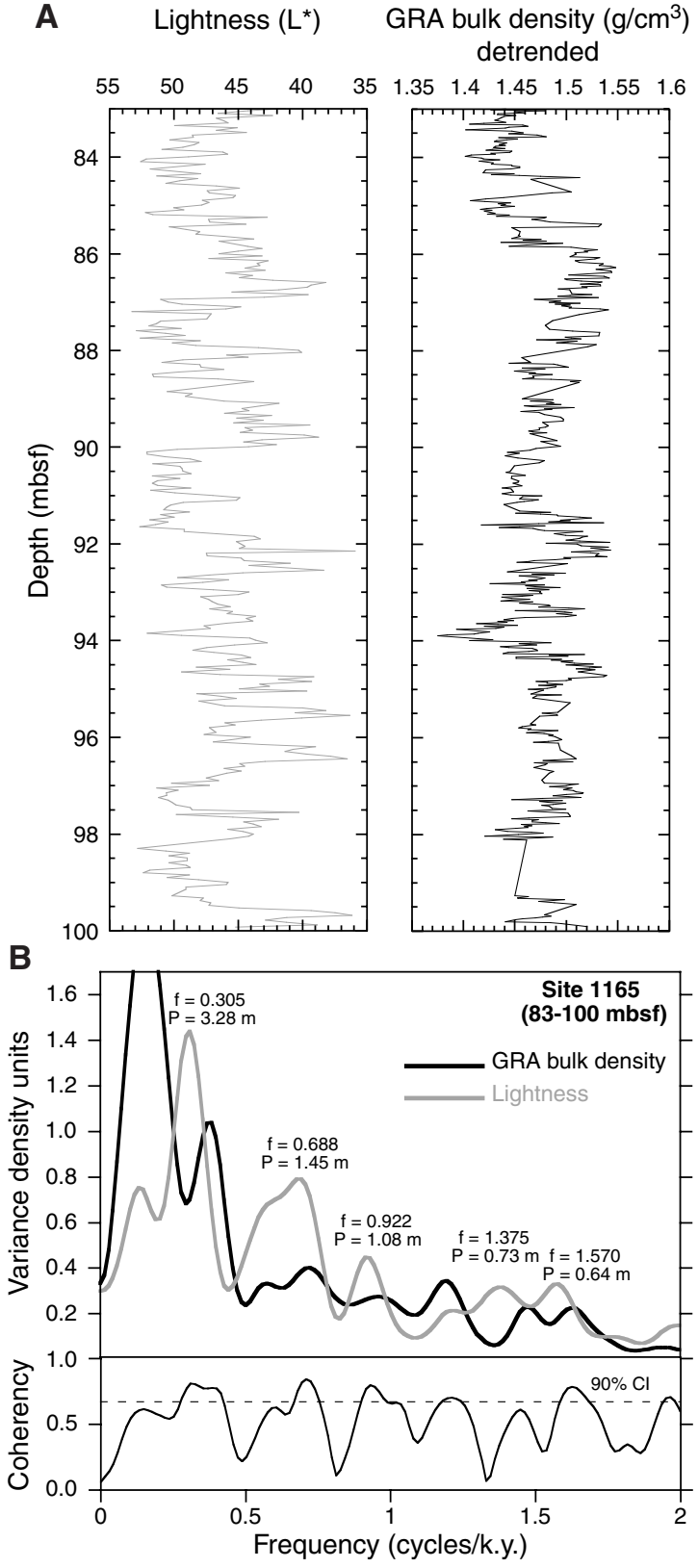

Figure F57. A. Lightness (L*) and GRA bulk density for the interval between 107 and 123 mbsf. **B.** Cross spectra (Blackman-Tuckey method) of the L* and density measurements calculated in the depth domain. CI = confidence interval.

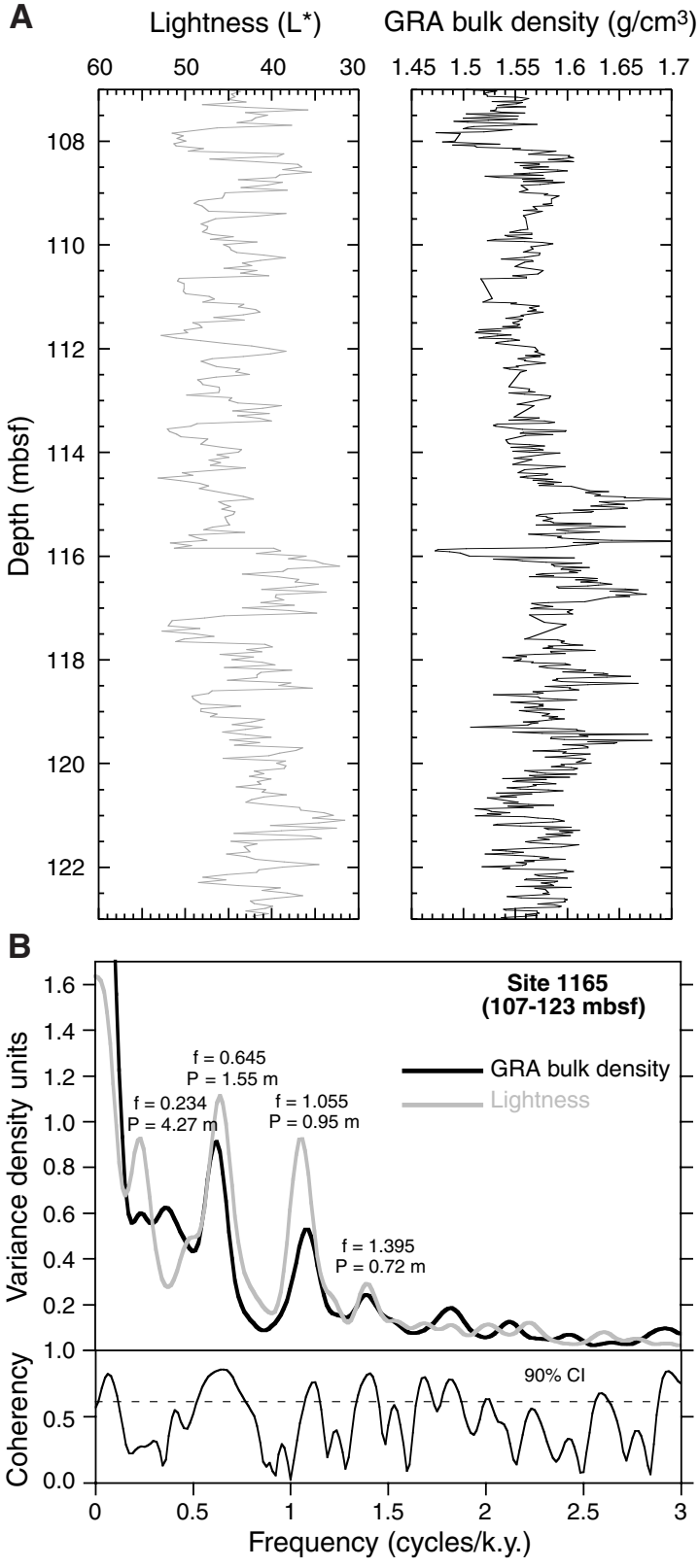

Figure F58. Spectral analyses on lightness values (L*) measured downcore over a 10-m interval every 2 m using the maximum entropy method.

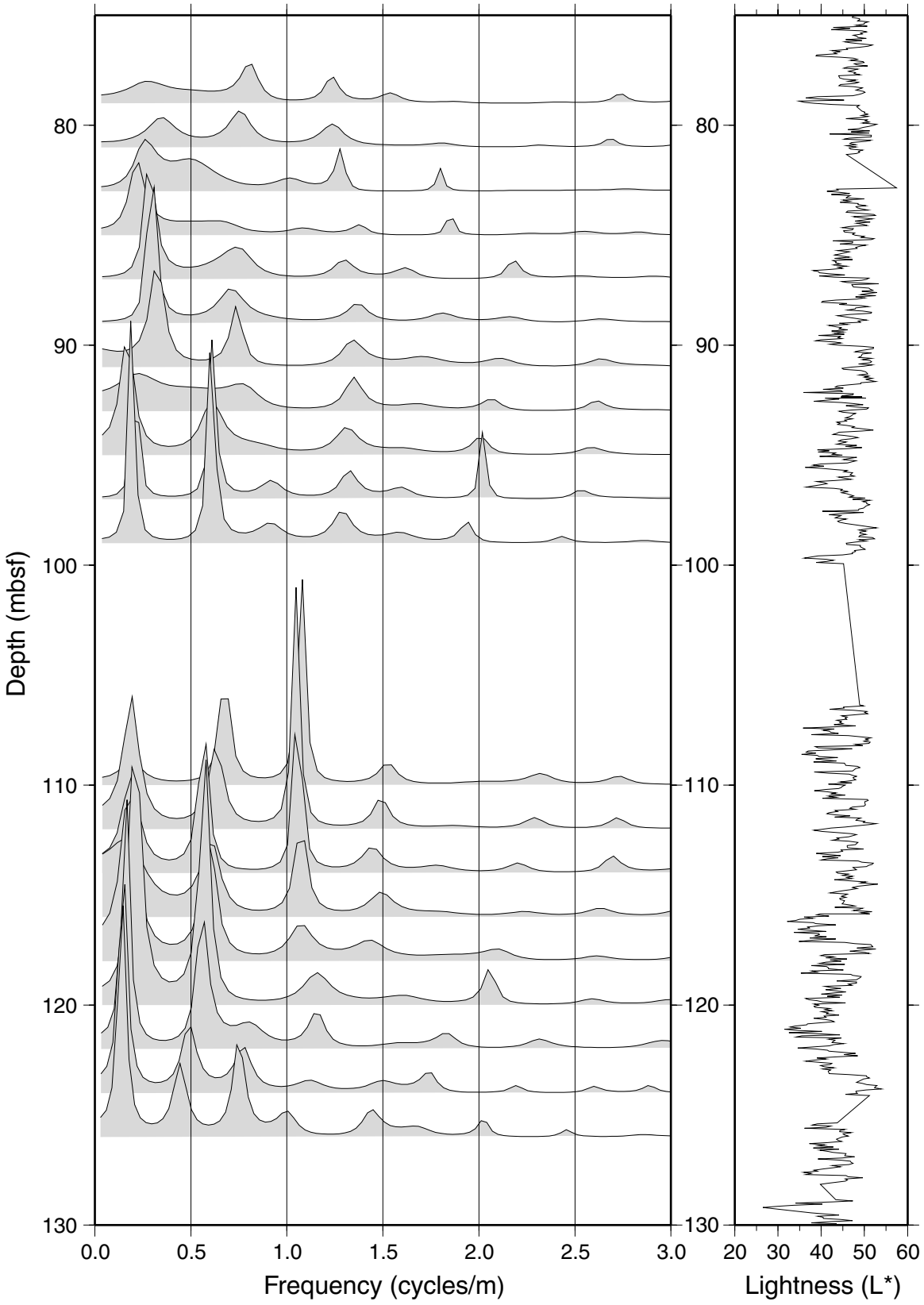

Figure F59. Magnetic susceptibility, GRA bulk density, *P*-wave velocity, and natural gamma measured with the MST on APC cores from Hole 1165B.

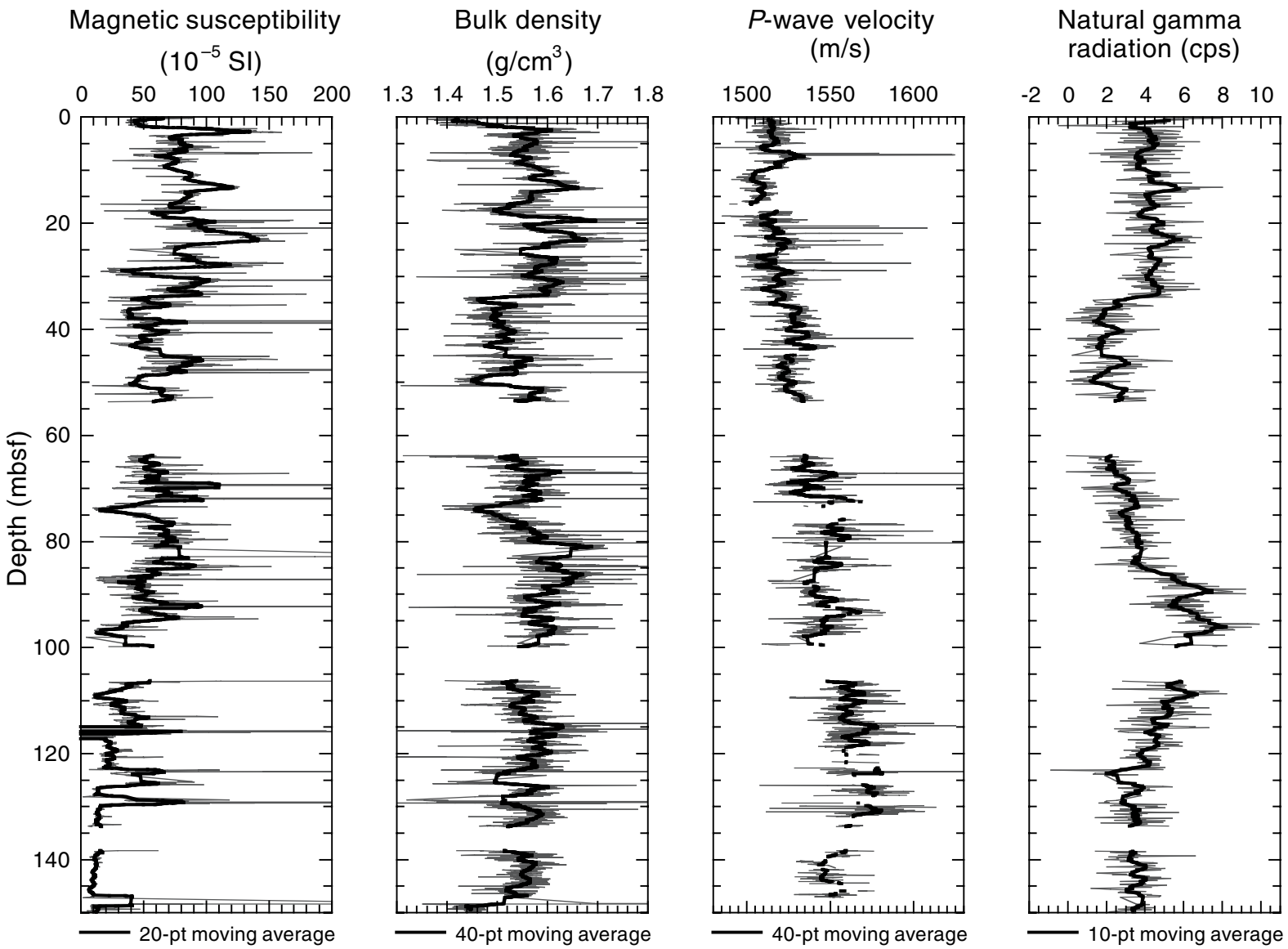

Figure F60. *P*-wave logger (PWL) and *P*-wave sensor (PWS) velocity data vs. depth at Site 1165.

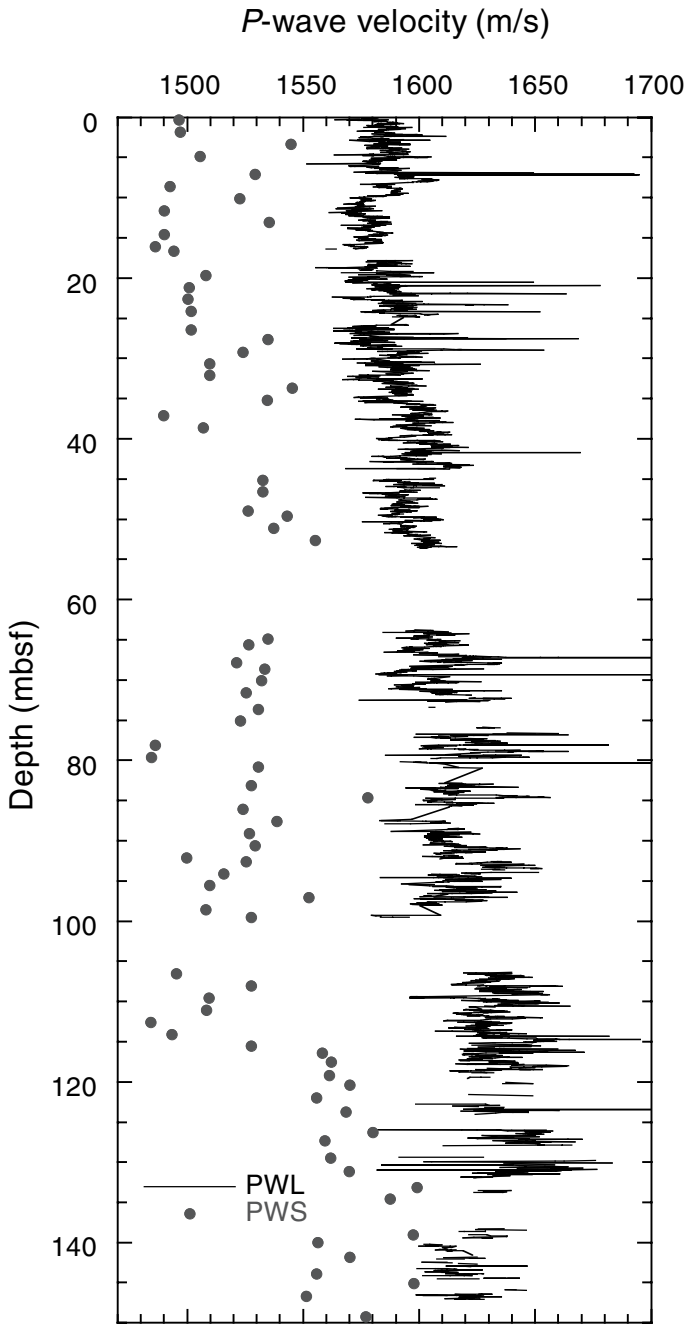

Figure F61. Bulk mineralogy from X-ray diffraction (XRD), natural gamma-ray (NGR), and binned natural gamma spectra vs. depth at Site 1165. Core recovery and lithostratigraphic units are shown on the left. The line through the NGR data is a 20-m moving average. The binned NGR spectra show channels 100 through 248 (1.16 to 2.99 MeV) from the MST natural gamma detector. The characteristic peak positions of gamma radiation associated with potassium (K), uranium (U), and thorium (Th) are shown on the lowermost spectrum.

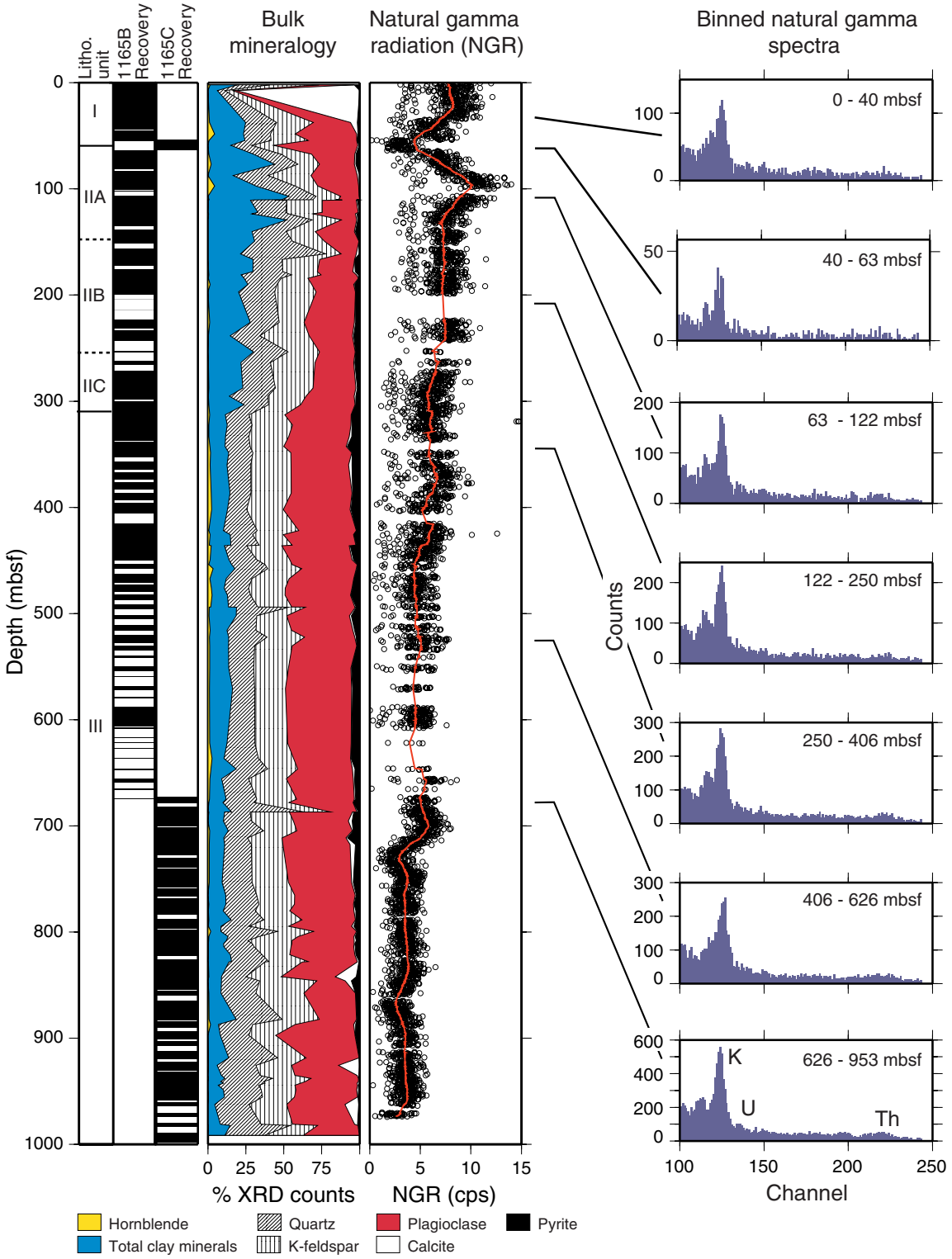

Figure F62. Comparison of magnetic susceptibility, GRA bulk density, and color parameter L* (lightness) measurements on Cores 188-1165B-14H and 15H.

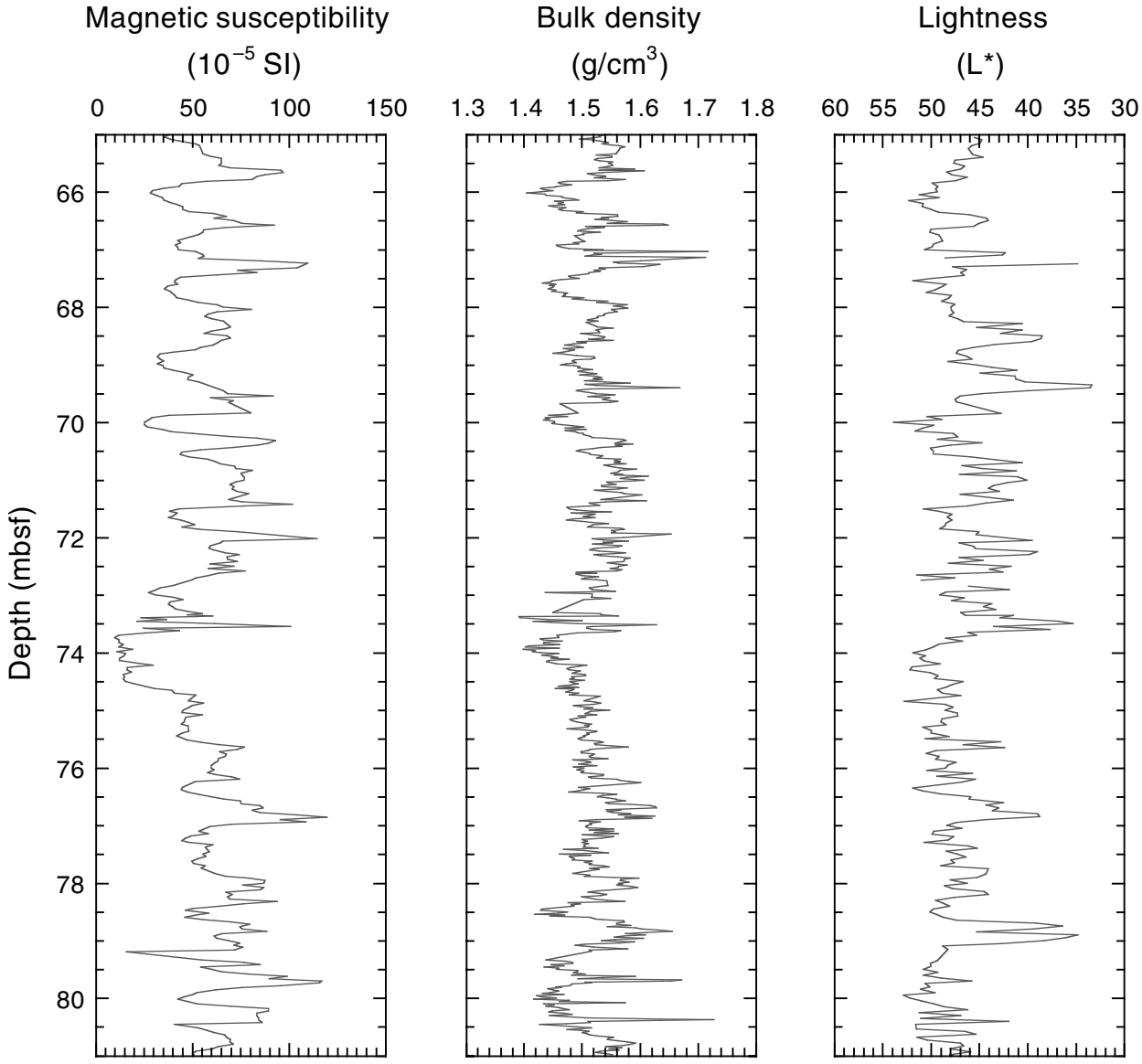

Figure F63. (A) Grain density and (B) porosity from discrete measurements. The column on the right shows lithostratigraphic units.

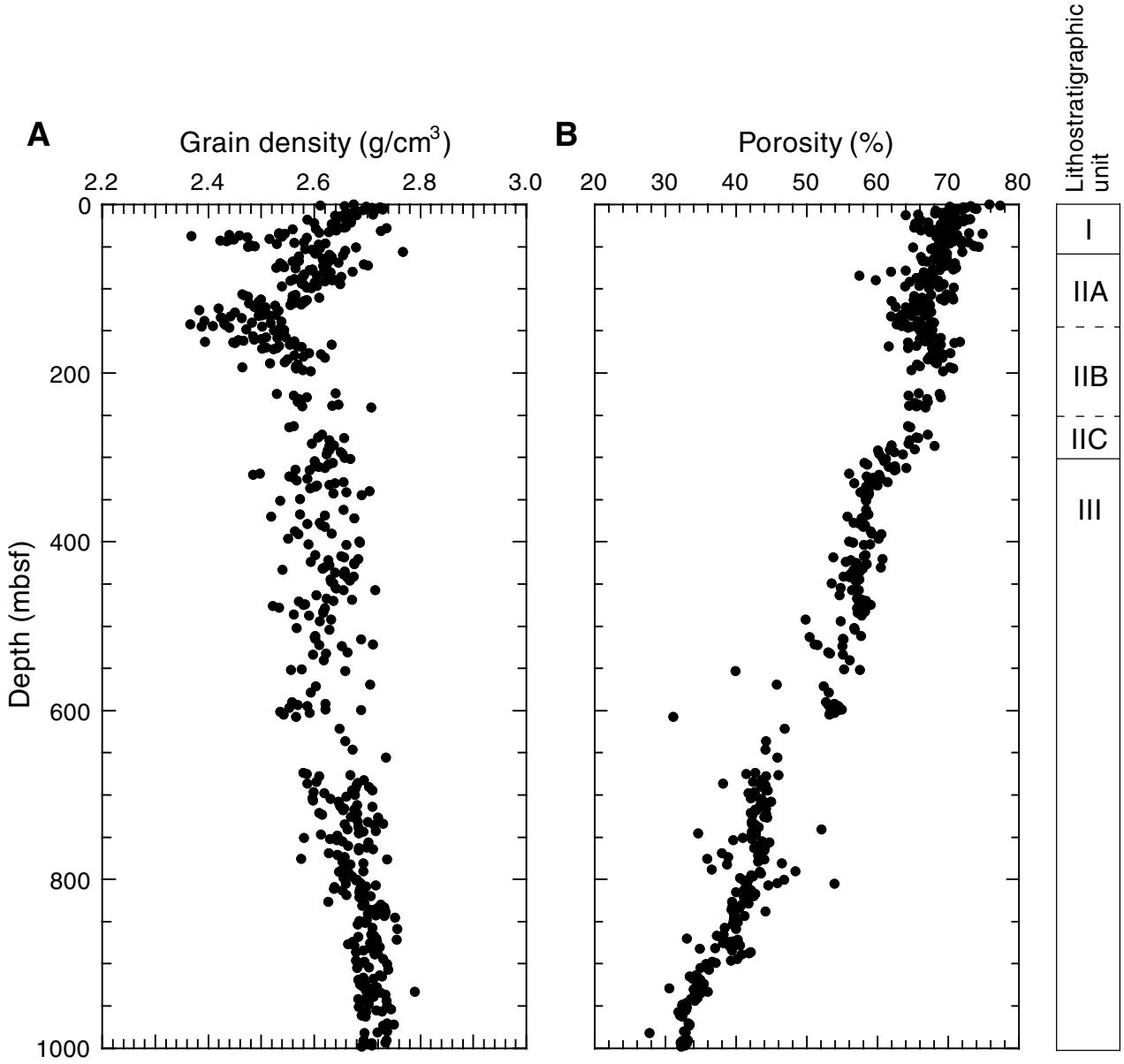

Figure F64. (A) Bulk density and (B) dry density from discrete measurements. The column on the right shows lithostratigraphic units.

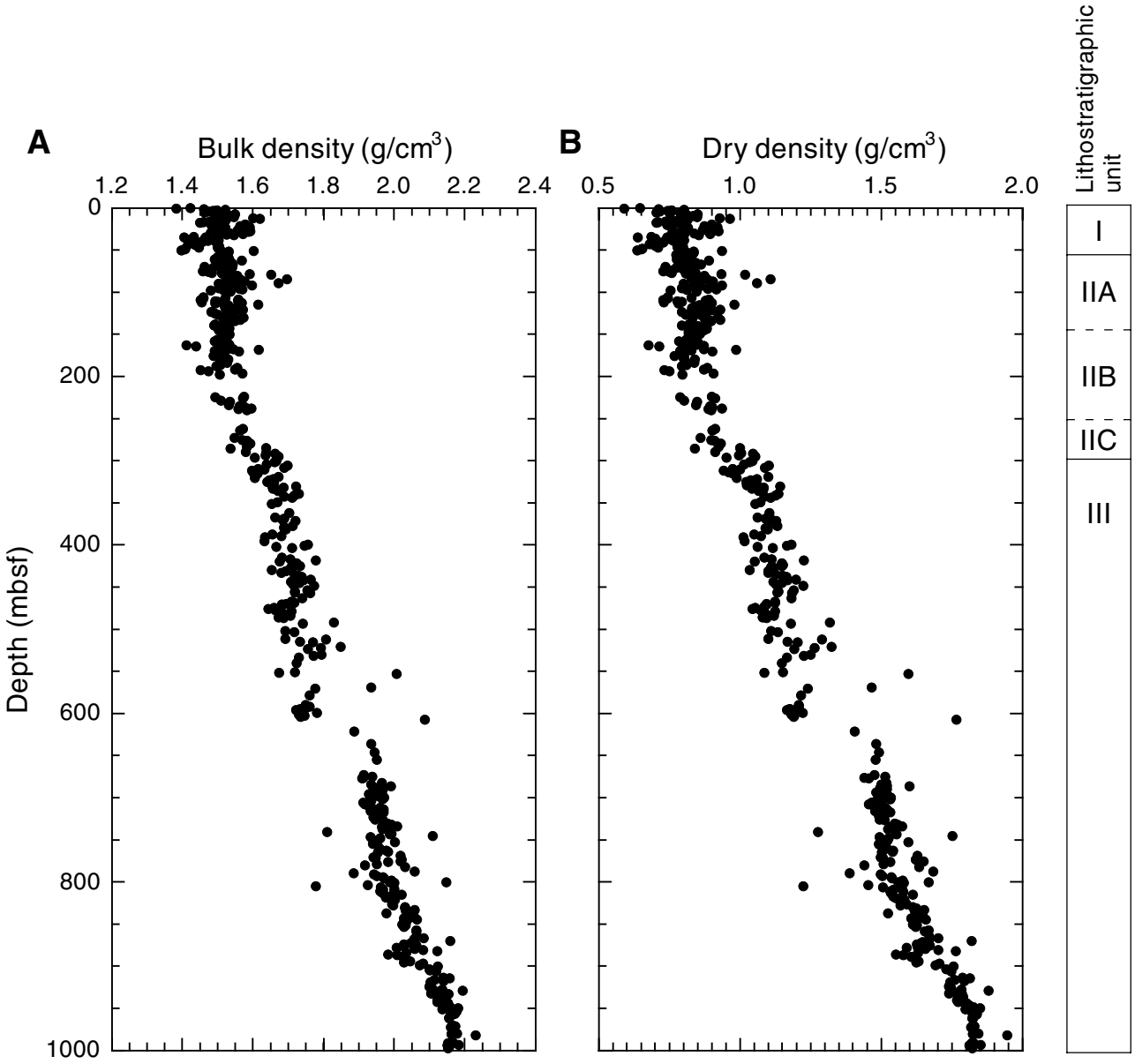

Figure F65. (A) Water content and (B) void ratio from discrete measurements. The column on the right shows lithostratigraphic units.

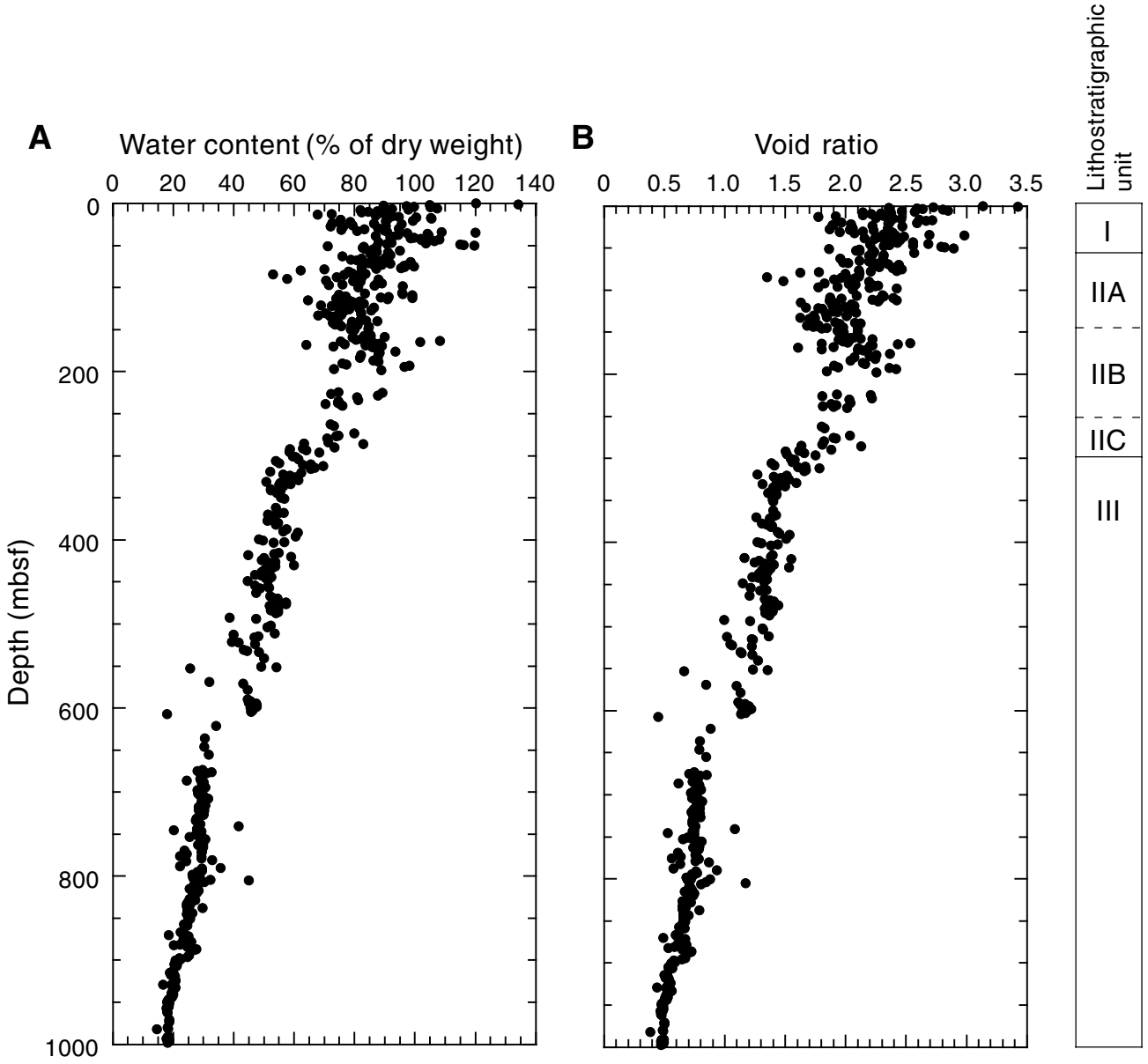

Figure F66. A. Comparison of gamma-ray attenuation (GRA) bulk-density data and bulk density from discrete measurements. **B.** Ratio of discrete measurement of bulk density to bulk density from GRA measurements. The column on the right shows lithostratigraphic units. RCB = rotary core barrel; XCB = extended core barrel.

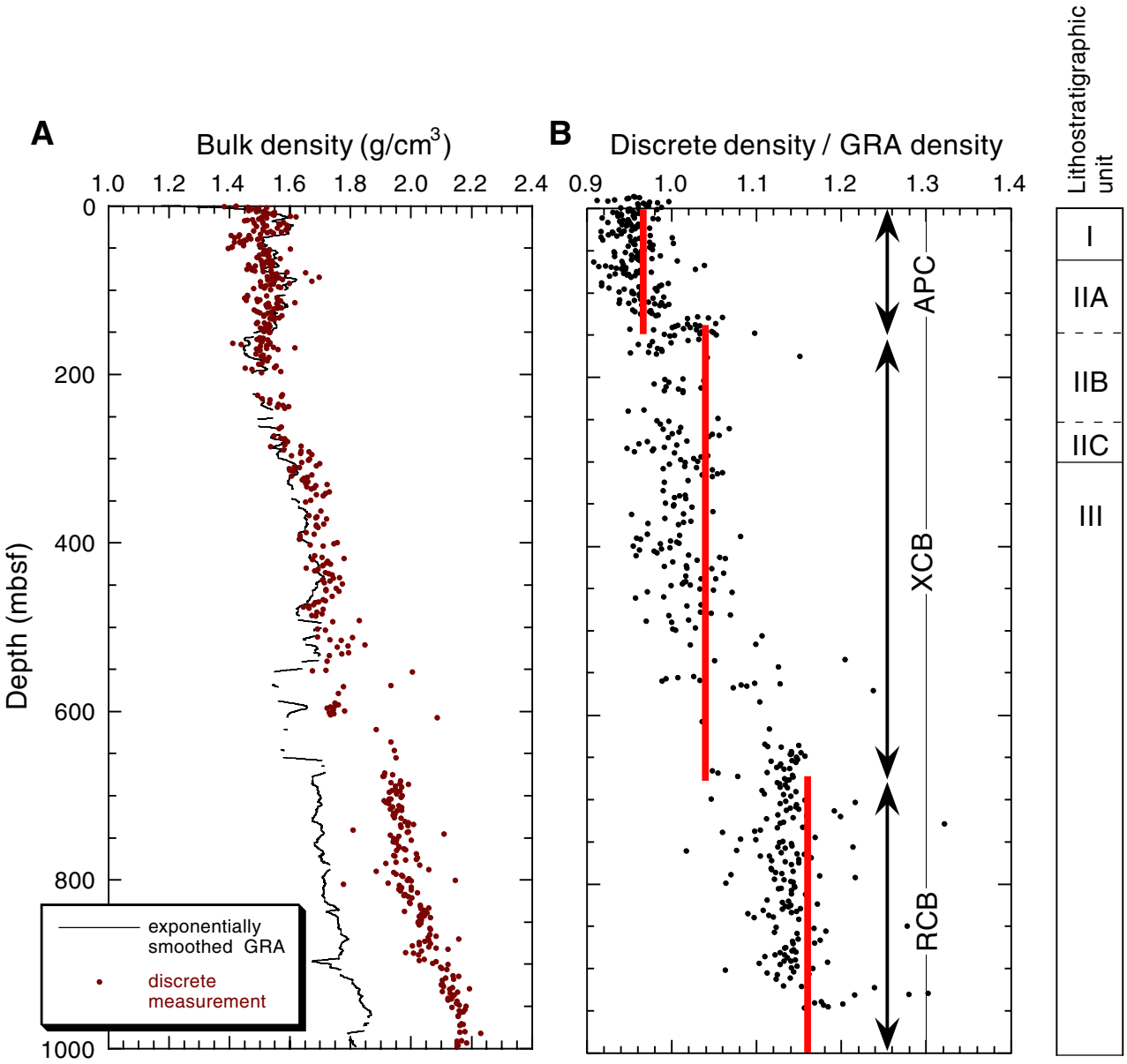

Figure F67. Calculated overburden pressure based on discrete measurements compared to results obtained from GRA data.

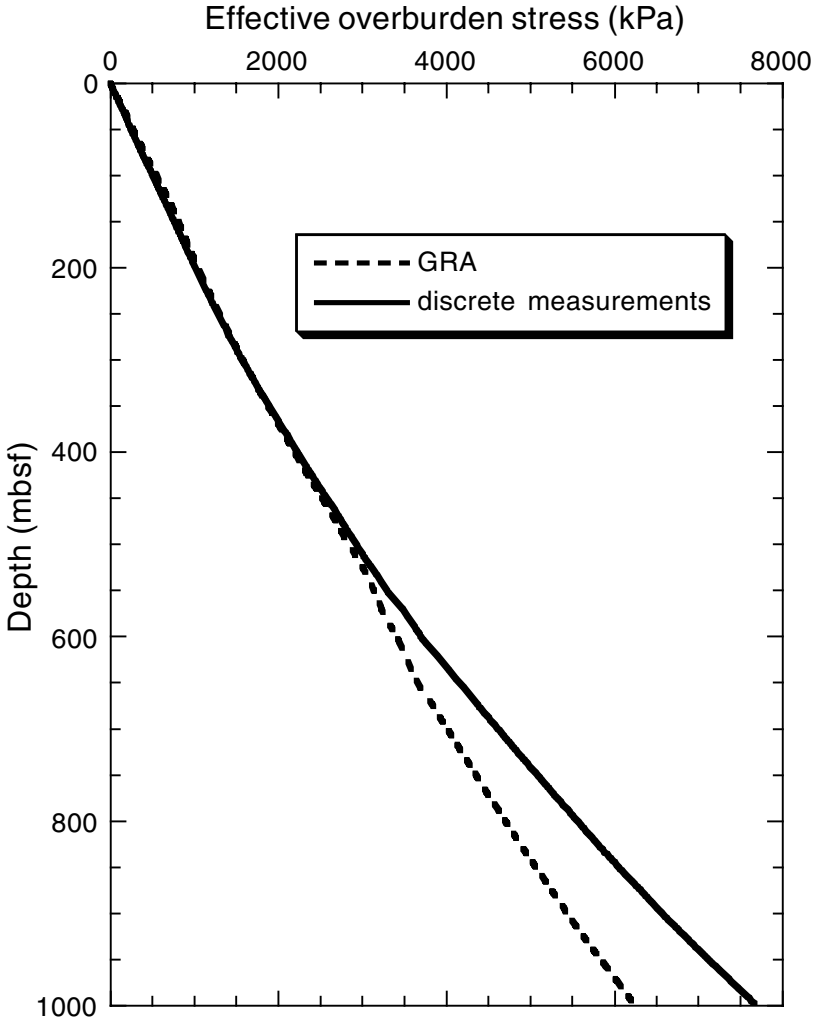

Figure F68. Discrete velocity measurements obtained with the PWS at Site 1165. The column on the right shows lithostratigraphic units.

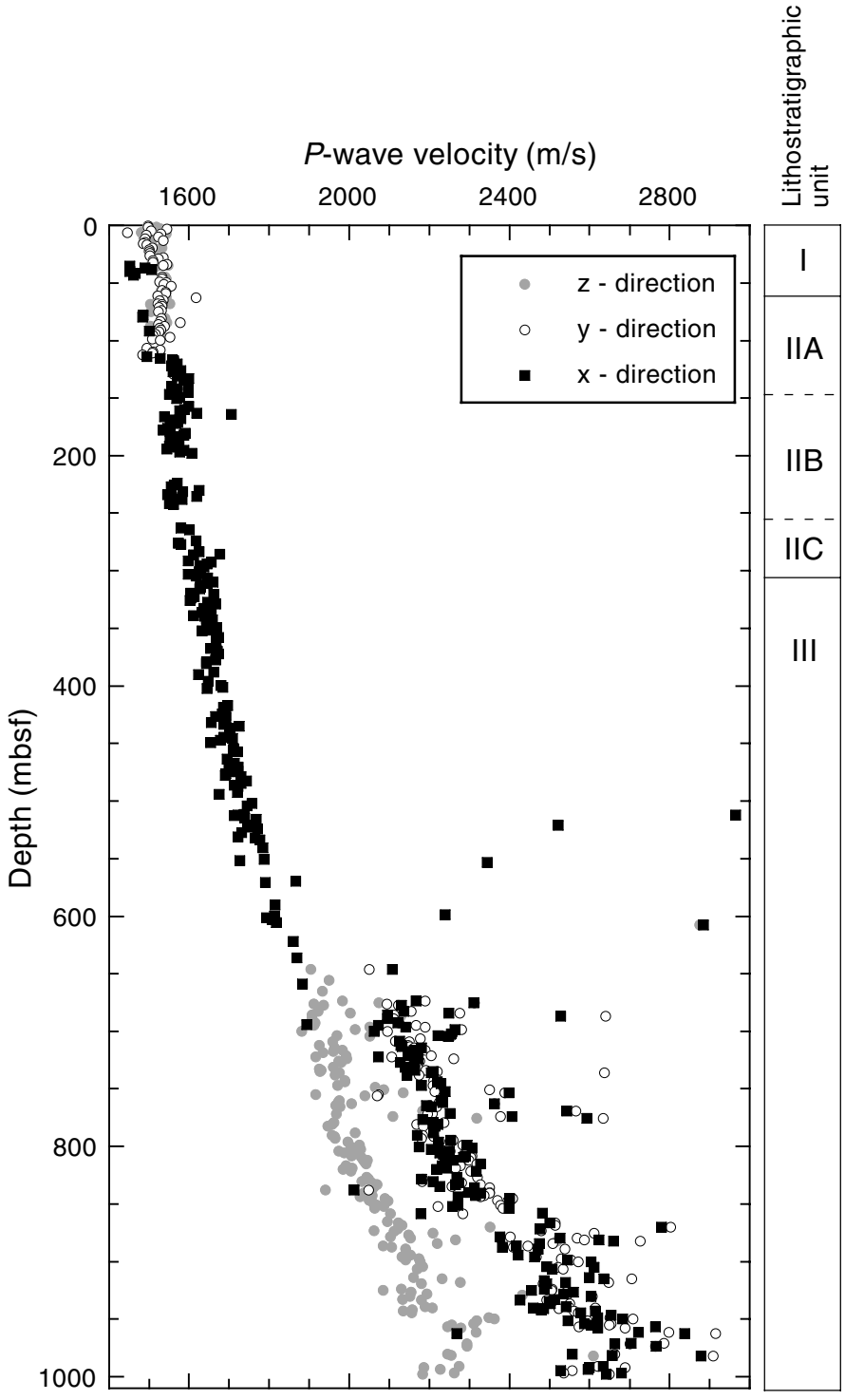

Figure F69. Measurements of undrained shear strength from Site 1165, using the automated vane shear (AVS), fall cone (FC), and pocket penetrometer (PP). The column on the right shows lithostratigraphic units.

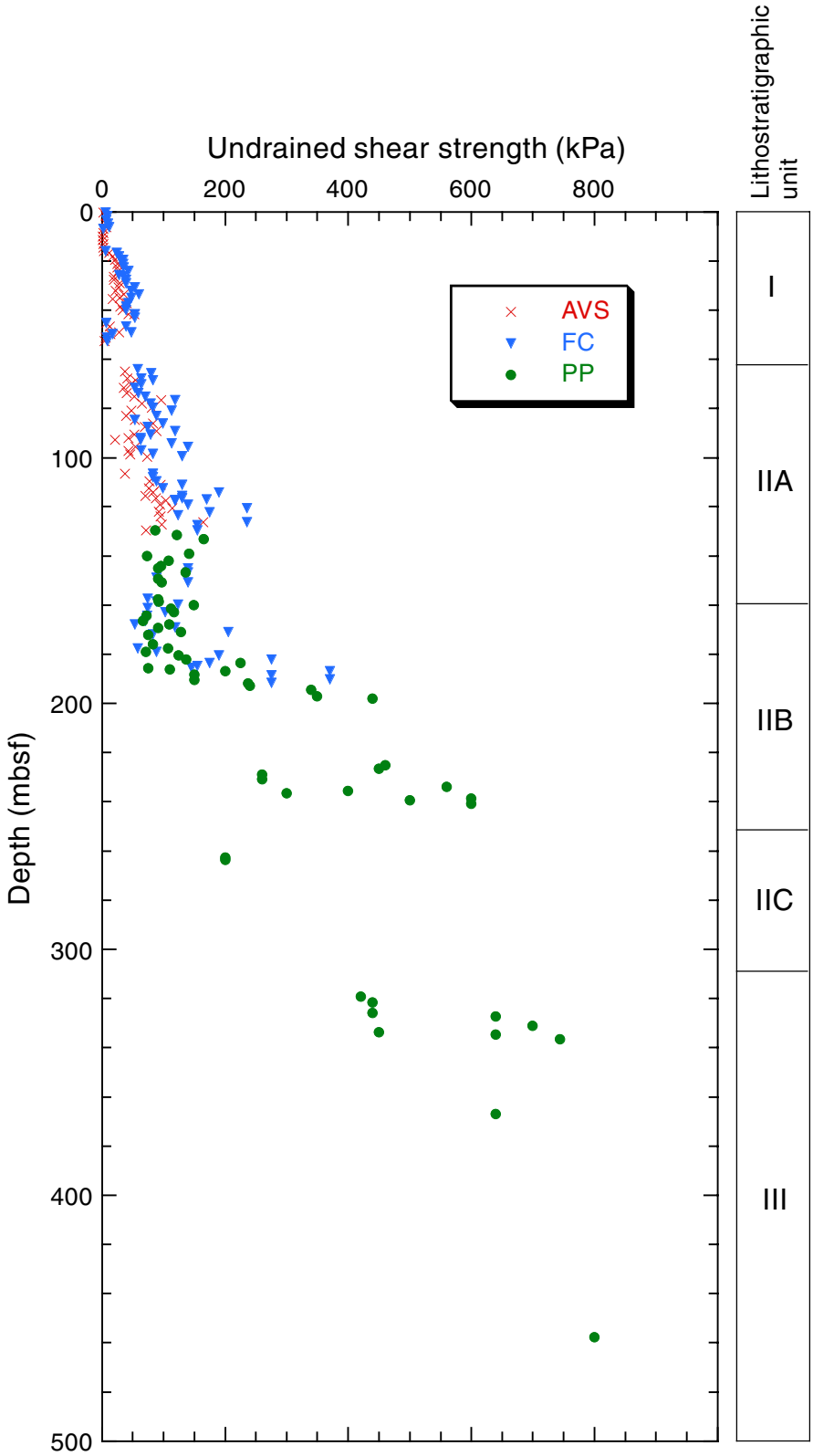

Figure F70. Normalization of undrained shear strength with respect to effective overburden pressure. The column on right shows lithostratigraphic units. AVS = automated vane shear; FC = fall cone; and PP = pocket penetrometer.

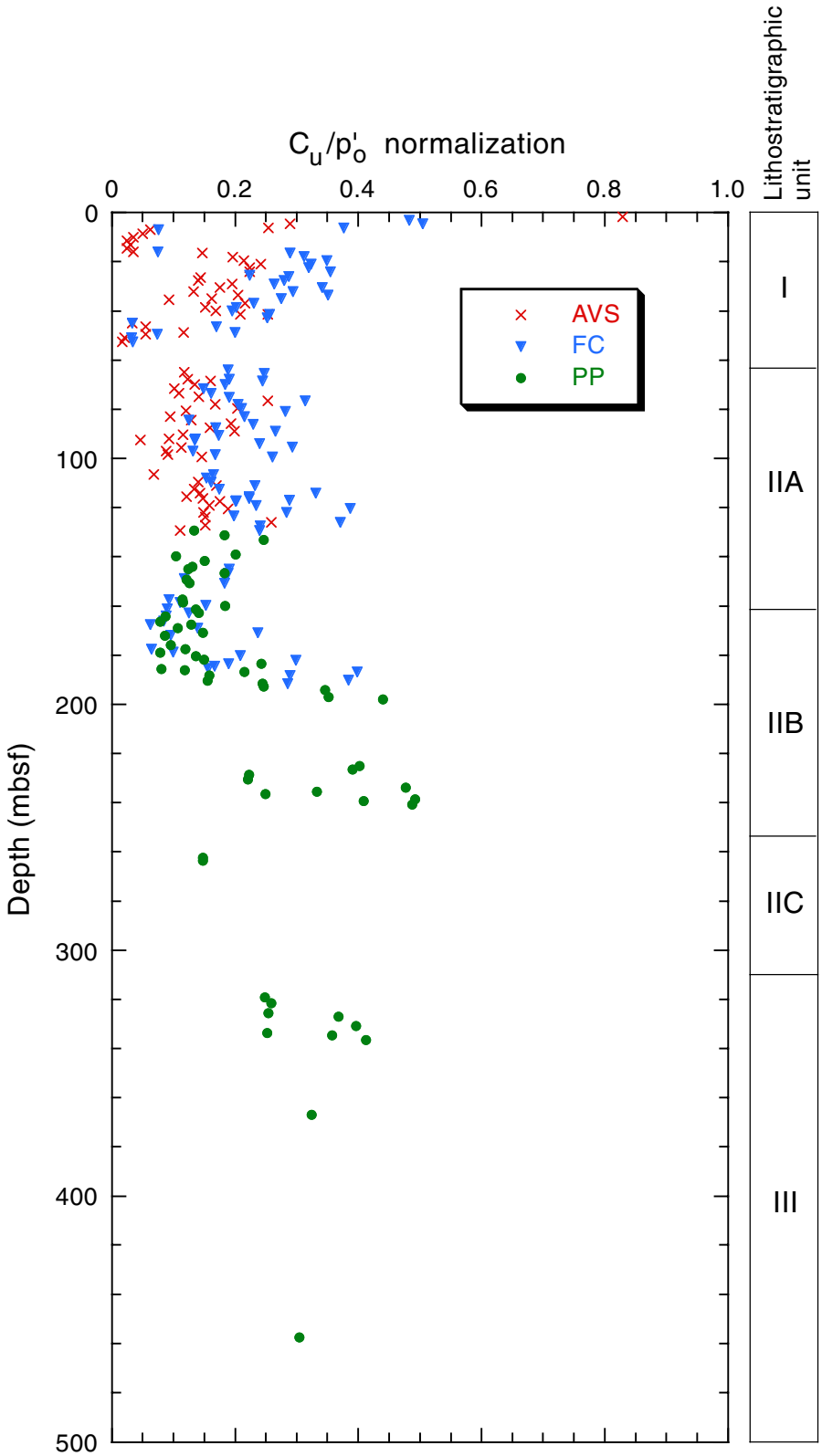

Figure F71. Thermal conductivity measured at Site 1165 (solid circles) with a trend (solid line) that best represents in situ conditions.

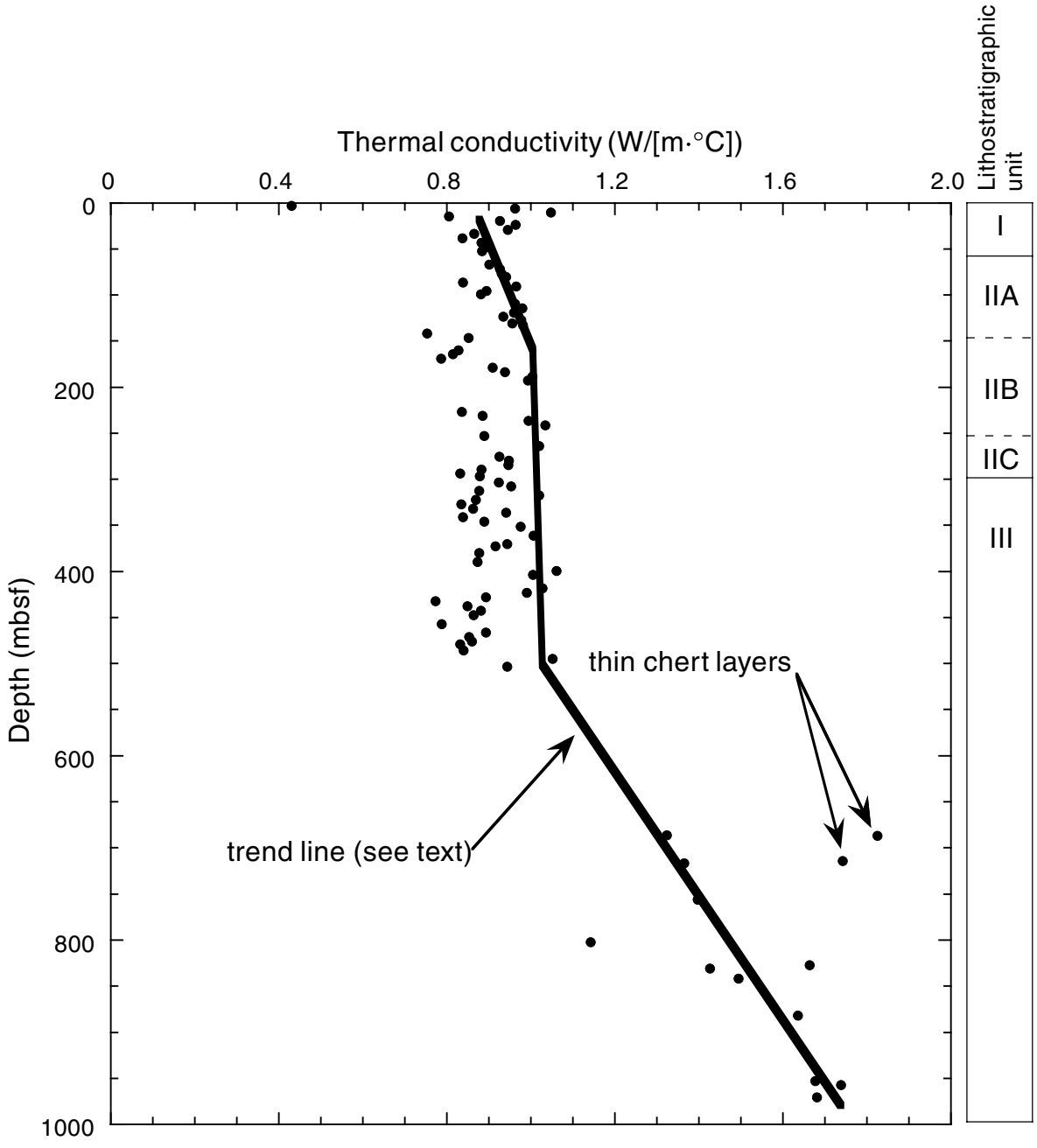

Figure F72. Measured temperature vs. time from deployment of the Adara temperature tool for Core 188-1165B-4H (35.3 mbsf). T_{SF} = seafloor temperature; APC = advanced hydraulic piston corer.

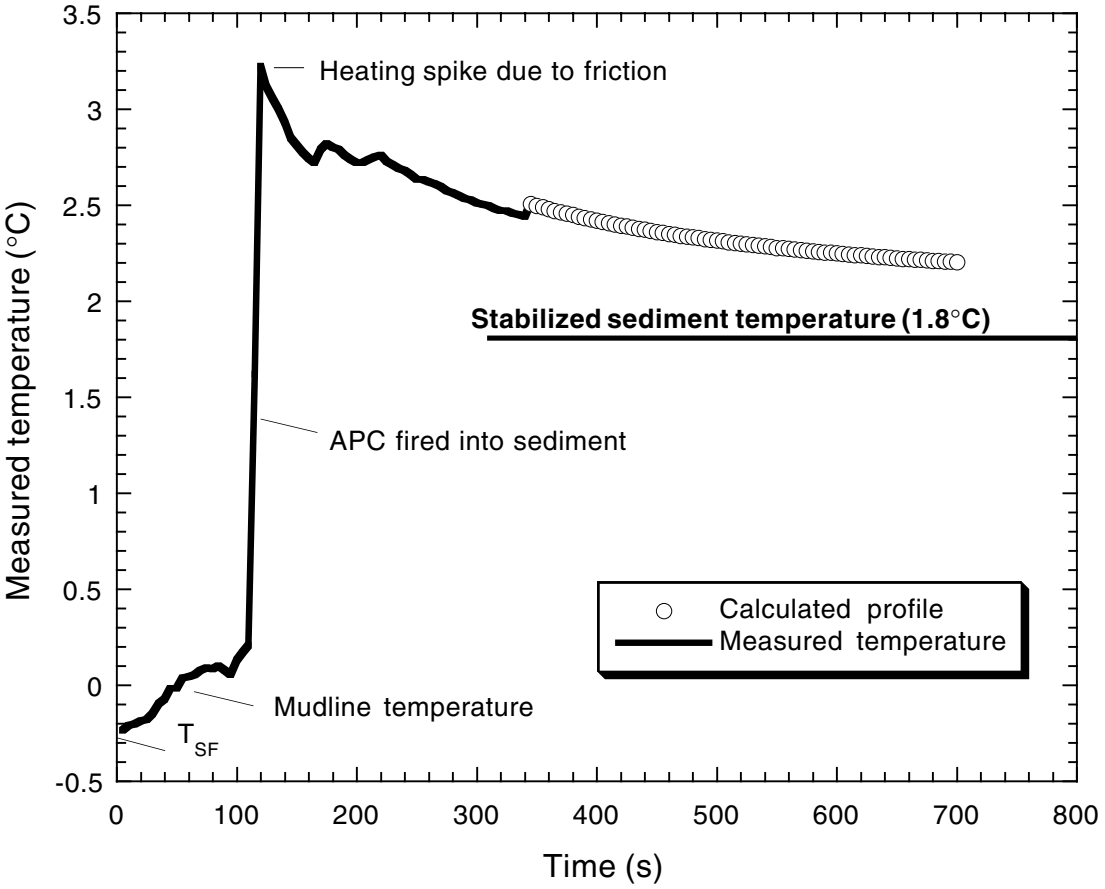

Figure F73. Measured temperature vs. time from deployment of the Adara temperature tool for Core 188-1165B-10H (92.3 mbsf). T_{SF} = seafloor temperature; APC = advanced hydraulic piston corer.

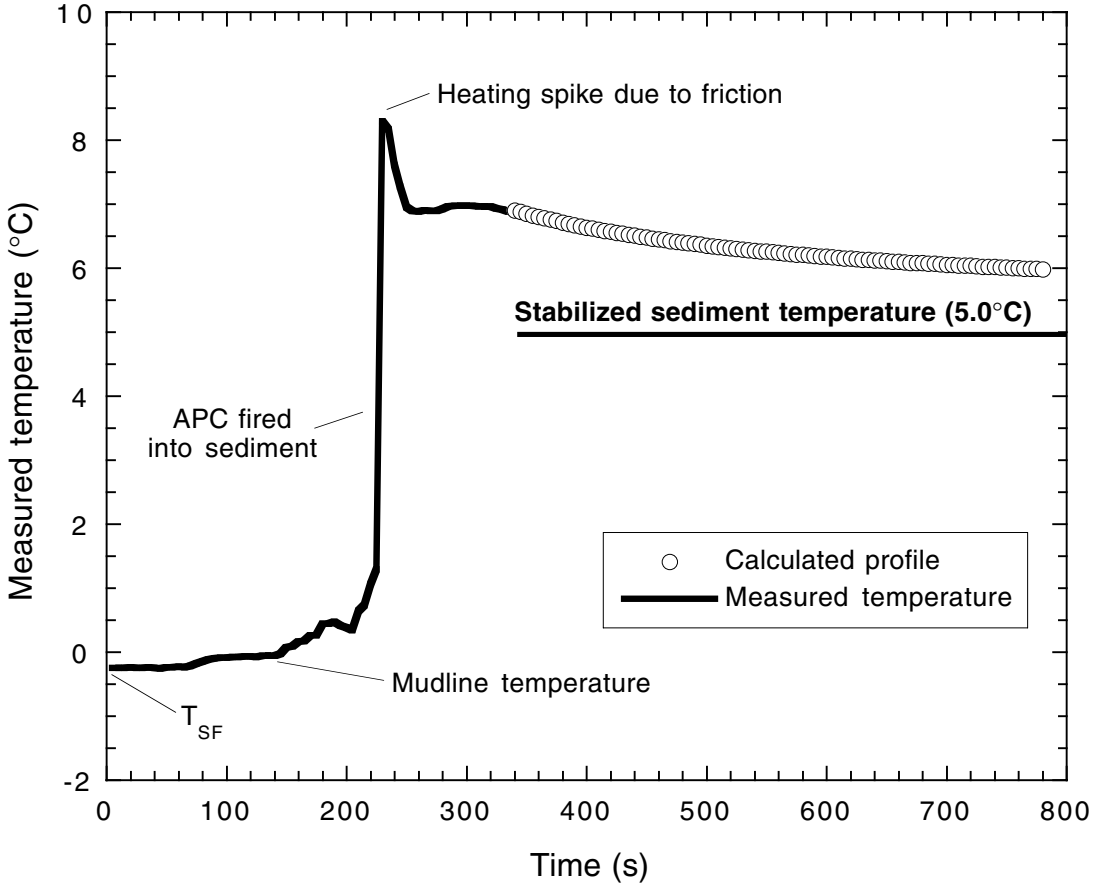

Figure F74. Measured temperature vs. time from deployment of the Adara tool for Core 188-1165B-14H (125.8 mbsf). T_{SF} = seafloor temperature; APC = advanced hydraulic piston corer.

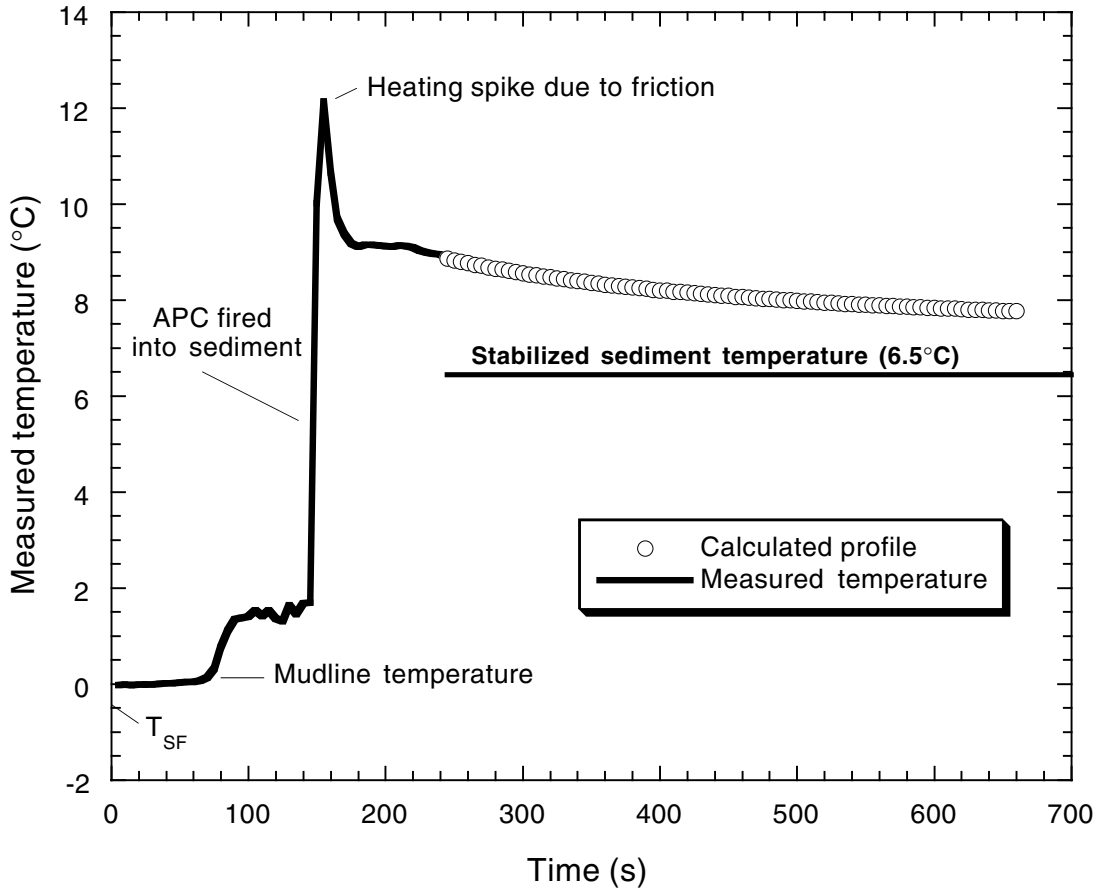

Figure F75. Measured and estimated temperature vs. depth profile for Site 1165.

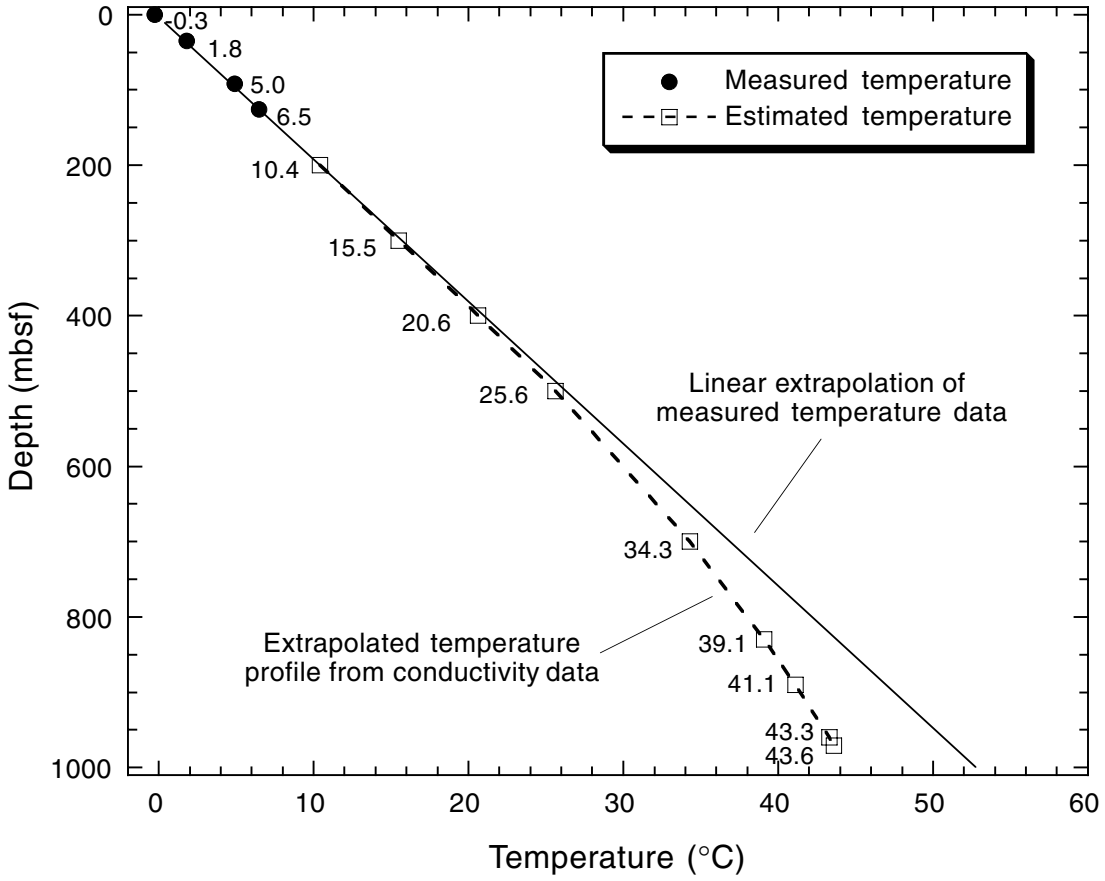

Figure F76. Logging summary diagram showing log, pipe, and seafloor depths.

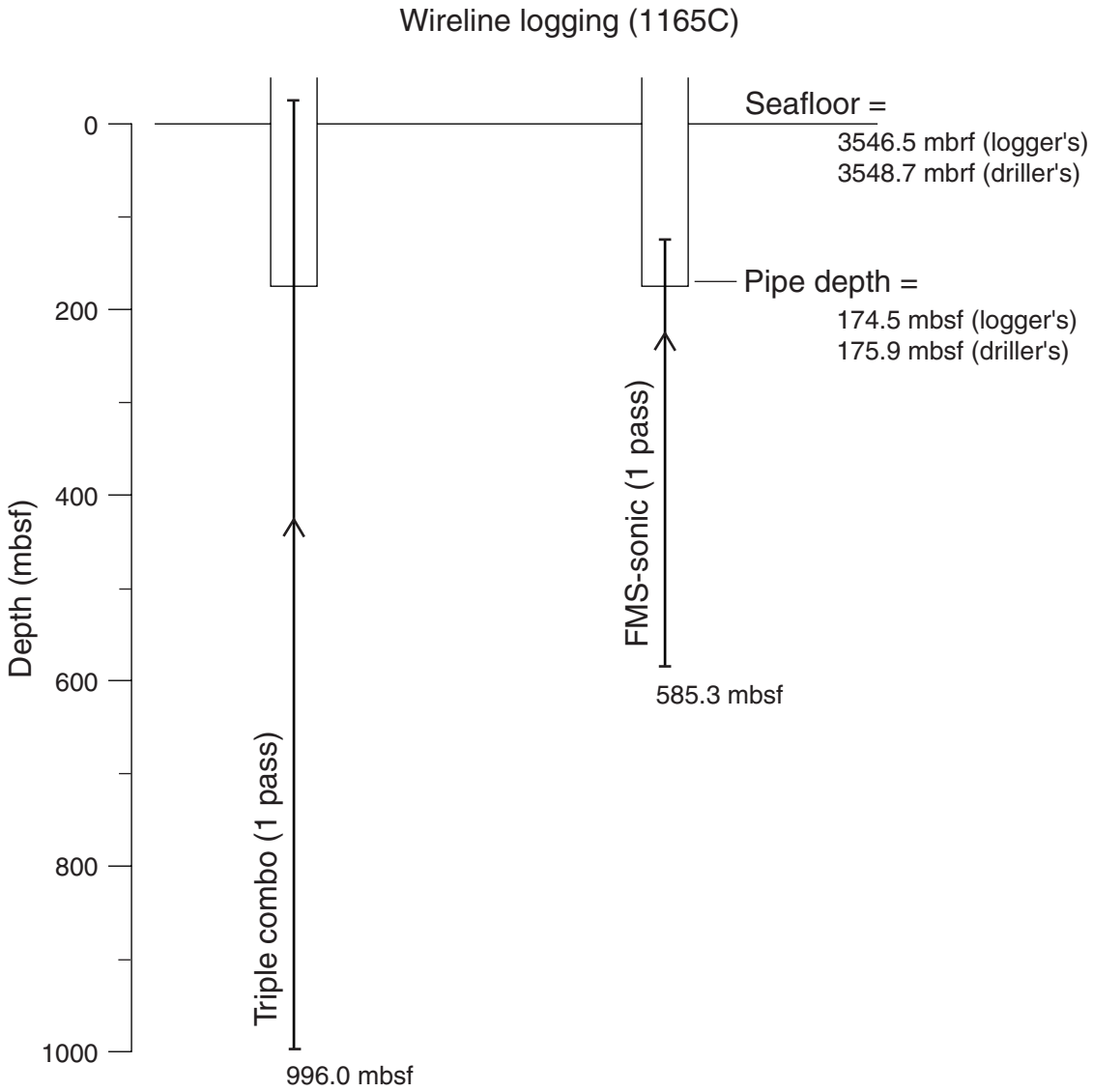

Figure F77. Gamma-ray, density, porosity, resistivity, and sonic velocity logs. Core measurements of density, porosity and velocity are also plotted for comparison with downhole logs. See **"Downhole Measurements,"** p. 25, in the "Explanatory Notes" chapter for explanation of acronyms and types of measurements.

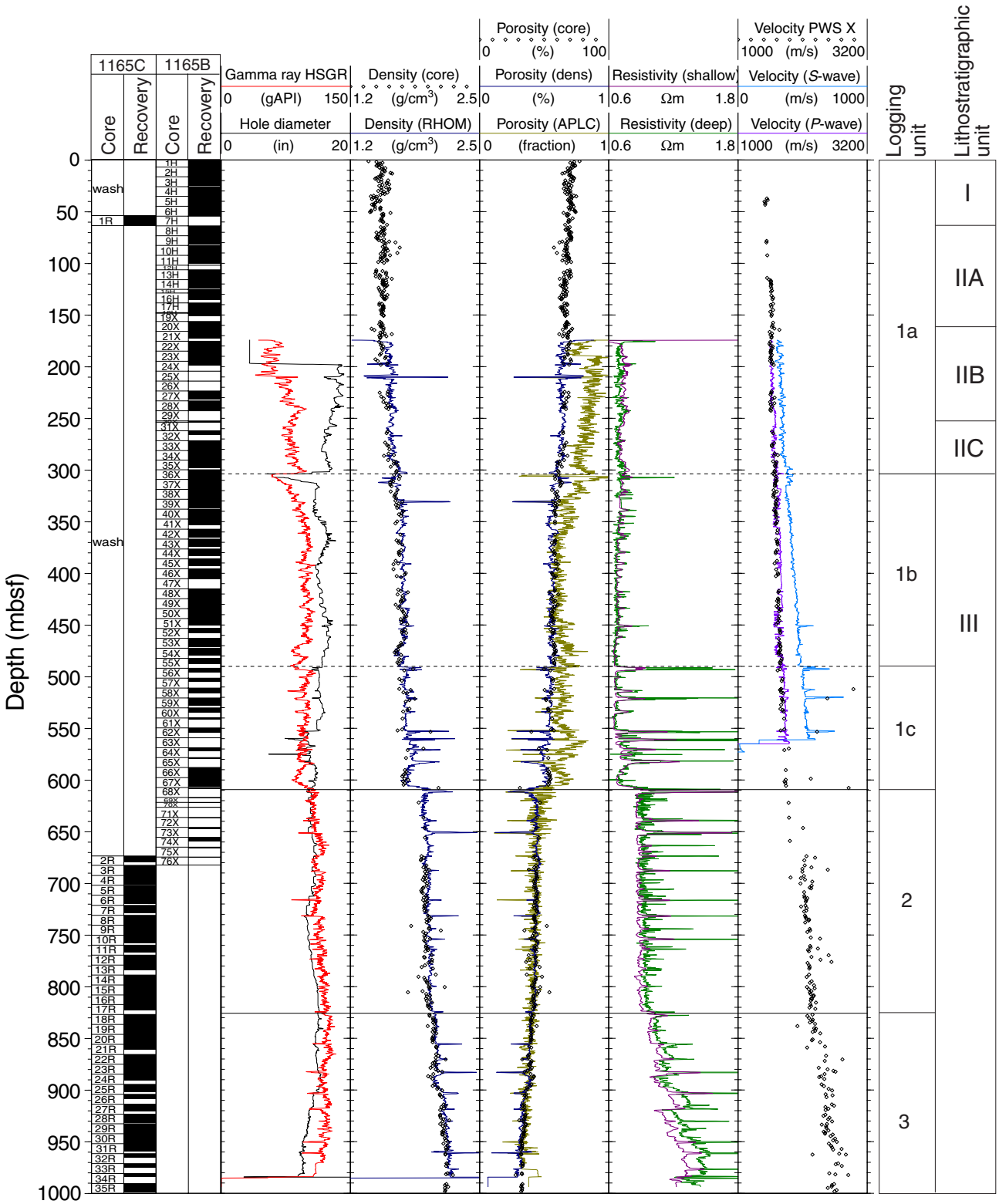

Figure F78. Total spectral gamma-ray, uranium, thorium, potassium, and photoelectric effect (PEF) logs. Gamma ray and susceptibility measured on cores are also shown.

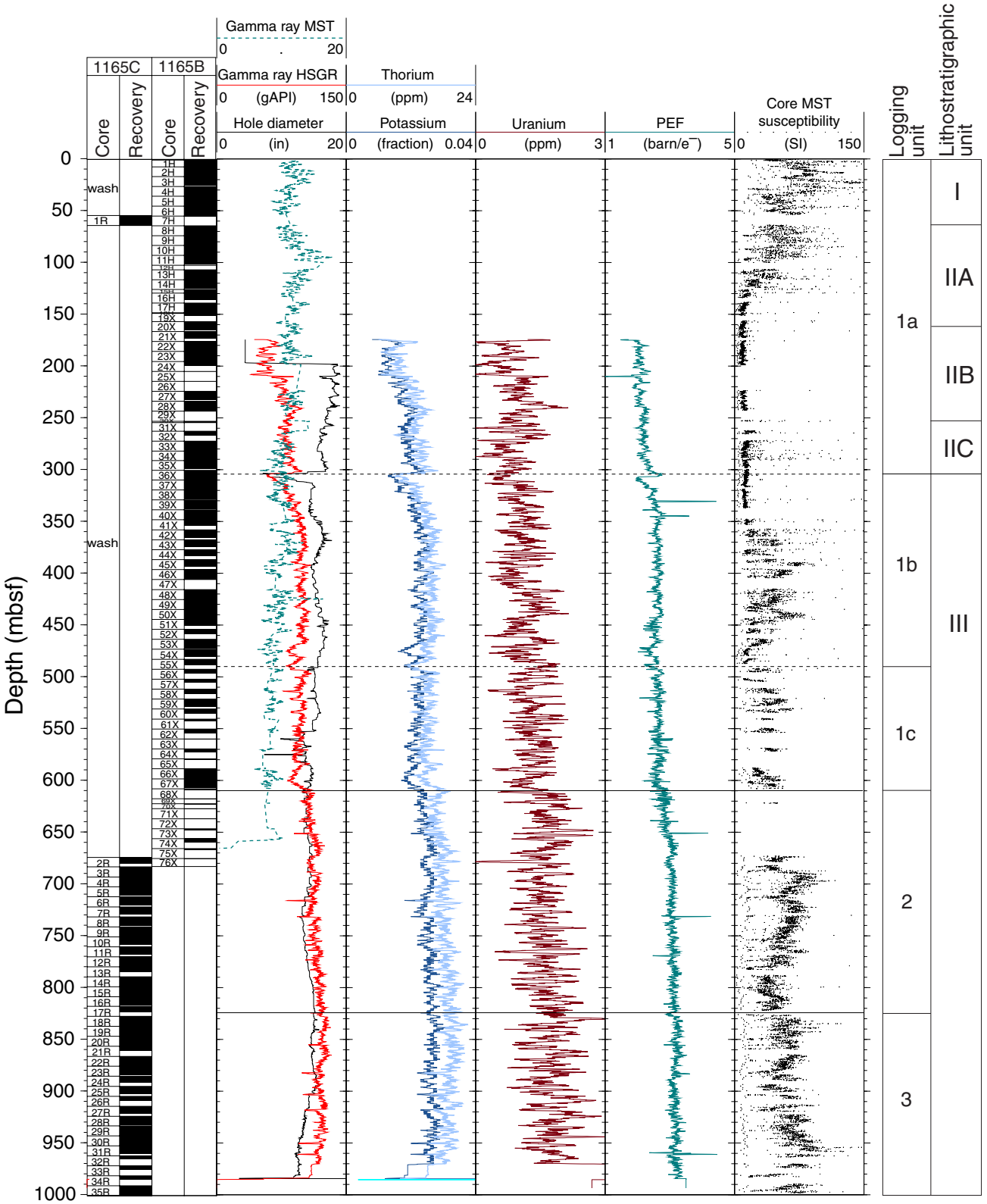

Figure F79. Comparison of HSGR gamma-ray log (downhole) and gamma ray measured on core. The core gamma-ray values are from the high-energy end of the gamma-ray energy spectrum, above 1100 eV, the same range as the log data. Solid lines show possible correlation of peaks.

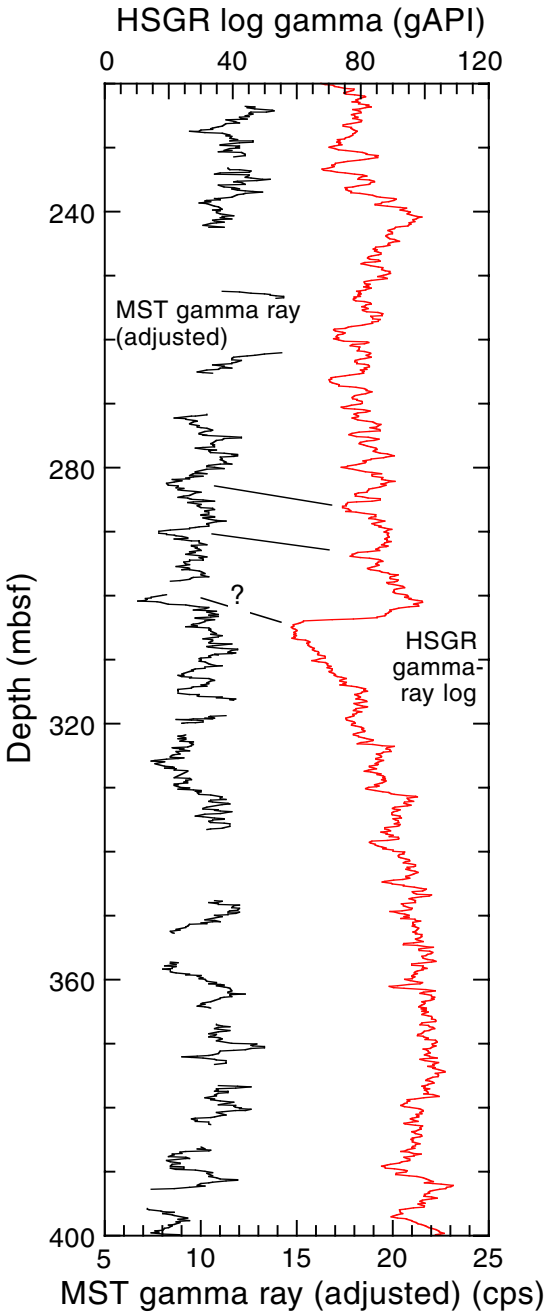

Figure F80. Expanded sections from logging Units 2 and 3 showing both large amplitude peaks (the log signature of calcified beds) and the smaller peaks in between.

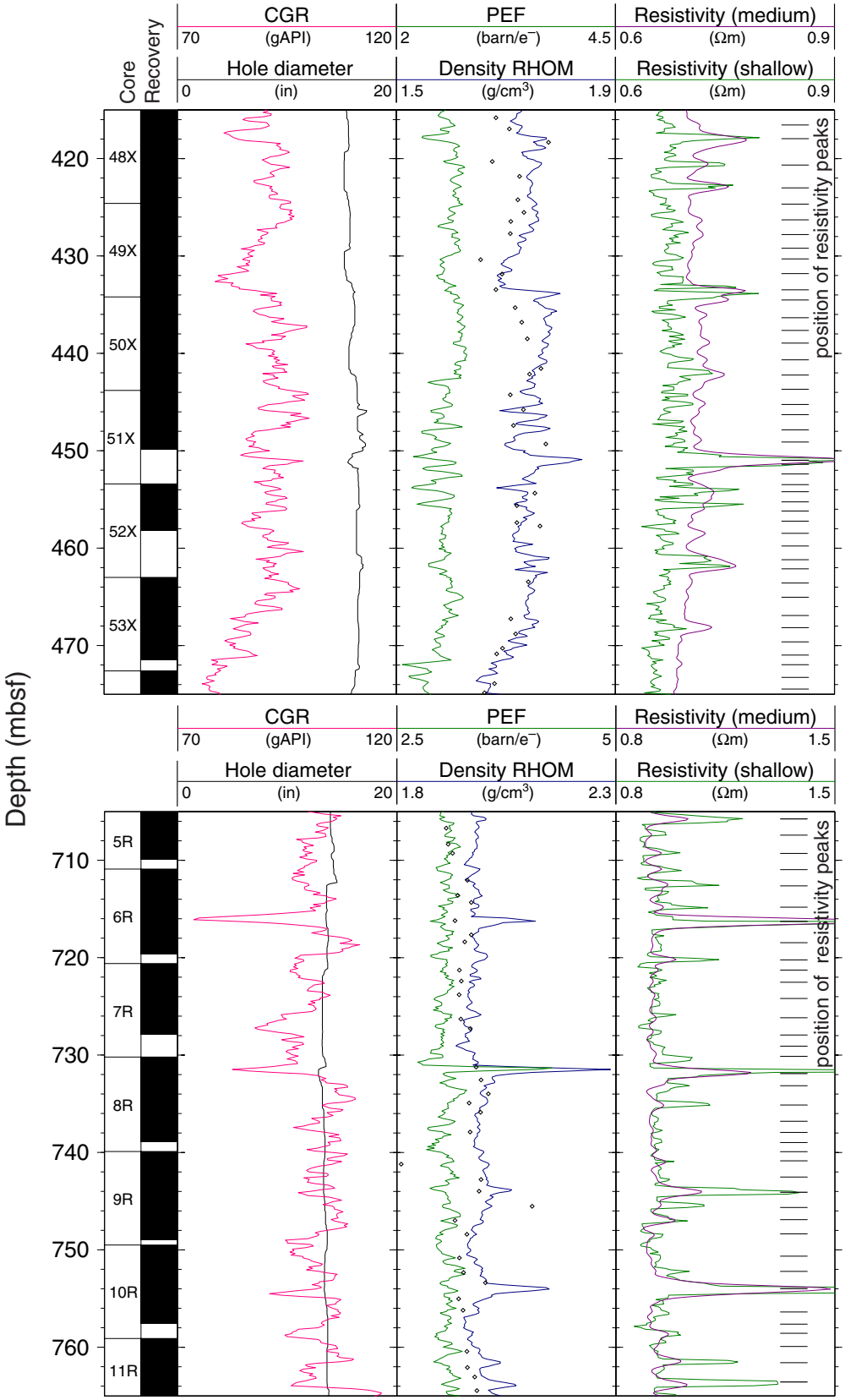

Figure F81. Comparison of MAD bulk density (corrected for in situ conditions) and log bulk density.

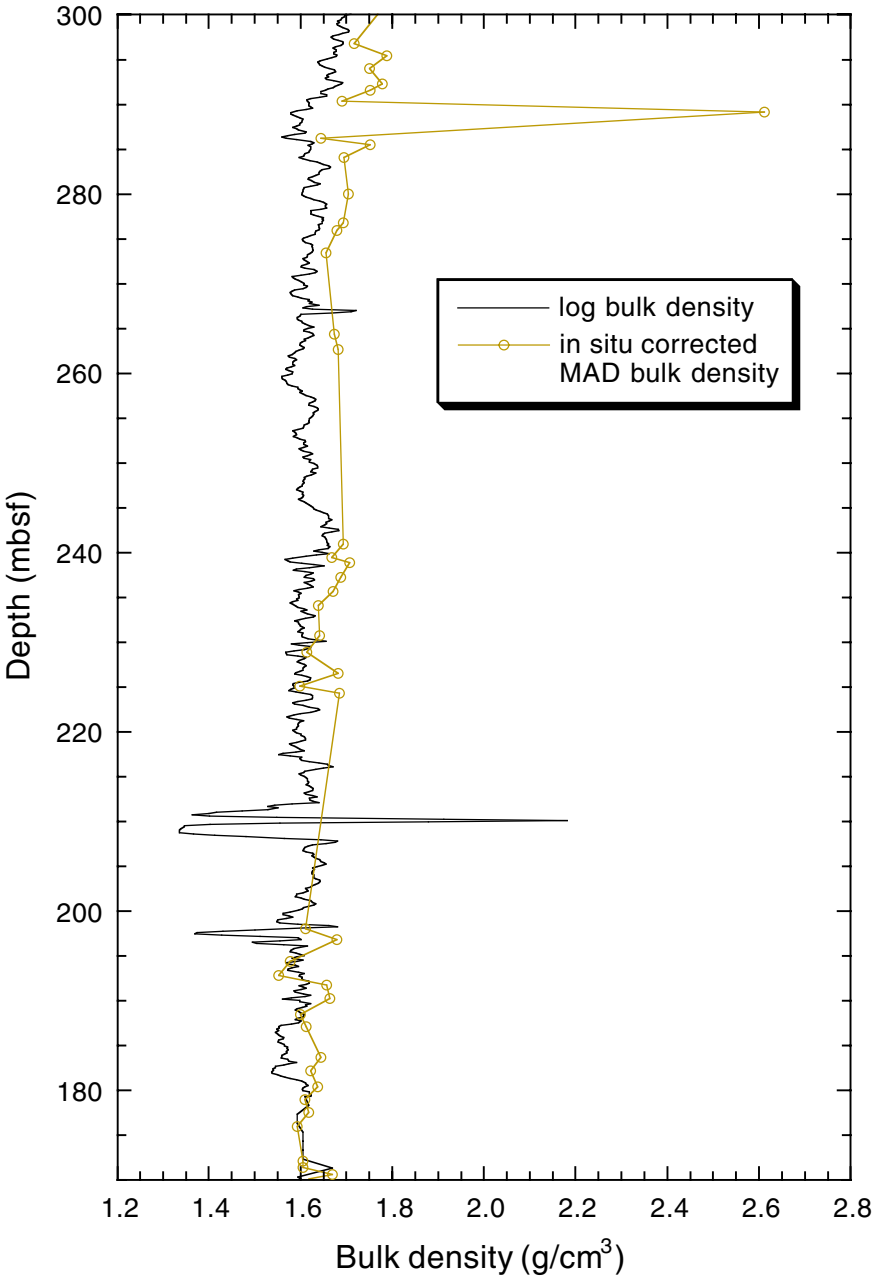

Figure F82. Comparison of z-direction core *P*-wave velocity measurements (corrected for in situ conditions) and log *P*-wave velocity for the upper portion of the logged interval.

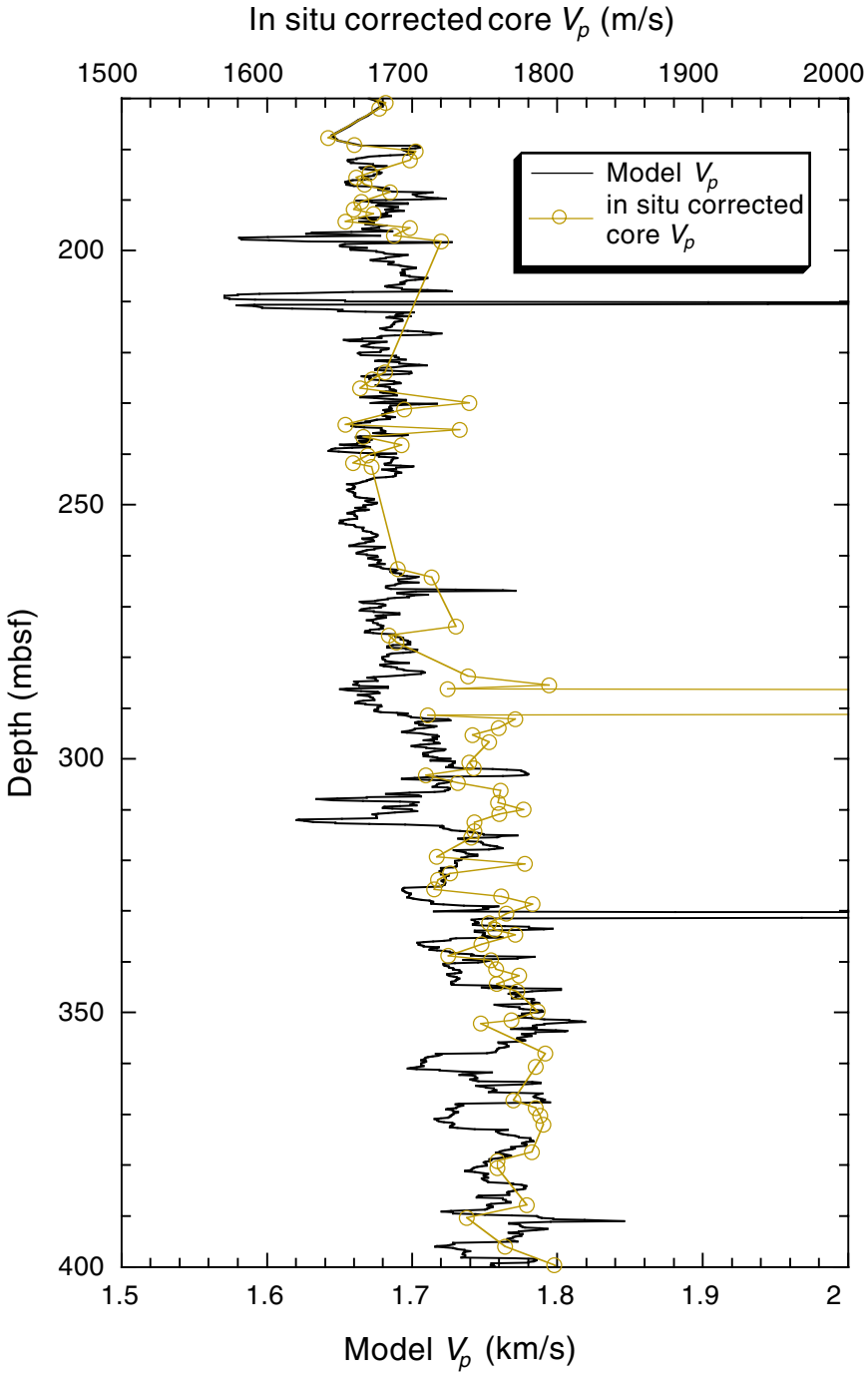

Figure F83. Comparison of z-direction core *P*-wave velocities (corrected for in situ conditions) and *P*-wave velocity derived from the density-porosity log values using a shale fraction of 0.9 in the lowermost portion of the hole where lithology becomes a control on velocity.

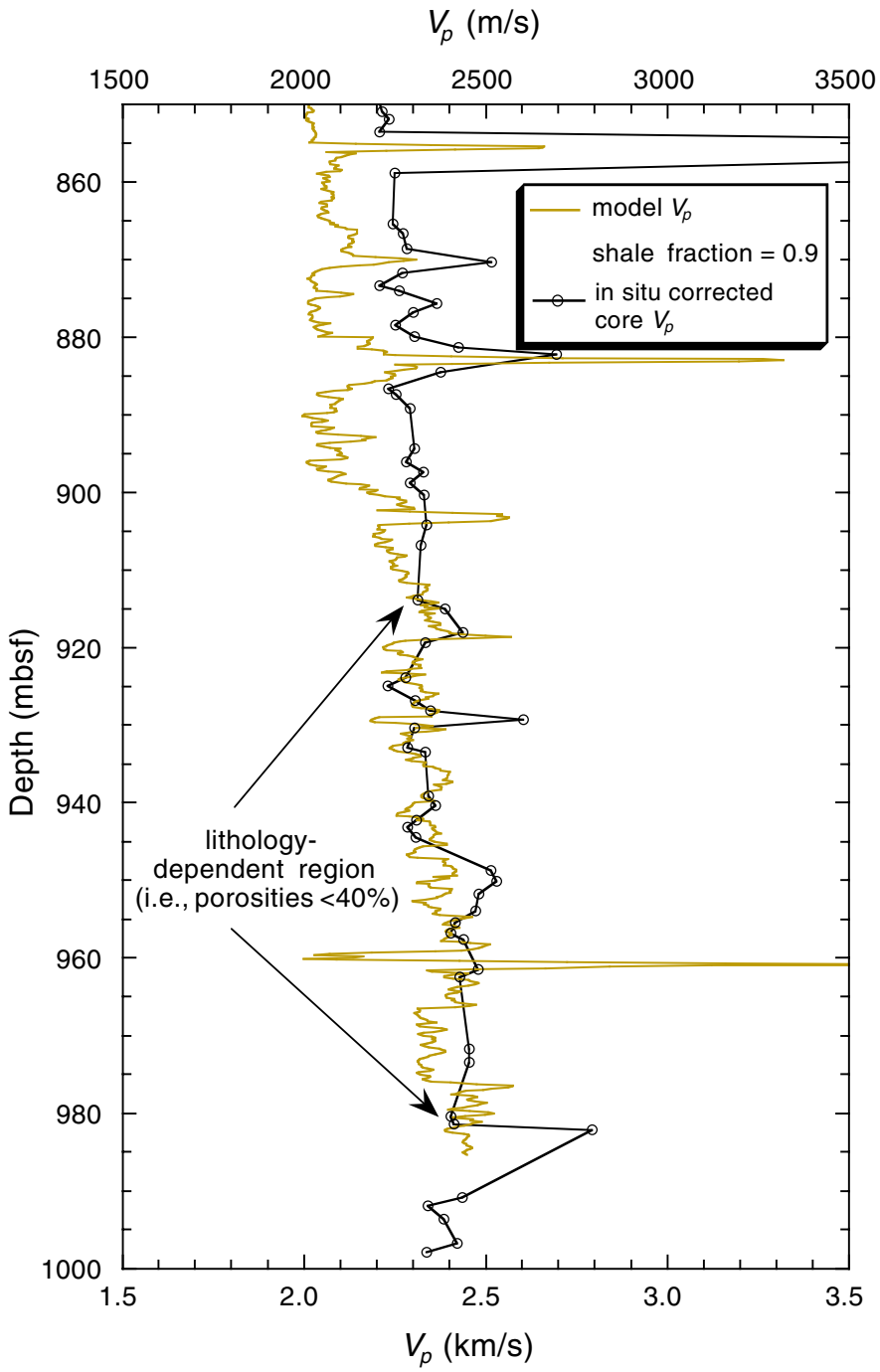

Figure F84. Wavelet used to produce the synthetic seismograms, digitized from a seafloor reflection of the site survey.

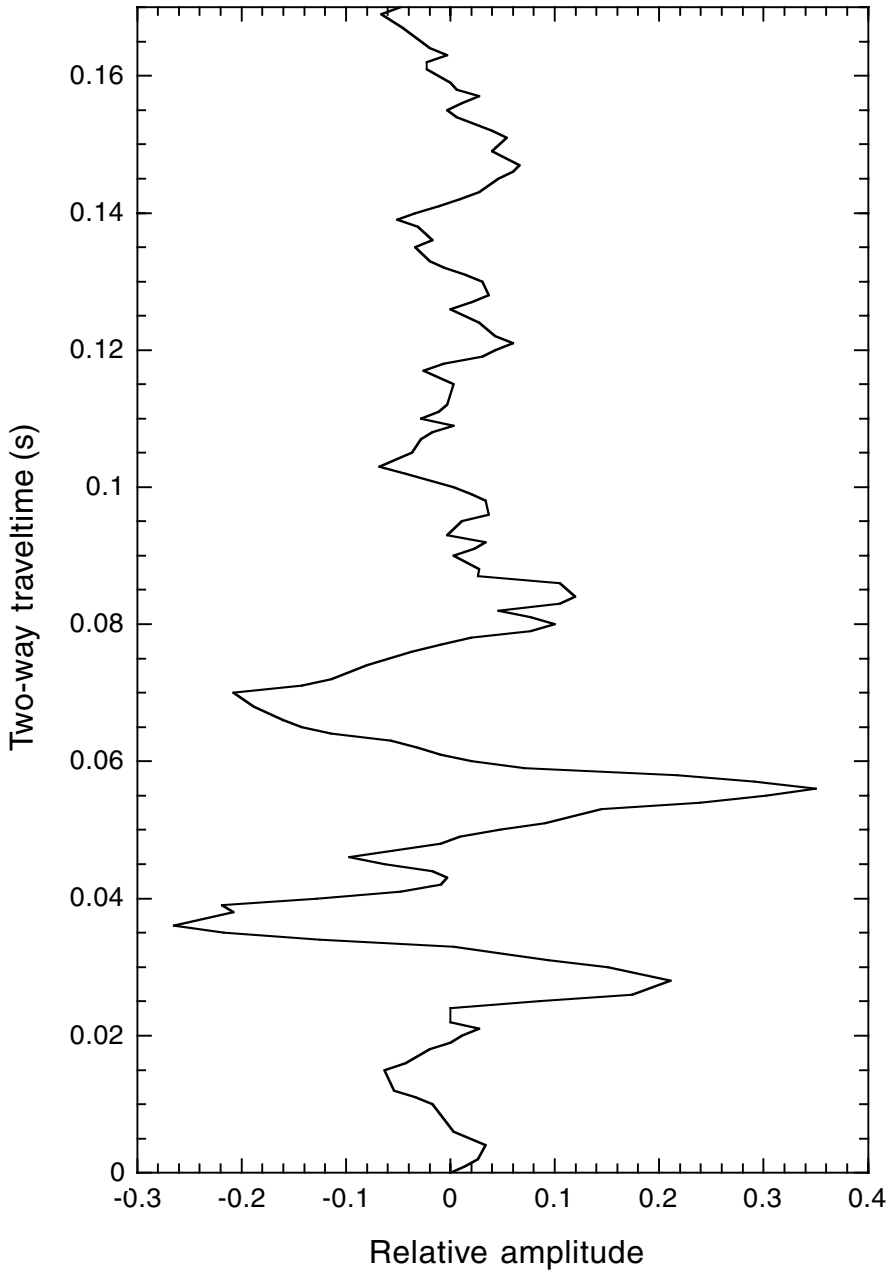

Figure F85. Synthetic seismogram overlain on the site-survey profile. This synthetic is based on a velocity log derived from density-derived porosity log, using a shale fraction of 0.5.

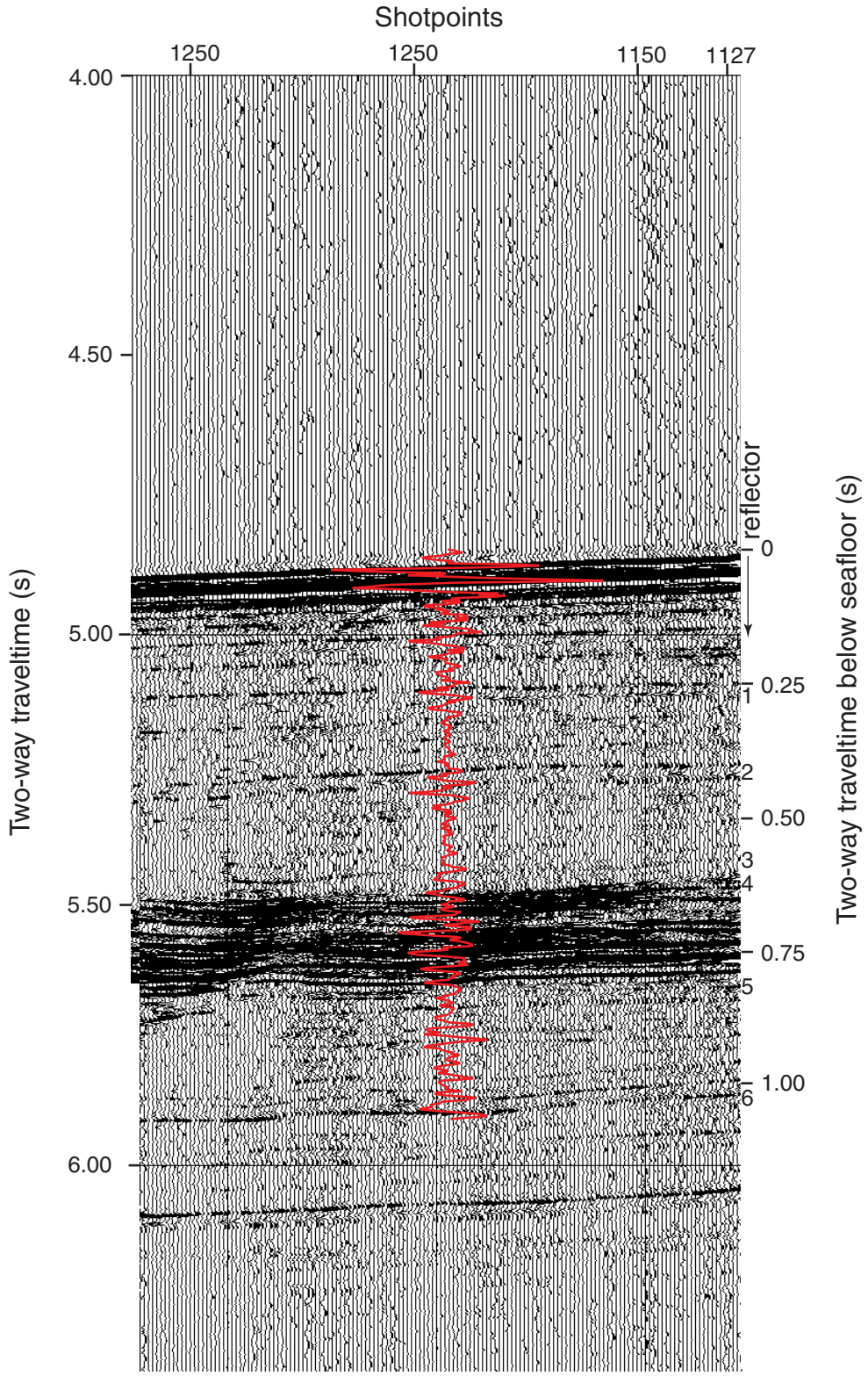

Figure F86. Comparison of x-direction core *P*-wave velocities (corrected for in situ conditions) and *P*-wave velocity derived from the density-derived porosity using a shale fraction of 0.5 in the lowermost portion of the hole where lithology becomes a control on velocity.

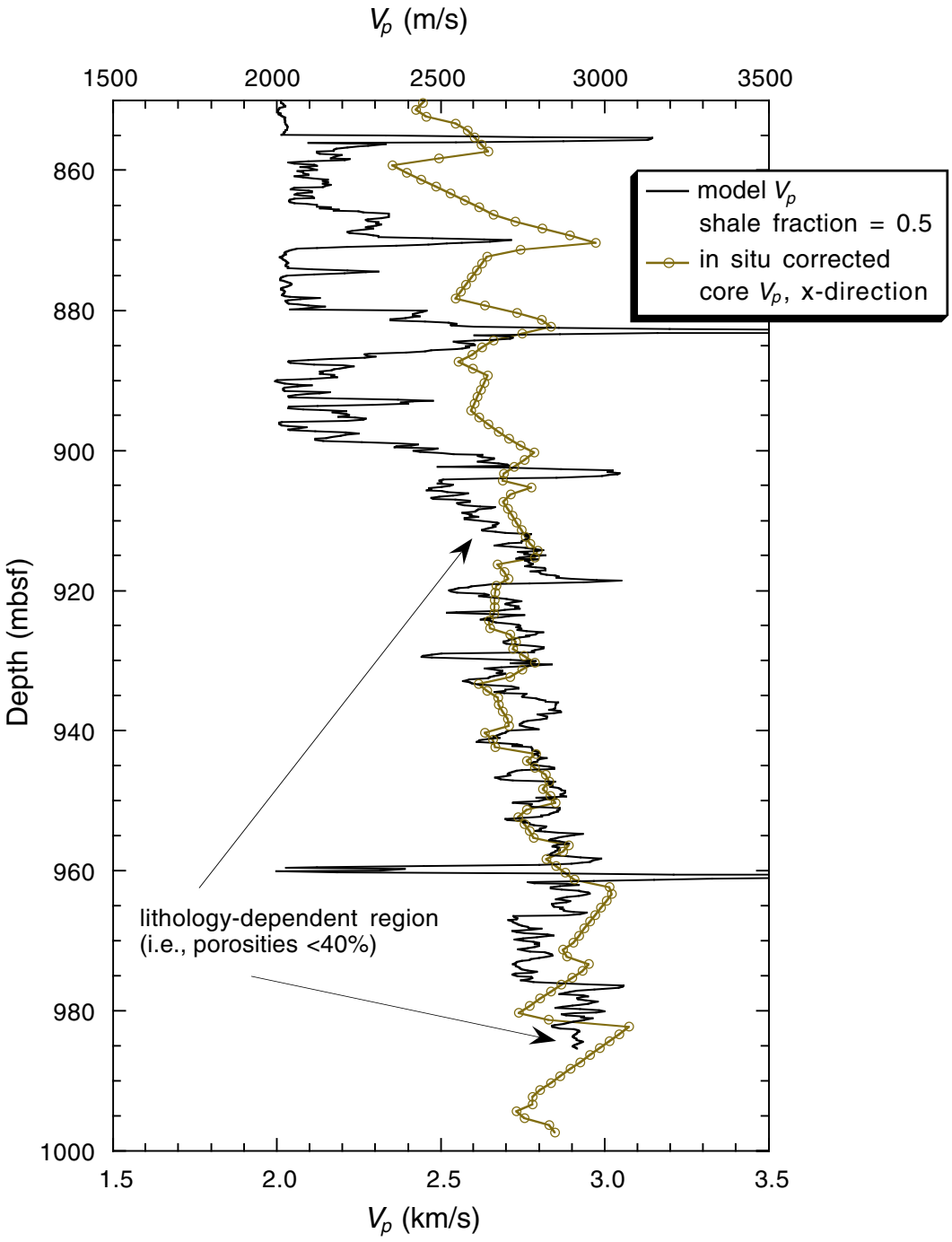

Figure F87. Synthetic seismogram wave trace placed on a depth axis with the impedance log and lithostratigraphy.

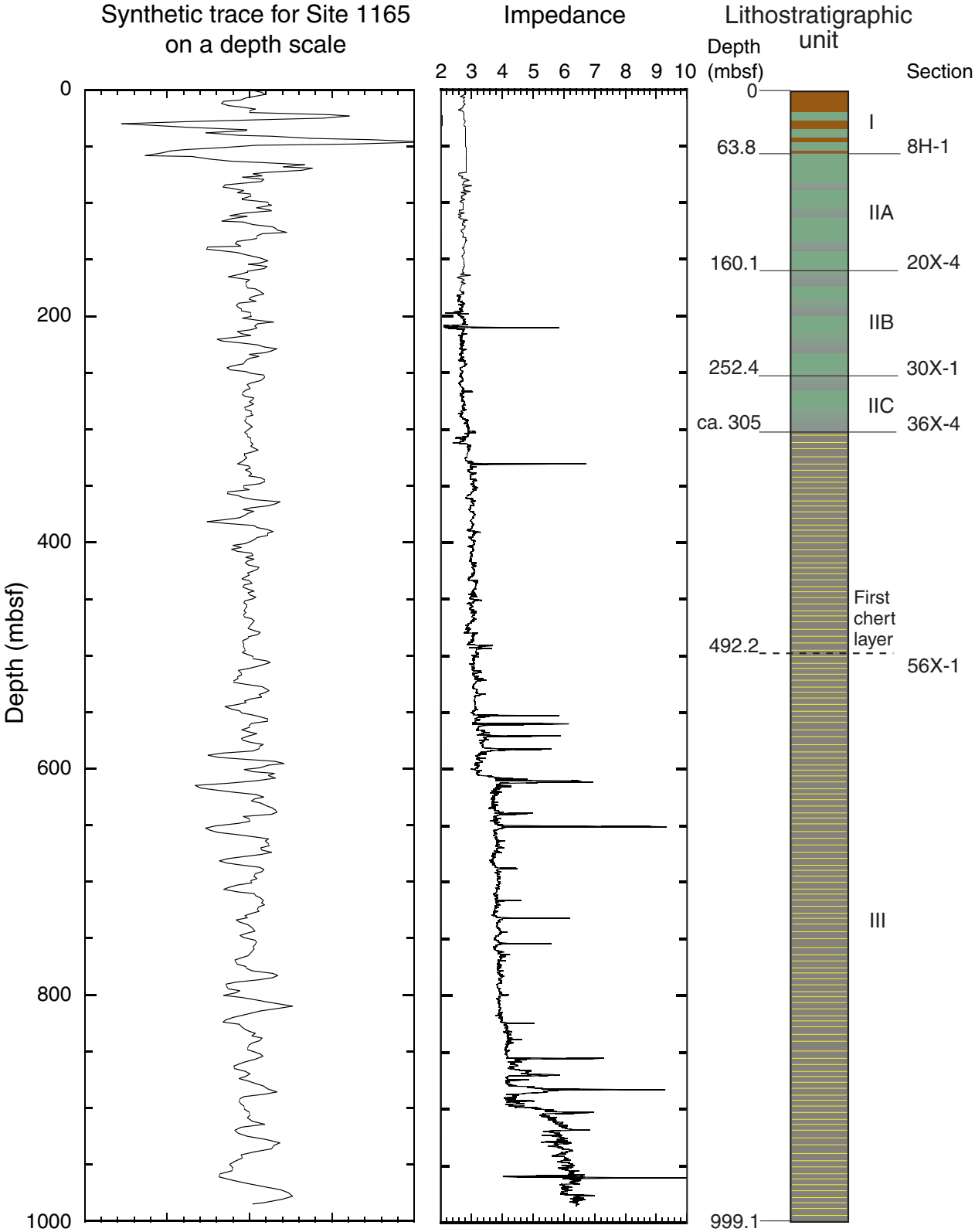

Figure F88. Reflection coefficient log on both traveltime and depth axes.

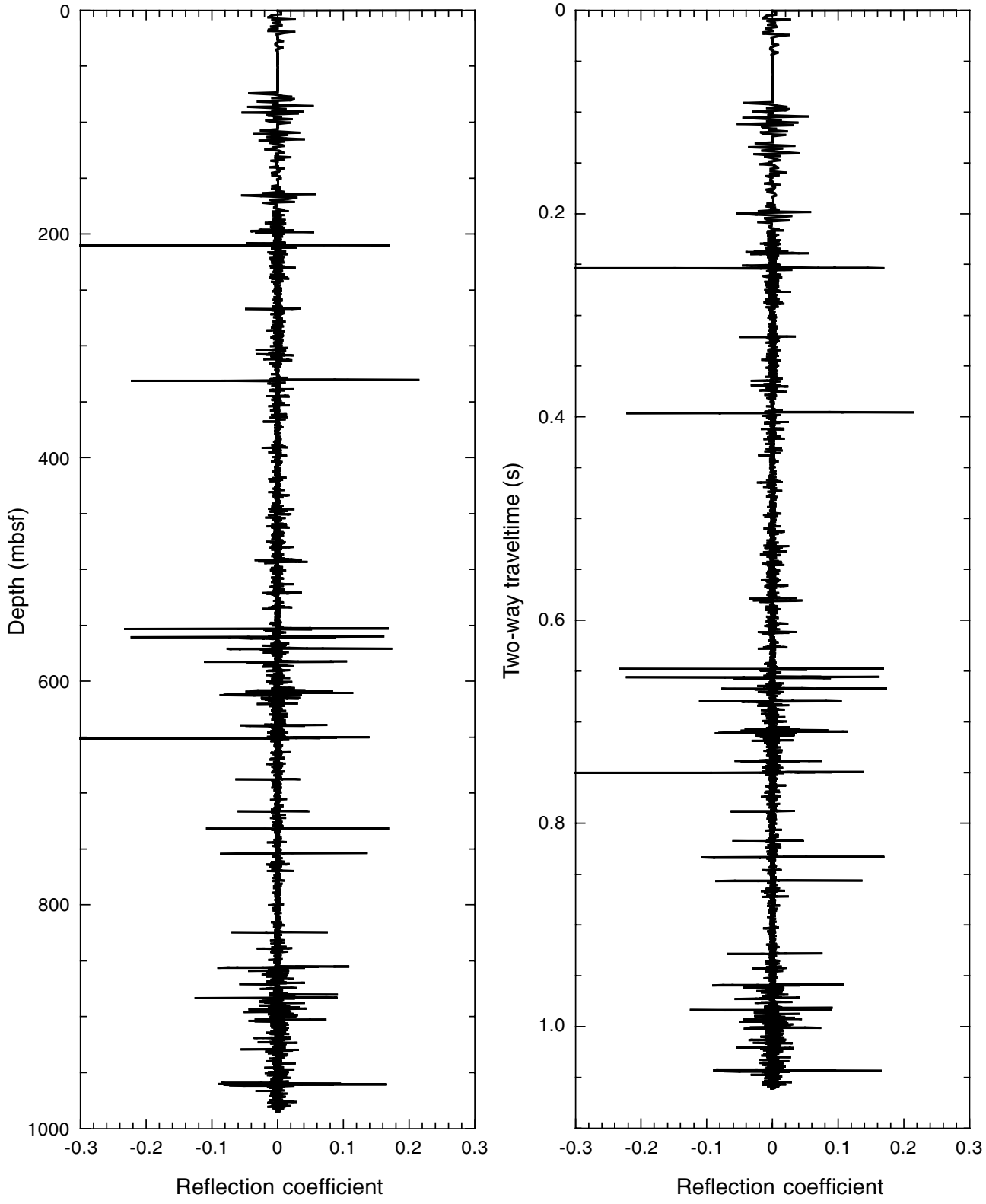

Figure F89. Downhole temperature from the temperature, acceleration, and pressure tool.

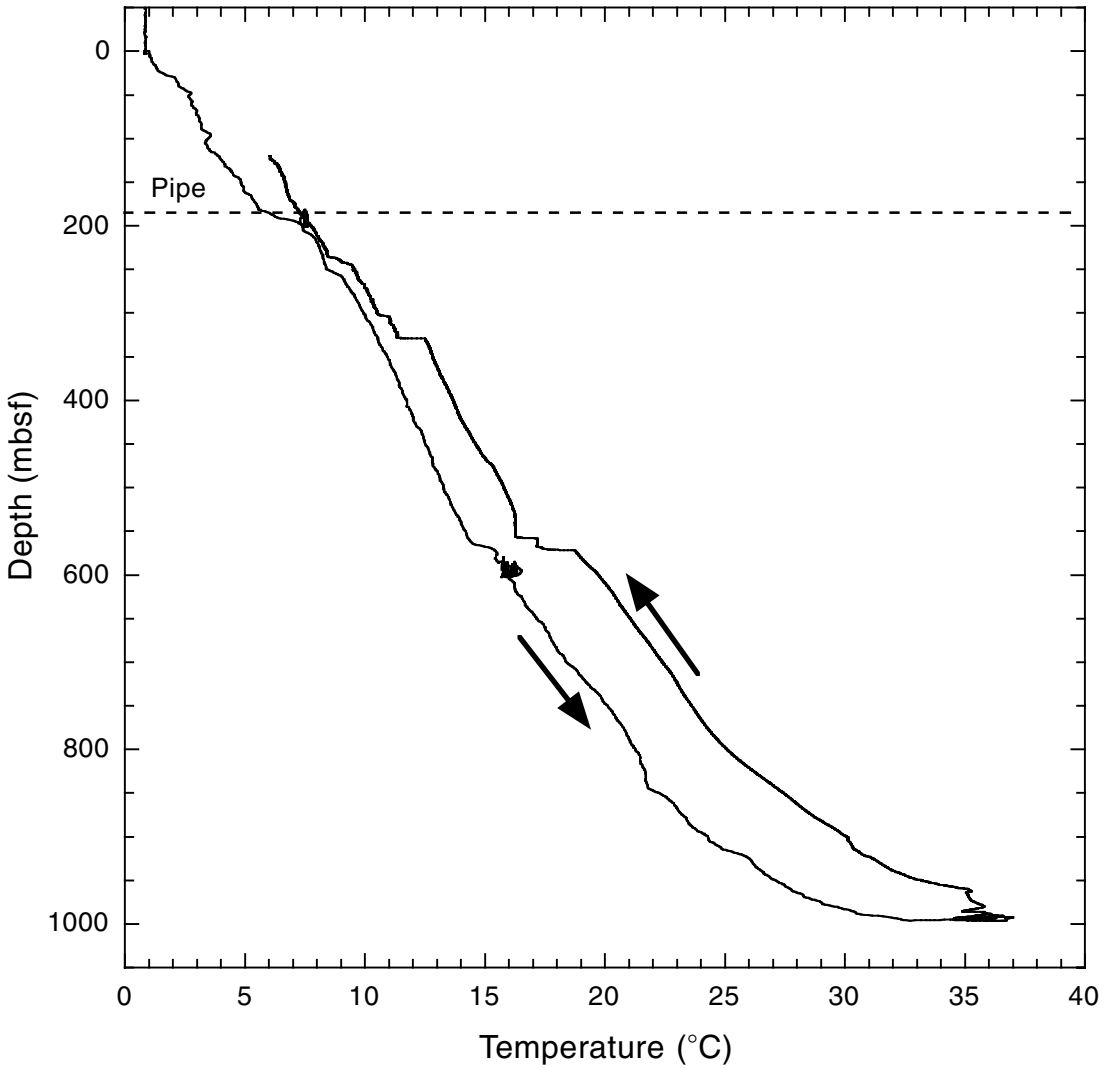

Table T1. Coring summary, Site 1165.

Core	Date (2000)	Ship local time	Depth (mbsf) Top	Depth (mbsf) Bottom	Length (m) Cored	Length (m) Recovered	Recovery (%)
188-1165A-							
1H	29 Jan	0515	0.0	5.4	5.4	5.43	100.6
				Cored:	5.4	5.43	100.6
				Drilled:	0.0		
				Total:	5.4		
188-1165B-							
1H	29 Jan	0630	0.0	6.8	6.8	6.86	100.9
2H	29 Jan	0730	6.8	16.3	9.5	9.83	103.5
3H	29 Jan	0835	16.3	25.8	9.5	8.76	92.2
4H	29 Jan	0955	25.8	35.3	9.5	10.05	105.8
5H	29 Jan	1050	35.3	44.8	9.5	8.88	93.5
6H	29 Jan	1145	44.8	54.3	9.5	9.69	102.0
7H	29 Jan	1215	54.3	63.8	9.5	0.00	0.0
8H	29 Jan	1420	63.8	73.3	9.5	9.93	104.5
9H	29 Jan	1510	73.3	82.8	9.5	8.24	86.7
10H	29 Jan	1615	82.8	92.3	9.5	9.92	104.4
11H	29 Jan	1705	92.3	101.8	9.5	8.12	85.5
12H	29 Jan	1800	101.8	106.3	4.5	0.10	2.2
13H	29 Jan	1900	106.3	115.8	9.5	9.82	103.4
14H	29 Jan	2015	115.8	125.3	9.5	8.86	93.3
15H	29 Jan	2120	125.3	128.8	3.5	3.38	96.6
16H	29 Jan	2220	128.8	138.3	9.5	6.33	66.6
17H	29 Jan	2320	138.3	147.8	9.5	9.31	98.0
18H	30 Jan	0015	147.8	148.3	0.5	0.10	20.0
19X	30 Jan	0205	148.3	156.2	7.9	2.80	35.4
20X	30 Jan	0315	156.2	165.8	9.6	8.84	92.1
21X	30 Jan	0425	165.8	175.5	9.7	6.97	71.9
22X	30 Jan	0530	175.5	185.1	9.6	9.68	100.8
23X	30 Jan	0635	185.1	194.7	9.6	9.65	100.5
24X	30 Jan	0740	194.7	204.3	9.6	4.55	47.4
25X	30 Jan	0850	204.3	213.9	9.6	0.00	0.0
26X	30 Jan	0955	213.9	223.5	9.6	0.01	0.1
27X	30 Jan	1055	223.5	233.1	9.6	8.24	85.8
28X	30 Jan	1200	233.1	242.8	9.7	9.63	99.3
29X	30 Jan	1315	242.8	252.4	9.6	0.00	0.0
30X	30 Jan	1930	252.4	253.8	1.4	1.41	100.7
31X	30 Jan	2140	253.8	262.0	8.2	0.10	1.2
32X	30 Jan	2300	262.0	271.6	9.6	3.80	39.6
33X	31 Jan	0040	271.6	281.2	9.6	9.83	102.4
34X	31 Jan	0150	281.2	290.5	9.3	9.79	105.3
35X	31 Jan	0305	290.5	299.8	9.3	7.98	85.8
36X	31 Jan	0415	299.8	309.1	9.3	9.79	105.3
37X	31 Jan	0520	309.1	318.7	9.6	9.85	102.6
38X	31 Jan	0635	318.7	328.4	9.7	9.18	94.6
39X	31 Jan	0745	328.4	338.0	9.6	8.59	89.5
40X	31 Jan	0855	338.0	347.6	9.6	9.09	94.7
41X	31 Jan	1010	347.6	357.2	9.6	5.46	56.9
42X	31 Jan	1135	357.2	366.9	9.7	7.66	79.0
43X	31 Jan	1250	366.9	376.5	9.6	6.85	71.4
44X	31 Jan	1425	376.5	386.1	9.6	6.35	66.1
45X	31 Jan	1600	386.1	395.7	9.6	6.93	72.2
46X	31 Jan	1735	395.7	405.3	9.6	8.89	92.6
47X	31 Jan	1915	405.3	414.9	9.6	0.15	1.6
48X	31 Jan	2055	414.9	424.6	9.7	9.88	101.9
49X	31 Jan	2215	424.6	434.2	9.6	9.87	102.8
50X	1 Feb	0005	434.2	443.8	9.6	9.89	103.0
51X	1 Feb	0200	443.8	453.4	9.6	6.10	63.5
52X	1 Feb	0350	453.4	463.0	9.6	4.82	50.2
53X	1 Feb	0525	463.0	472.6	9.6	8.48	88.3
54X	1 Feb	0700	472.6	482.2	9.6	7.00	72.9
55X	1 Feb	0850	482.2	491.8	9.6	5.37	55.9
56X	1 Feb	1055	491.8	501.4	9.6	4.01	41.8
57X	1 Feb	1300	501.4	511.0	9.6	3.26	34.0
58X	1 Feb	1455	511.0	520.7	9.7	5.13	52.9
59X	1 Feb	1700	520.7	530.3	9.6	7.25	75.5
60X	1 Feb	1840	530.3	540.0	9.7	4.35	44.8
61X	1 Feb	2045	540.0	549.6	9.6	1.75	18.2
62X	1 Feb	2300	549.6	559.2	9.6	4.25	44.3
63X	2 Feb	0150	559.2	568.8	9.6	0.43	4.5
64X	2 Feb	0400	568.8	578.4	9.6	3.38	35.2
65X	2 Feb	0610	578.4	588.0	9.6	0.82	8.5
66X	2 Feb	0850	588.0	597.7	9.7	9.75	100.5
67X	2 Feb	1100	597.7	607.3	9.6	8.61	89.7
68X	2 Feb	1410	607.3	616.9	9.6	0.97	10.1
69X	2 Feb	1640	616.9	621.6	4.7	0.23	4.9
70X	2 Feb	1845	621.6	626.5	4.9	0.65	13.3
71X	2 Feb	2145	626.5	636.2	9.7	0.29	3.0
72X	3 Feb	0135	636.2	645.8	9.6	0.55	5.7
73X	3 Feb	0510	645.8	655.4	9.6	1.38	14.4
74X	3 Feb	0845	655.4	665.0	9.6	3.78	39.4
75X	3 Feb	1200	665.0	674.6	9.6	1.00	10.4
76X	3 Feb	1450	674.6	682.2	7.6	0.46	6.1
				Cored:	682.2	433.96	63.6
				Drilled:	0.0		
				Total:	682.2		
188-1165C-							
1R	4 Feb	2125	54.0	63.6	9.6	9.70	101.0
2R	6 Feb	0945	673.0	682.0	9.0	5.78	64.2
3R	6 Feb	1150	682.0	691.7	9.7	8.99	92.7
4R	6 Feb	1340	691.7	701.3	9.6	8.98	93.5
5R	6 Feb	1530	701.3	710.9	9.6	8.61	89.7
6R	7 Feb	1225	710.9	720.6	9.7	8.69	89.6
7R	7 Feb	1420	720.6	730.2	9.6	7.28	75.8
8R	7 Feb	1610	730.2	739.9	9.7	8.75	90.2
9R	7 Feb	1755	739.9	749.5	9.6	9.09	94.7
10R	7 Feb	1945	749.5	759.1	9.6	8.05	83.9
11R	7 Feb	2130	759.1	768.7	9.6	7.48	77.9
12R	7 Feb	2310	768.7	778.3	9.6	9.72	101.3
13R	8 Feb	0100	778.3	788.0	9.7	4.89	50.4
14R	8 Feb	0245	788.0	797.6	9.6	9.25	96.4
15R	8 Feb	0435	797.6	807.2	9.6	9.60	100.0
16R	8 Feb	0615	807.2	816.5	9.3	8.73	93.9
17R	8 Feb	0750	816.5	826.1	9.6	5.67	59.1
18R	8 Feb	0940	826.1	835.7	9.6	9.75	101.6
19R	8 Feb	1115	835.7	845.4	9.7	9.82	101.2
20R	8 Feb	1245	845.4	855.0	9.6	9.08	94.6
21R	8 Feb	1440	855.0	864.7	9.7	4.55	46.9
22R	8 Feb	1630	864.7	874.3	9.6	9.77	101.8
23R	8 Feb	1825	874.3	883.9	9.6	8.57	89.3
24R	8 Feb	2020	883.9	893.6	9.7	6.03	62.2
25R	9 Feb	1730	893.6	903.2	9.6	7.07	73.6
26R	9 Feb	1930	903.2	912.8	9.6	4.17	43.4
27R	9 Feb	2130	912.8	922.5	9.7	7.03	72.5
28R	9 Feb	2330	922.5	931.7	9.2	8.25	89.7
29R	10 Feb	0150	931.7	941.3	9.6	9.77	101.8
30R	10 Feb	0350	941.3	951.0	9.7	9.25	95.4
31R	10 Feb	0550	951.0	960.6	9.6	7.40	77.1
32R	10 Feb	0815	960.6	970.2	9.6	3.56	37.1
33R	11 Feb	1205	970.2	979.8	9.6	3.82	39.8
34R	12 Feb	1915	979.8	989.5	9.7	3.41	35.2
35R	11 Feb	2155	989.5	999.1	9.6	8.77	91.4
				Cored:	335.7	269.33	80.2
				Drilled:	663.4		
				Total:	999.1		

Notes: NA = not applicable. This table is also available in **ASCII format.**

Table T2. Expanded coring summary, Site 1165.

Core	Date (2000)	Ship local time	Core depth (mbsf) Top	Core depth (mbsf) Bottom	Length (m) Cored	Length (m) Recovered	Recovery (%)	Section	Length (m) Liner	Length (m) Curated	Section depth (mbsf) Top	Section depth (mbsf) Bottom	Catwalk samples	Comment
Position: 64.37964°S, 67.21906°E Water depth (mbrf; APC calculation): 3548.1														
188-1165A-														
1H	29 Jan	0515	0.0	5.4	5.4	5.43	100.6							
								1	0.50	0.50	0.00	0.50	IW, PAL	
								2	0.50	0.50	0.50	1.00	IW	
								3	0.50	0.50	1.00	1.50	IW	
								4	0.50	0.50	1.50	2.00	IW	
								5	0.50	0.50	2.00	2.50	IW	
								6	0.50	0.50	2.50	3.00	IW	
								7	0.50	0.50	3.00	3.50	IW	
								8	0.50	0.50	3.50	4.00	IW, PAL	
								9	0.50	0.50	4.00	4.50	IW	
								10	0.50	0.50	4.50	5.00	IW	
								11	0.22	0.22	5.00	5.22		
								CC (w/11)	0.21	0.21	5.22	5.43	PAL	
									5.43	5.43				
				Totals:	5.4	5.43	100.6							
Position: 64.37964°S, 67.21906°E Water depth (mbrf; APC calculation): 3548.7														
188-1165B-														
1H	29 Jan	0630	0.0	6.8	6.8	6.86	100.9							
								1	1.50	1.50	0.00	1.50		
								2	1.50	1.50	1.50	3.00		
								3	1.50	1.50	3.00	4.50		
								4	1.50	1.50	4.50	6.00	IW	
								5	0.66	0.66	6.00	6.66	HS	
								CC (w/5)	0.20	0.20	6.66	6.86	PAL	
									6.86	6.86				
2H	29 Jan	0730	6.8	16.3	9.5	9.83	103.5							
								1	1.50	1.50	6.80	8.30		
								2	1.50	1.50	8.30	9.80	IW	
								3	1.50	1.50	9.80	11.30	IW	
								4	1.50	1.50	11.30	12.80	IW	
								5	1.50	1.50	12.80	14.30	HS, IW	
								6	1.50	1.50	14.30	15.80	IW	
								7	0.68	0.68	15.80	16.48		
								CC (w/7)	0.15	0.15	16.48	16.63	PAL	
									9.83	9.83				

Notes: CC = core catcher (number in parenthesis indicates which section the core catcher is stored with). NS = all of the core catcher was used for paleontology sample, IW = interstitial water, HS = headspace sample, PAL = paleontology sample, CARL = whole round for geotechnical experiments, HSTL = headspace sample for shore-based analysis. Only a portion of the table appears here. The complete table is available in **ASCII format.**

Table T3. Facies description and characteristics, Site 1165.

Facies	Description	Structure	Bioturbation	IRD content
I-1	Yellowish gray to brown diatom clay and foraminifer-bearing diatom clay	Red color banding, red and dark mottling	Strong	Common
I-2	Interbedded greenish gray and dark grayish brown to dark gray diatom clay	Silt laminae, stringers	Strong	Rare
I-3	Dark grayish brown diatom ooze	Structureless	Strong	Rare
I-4	Deformed facies I-1 and I-2	Flame-like injection structures, mud chips	Strong	Common
II-1	Greenish gray diatom clay	Structureless and burrowed	Moderate	Common
II-2	Dark gray diatom-bearing clay	Color banding, rare silt laminae	Moderate	Rare
II-3	Nannofossil chalk and nannofossil clay	Burrowed	Moderate	Absent
III-1	Dark gray to black claystone with silt partings and laminae	Planar lamination, rare cross-lamination	Rare	Rare
III-2	Greenish gray claystone and diatom-bearing claystone	Structureless/burrowed, rare lamination	Moderate	Common

Note: IRD = ice-rafted debris.

Table T4. Lonestone content of different-colored facies from X-radiographs, Site 1165.

Core	Section	Interval (cm)	X-ray ID code	Color	IRD content
188-1165B-					
10H	2	10-36	U 56	G	A
10H	3	93-119	L 56	G	A
10H	3	93-119	L 56	B	C
13H	1	56-81	L 13H	G	C
13H	2	56-81	U 13H	G	R
23X	5	59-81	L 777	G	R
33X	4	82-111	U YYY	G	R
33X	4	82-111	U YYY	B	N
34X	2	42-67	L 55	G	N
34X	2	42-67	L 55	B	N
34X	6	34-59	U 55	G	A
35X	2	91-115	L 59	G	R
38X	2	9-38	U 777	G	N
38X	2	90-116	L 5	G	N
38X	2	90-116	L 5	B	N
42X	2	17-45	U 9	G	C
42X	3	31-58	U 5	G	C
42X	3	31-58	U 5	B	C
48X	3	4-28	U 95	B	R
48X	3	23-49	U 65	G	R
48X	3	23-49	U 65	B	N
48X	3	44-69	U 59	G	C
50X	1	53-78	L 65	G	A
50X	6	116-140	L 95	B	N
58X	2	64-93	L BB	G	N
58X	3	89-117	U BB	G	C
59X	1	57-85	L B	G	R
62X	3	25-54	U B	G	R
67X	4	26-55	L YYY	G	R
67X	4	26-55	L YYY	B	R
188-1165C-					
3R	1	70-95	L 3RB	B	N
3R	3	70-95	U 3RB	B	N
3R	4	78-103	U 3RB	G	C
3R	6	43-68	L 3RB	G	N
3R	6	43-68	L 3RB	B	N
5R	3	77-102	L RB	G	C
5R	3	77-102	L RB	B	N
5R	5	101-126	U RB	G	N
5R	5	101-126	U RB	B	N

Notes: X-ray identification code: U = upper, L = lower. Color of facies: G = greenish gray clay (stone), B = dark gray clay (stone). IRD (ice-rafted debris) content: A = abundant, C = common, R = rare, N = none.

Table T5. Summary of diatom datums identified, Holes 1165B and 1165C.

Upper sample		Lower sample			
Core, section, interval (cm)	Interval depth (mbsf)	Core, section, interval (cm)	Interval depth (mbsf)	Event	Taxon
188-1165B-		188-1165B-			
1H-2, 20-21	1.70	**1H-5, 20-21**	**6.20**	LO	*Actinocylclus ingens*
1H-5, 20-21	6.20	**2H-2, 95-96**	**9.25**	LO	*Fragilariopsis barronii*
2H-2, 95-96	9.25	**3H-1, 95-96**	**17.25**	LO	*Thalassiosira kolbei*
3H-1, 95-96	17.25	**3H-2, 20-21**	**18.00**	LO	*Thalassiosira vulnifica*
3H-2, 20-21	18.00	**3H-3, 20-21**	**19.50**	LO	*Thalassiosira insigna*
3H-CC	**25.01**	4H-1, 20-21	26.00	FO	*Thalassiosira vulnifica*
5H-1, 127-128	**36.57**	5H-2, 127-128	38.07	FO	*Fragilariopsis interfrigidaria*
5H-4, 95-96	**40.75**	5H-5, 60-61	41.90	FO	*Fragilariopsis barronii*
6H-3, 95-96	**48.75**	6H-4, 59-60	49.89	FO	*Thalassiosira inura*
9H-CC	**81.39**	**10H-1, 20-21**	**83.00**	FO	*Hemidiscus triangularus*
11H-CC	**100.32**	12H-CC	101.80	FO	*Hemidiscus ovalis*
12H-CC	101.80	13H-6, 70-71	114.50	FO	*Thalassiosira torokina*
23X-3, 20-21	188.30	**23X-CC**	**194.70**	LO	*Denticulopsis dimorpha*
27X-CC	**231.69**	28X-CC	242.68	FO	*Denticulopsis dimorpha*
28X-CC	**242.68**	30X-CC	253.71	FO	*Denticulopsis praedimorpha*
33X-CC	**265.70**	34X-CC	290.89	FO	*Nitzschia denticuloides*
35X-CC	**298.38**	36X-CC	309.52	FCO	*Denticulopsis simonsenii*
38X-CC	**327.78**	39X-CC	336.89	FO	*Actinocyclus ingens* v. *nodus*
50X-CC	**443.99**	51X-CC	449.80	FCO	*Actinocyclus ingens*
55X-CC	**487.52**	56X-CC	495.81	FO	*Denticulopsis maccollumii*
55X-CC	**487.52**	56X-CC	495.81	FO	*Crucidenticula kanayae*
59X-CC	527.92	**60X-CC**	**534.60**	LO	*Thalassiosira praefraga*
188-1165C-		188-1165C-			
10R-3, 127-129	**750.77**	—	—	FO	*Thalassiosira praefraga*

Notes: Sample designations and depths in bold type represent the occurrence of each taxon, and plain type represents sample-spacing uncertainty for each datum. LO = last occurrence, FO = first occurrence, FCO = first common occurrence. — = not identified due to opal-A dissolution.

Table T6. Summary of diatom and radiolarian biostratigraphic datums recognized in Holes 1165B and 1165C and calibrated ages for each datum event.

Upper sample		Lower sample					
Core, section, interval (cm)	Interval depth (mbsf)	Core, section, interval (cm)	Interval depth (mbsf)	Event	Taxon	Constraint	Calibrated age (Ma)
Diatoms:							
188-1165B-,		188-1165B-					
1H-2, 20-21	1.70	**1H-5, 20-21**	**6.20**	LO	*Actinocylclus ingens*	<	0.66
1H-5, 20-21	6.20	**2H-2, 95-96**	**9.25**	LO	*Fragilariopsis barronii*	>	1.35
2H-2, 95-96	9.25	**3H-1, 95-96**	**17.25**	LO	*Thalassiosira kolbei*	>	1.8-2.0
3H-1, 95-96	17.25	**3H-2, 20-21**	**18.00**	LO	*Thalassiosira vulnifica*	>	2.2-2.3
3H-2, 20-21	18.00	**3H-3, 20-21**	**19.50**	LO	*Thalassiosira insigna*	>	2.5-2.6
3H-CC	**25.01**	4H-1, 20-21	26.00	FO	*Thalassiosira vulnifica*	<	2.8-3.2
5H-1, 127-128	**36.57**	5H-2, 127-128	38.07	FO	*Fragilariopsis interfrigidaria*	<	3.7-3.8
5H-4, 95-96	**40.75**	5H-5, 60-61	41.90	FO	*Fragilariopsis barronii*	<	4.2-4.4
6H-3, 95-96	**48.75**	6H-4, 59-60	49.89	FO	*Thalassiosira inura*	<	4.8-4.9
12H-CC	**101.80**	13H-6, 70-71	114.50	FO	*Thalassiosira torokina*	<	8.5-10.0
23X-3, 20-21	188.30	**23X-CC**	**194.70**	LO	*Denticulopsis dimorpha*	>	11.0-11.1
27X-CC	**231.69**	28X-CC	242.68	FO	*Denticulopsis dimorpha*	<	12.2-12.8
28X-CC	**242.68**	30X-CC	253.71	FO	*Denticulopsis praedimorpha*	<	12.8-13.1
35X-CC	**298.38**	36X-CC	309.52	FCO	*Denticulopsis simonsenii*	<	14.1-14.6
38X-CC	**327.78**	39X-CC	336.89	FO	*Actinocyclus ingens* v. *nodus*	<	14.5-14.7
50X-CC	**443.99**	51X-CC	449.80	FCO	*Actinocyclus ingens*	<	15.9-16.4
55X-CC	**487.52**	56X-CC	495.81	FO	*Denticulopsis maccollumii*	<	16.7-17.0
55X-CC	**487.52**	56X-CC	495.81	FO	*Crucidenticula kanayae*	<	17.5-17.7
59X-CC	527.92	**60X-CC**	**534.60**	LO	*Thalassiosira praefraga*	>	18.3-19.1
188-1165C-		188-1165C-					
10R-3, 127-129	**750.77**	—	—	FO	*Thalassiosira praefraga*	<	19.9-20.8
Radiolarians:							
188-1165B-		188-1165B-					
3H-CC	25.01	**4H-CC**	**35.75**	LO	*Prunopyle titan*	>	3.5
4H-CC	**35.75**	5H-CC	44.08	FO	*Helotholus vema*	<	4.57
6H-CC	54.39	**1R-CC**	**63.60**	LCO	*Lychnocanoma grande*	>	5.03
11H-CC	**100.32**	12H-CC	101.80	FO	*Acrosphaera? labrata*	<	7.71
12H-CC	101.80	**13H-CC**	**116.02**	LO	*Cycladophora spongothorax*	>	9.12
15H-CC	**128.58**	16H-CC	135.03	FCO	*Ceratocyrtis stigi*	<	9.32
21X-CC	**172.67**	22X-CC	185.08	FO	*Acrosphaera australis*	<	10.36
21X-CC	172.67	**22X-CC**	**185.08**	LO	*Cycladophora humerus*	>	10.53
23X-CC	194.70	**24X-CC**	**199.15**	LO	*Actinonomma golownini*	>	10.77
38X-CC	**327.78**	39X-CC	336.89	FO	*Cycladophora spongothorax*	<	12.55
38X-CC	**327.78**	39X-CC	336.89	FO	*Cycladophora humerus*	<	14.18
54X-CC	**479.50**	55X-CC	487.52	FO	*Cycladophora golli regipileus*	<	19.11

Notes: Sample designations and depths in bold type represent the occurrence of each taxon, and plain type represents sample-spacing uncertainty for each datum. LO = last occurrence, FO = first occurrence, FCO = first common occurrence, LCO = last common occurrence. — = not identified due to opal-A dissolution.

Table T7. Interstitial water chemistry from shipboard measurements, Site 1165.

Core, section	Depth (mbsf)	Salinity	pH	Alk (mM)	Cl (mM)	SO_4 (mM)	NH_4 (µM)	PO_4 (µM)	H_4SiO_2 (µM)	Ca (mM)	Mg (mM)	Sr (µM)	K (mM)	Na (mM)	Li (µM)	Mn (µM)
188-1165A-																
1H-1	0.45	35.0	7.75	2.93	564.5	28.9	35.7	2.8	522.0	10.8	54.2	105.6	12.1	483.3	29.1	3.4
1H-2	0.95	35.0	7.97	2.55	555.0	28.2	21.4	4.2	648.0	10.7	53.4	107.7	13.2	472.3	30.6	0.8
1H-3	1.45	35.0	8.28	2.82	564.0	28.8	20.0	4.4	608.0	10.8	53.6	101.8	12.3	483.4	30.4	1.5
1H-4	1.95	35.0	7.92	2.72	559.0	28.8	21.4	2.8	602.0	10.6	52.2	112.7	12.2	481.6	33.2	5.1
1H-5	2.45	35.0	8.25	2.74	557.0	28.0	20.0	4.4	642.0	10.6	52.4	104.2	12.4	477.3	35.6	1.4
1H-6	2.95	35.0	7.92	3.00	559.0	27.9	54.3	3.5	658.0	10.7	51.8	113.3	13.2	479.8	43.4	3.9
1H-7	3.45	35.0	8.15	2.75	554.0	28.1	52.9	4.7	576.0	11.0	53.8	113.4	12.7	470.6	32.1	1.9
1H-8	3.95	35.0	8.01	2.89	561.0	28.8	50.0	5.1	570.0	10.9	52.8	100.3	12.0	482.1	31.3	1.1
1H-9	4.45	35.0	8.19	2.96	562.0	28.9	48.6	5.8	622.0	11.0	52.9	117.3	12.5	482.5	37.6	2.6
1H-10	4.95	35.0	8.09	3.05	563.5	28.3	52.9	5.3	610.0	10.9	51.9	105.7	9.6	487.9	29.7	1.9
188-1165B-																
1H-4	5.95	35.0	7.84	3.35	559.5	27.8	51.4	4.2	612.0	11.0	52.2	106.9	9.7	482.3	31.1	4.1
2H-2	9.75	35.0	7.83	3.22		27.1	54.3	4.4	712.0	11.0	50.3	107.9	9.9	492.9	27.5	5.1
2H-3	11.25	35.0	7.93	3.43	561.0	27.2	58.6	5.8	700.0	10.9	50.3	109.5	10.6	485.9	30.5	11.0
2H-4	12.75	35.0	7.65	3.65	567.5	26.2	62.9	6.3	764.0	11.5	51.2	109.9	11.3	487.0	31.1	24.3
2H-5	14.25	35.0	7.88	3.54	564.0	25.6	61.4	6.5	682.0	11.2	52.2	111.1	11.0	480.9	28.9	53.4
2H-6	15.75	35.0	7.65	3.56	566.5	25.5	64.3	6.0	680.0	11.0	51.0	114.9	11.4	485.6	29.3	58.8
3H-1	17.75	35.0	7.29	3.60	568.0	25.3	72.9	8.1	634.0	11.1	51.4	119.7	11.1	486.0	30.3	94.0
3H-2	19.25	35.0	7.80	3.75	559.0	24.6	82.9	7.9	676.0	11.1	50.9	110.3	11.1	476.9	30.1	108.2
3H-3	20.75	35.0	7.89	3.72	568.0	24.7	84.3	7.9	662.0	11.0	50.5	112.8	11.5	486.4	28.5	126.7
3H-4	22.25	35.0	7.88	3.84	569.1	25.1	82.9	8.1	744.0	10.9	49.7	111.7	12.5	489.3	29.3	143.9
3H-5	23.75	35.0	7.83	3.69	570.1	24.5	91.4	8.8	662.0	11.1	50.0	114.2	12.4	488.0	26.3	143.8
4H-1	27.20	35.0	7.91	4.00	565.0	23.0	101.4	9.8	678.0	10.9	49.0	112.2	11.7	483.5	27.2	154.3
4H-2	28.70	35.0	7.93	4.11	567.5	23.6	111.4	7.9	688.0	11.0	48.1	109.7	12.3	488.3	27.3	156.7
4H-4	31.70	35.0	7.86		573.1	22.7	118.6	6.5	776.0	10.8	48.9	118.7	11.9	487.1	29.6	168.3
4H-5	33.20	35.0	7.93	4.34	568.0	22.6	124.3	8.6	790.0	10.8	48.5	119.9	12.2	486.9	27.1	160.8
4H-6	34.70	35.0	7.94	4.20	571.1	22.0	131.4	7.4	744.0	11.0	49.6	123.4	11.4	486.6	27.6	167.1
5H-1	36.70	35.0	7.97	4.22	566.0	22.5	148.6	8.4	772.0	11.1	49.5	127.1	11.6	482.3	31.9	162.5
5H-2	38.20	35.0	7.80	3.75	572.1	22.2	152.9	9.1	738.0	11.0	49.0	113.2	11.9	488.4	26.8	156.8
5H-3	39.70	34.5	8.02	4.08	567.5	23.9	162.9	8.8	748.0	10.9	48.7	117.8	11.5	488.7	30.1	162.8
5H-4	41.20	34.5	8.08	4.27	567.5	19.1	164.3	8.4	704.0	9.7	45.4	128.6	9.8	490.0	29.2	156.8
5H-5	42.70	34.0	7.73	4.26	570.6	20.5	165.7	8.6	670.0	11.0	48.3	129.8	10.9	486.1	28.8	157.6
6H-1	46.20	34.0	7.66	4.23	567.5	19.8	142.9	7.4	742.0	10.4	46.2	111.3	10.9	487.4	27.0	151.1
6H-2	47.70	34.0	7.50	4.29	549.4	19.6	132.9	7.9	788.0	10.8	47.2	117.4	11.0	465.9	29.0	162.2
6H-3	49.20	34.0	7.86	4.24	573.1	19.4	141.4	7.9	752.0	10.7	47.4	124.2	11.5	488.2	29.5	159.7
6H-4	50.70	34.0	7.93	4.59	571.6	18.6	155.7	6.5	856.0	10.6	46.5	129.5	11.6	487.7	30.3	152.8
6H-5	52.20	34.0	7.78	4.51	568.0	19.1	162.9	5.8	778.0	10.4	45.3	127.5	11.2	488.3	30.1	149.7
6H-6	53.70	34.0	8.04	4.45	567.0	18.0	162.9	6.7	774.0	10.9	47.0	105.2	11.0	480.6	26.7	154.3
8H-4	69.70	34.0	7.86	5.34	565.0	15.1	208.6	5.8	866.0	10.3	44.2	141.5	10.2	481.1	33.7	127.6
9H-4	79.20	33.0	7.88	5.45	558.0	14.1	250.0	5.8	836.0	10.4	44.3	138.3	9.7	472.5	32.3	102.0
10H-4	88.70	33.0	7.91	5.83	570.6	11.3	254.3	7.2	900.0	9.8	41.5	134.5	9.4	487.0	30.1	83.6
11H-4	98.15	33.0	7.79	5.81	568.0	10.0	292.9	7.9	822.0	9.8	41.0	129.6	8.7	483.4	29.6	77.6
15H-2	128.20	32.0	7.93	7.34	564.5	2.9	394.3	9.8	844.0	9.0	36.8	149.2	7.4	478.8	25.5	23.9
19X-1	149.70	31.5	8.07	7.43	566.5	2.2	384.3	5.1	840.0	8.7	36.6		6.9	481.0		
23X-4	191.00	31.5	7.88	6.54	558.0	0.4	482.9	2.3	988.0	9.4	34.5	159.5	6.0	471.4	28.3	7.4
27X-3	227.90	31.5	7.97	6.25	559.0	0.1	535.7	0.9	866.0	10.7	32.1	192.5	5.6	474.0	35.7	15.1
32X-2	264.90	31.5	7.97	6.54	570.6	0.0	612.9	0.9	946.0	12.8	31.8	205.0	5.1	482.9	39.2	23.2
35X-4	296.40	31.5	8.18	6.05	569.1	0.5	625.7	0.9	860.0	13.7	30.6	204.4	4.9	482.4	41.7	17.7
38X-4	324.60	31.5	8.02	5.76	568.6	0.0	700.0	0.7	984.0	14.9	30.4	243.9	4.1	479.5	50.9	11.8
41X-3	352.00	32.0	8.08	5.66	558.5	0.5	760.0	0.9	932.0	16.0	29.3	220.5	3.7	470.8	49.3	17.5
44X-4	382.40	31.5	8.01	5.35	561.5	0.0	807.1	0.5	930.0	17.6	28.3	247.7	3.8	471.3	58.8	14.3
48X-4	420.75	31.5	7.78	4.91	560.5	1.7	764.3	0	972.0	19.2	29.9	216.9	3.1	467.4	49.8	21.9
51X-3	448.15	32.0	7.78	4.91	558.0	0.7	791.4	0	772.0	20.3	27.4	164.5	2.8	461.0	36.5	11.5
55X-3	486.70	31.5	7.88	4.58	565.0	0.2	790.0	0	920.0	19.9	24.3	266.8	2.2	479.4	65.3	23.2
58X-2	513.85	31.5	7.93	3.77	555.5	1.4	810.0	0	792.0	23.2	26.5	274.3	2.4	460.2	70.7	14.7
62X-2	552.40	31.5	7.99	3.33	555.0	1.7	787.1	0	688.0	25.0	26.4		2.6	456.4		
67X-3	602.10	31.5	7.97	2.54	546.9	2.2	705.7	0	688.0	29.7	25.2	123.3	2.0	441.9	26.0	11.1
72X-1	636.60	32.0	7.97	2.54		0.9			486.0	36.6	27.9		3.8			
188-1165C-																
1R-4	59.90	34.0	7.80	4.09		19.7	175.7		755.0	10.4	45.3	121.9	10.4	480.6	29.1	120.8
2R-3	677.33	31.0	8.04	1.96		2.0	824.2		492.9	38.6	22.3	352.0	1.5	427.7	79.1	24.6
5R-4	706.98	30.5	8.12	1.81		1.6	907.2		396.4	43.6	20.6	366.1	1.4	419.2	75.7	21.7
8R-4	735.55	31.0	8.27	1.80		1.8	887.5		377.5	44.9	19.0	401.8	1.7	423.5	67.6	20.4
11R-4	765.00	31.0	8.36	1.27		1.3	881.5		258.0	50.3	17.4	379.3	1.5	411.8	54.7	17.5
14R-4	793.85	31.5				1.7	857.8		390.1	52.9	16.9	495.3	1.3		56.8	26.4

Notes: Alk = alkalinity. Only a portion of the table appears here. The complete table is available in **ASCII format.**

Table T8. Headspace gas concentrations of C_1, C_2, and C_3, Site 1165.

Core, section, interval (cm)	Depth (mbsf)	C_1 (ppmv)	C_2 (ppmv)	C_3 (ppmv)	C_1/C_2
188-1165B-					
1H-5, 0-5	6.00	2			
2H-5, 0-5	12.80	2			
3H-5, 0-5	22.30	5			
4H-5, 0-5	31.80	10			
5H-5, 0-5	41.30	15			
6H-5, 0-5	50.80	24			
8H-5, 0-5	69.80	48			
9H-5, 0-5	79.30	72			
10H-5, 0-5	88.80	105			
11H-5, 0-5	98.25	157			
13H-5, 0-5	112.30	247			
14H-5, 0-5	121.65	307			
15H-5, 0-5	128.30	336			
16H-5, 0-5	133.54	432			
17H-5, 0-5	144.30	424			
19X-5, 0-5	149.80	1,009	2		505
20X-5, 0-5	162.20	2,082	2		1,041
21X-5, 0-5	170.30	4,322	7		617
22X-5, 0-5	181.50	7,548	5		1,510
23X-5, 0-5	191.10	11,162	11	1	1,015
24X-5, 0-5	196.20	7,872	4		1,968
27X-5, 0-5	228.00	16,220	8		2,028
28X-5, 0-5	239.10	22,093	11		2,008
30X-5, 0-5	252.40	1,354	1		1,354
32X-5, 0-5	265.00	27,678	12		2,307
33X-5, 0-5	279.10	25,838	14	1	1,846
34X-5, 0-5	287.20	27,109	12		2,259
35X-5, 0-5	296.50	17,211	8		2,151
36X-5, 0-5	305.80	24,623	11		2,238
37X-5, 0-5	315.10	21,428	9		2,381
38X-5, 0-5	324.70	12,952	6		2,159
39X-5, 0-5	334.40	23,529	12		1,961
40X-5, 0-5	342.05	14,125	6		2,354
41X-5, 0-5	352.10	16,294	8		2,037
42X-5, 0-5	363.23	31,952	15		2,130
43X-5, 0-5	372.90	23,396	11		2,127
44X-5, 0-5	382.50	14,869	7		2,124
45X-5, 0-5	392.10	24,142	11		2,195
46X-5, 0-5	401.70	21,963	10		2,196
48X-5, 0-5	420.90	34,294	14	1	2,450
49X-5, 0-5	430.60	26,414	12	1	2,201
50X-5, 0-5	440.20	32,738	13		2,518
51X-5, 0-5	448.30	33,768	14		2,412
52X-5, 0-5	456.40	13,634	6		2,272
53X-5, 0-5	469.00	18,891	8		2,361
54X-5, 0-5	478.60	8,631	5		1,726
55X-5, 0-5	486.80	35,022	18		1,946
56X-5, 0-5	494.85	7,557	9		840
57X-5, 0-5	504.40	60,202	57		1,056
58X-5, 0-5	514.00	34,462	41		841
59X-5, 0-5	526.72	47,276	52		909
60X-5, 0-5	533.30	29,802	33		903
62X-5, 0-5	552.60	32,822	39		842
64X-5, 0-5	571.80	49,849	97		514
65X-5, 0-5	578.40	34,434	64		538
66X-5, 0-5	594.00	82,495	140	6	589
68X-5, 0-5	607.30	34,942	69	3	506
72X-5, 0-5	636.20	35,934	70	2	513
73X-5, 0-5	645.80	26,329	50	2	527
74X-5, 0-5	658.40	18,994	43		442
75X-5, 0-5	665.00	7,232	19		381
188-1165C-					
1R-5, 0-5	60.00	41			
2R-5, 0-5	677.48	38,603	79		489
3R-5, 0-5	687.74	29,329	48		611
5R-5, 0-5	707.08	47,097	116		406
6R-5, 0-5	716.56	29,069	90		323
7R-5, 0-5	724.91	33,070	97		341
8R-5, 0-5	735.65	40,031	114		351
9R-5, 0-5	745.86	93,825	215		436
10R-5, 0-5	754.00	51,772	97		534
11R-5, 0-5	765.10	77,722	201		387
12R-5, 0-5	774.70	102,030	275		371
13R-5, 0-5	781.30	88,575	250		354
14R-5, 0-5	791.00	74,576	236		316
15R-5, 0-5	803.60	81,692	238		343
16R-5, 0-5	813.00	44,822	154		291
17R-5, 0-5	821.00	73,676	243	2	303
18R-5, 0-5	835.10	62,919	236	2	267
19R-5, 0-5	843.20	45,506	149	2	305
20R-5, 0-5	851.40	36,529	152	4	240
21R-5, 0-5	856.50	29,056	130	3	224
22R-5, 0-5	870.70	39,667	165	8	240
23R-5, 0-5	880.30	60,171	225	11	267
24R-5, 0-5	886.90	62,641	216	9	290
25R-5, 0-5	895.10	76,328	271	13	282
26R-5, 0-5	906.20	61,983	200	11	310
27R-5, 0-5	917.30	42,386	166	15	255
28R-5, 0-5	928.50	60,355	259	26	233
29R-5, 0-5	937.70	24,450	73	4	335
30R-5, 0-5	947.30	66,472	302	41	220
31R-5, 0-5	957.00	37,528	147	18	255
32R-5, 0-5	962.10	54,220	255	48	213
34R-2, 0-5	981.30	72,177	279	38	259
35R-5, 0-5	995.50	52,365	243	37	215

Notes: C_1 = methane, C_2 = ethane, C_3 = propane. ppmv = parts per million by volume.

Table T9. Recalculation of headspace gas CH_4 concentrations as microliter CH_4 per liter of wet sediment and as millimolar dissolved CH_4 in pore water, Site 1165.

Core, section, interval (cm)	Depth (mbsf)	Sample weight (g)	Sample volume (mL)*	CH_4 (mL/L)†	CH_4 (mM)‡
188-1165B-					
1H-5, 0-5	6.00	6.5	4.4	7	0
2H-5, 0-5	12.80	6.6	4.4	7	0
3H-5, 0-5	22.30	7.3	4.9	15	0
4H-5, 0-5	31.80	6.6	4.4	35	0
5H-5, 0-5	41.30	7.4	4.9	46	0
6H-5, 0-5	50.80	4.6	3.1	133	0
8H-5, 0-5	69.80	5.2	3.4	231	0
9H-5, 0-5	79.30	5.9	3.9	298	0
10H-5, 0-5	88.80	9.6	6.3	228	0
11H-5, 0-5	98.25	7.5	4.9	482	0
13H-5, 0-5	112.30	6.6	4.3	901	0.1
14H-5, 0-5	121.65	6.5	4.2	1,146	0.1
15H-5, 0-5	128.30	6.2	4.0	1,334	0.1
16H-5, 0-5	133.54	5.6	3.6	1,950	0.1
17H-5, 0-5	144.30	7.2	4.6	1,401	0.1
19X-5, 0-5	149.80	7.3	4.7	3,282	0.2
20X-5, 0-5	162.20	8.4	5.4	5,644	0.4
21X-5, 0-5	170.30	7.3	4.7	14,185	1.0
22X-5, 0-5	181.50	8.5	5.4	20,317	1.4
23X-5, 0-5	191.10	8.2	5.2	31,696	2.2
24X-5, 0-5	196.20	5.9	3.7	34,212	2.4
27X-5, 0-5	228.00	6.0	3.8	70,027	4.9
28X-5, 0-5	239.10	7.4	4.6	73,546	5.2
30X-5, 0-5	252.40	5.3	3.3	6,870	0.5
32X-5, 0-5	265.00	7.1	4.4	98,416	7.1
33X-5, 0-5	279.10	7.6	4.7	84,721	6.2
34X-5, 0-5	287.20	7.2	4.4	95,715	7.0
35X-5, 0-5	296.50	6.4	3.9	70,832	5.2
36X-5, 0-5	305.80	8.0	4.9	76,511	5.7
37X-5, 0-5	315.10	6.9	4.2	80,989	6.1
38X-5, 0-5	324.70	7.3	4.4	45,785	3.4
39X-5, 0-5	334.40	7.9	4.8	75,453	5.7
40X-5, 0-5	342.05	4.7	2.8	86,061	6.6
41X-5, 0-5	352.10	6.3	3.8	70,278	5.4
42X-5, 0-5	363.23	8.5	5.1	94,448	7.3
43X-5, 0-5	372.90	7.5	4.4	81,916	6.4
44X-5, 0-5	382.50	6.3	3.7	65,127	5.1
45X-5, 0-5	392.10	7.5	4.4	85,401	6.7
46X-5, 0-5	401.70	7.7	4.5	75,497	6.0
48X-5, 0-5	420.90	8.8	5.1	99,953	8.0
49X-5, 0-5	430.60	7.5	4.3	95,415	7.7
50X-5, 0-5	440.20	8.4	4.8	102,641	8.4
51X-5, 0-5	448.30	8.8	5.0	99,992	8.2
52X-5, 0-5	456.40	5.4	3.1	74,688	6.2
53X-5, 0-5	469.00	6.5	3.7	83,340	7.0
54X-5, 0-5	478.60	7.3	4.1	33,135	2.8
55X-5, 0-5	486.80	9.9	5.6	90,400	7.6
56X-5, 0-5	494.85	6.0	3.4	37,258	3.2
57X-5, 0-5	504.40	8.0	4.5	208,709	17.9
58X-5, 0-5	514.00	9.7	5.4	93,046	8.0
59X-5, 0-5	526.72	8.2	4.5	160,838	14.0
60X-5, 0-5	533.30	7.3	4.0	118,006	10.3
62X-5, 0-5	552.60	9.9	5.4	88,280	7.9
64X-5, 0-5	571.80	13.4	7.3	87,251	7.9
65X-5, 0-5	578.40	8.2	4.4	120,803	11.0
66X-5, 0-5	594.00	12.8	6.9	157,505	14.5
68X-5, 0-5	607.30	9.6	5.1	101,452	9.4
72X-5, 0-5	636.20	12.4	6.5	74,162	7.1
73X-5, 0-5	645.80	9.3	4.9	81,724	7.9
74X-5, 0-5	658.40	8.2	4.3	69,951	6.8
75X-5, 0-5	665.00	7.4	3.8	30,415	3.0
188-1165C-					
1R-5, 0-5	60.00	11.9	7.9	63	0
2R-5, 0-5	677.48	10.1	5.2	109,524	10.8
3R-5, 0-5	687.74	8.7	4.5	101,977	10.2
5R-5, 0-5	707.08	11.6	5.9	112,547	11.4
6R-5, 0-5	716.56	9.1	4.6	97,123	9.9
7R-5, 0-5	724.91	10.4	5.2	93,064	9.6
8R-5, 0-5	735.65	9.7	4.9	124,544	13.0
9R-5, 0-5	745.86	14.2	7.1	171,008	18.0
10R-5, 0-5	754.00	9.7	4.8	163,024	17.3
11R-5, 0-5	765.10	12.8	6.3	168,000	18.0
12R-5, 0-5	774.70	13.4	6.6	207,584	22.5
13R-5, 0-5	781.30	13.5	6.6	179,104	19.5
14R-5, 0-5	791.00	10.6	5.2	213,860	23.5
15R-5, 0-5	803.60	10.5	5.1	239,311	26.6
16R-5, 0-5	813.00	8.2	4.0	181,779	20.4
17R-5, 0-5	821.00	10.1	4.9	229,959	26.0
18R-5, 0-5	835.10	10.8	5.2	181,323	20.8
19R-5, 0-5	843.20	8.2	3.9	188,115	21.8
20R-5, 0-5	851.40	10.4	4.9	111,955	13.1
21R-5, 0-5	856.50	11.2	5.3	80,902	9.5
22R-5, 0-5	870.70	10.5	4.9	121,625	14.5
23R-5, 0-5	880.30	10.8	5.0	178,874	21.6
24R-5, 0-5	886.90	11.5	5.3	171,865	20.9
25R-5, 0-5	895.10	12.4	5.7	189,801	23.2
26R-5, 0-5	906.20	10.7	4.9	189,907	23.5
27R-5, 0-5	917.30	9.4	4.3	154,817	19.4
28R-5, 0-5	928.50	8.8	4.0	241,344	30.7
29R-5, 0-5	937.70	3.8	1.7	259,941	33.4
30R-5, 0-5	947.30	10.3	4.6	220,206	28.6
31R-5, 0-5	957.00	8.8	3.9	152,870	20.1
32R-5, 0-5	962.10	9.3	4.2	206,770	27.3
34R-2, 0-5	981.30	13.7	6.1	166,049	22.5
35R-5, 0-5	995.50	8.8	3.9	218,720	30.1

Notes: * = sample weight/density, where density = $[0.0000004(\text{depth})^2 + 0.0004(\text{depth}) + 1.4832]$. † = ppmv $CH_4 \times [(20 - \text{sample volume})/\text{sample volume}]$. ‡ = µL/L $CH_4/(f \times 1000 \times 22.4)$, where $f = -0.0004 \times \text{depth} + 0.7224$.

Table T10. Carbon, nitrogen, and sulfur analyses of sediments, Site 1165.

Core, section, interval (cm)	Depth (mbsf)	IC (wt%)	$CaCO_3$ (wt%)	TC (wt%)	OC (wt%)	TN (wt%)	TS (wt%)
188-1165B-							
1H-2, 49-50	1.99	0.072	0.60				
1H-2, 60-61	2.10	0.051	0.43				
1H-5, 60-61	6.60	1.621	13.50				
2H-1, 52-53	7.29	4.840	40.32				
2H-2, 60-61	8.90	2.936	24.46				
2H-6, 60-61	14.90	0.054	0.45	0.12	0.06	0.003	0.062
3H-2, 60-61	18.40	0.013	0.11				
3H-6, 60-61	24.40	0.013	0.11	0.18	0.17	0.009	0
4H-2, 60-61	27.90	0.016	0.13	0.82	0.80	0.024	0
4H-6, 60-61	33.90	0.014	0.12				
5H-1, 33-34	35.63	0.012	0.10				
5H-3, 34-35	38.64	0.007	0.06				
5H-4, 24-25	40.04	0.014	0.12				
5H-5,34-35	41.64	0.011	0.10				
6H-2, 60-61	46.90	0.009	0.08				
6H-5, 60-61	51.40	0.012	0.10				
8H-1, 113-114	54.30	0.017	0.14	0.41	0.39	0.020	0
8H-3, 112-113	59.00	0.016	0.13				
8H-5, 34-35	61.20	0.019	0.16				
9H-1, 39-40	73.69	0.016	0.13				
9H-3, 38-39	76.68	0.023	0.19				
9H-5, 39-40	79.69	0.052	0.44				
10H-1, 112-113	83.92	0.015	0.12				
10H-3, 32-33	86.12	0.029	0.24	0.63	0.60	0.026	0
10H-5, 32-33	89.12	0.026	0.22	0.47	0.45	0.019	0
11H-1, 55-56	92.85	0.018	0.15	0.02	0	0	0
11H-4, 54-55	97.34	0.016	0.13				
13H-1, 67-68	106.97	0.028	0.23				
13H-3, 88-89	110.18	0.033	0.28	0.33	0.30	0.005	0
13H-4, 87-88	111.67	0.023	0.19				
14H-2, 142-143	118.72	0.023	0.19				
14H-4, 114-115	121.29	0.025	0.21	1.83	1.81	0.088	0.131
14H-5, 43-44	122.08	0.031	0.26	2.00	1.97	0.099	0.189
14H-6, 49-50	123.55	0.047	0.39				
16H-2, 32-33	130.62	0.038	0.32	0.33	0.30	0.007	0.050
16H-4, 33-34	132.37	0.017	0.14				
16H-6, 33-34	134.22	0.086	0.71				
17H-1, 80-81	139.10	0.032	0.27	0.68	0.65	0.019	0.220
17H-3, 55-56	141.85	0.021	0.17	0.83	0.81	0.019	0.170
17H-5, 84-85	145.14	0.016	0.14				
19X-1, 97-98	149.27	0.031	0.25	0.16	0.14	0.005	0.132
19X-2, 97-98	150.77	0.022	0.18				
20X-2, 110-111	158.80	0.022	0.18				
20X-4, 65-66	161.35	0.026	0.21				
20X-6, 33-34	164.03	0.056	0.47				
21X-1, 50-51	166.30	0.025	0.21				
21X-4, 111-112	171.41	0.023	0.19				
22X-2, 52-53	177.52	0.022	0.19	0.78	0.75	0.021	0.261
22X-3, 49-50	178.99	0.022	0.18				
22X-5, 65-66	182.15	0.030	0.25				
23X-4, 49-50	190.09	0.025	0.21	0.41	0.39	0.006	0.457
24X-2, 79-80	196.99	0.031	0.26				
27X-2, 79-80	225.79	0.030	0.25				
28X-4, 89-90	238.49	0.025	0.21				
30X-1, 106-107	253.46	0.030	0.25				
32X-2, 6-7	263.56	0.027	0.23	0.53	0.50	0.011	0.054
33X-1, 124-125	272.84	7.468	62.21				
34X-1, 122-123	282.42	0.031	0.26	0.05	0.02	0	0
34X-3, 126-127	285.46	0.032	0.26				
34X-5, 25-26	287.45	7.264	60.51				
34X-6, 36-37	289.06	0.042	0.35				
35X-1, 35-36	290.85	0.033	0.28	0.23	0.20	0	0.040
35X-3, 34-35	293.84	0.031	0.25				

Notes: IC = inorganic carbon, $CaCO_3$ = calcium carbonate, TC = total carbon, OC = organic carbon, TN = total nitrogen, TS = total sulfur. Only a portion of the table appears here. The complete table is available in **ASCII format.**

Table T11. Organic carbon and Rock-Eval pyrolysis on selected samples, Site 1165.

Core, section, interval (cm)	Depth (mbsf)	OC (wt%)	S_1 (mg/g)	S_2 (mg/g)	S_3 (mg/g)	HI (mg/g C)	OI (mg/g C)	T_{max} (°C)
188-1165B-								
4H-2, 60-61	27.90	0.80	0.12	0.21	0.92	26	115	479
10H-3, 32-33	76.70	0.60	0.09	0.15	1.34	25	223	540
14H-4, 114-115	110.20	1.81	0.27	0.70	2.87	39	159	434
14H-5, 43-44	111.70	1.97	0.23	0.60	3.95	30	201	439
17H-4, 80-81	130.60	0.65	0.22	0.37	1.04	57	161	420
17H-3, 55-56	132.40	0.81	0.25	0.50	0.82	61	101	426
22X-2, 52-53	164.00	0.75	0.33	0.47	0.62	62	82	425
32X-2, 6-7	225.80	0.50	0.35	0.38	0.31	75	61	424
53X-5, 126-127	457.70	0.56	0.38	0.48	0.85	86	152	398
188-1165C-								
13R-1, 71-72	779.00	0.56	0.38	0.60	1.21	106	214	432
18R-2, 22-23	827.80	1.31	0.35	0.63	1.43	48	109	437
23R-6, 87-88	882.70	0.62	0.33	0.11	0.00	18	0	439
28R-3, 16-18	925.70	0.51	0.29	0.17	2.88	33	563	439

Note: For explanation of column headings, see **"Organic Matter Characterization,"** p. 21, in "Organic Geochemistry" in the "Explanatory Notes" chapter.

Table T12. Discrete *P*-wave measurements, Site 1165.

Leg	Site	Hole	Core	Type	Section	Top (cm)	Bottom (cm)	Depth (mbsf)	Direction	Velocity (m/s)	Core temperature (°C)	Method
188	1165	B	5	H	1	30.6	30.6	35.61	x	1452	23.5	PWS3
188	1165	B	5	H	2	34.0	34.0	37.14	x	1490	21.6	PWS3
188	1165	B	5	H	3	31.7	31.7	38.62	x	1507	23.1	PWS3
188	1165	B	5	H	4	30.0	30.0	40.10	x	1452	20.9	PWS3
188	1165	B	5	H	5	33.1	33.1	41.63	x	1465	21.0	PWS3
188	1165	B	5	H	6	33.4	33.4	43.13	x	1461	20.8	PWS3
188	1165	B	9	H	4	37.5	37.5	78.18	x	1486	22.7	PWS3
188	1165	B	9	H	5	33.5	33.5	79.64	x	1485	21.5	PWS3
188	1165	B	10	H	7	36.5	36.5	92.17	x	1500	20.8	PWS3
188	1165	B	13	H	6	34.6	34.6	114.15	x	1494	22.8	PWS3
188	1165	B	13	H	7	33.2	33.2	115.63	x	1528	22.9	PWS3
188	1165	B	14	H	1	68.1	68.1	116.48	x	1558	23.1	PWS3
188	1165	B	14	H	2	30.2	30.2	117.60	x	1562	23.1	PWS3
188	1165	B	14	H	3	41.9	41.9	119.22	x	1561	22.6	PWS3
188	1165	B	14	H	4	26.3	26.3	120.41	x	1570	22.6	PWS3
188	1165	B	14	H	5	42.6	42.6	122.08	x	1556	21.6	PWS3
188	1165	B	14	H	6	72.9	72.9	123.79	x	1568	22.0	PWS3
188	1165	B	15	H	1	102.2	102.2	126.32	x	1580	23.6	PWS3
188	1165	B	15	H	2	55.2	55.2	127.35	x	1560	22.5	PWS3
188	1165	B	16	H	2	92.0	92.0	131.22	x	1570	21.8	PWS3
188	1165	B	16	H	4	110.7	110.7	133.15	x	1599	21.4	PWS3
188	1165	B	16	H	6	77.0	77.0	134.66	x	1587	21.1	PWS3
188	1165	B	17	H	1	81.1	81.1	139.11	x	1598	22.5	PWS3
188	1165	B	17	H	2	26.0	26.0	140.06	x	1556	21.7	PWS3
188	1165	B	17	H	3	57.7	57.7	141.88	x	1570	21.6	PWS3
188	1165	B	17	H	5	83.5	83.5	145.13	x	1598	21.8	PWS3
188	1165	B	17	H	6	94.9	94.9	146.75	x	1551	21.8	PWS3
188	1165	B	19	X	1	97.0	97.0	149.27	x	1577	22.4	PWS3
188	1165	B	19	X	2	100.2	100.2	150.80	x	1569	22.7	PWS3
188	1165	B	20	X	1	124.2	124.2	157.44	x	1599	22.4	PWS3
188	1165	B	20	X	3	71.7	71.7	159.92	x	1588	21.9	PWS3
188	1165	B	20	X	4	59.7	59.7	161.30	x	1577	22.0	PWS3
188	1165	B	20	X	5	80.9	80.9	163.01	x	1619	22.1	PWS3
188	1165	B	20	X	6	51.0	51.0	164.21	x	1705	22.0	PWS3
188	1165	B	21	X	1	55.7	55.7	166.36	x	1539	21.4	PWS3
188	1165	B	21	X	2	55.1	55.1	167.85	x	1580	21.7	PWS3
188	1165	B	21	X	3	29.9	29.9	169.10	x	1552	23.0	PWS3
188	1165	B	21	X	4	66.2	66.2	170.96	x	1572	22.5	PWS3
188	1165	B	21	X	5	24.0	24.0	172.04	x	1567	22.4	PWS3
188	1165	B	22	X	1	69.7	69.7	176.20	x	1546	22.3	PWS3
188	1165	B	22	X	2	77.1	77.1	177.77	x	1535	22.1	PWS3
188	1165	B	22	X	3	66.7	66.7	179.17	x	1552	21.3	PWS3
188	1165	B	22	X	4	38.8	38.8	180.39	x	1591	22.2	PWS3
188	1165	B	22	X	5	65.1	65.1	182.15	x	1587	22.0	PWS3
188	1165	B	23	X	6	65.9	65.9	183.65	x	1561	21.8	PWS3
188	1165	B	22	X	7	22.7	22.7	184.73	x	1561	21.4	PWS3
188	1165	B	23	X	1	43.9	43.9	185.54	x	1553	21.9	PWS3
188	1165	B	23	X	2	45.6	45.6	187.06	x	1558	21.4	PWS3
188	1165	B	23	X	3	34.9	34.9	188.45	x	1575	21.8	PWS3
188	1165	B	23	X	4	77.1	77.1	190.37	x	1556	21.5	PWS3
188	1165	B	23	X	5	68.5	68.5	191.79	x	1551	21.4	PWS3
188	1165	B	23	X	6	22.0	22.0	192.82	x	1564	21.9	PWS3
188	1165	B	23	X	7	13.6	13.6	194.24	x	1545	21.4	PWS3
188	1165	B	24	X	1	77.7	77.7	195.48	x	1587	21.4	PWS3
188	1165	B	24	X	2	83.7	83.7	197.04	x	1577	21.6	PWS3
188	1165	B	24	X	3	44.3	44.3	198.14	x	1607	21.2	PWS3
188	1165	B	27	X	1	40.2	40.2	223.90	x	1571	21.2	PWS3
188	1165	B	27	X	2	33.8	33.8	225.34	x	1563	21.3	PWS3
188	1165	B	27	X	3	57.4	57.4	227.07	x	1555	21.0	PWS3
188	1165	B	27	X	5	42.8	42.8	229.93	x	1625	21.7	PWS3
188	1165	B	27	X	6	15.6	15.6	231.16	x	1584	21.8	PWS3
188	1165	B	28	X	1	104.5	104.5	234.15	x	1546	19.9	PWS3
188	1165	B	28	X	2	62.5	62.5	235.23	x	1619	20.1	PWS3
188	1165	B	28	X	3	54.6	54.6	236.65	x	1557	20.0	PWS3

Notes: PWS1 = *P*-wave sensor 1, PWS2 = *P*-wave sensor 2, PWS3 = *P*-wave sensor 3. H = advanced hydraulic piston core, X = extended core barrel, R = rotary core. Only a portion of the table appears here. The complete table is available in **ASCII format.**

Table T13. Measurements of undrained shear strength, Site 1165.

Automated vane shear data		Fall cone data		Pocket penetrometer data	
Depth (mbsf)	C_u (kPa)	Depth (mbsf)	C_u (kPa)	Depth (mbsf)	C_u (kPa)
0.40	3	0.34	6	129.55	87
1.84	6	1.83	9	131.37	122
4.84	6	3.33	7	133.18	166
6.36	7	4.84	9	139.11	142
7.14	2	6.33	11	139.99	73
8.64	2	7.13	3	141.83	108
10.13	2	16.13	6	144.19	96
11.65	1	16.63	24	145.20	92
13.14	2	18.14	28	146.71	136
14.63	2	19.66	34	149.31	92
16.15	3	21.21	34	150.79	97
16.66	12	22.63	36	157.54	92
18.16	18	24.13	43	158.70	93
19.68	21	25.64	28	159.98	149
21.23	25	26.13	36	161.40	112
22.62	25	27.72	39	162.90	117
24.13	27	29.15	39	164.26	73
26.45	19	30.63	53	166.45	67
27.63	20	32.22	48	167.85	109
29.22	29	33.67	60	169.20	92
30.65	27	35.14	48	170.96	128
32.14	22	38.63	39	172.15	75
33.74	35	37.16	43	175.95	83
35.19	29	40.08	39	177.70	108
35.60	17	43.08	53	179.05	72
37.14	40	45.20	7	180.50	125
38.61	29	41.65	53	182.00	137
40.10	34	46.63	39	183.70	225
41.63	43	49.00	48	185.80	75
41.63	52	49.63	18	186.16	110
45.20	7	51.13	8	186.90	200
46.64	13	52.63	9	188.40	150
49.01	28	64.13	58	190.45	150
49.64	13	65.62	80	191.85	238
51.15	5	67.92	64	192.82	240
52.65	4	68.64	83	194.48	340
64.93	38	70.14	64	197.03	350
67.90	41	71.65	53	198.02	440
68.63	54	75.14	71	225.10	460
70.13	47	73.69	59	226.55	450
71.63	36	76.65	119	228.83	260
73.70	40	117.20	119	230.75	260
75.13	52	117.10	170	234.02	560
76.64	96	78.19	79	235.65	400
78.17	64	79.70	83	236.60	300
79.65	81	80.86	113	238.83	600
80.85	48	83.12	89	239.44	500
83.16	39	84.66	53	240.90	600
84.63	54	86.16	99	262.65	200
86.13	83	87.62	74	263.72	200
87.66	70	89.15	119	319.34	420
89.13	89	90.65	79	321.58	440
90.63	52	92.15	63	325.75	440
92.16	43	92.65	63	327.20	640
92.63	21	94.07	113	331.05	700
95.64	54	95.58	140	333.76	450
97.16	43	97.10	64	334.69	640
98.62	45	98.53	83	336.60	744
99.58	73	99.51	130	367.05	640
106.61	37	106.58	83	457.75	800
109.68	78	108.07	83		
111.18	95	109.62	89		
112.65	76	111.12	130		
114.15	82	112.60	99		
115.63	71	114.10	190		
116.46	87	115.60	130		
117.57	104	116.40	130		
119.19	95	117.54	119		
120.58	115	119.20	140		
122.11	92	120.56	235		
123.89	95	122.12	175		
126.29	164	123.53	123		
127.39	97	126.27	235		
129.49	72	127.40	155		
		129.50	155		
		145.17	140		
		146.67	140		
		148.85	89		
		150.86	140		
		157.44	74		
		158.62	89		
		159.89	123		
		161.30	74		
		162.94	103		
		164.16	73		
		167.86	53		
		166.35	71		
		169.10	119		
		170.96	205		
		172.05	83		
		177.69	58		
		178.96	89		
		180.40	190		
		182.15	275		
		183.56	175		
		184.65	155		
		185.53	145		
		186.90	370		
		188.46	275		
		190.30	370		
		191.66	275		

Note: This table is also available in **ASCII format.**

Table T14. Thermal conductivity measurements, APC and XCB cores, using full-space needle, Site 1165.

Core, section	Depth (mbsf)	Thermal conductivity (W/[m·°C]) Reading 1	Reading 2	Reading 3	Average
188-1165B-					
1H-3	3.75	0.431	0.457	0.407	0.432
1H-5	6.34	0.973	0.965	0.952	0.963
2H-3	10.55	1.071	1.015	1.060	1.049
2H-6	15.05	0.835	0.827	0.755	0.806
3H-3	20.05	0.934	0.937	0.909	0.927
3H-6	24.55	0.929	0.993	0.972	0.965
4H-3	29.55	0.921	0.953	0.962	0.945
4H-6	34.05	0.873	0.850	0.876	0.866
5H-3	39.05	0.838	0.851	0.824	0.838
5H-6	43.55	0.884	0.889	0.877	0.883
6H-3	48.55	0.889	0.867	0.923	0.893
6H-6	53.05	0.949	0.887	0.818	0.885
8H-3	67.55	0.914	0.909	0.884	0.902
8H-6	72.05	0.937	0.922	0.922	0.927
9H-3	77.05	0.921	0.925	0.948	0.931
9H-6	80.98	0.918	0.937	0.969	0.941
10H-3	86.55	0.840	0.836	0.839	0.838
10H-6	91.05	0.941	0.986	0.969	0.965
11H-3	96.05	0.875	0.888	0.923	0.895
11H-6	99.73	0.873	0.888	0.883	0.881
13H-3	110.05	0.979	0.961	0.950	0.963
13H-6	114.55	0.997	0.956	0.986	0.980
14H-3	119.55	0.915	0.984	0.980	0.960
14H-6	123.81	0.927	0.935	0.944	0.935
15H-2	127.55	0.949	0.994	0.989	0.977
16H-2	131.05	0.959	0.955	0.955	0.956
16H-4	132.79	0.946	0.996	1.004	0.982
17H-3	142.05	0.761	0.740	0.760	0.754
17H-6	146.55	0.869	0.853	0.837	0.853
20X-3	159.95	0.816	0.862	0.807	0.828
20X-6	164.45	0.792	0.822	0.833	0.816
21X-3	169.55	0.804	0.779	0.779	0.787
22X-3	179.25	0.892	0.911	0.925	0.909
22X-6	183.75	0.930	0.925	0.964	0.940
23X-3	188.85	1.039	1.036	0.938	1.004
23X-6	193.35	1.035	0.976	0.970	0.994
27X-3	227.25	0.852	0.812	0.844	0.836
27X-6	231.25	0.880	0.884	0.891	0.885
28X-3	236.85	0.988	1.001	0.996	0.995
28X-6	241.35	1.051	1.017	1.036	1.035
30X-1	253.15	0.887	0.894	0.890	0.890
32X-2	264.25	0.994	1.032	1.034	1.020
33X-3	275.35	0.925	0.925	0.928	0.926
33X-6	279.85	0.933	0.966	0.947	0.949
34X-3	284.95	0.964	0.959	0.918	0.947
34X-6	289.50	0.879	0.889	0.880	0.883
35X-3	294.25	0.833	0.830	0.833	0.832
35X-5	297.25	0.885	0.882	0.870	0.879
36X-3	303.55	0.905	0.940	0.931	0.925
36X-6	308.05	0.969	0.964	0.929	0.954
37X-3	312.85	0.881	0.883	0.870	0.878
37X-6	317.35	1.013	1.016	1.031	1.020
38X-3	322.45	0.884	0.876	0.851	0.870
38X-6	326.95	0.842	0.827	0.838	0.836
39X-3	332.15	0.862	0.872	0.856	0.863
39X-6	336.40	0.927	0.944	0.954	0.942
40X-3	341.30	0.845	0.849	0.821	0.838
40X-6	345.95	0.896	0.890	0.882	0.889
41X-3	351.35	1.049	0.914	0.966	0.976
42X-3	361.03	1.014	0.979	1.030	1.008
43X-3	370.65	0.908	0.937	0.987	0.944
43X-5	373.20	0.961	0.940	0.847	0.916
44X-3	380.25	0.881	0.881	0.873	0.878
45X-3	389.85	0.869	0.886	0.866	0.874
46X-3	399.45	1.160	1.078	0.947	1.062
46X-6	403.95	1.016	1.026	0.976	1.006
48X-3	418.65	1.053	1.008	1.024	1.028
48X-6	423.15	0.990	0.995	0.991	0.992
49X-3	428.35	0.893	0.894	0.895	0.894
49X-6	432.85	0.778	0.768	0.774	0.773
50X-3	437.95	0.850	0.832	0.867	0.850
50X-6	442.45	0.860	0.876	0.908	0.881
51X-3	447.55	0.863	0.835	0.893	0.864
52X-3	457.15	0.782	0.792	0.791	0.788
53X-3	466.75	0.888	0.905	0.886	0.893
53X-6	471.10	0.858	0.839	0.863	0.853
54X-3	476.35	0.864	0.866	0.853	0.861
54X-5	479.10	0.826	0.842	0.831	0.833
55X-3	485.95	0.844	0.838	0.838	0.840
56X-3	495.30	1.046	1.072	1.038	1.052
57X-2	503.65	0.919	0.988	0.928	0.945

Note: This table is also available in **ASCII format.**

Table T15. Thermal conductivity measurements, RCB cores, using half-space needle, Site 1165.

Core, section	Depth (mbsf)		Thermal conductivity (W/[m·°C])				
	Top	Bottom	Reading 1	Reading 2	Reading 3	Reading 4	Average
188-1165C-							
3R-4	687.08	687.13	1.757	2.108	1.587	1.848	1.825
3R-4	686.30	686.36	1.386	1.365	1.337	1.210	1.325
6R-3	714.50	714.54	2.202	2.872	1.806	0.089	1.742
6R-5	716.68	716.78	1.507	1.352	1.239		1.366
10R-5	756.10	756.16	1.268	1.272	1.641	1.407	1.397
15R-4	802.72	802.80	1.160	1.127			1.144
18R-1	827.12	827.20	0.965	1.283	2.684	1.723	1.664
18R-4	831.28	831.38	1.413	1.447	1.411	1.436	1.427
19R-5	842.12	842.20	1.432	1.487	1.576	1.484	1.495
23R-6	881.83	881.95	1.628	1.653	1.641	1.627	1.637
31R-2	953.21	953.47	1.774	1.535	1.720	1.679	1.677
31R-5	957.00	957.19	1.818	1.735	1.667	1.735	1.739
33R-1	970.60	970.68	1.679	1.734	1.780	1.535	1.682

Note: This table is also available in **ASCII format.**

Table T16. Measured and estimated temperatures, geothermal gradients, and heat-flow estimations, Site 1165.

Depth (mbsf)	Measured conductivity (W/[m·°C])	Stabilized temperature (°C)	Thermal gradient (°C/km)	Heat flow (mW/m²)	Average thermal gradient (°C/km)
0.0		**–0.3**			
35.3	**0.90**	**1.8**			
63.8	**0.90**	**ND**			
92.3	**0.90**	**5.0**			
125.8	**0.96**	**6.5**	**53.4**	**51.4**	**53.4**
200.0	1.00	10.4	51.4	**51.4**	53.3
300.0	1.02	15.5	50.6	**51.4**	52.6
400.0	1.02	20.6	50.4	**51.4**	52.0
500.0	1.04	25.6	49.5	**51.4**	51.6
700.0	1.36	34.3	37.7	**51.4**	49.3
830.0	1.42	39.1	36.1	**51.4**	47.4
890.0	1.63	41.1	31.5	**51.4**	46.5
960.0	1.70	43.3	30.1	**51.4**	45.3
970.5	1.70	43.6	30.2	**51.4**	45.2

Notes: Bold numbers indicate measured volume. All others are estimated values based on projection of temperature gradient. ND = no data.

Table T17. Logging operations summary, Hole 1165C.

Operations depth summary	Run 1 Triple combo (main)	Run 2 FMS-sonic (pass 1)	Comments
			Logging operations commenced at 0700 hr on 02/13/00. A total of 30 barrels of sepiolite was circulated; no KCl used. Sea state/heave: average 1.0–1.5 m; maximum 3.2 m.
Water depth, seafloor or mudline:			
Mudline (mbrf): driller's depth	3548.7	3548.7	Run into hole speed = 10,000 ft/hr.
Mudline (mbrf): logger's depth	3546.5		Triple combo uprun speed = 900 ft/hr.
Mudline (mbsl)	3537.6	3537.6	FMS-sonic uprun speed = 500 ft/hr.
			Logging operations ceased at 0940 hr on 02/14/00.
Drill-pipe depth during logging:			
Initial pipe depth (mbrf): driller's depth	3638.4	3724.6	Drill pipe initially set at 89.7 mbsf, then three stands of pipe were added to 175.9 mbsf to push through an obstruction.
Initial pipe depth (mbsf): using driller's depth	89.7	175.9	
Final pipe depth (mbrf): driller's depth	3724.6	3724.6	Drill pipe remained in place at 175.9 mbsf throughout logging operations to prevent the possibility of the logging tools getting stuck on the uprun.
Final pipe depth (mbrf): depth from logs	3721	3721	
Final pipe depth (mbsf): using driller's depth	175.9	175.9	
Final pipe depth (mbsf): using logger's depth	174.5	174.5	Final pipe depth = initial log depth.
Sticking encountered during logging:			
Depth of first bridge or ledge (mbrf; winch)	3666	3850	First ledge encountered at 119 mbsf, 20 m below the base of the pipe. Attempts to break through the obstruction failed, so the tool string was partially rigged down and three stands of drill pipe were added. Pipe remained in place at this depth throughout the logging operations.
Depth of first bridge or ledge (mbsf)	119	303	
Depth of second bridge or ledge (mbrf; winch)	3742	4131	
Depth of second bridge or ledge (mbsf)	195	584	
Depth of third bridge or ledge (mbrf; winch)	3850		
Depth of third bridge or ledge (mbsf)	303		Second and third ledges, encountered at 195 and 303 mbsf, posed no real threat to operations on either run.
Depth of fourth bridge or ledge (mbrf; winch)	4132		
Depth of fourth bridge or ledge (mbsf)	585		A tight spot at 585 mbsf prevented run 2 from reaching bottom.
Final tool depth:			
(mbrf; winch)	4542.5	4131.8	Triple combo reached bottom, but FMS-sonic was halted by an obstruction at 585 mbsf, where sticking was noted on first run.
(mbsf): using logger's depth	996.0	585.3	
Total hole depth (m):	999.1	999.1	
Length of logging run (m):	821.5	410.8	

Note: FMS = Formation MicroScanner; mbrf = meters below rig floor; mbsl = meters below sea level.

Table T18. Correlation of density, resistivity, and PEF peaks observed in the downhole logs to carbonate-cemented intervals in the cores, Site 1165.

Log depth (peak) (mbsf)	PEF (peak)	Density (peak)	Resistivity (peak)	Gamma (negative peak)	Core, section, interval (cm)	Core depth (mbsf)	Description
					188-1165B-		
650.8	B	B	B	B	73X-1, 25-33	646.05-646.13	Carbonate-cemented greenish claystone
					188-1165C-		
687.9	N	S	B	S	3R-4, 65-105	686.89-687.29	Claystone with sand grains, calcareous at top
716.3	N	S	S	B	6R-3, 71-96	714.50-714.75	Carbonate interval with sand grains and lonestones
731.8	B	B	S	S	8R-1, 33-57	763.20-763.44	Carbonate interval with sand grains and lonestones
744.0	N	S	S	S	9R-3, 55-70	743.41-743.56	Structureless coarser grained material (IRD)
753.9	N	S	B	S	10R-3, 100-150	753.50-754.00	Coarser grained material (IRD)
800.0	N	S	S	S	14R-6, 105-150	796.55-797.00	Small chert nodule
805.0	N	S	S	S	15R-5, 30-35	803.90-803.95	Small carbonate nodule and small chert nodule
855.5	S	B	B	S	21R-1, 30-50	855.30-855.50	Massive calcareous interval
870.0	N	S	S	N	22R-2, 15-68	866.35-866.88	Calcareous silt laminae
883.1	B	B	B	B	23R-6, >85	>882.65	Massive calcareous interval >30 cm thick
903.1	N	B	B	B	26R-3, >74	>906.94	Silt laminae with calcareous material
918.4	N	S	B	B	27R-5, 0-20	918.80-919.00	Lighter nodule, possibly calcified
930.2	S	S	S	S	28R-5, >67	>929.19	Calcite-filled laminations
960.9	B	B	B	B	32R-2, 35-50	962.45-962.60	Calcite-rich laminations

Notes: IRD = ice-rafted debris. PEF = photoelectric effect. B = big peak, N = no peak, S = small peak.

Table AT1. Summary of accessory components identified in foraminiferal residues, Site 1165.

Core, section, interval (cm)	Residue	Sorting	Planktonic foraminifers	Benthic foraminifers	Sponge spicules	Ostracods	Echinoid spines	Bone, teeth	Orosphaerid radiolaria	Glauconite	Chert	Dolomite	Crystalline pyrite	Framboidal pyrite	Volcanic glass	Micrometeorite
188-1165A-																
1H-CC	0	P	R	R	Tr					Tr						
188-1165B-																
1H-CC	0		C	C		X	X									
2H-CC	0	P	R	R	Tr			Tr		Tr					N	
3H-CC	0	P	B	B	Tr					Tr						
4H-CC	0	P	B	B												
5H-CC	0	P	B	R						Tr					Tr	
6H-5, 70-75	0	P	C	B	Tr								N			
6H-CC	0	P	Tr	B	Tr					Tr						
8H-CC	S	P	B	B	Tr											
9H-CC	0	P	B	B	Tr					Tr						
10H-CC	0	P	B	B	Tr					Tr						
11H-CC	0		B	B						N						
12H-CC	0	P	B	B	Tr					N					Tr	
13H-CC	S	P	B	R						Tr						
14H-CC	0	P	C	C	Tr		X			Tr						X
15H-CC	0	P	B	B						Tr						
16H-CC	S	P	B	B	Tr			Tr		Tr						
17H-CC	0	P	B	R	Tr					Tr						
18H-CC	0	P	B	R	Tr					Tr			Tr			
19X-CC	0	P	B	B	Tr											
20X-5, 120	S		B	C												
20X-CC	S	G	B	B				Tr		Tr						
21X-CC	M		B	B	Tr											
22X-CC	S	P	B	B						Tr						
23X-CC	M	P	B	B						Tr						
24X-CC	S		C	C												
26X-CC	S		B	R						Tr						
27X-CC	M		B	B												
28X-CC	M		B	B												
30X-CC	S	P	B	B												
32X-CC	M		B	B					N				X			
33X-CC	M	P	B	B					N							
34X-CC	M	P	B	B					N				X			
35X-CC	0	P	B	B					N				Tr			
36X-CC	S		B	B					Tr							
37X-CC	0		B	B									C			
38X-CC	S	P	B	B	Tr			TB	Tr				Tr			
39X-CC	S	G	B	B	Tr			Tr	Tr							
40X-CC	0		B	B							N		X			
41X-CC	M		B	B									Tr			
42X-CC	0		B	B												
43X-CC	S	G	B	B							Tr		Tr			
44X-CC	M		B	B									Tr			
45X-CC	M		B	B			Tr						X	X		
46X-CC	M		B	B							Tr					
48X-CC	M		B	B												
49X-CC	M		B	B												
50X-CC	M		B	B												
51X-CC	M		B	B												
52X-CC	M		B	B							Tr					
53X-CC	0		B	B							Tr					
54X-CC	M		B	B												
55X-CC	S	G	B	B	Tr			T								
56X-CC	0		B	B							X					
57X-CC	0		B	B												
58X-1, 134	S		B	C												
58X-CC	0		B	B												
59X-CC	0		B	B												
60X-CC	0		B	B												
61X-CC	0		B	B												
62X-CC	0		B	R												
63X-CC	0		B	B												
64X-CC	0		B	B							Tr					
65X-CC	0		B	B												
66X-CC	0		B	B												
67X-CC	0		B	B							N					
68X-CC	0		B	B							N					
69X-CC	0		B	B												
70X-CC	0		B	B							Tr					
71X-CC	0		B	B							N					
72X-CC	0		B	B							N					
73X-CC	M		B	B							Tr					
74X-1, 26	0		R	B												
74X-CC	S		R	R					Tr		N					
75X-CC	M		B	B							N					
76X-CC	0		B	B							A					
188-1165C-	0															
1R-CC	0	P	B	B						N					Tr	
2R-1, 36	M		B	R												
2R-3, 83	0		B	R												
2R-CC	0		R	B												
3R-CC	0		B	R												
4R-CC	M		B	R												
5R-CC	0		B	B										Tr		
6R-CC	M		B	B												
7R-CC	M		B	B												
8R-CC	0		B	B												
9R-CC	0		B	B												
10R-CC	0		B	B							Tr					
11R-CC	0		R	B												
12R-CC	0		B	R												
13R-CC	0		B	R												
14R-CC	0		B	R												
15R-CC	0		B	R												
16R-CC	0		B	R												
17R-CC	0		B	R												
18R-2, 56-58	0		B	R					T							
18R-CC	0		B	R												
19R-CC	0		B	B												
20R-CC	0		B	R												
21R-CC	0		B	R												
22R-CC	0		B	R												
23R-CC	0															
24R-CC	0		B	B												
25R-CC	0		B	R												X
26R-CC	0		B	R												
27R-CC	0		B	B												
28R-CC	0		B	B												
29R-4, 130-150	0		B	C	Tr											
29R-CC	0		B	B												
30R-3, 142-144	0		B	R					Tr							
30R-5, 34-36	0		B	A												
30R-CC	0		B	B												
31R-CC	0		B	B												
32R-CC	0		B	B												
33R-CC	0		B	B												
34R-CC	0		B	B												
35R-CC	0		B	B												

Notes: Residue size: L = large, M = moderate, S = small, 0 = none. Sorting of terrigenous fraction: G = good, P = poor. Foraminifers: C = common, F = few, R = rare, B = barren. Other components: X = present, Tr = trace, N = noteworthy.